Computational Fluid Dynamics Modelling of a Polymer Electrolyte Membrane Fuel Cell under Transient Automotive Operations

Pattarapong Choopanya

A Thesis Submitted in Partial Fulfilment of the
Requirements for the Degree of

Doctor of Philosophy

Department of Engineering and Design

Computational Fluid Dynamics Modelling of a Polymer Electrolyte Membrane Fuel Cell under Transient Automotive Operations

Pattarapong Choopanya

Bachelor of Automotive Engineering, Loughborough University, 2009
Master of Automotive Engineering, Loughborough University, 2010

Advisory Committee

Dr Zhiyin Yang, Main Supervisor
Thermo-fluid Mechanics Research Centre, University of Sussex
Dr William Wang, Second Supervisor
Department of Engineering and Design, University of Sussex

Declaration

I hereby declare that this thesis has not been and will not be submitted in whole or in part to another University for the award of any other degree.

Signature:

Pattarapong Choopanya
August, 2015

Abstract

A polymer electrolyte membrane (PEM) fuel cell is probably the most promising technology that will replace conventional internal combustion engines in the near future. As a primary power source for an automobile, the transient performance of a PEM fuel cell is of prime importance. In this thesis, a comprehensive, three-dimensional, two-phase, multi-species computational fuel cell dynamics model is developed in order to investigate the effect of flow-field design on the magnitude of current overshoot/undershoot and characteristics of current response when the cell is subjected to different voltage change patterns representing an automotive operation.

The meshing strategy specific to PEM fuel cell modelling is studied in a systematic manner and employed in all analyses presented in this thesis. The predicted results compare very well with experimental data under both steady-state and transient operations. Two computational domains are used – the straight single-channel and practical-scale square cells with parallel, single-serpentine, and triple-serpentine flow-fields.

The results from the straight single-channel cell suggest that the magnitude of current overshoot/undershoot increases with the voltage change rate. The behaviour of a current response curve is the result of complex interplay between water content at both sides of the membrane. It is also found that current overshoot/undershoot is amplified with the presence water flooding in the cell. The results from the square cell reveal that current overshoot/undershoot is caused by non-uniformity of local current density over the active area confirming the effect of flow-field geometry on transient response of the cell. By comparing the transient performance between the three flow-fields, a direct relationship between degree of water flooding in the cell and magnitude of current overshoot/undershoot has been found. A conclusion has been drawn which states that a cell with superior water removal ability will experience smaller current overshoot/undershoot.

Acknowledgements

Upon completion of this thesis, I would like to make grateful acknowledgement to my supervisor, Dr Zhiyin Yang, who introduced me to the fascinating world of computational fluid dynamics back then in my undergraduate time at Loughborough University and later becomes my supervisor at the University of Sussex. All the work presented in this thesis has benefitted from his constructive comments and expertise in CFD. His support, motivation, and encouragement during the past three years are deeply appreciated.

My thanks also go to Dr Zhijun Peng from the University of Hertfordshire, my previous main supervisor, who initiated this PEM fuel cell modelling project. I would like to thank Dr Sirivatch Shimpalee from the University of South Carolina for always being there to give me answers regarding fuel cell modelling whenever I have a question even though we have not even met in person. Special thanks go to the two awesome chaps at Sussex High Performance Computing facility, Jeremy Maris and Tom Armour. The completion of my Ph.D. thesis is highly attributable to their kind help and 24/7 support.

I thank my wonderful friends and colleagues whom I meet here in Sussex including Dr Siska Riefelyna, Dr Raouf Mobasheri, Dr Thana Cheepsomsong, Dr Pavlos Dimitriou, Dr Jirapas Jongjitwimol, Dr Li Cheng, Dr Prapanporn Rattana, and those who are to become doctors soon; Mohammed Al-darkazali, Jun Liang, Yeru Shang, Xingnan Zhang, for letting me be part of this big family during my time in Sussex. Thank you Hung Wan-Leng, Sarote Boonseng, Supojjanee Sansook, Nitipon Piwmow, and Kiattisak Thepsuriya for your love and support in both academic and non-academic issues.

Words cannot express how grateful I am to my father, my mother, and my two sisters. Your love, support, encouragement, and patience throughout this lifelong journey in pursuit of my dream mean so much to me – especially when there is a 6000-mile distance between us. Finally, I would like to express my sincere gratitude to the Royal Thai Government for their financial support during my study and for giving me an opportunity to study in this beautiful country, to live and to learn, and to experience things money cannot buy. Thank you very much.

Pattarapong Choopanya

25 August 2015

Hove, United Kingdom

To my beloved dad, mum, and two beautiful sisters. This thesis would not have been completed without your love and support.

Contents

List of Tables

List of Figures

Nomenclature

a	[-]	Liquid water activity
	[m^2]	Area
	[m^{-1}]	Specific active surface area
C_i	[kmol m^{-3}]	Local molar concentration of species *i*
$D_{j,i}$	[m^2s^{-1}]	Diffusion coefficient of species *i*, in *j* direction
E	[Jkg^{-1}]	Specific total energy
F	[$Cmol^{-1}$]	Faraday's constant, 96 487
h_0	[Jkg^{-1}]	Specific total enthalpy
i	[Am^{-2} or Acm^{-2}]	Local current density
	[Jkg^{-1}]	Specific internal energy
$\boldsymbol{J}_{j,i}$	[$kgm^{-2}s^{-1}$]	Diffusional mass flux of species *i*, in *j* direction
$j_{an.0}^{ref}, j_{ca.0}^{ref}$	[Am^{-2}]	Reference exchange current density
k	[m^2]	Permeability
	[$Wm^{-1}K^{-1}$]	Thermal conductivity
M	[kg $kmol^{-1}$]	Molar mass
n_d	[-]	Osmotic drag coefficient
P	[Pa]	Pressure
R	[$Jmol^{-1}K^{-1}$]	Universal gas constant, 8.314
R_{an}, R_{ca}	[Am^{-3}]	Transfer current density
r_w	[$kgm^{-3}s^{-1}$]	Liquid water condensation rate
s	[-]	Liquid water saturation
T	[K]	Absolute temperature
$\boldsymbol{V}$	[ms^{-1}]	Velocity vector
w_i	[-]	Mass fraction of species *i*
x_i	[-]	Mole fraction of species *i*

Greek characters

α	[-]	Charge transfer coefficient
γ	[-]	Concentration parameter
ε	[-]	Porosity
η	[V]	Overpotential
λ	[-]	Membrane water content
μ	[Pa·s]	Dynamic viscosity
ξ	[-]	Stoichiometric ratio

ρ	[kgm^{-3}]	Density
σ	[Sm^{-1}]	Electrical/protonic conductivity
	[Nm^{-1}]	Surface tension
$\bar{\bar{\tau}}$	[Nm^{-2}]	Stress tensor
ϕ	[V]	Electric potential

Subscripts and Superscripts

an	Anode
ca	Cathode
eff	Effective
liq	Liquid phase
m	Membrane phase
ref	Reference
s	Solid phase
sat	Saturation

Abbreviations

APU	Auxiliary power unit
CFCD	Computational fuel cell dynamics
CFD	Computational fluid dynamics
CL	Catalyst layer
DPM	Diesel particulate matter
EV	Electric vehicle
GDL	Gas diffusion layer
GHG	Green house gas
HFCV	Hydrogen-fuel cell vehicle
HICEV	Hydrogen-internal combustion engine vehicle
HOR	Hydrogen oxidation reaction
ICE	Internal combustion engine
LEV	Low emission vehicle
MEA	Membrane electrode assembly
ORR	Oxygen reduction reaction
PEM	Polymer electrolyte membrane
PPU	Primary power unit
ULEV	Ultra-low emission vehicle
ZEV	Zero emission vehicle

Chapter 1
Introduction

"Whereas the 19th Century was the century of the steam engine and the 20th Century was the century of the internal combustion engine, it is likely that the 21st Century will be the century of the fuel cell."

Brian Cook, Heliocentris

As electrical devices become common in our daily lives and more conventional tools become electrified, we tend to perceive that the word "electric" signifies something hi-tech, sophisticated, and futuristic. Recent attentions on hybrid or electric hybrid vehicle and alternative energy might delusively mislead some people to think that these are cutting-edge innovations. The concept of an electric car, nevertheless, is nothing new. In fact, its history is as old as a gasoline-powered vehicle or even the development of an automobile itself [1]. Moreover, before the invention of a gasoline-powered automobile by Karl Benz in 1886, early automobiles were already powered by various alternatives such as steam engines, batteries, or even hydrogen internal combustion engines (ICE). However, owing to a great advancement in the internal combustion engine technology and major barriers of batteries such as cost, weight, capacity, and charging time at that period, gasoline and diesel-powered vehicles have therefore overshadowed their rivals for almost a century.

As a trade-off, the by-products from the combustion of gasoline and diesel are released to the atmosphere as harmful carbon dioxide, carbon monoxide, oxides of nitrogen known as NO_X, and unburned hydrocarbons such as diesel particulate matters or diesel soot. The effect of such chemicals did not reach a worrying level until recently. Their hazardous effect has been accumulating over a century and finally starts to threaten the environment and in turn people's health around the world. Scientists and engineers therefore need to look back at those once-abandoned technologies in order to find an alternative and preferably sustainable substitute to the ICEs. It has been said that the most promising technology that will replace ICEs in the near future is a polymer electrolyte membrane (PEM) fuel cell which will be referred to as a PEM fuel cell throughout the thesis henceforth.

In order to pave the way to the discussions and analyses in later chapters, this chapter addresses major aspects of a PEM fuel cell in detail starting off with background knowledge of hydrogen economy which is then followed by a brief introduction to fuel cell technology. The operating principles and major components of a PEM fuel cell are explained next and finally the chapter ends with research objectives and thesis outline.

1.1 A Transition to Hydrogen Economy

1.1.1 Fossil Fuels and Current Status

Petrol and diesel are petroleum products after certain refinement and/or blending processes. However, the petroleum or crude oil is also known as fossil fuel which is a product of a naturally occurring decomposition process of dead organisms inside the geological layers over millions of years. These carbon-rich fuels also include coal and natural gas and has dominated other types of fuel in the power generation application for over a century. However, there are issues that require attention and re-examination from scientists and engineers or even governments as discussed separately in the following sections.

Oil Depletion and National Security

Despite the fact that a decomposition cycle of dead animals and plants has always been taking place and will continue to do so, this process is prohibitively slow. It takes several hundreds of millions of years for the crude oil to form. Therefore this slow generation rate will never keep up with the ever-increasing oil consumption and the world will eventually arrive at the era when crude oil is completely depleted. In this sense, fossil fuels are considered non-renewable.

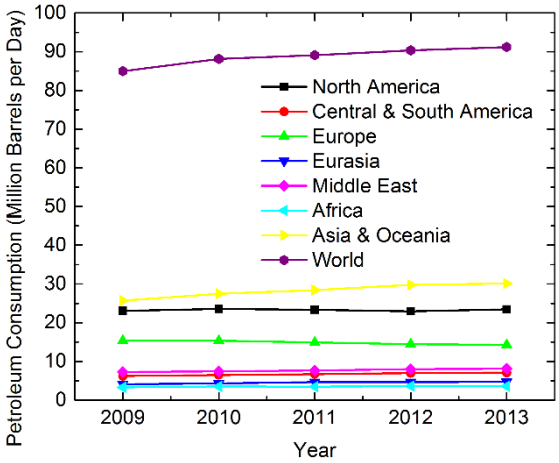

Figure 1.1 World's petroleum consumption by region between years 2009-2013 in million barrels per day (reproduced from [2]).

A statistical report on the world's petroleum consumption by region between the years 2009-2013 from the United States Energy Information Administration (EIA) is given in Figure 1.1. Although the oil consumption decreases in Europe, more oil is needed in those developing countries in the Middle East and Asia-Pacific regions and therefore the net oil consumption of the world is increasing. It is estimated that if the oil reserves discovery and oil consumption rates are following the current trends, then the world's oil reserves will be depleted by 2038 [3] as illustrated in Figure 1.2.

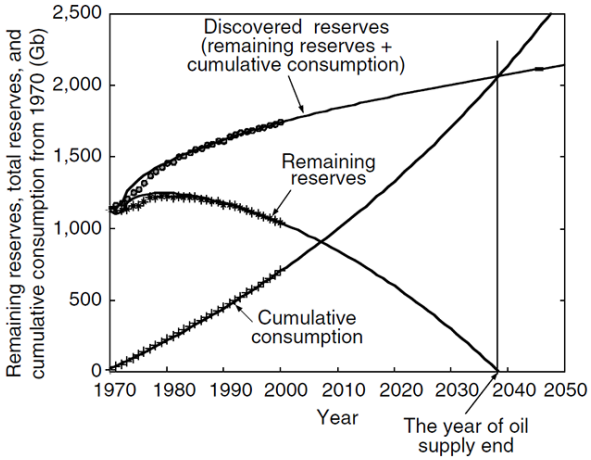

Figure 1.2 World's oil discovery, remaining reserves, and cumulative consumption [3].

At the present day, most petroleum is taken from easily accessible reserves while it becomes more difficult to discover the new oil reserves. This means that if the oil demand is not reduced, the oil price will increase inevitably. A study in the latest US EIA's publication [4] predicts that, though the price seems to fluctuate in the past, in overall the prices of crude oil and gasoline for vehicle will continue to increase until at least the year 2040.

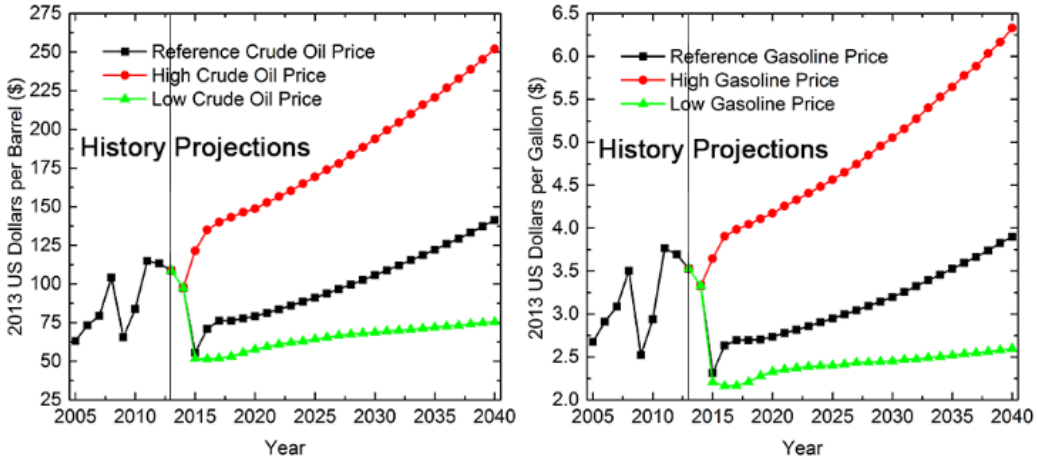

Figure 1.3 Predictions of North Sea Brent crude oil price (left) and gasoline price (right) (reproduced from [4]).

Because most petroleum reserves are located in those regions with political instability, this has a strong effect on the oil price and consequently the national administrative policies. It is therefore the interest of the governments around the world to seek for the way to reduce the oil import in order to lessen their dependence on this highly fragile fuel and improve the national security.

Induced Costs of Fossil Oils

In addition to the oil price which is very likely to continue to increase, the use of these fossil oils induces extra costs such as medical expense due to health issues and maintenance costs for cleanliness of the environment. Though not directly related to the oil price, under certain circumstances these costs can be greater than the operating cost of an ICE-powered vehicle itself. The most infamous example is the Greenhouse Effect which is caused by an excessive amount of carbon dioxide released to the atmosphere from a combustion process inside car engines. These induced costs cannot be overlooked and should definitely be taken into consideration from the national energy policy standpoint.

The major emissions from the combustion of petrol or diesel that are considered harmful to human and environment include carbon dioxide (CO_2), carbon monoxide (CO), oxides of nitrogen (NO_X), and diesel particulate matters (DPM). Among the four emissions, carbon dioxide receives most attention from scientists and engineers because it is the major constituent of the greenhouse gas (GHG) which causes the Greenhouse Effect. The amount of carbon dioxide emitted to the atmosphere through different human activities in the United States during the years 1990-2013 is given in Figure 1.4 and it is found that an ICE was one of the major contributors.

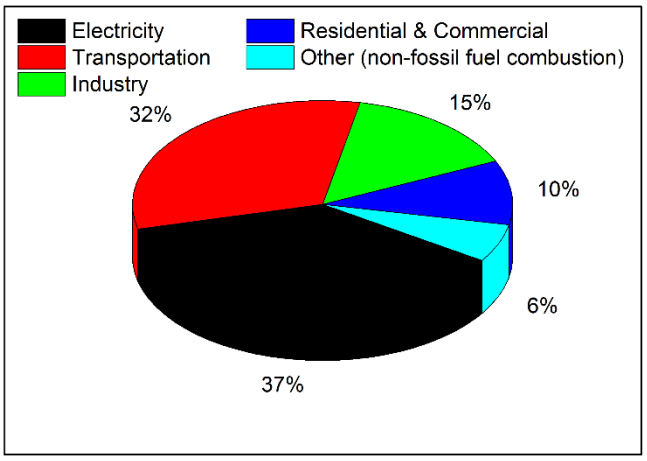

Figure 1.4 Sources of carbon dioxide emission in the United States during 1990-2013 (reproduced from [5]).

Unfortunately, according to the combustion equation of hydrocarbon fuels, carbon dioxide is the most plentiful emission released from ICEs and it is estimated that a typical passenger car will emit 8887 and 10 180 grams of CO_2 per gallon [6] using petrol and diesel as a fuel, respectively. The global carbon dioxide footprint from the exploitation of fossil fuels and cement production together with the CO_2 emission per capita in the past century are given in Figure 1.5. It is clear from the left figure that fossil oils such as petrol and diesel are the main contributors to the total CO_2 emission. This stresses the significance of CO_2 emission from the transportation sector and necessitates the need for a CO_2-free fuel or, at least, an effective means to reduce the tailpipe CO_2 emission.

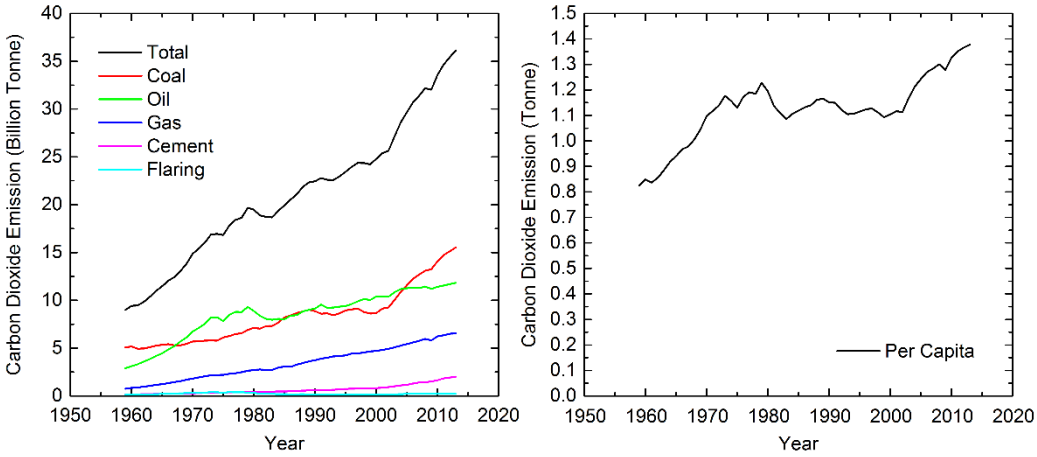

Figure 1.5 Global CO_2 emission by fossil fuel types (left) and per capita (right) (reproduced from [7]).

If an engine is operated under a rich mixture, then oxygen might become insufficient to complete the combustion and carbon monoxide is formed. This chemical intoxicates humans and animals if breathed in. Because of a much stronger bond between CO and haemoglobin molecules compared to oxygen, it tends to attach to the haemoglobin once it reaches the red blood cell. This in turn weakens the oxygen transport to bodily organs by the red blood cells. The common symptoms include headache, dizziness, nausea, and vomiting. Moreover, this carbon monoxide poisoning can cause death to a patient with high intake but receives no immediate medical treatment.

The high operating pressure and temperature of the ICEs make a perfect condition for the oxides of nitrogen to form. The most common one is nitric oxide (NO) which tends to combine with oxygen in the atmosphere to form nitrogen dioxide (NO_2). This acrid substance can be detected by its smell even at a very low concentration and is poisonous to the body once inhaled. There is a potential risk for a person to suffer from respiratory system-

related diseases if exposed to this gas for a long period of time [8]. Additionally, NO_2 can also combine with water molecules in the atmosphere to form nitric acid (HNO_3). Once dissolved in the rain, it will create the so-called "acid rain" which destroys the forests and any marble-based structures.

Finally, the particulate matters (PM) or diesel particulate matters (DPM), sometimes called soot, are unburned hydrocarbons emitted from the tailpipe as a black smoke. This airborne contaminant is regarded as one of the most sophisticated diesel emissions in which its formation and effect on human's health are not fully understood despite considerable effort has been put into research. A direct contact to these particulate matters should be avoided as they have a broad impact to the body's respiratory system.

1.1.2 Alternative, Renewable, and Sustainable Energy

It is clear that there is a need to seek for an alternative way of powering this ever-changing world that leaves little to zero detrimental effect to our planet and many generations to come. In fact, many people tend to think that the word "renewable energy" has the same meaning as the word "sustainable energy" and use them interchangeably. Technically, a renewable energy refers to an energy from the natural resources which can be constantly replenished on a practical timescale and all renewable energy sources are clean, safe, and environmentally-friendly without harmful effect to human beings or ecosystems. The term "sustainable energy", on the other hand, has a broader meaning in which it includes all sources of energy that exist in an excessive amount with the ability to endure regardless of the increasing demand in the future.

From this perspective, all renewable energy resources are sustainable, but not vice versa. Some sustainable energy resources are natural and plentiful. However, they have to undergo a very slow natural process and humans are not capable of re-producing them immediately when they are needed. Therefore these types of energy source are practically limited whereas the energy from a renewable source is always "there" waiting to be harvested.

Due to the increasing awareness of oil depletion and the pollutions it gives to the environment, a clean and inexhaustible energy source is sought after and therefore a renewable energy source is specifically favoured over a sustainable energy source. Good examples of renewable energy resources include solar energy, wind and tidal energy for electricity generation, hydro energy which exploits the flow of water under the earth's gravity, and geo-thermal energy.

It should be noted that these energy sources are location-specific, meaning an energy source may be available only in certain areas but not in the others. The harvest of solar energy by solar panels, for example, might be suitable in the Middle East countries where light intensity is high all year round but not in England where summer only lasts for a few months in a year. These energy resources therefore find their use mainly in a stationary power generating application but not in portable nor transportation application.

1.1.3 Working with Hydrogen

The requirements for an energy source in a transport application are different from those in the stationary power generating systems because an automobile is not stationary. It needs an energy source that can fulfil the power demand regardless of the location nor time it is travelling. Such challenging requirements cannot be answered by all above renewable energy sources and the solution to this is to use hydrogen as a fuel. Hydrogen is the most plentiful element in the observable universe therefore it will never run out. As a consequence, it receives a lot of attentions from the research community and is regarded as the fuel for the future. Similar to all new technologies in the past when they were first introduced, some technical difficulties exist at this early stage and need to be solved before the transition of fossil fuel-based society to the hydrogen fuel-based society can take place and these are addressed as follows.

Hydrogen as a Fuel

At the present, two technologies of using hydrogen to power a vehicle that have been proved a viability are those found in hydrogen internal combustion engine vehicles (HICEVs) and hydrogen fuel cell vehicles (HFCVs). Though both technologies use hydrogen as a fuel, their operating principles are completely different. Despite the fact that the main focus of this thesis is the hydrogen PEM fuel cell and the remaining issues throughout the chapter are discussed from a HFCV viewpoint rather than HICEV, it is worth pointing out the major differences between these two technologies before we proceed.

For comparison purposes only, the highly simplified powertrain diagrams of a HICE vehicle and HFC vehicle are given in Figure 1.6 and Figure 1.7, respectively. A hydrogen internal combustion engine can be thought of as a variant of conventional internal combustion engines and therefore their operating principles are effectively the same. Similarly, hydrogen is refilled from a hydrogen station and stored as liquid hydrogen or compressed hydrogen gas in an on-board tank. The hydrogen is then drawn to the cylinders

and burned in a combustion process producing high pressure which pushes down the pistons. This translational movement of pistons is in turn transferred to a rotational motion of the wheels through the transmission system. To summarise, a hydrogen ICE vehicle burns hydrogen instead of hydrocarbon fuels therefore its tailpipe emission is greatly reduced. However, because the generated power has to undergo several conversion processes before reaching the wheels, significant amount of power is lost through some irreversible processes and frictions therefore restricting the maximum efficiency of such a technology to the same level as an advanced diesel engine [9].

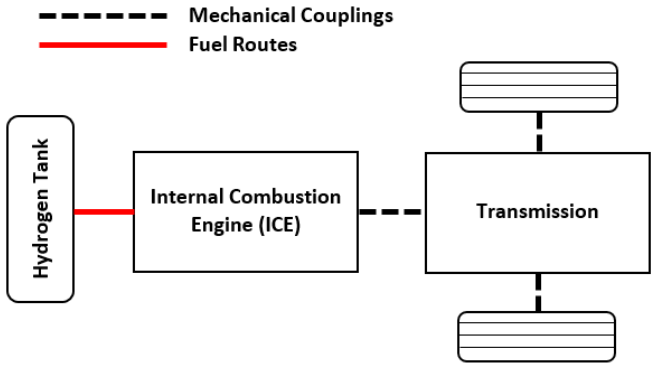

Figure 1.6 A highly simplified powertrain of an HICEV.

This is the main reason why an HICEV was receiving interests from automotive manufacturers for only a certain period of time. Due to the ever increasing environmental awareness, a clean fuel is currently at the centre of attention of every societies and has been integrated into many development plans for a sustainable society. A low-carbon engine is no longer sufficient to comply with the regulations on road vehicles which are becoming more stringent each year. As a consequence, the automotive industry is forced to find an alternative method to propel the vehicles with much less tailpipe emission (known as low-emission vehicles, LEVs or ultra-low emission vehicles, ULEVs) and better fuel economy.

A very promising solution to this is to move to electric propulsion. By switching to electricity, a vehicle could benefit from an electric drivetrain which is known to be much more efficient than a mechanical drivetrain. Depending on the types of a vehicle, either hybrid electric vehicle or pure electric vehicle configuration can be employed on the drivetrain and such vehicles are referred to as hybrid-electric vehicles (HEVs) and electric vehicles (EVs), respectively. Additionally, in some cities where the regulations on road vehicle emission are very stringent so that only zero-emission vehicles (ZEVs) are allowed, an all-electric vehicle seems to be the sole technology that can achieve this.

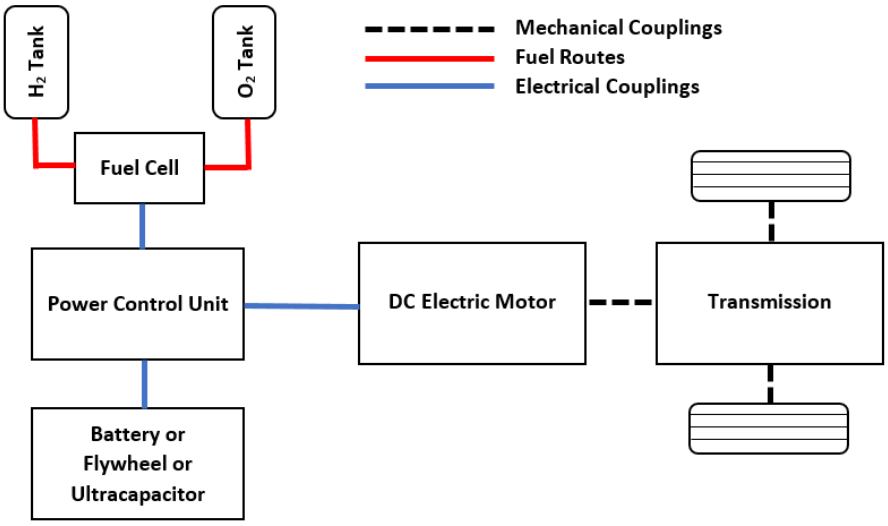

Figure 1.7 A highly simplified powertrain of an HFCV.

In contrast to an HICEV, an HFCV is considered an electric vehicle. A fuel cell stack module is the heart of the powertrain. It uses hydrogen from an on-board pressurised tank to generate electricity which is then used to power an electric motor directly as shown in the figure. It should be noted that in an ideal system a fuel cell stack alone will provide all of the vehicle's power demand throughout its entire trip just like an ICE in a conventional vehicle. However, with the current fuel cell technology, a fuel cell stack is usually hybridised with a scaled-down ICE or an energy storage device such as battery, ultra-capacitor, or flywheel to achieve a comparable performance as an ICE. In the former configuration, an ICE is the primary power unit (PPU) whereas the fuel cell stack acts as an auxiliary power unit (APU) that provides electricity to passenger-comfort, lighting, or entertainment sub-systems. The fuel cell stack in the latter configuration, on the other hand, provides most of the power during normal operation while the energy storage device is used to store excessive electricity from regenerative braking and acts as an energy buffer when the power from the fuel cell alone is not sufficient during a fast acceleration, for instance.

Hydrogen Production

Unlike fossil fuels which have been the dominant source of energy for human for more than a century and the distributing infrastructures of such fuels exist around the globe, the concept of using hydrogen as a fuel is relatively new in this aspect. Whether it is burned in an ICE or converted into electricity as in a fuel cell, the challenges regarding hydrogen infrastructures need to be overcome for the transition to the hydrogen economy to occur.

Even though hydrogen is the most ubiquitous element in nature, unfortunately it does not exist as single molecules that can be utilised promptly. In fact, hydrogen usually combines with other elements in the form of a chemical compound such as hydrocarbons which requires a method to extract hydrogen if it is to be used in a fuel cell engine. During the extracting process, other elements in this hydrogen compound or by-products from a chemical reaction are released. This makes a fuel cell vehicle a non-zero emission vehicle on a well-to-wheel basis.

Currently, most of hydrogen we use to feed the industry is extracted from hydrocarbon fuels [3] through the reforming process. Reforming or steam reforming in particular is an industrially well-established method for large-scale production of hydrogen [10]. The method uses hydrocarbon fuels such as methane (CH_4), gasoline (iso-octane C_8H_{18}), and preferably methanol (CH_3OH) [3] with high-temperature water steam to produce hydrogen via the following chemical reactions;

Methane $$CH_4 + 2H_2O + 258\ kJmol^{-1} CH_4 \rightarrow 4H_2 + CO_2 \quad (1.1)$$

Gasoline $$C_8H_{18} + 16H_2O + 1652.9\ kJmol^{-1} C_8H_{18} \rightarrow 25H_2 + 8CO_2 \quad (1.2)$$

Methanol $$CH_3OH + H_2O + 131\ kJmol^{-1} CH_3OH \rightarrow 3H_2 + CO_2 \quad (1.3)$$

The above reactions are highly endothermic which requires a large supply of heat during the process. Moreover, carbon monoxide (CO) can also exist in the product steam and even a small amount can be poisonous to the platinum catalyst used in a PEM fuel cell. These CO need to be further converted to hydrogen and CO_2 through a so-called water-gas shift reaction as given in Equation (1.4).

$$CO + H_2O + 4kJmol^{-1} CO \rightarrow H_2 + CO_2 \quad (1.4)$$

Even steam reforming of methanol yields a relatively high amount of hydrogen, the poisoning of the catalyst used in the reformer due to the impurity in the methanol fuel should be addressed. In addition, though the steam reforming of gasoline as shown in Equation (1.2) is possible, this method does not find its way into industry.

Hydrogen reforming can also be done on-board the vehicle which is known as internal reforming. Many studies have proposed a fuel cell engine layout with an integrated reformer. This means that the vehicle can also feed on conventional hydrocarbon fuels in addition to pure hydrogen which eliminates the need of a dedicated hydrogen refill station. It is known that a fuel cell releases heat from its electrochemical reaction, instead of simply being wasted to the surroundings, this heat is re-routed to power the integrated reformer. The extra benefit is that this is a very effective method for the cooling of the cell since the reforming process is highly endothermic therefore it acts as a good heat sink for the fuel cell

stack. However, this method is only possible with high-temperature fuel cells such as molten-carbonate fuel cell (500-800 °C) and solid-oxide fuel cell (1000-1200 °C) where the temperature gradient between the cell stack and surroundings is high. This is clearly not practical to a PEM fuel cell where the operating temperature is below 100 °C.

Another interesting technique is called thermal cracking. This method employs a large amount of heat in order to "crack" or break-down the bond between hydrogen and other elements in a heavy hydrocarbon compound. The heat-up process of hydrocarbon compounds without the presence of oxygen or any halogens is known as pyrolysis. However, this method can also be applied to ammonia (NH_3) which is a non-carbon-based hydrogen carrier hence offering a cleaner, carbon-free method for hydrogen production. This thermal cracking of ammonia is presented by a chemical reaction given in Equation (1.5).

$$2NH_3 \rightarrow N_2 + 3H_2 \tag{1.5}$$

However, carrying ammonia as a fuel on-board the vehicle poses some concerns to engineers since ammonia is toxic. A direct contact to ammonia causes severe burns to living tissues. A stringent safety measurement must be enforced when dealing with this type of fuel.

Perhaps the truly clean method of producing hydrogen with no harmful emission or by-product is only restricted to an electrolyser. An electrolyser relies on the electrolysis of water which is a decomposition of a water molecule into hydrogen gas and oxygen gas using an electric current and the overall reaction is given in Equation (1.6);

$$2H_2O(l) \rightarrow 2H_2(g) + O_2(g) \tag{1.6}$$

where oxygen gas is produced by an oxidation reaction at the anode while hydrogen gas is produced by a reduction reaction at the cathode. These two half-cell reactions are represented through Equations (1.7) and (1.8), respectively.

Anode $$2H_2O(l) \rightarrow O_2(g) + 4H^+(aq) + 4e^- \tag{1.7}$$

Cathode $$4H_2O(l) + 4e^- \rightarrow 2H_2(g) + 4OH^-(aq) \tag{1.8}$$

A stand-alone electrolyser can be employed at certain communal places or even at home in order to generate and store hydrogen during the night when it is ready for use in the next morning. The concept of using electricity to extract hydrogen and in turn use this hydrogen to generate electricity to propel a vehicle might sound relatively awkward. However, an electrolyser can operate at a relatively high efficiency [10] and if the electricity used to power this electrolysis process is from a renewable energy source such as wind turbine or solar panel, the resulting high overall system efficiency and virtually zero emission make this a very attractive strategy.

Hydrogen Storage

Hydrogen can be stored and carried on-board a vehicle in various ways and in all three forms – gas, liquid, or solid. Each of these has its own advantages and disadvantages. Currently, the most common method is to store hydrogen in a tank as a compressed gas under several hundred atmospheres ranging from 350-700 atm [3]. Such very high pressure combines with the fact that hydrogen gas is the smallest molecule, having the distance between the centre of two hydrogen atoms of only 0.74 Å [11], means that it is prone to leakage and can diffuse through the wall of a tank unless a special material is used. This requires a tank to be very strong but lightweight at the same time to prevent the tank from getting bulky which adds the weight penalty to the vehicle. A tank made from composite materials such as carbon fibre is the most popular choice.

Nevertheless, the amount of energy required to compress hydrogen gas and its energy content must be taken into the design consideration. For example, the energy contained within one litre of hydrogen gas under 350 bar is only equivalent to the energy content in 0.1 litres of gasoline while it requires twice as much energy to compress the gas further to 700 bar that has the same amount of energy of 0.2 litres of gasoline [3]. Moreover, there is a concern regarding the safety of a highly pressurised hydrogen tank. In addition to being highly volatile and flammable, the hydrogen atom is so small and light so that it mixes very fast with air and therefore becomes explosive.

Another possible way is to store hydrogen as a liquid under a cryogenic condition. In order to liquefy hydrogen, it is cooled down to a very low temperature of -259.2 °C [3] and the resulting liquid hydrogen is referred to as LH_2. However, there seem to be several issues to be addressed before this technology becomes mature. First of all, it is dangerous for non-professionals such as ordinary drivers and passengers without safety precautions to handle this liquid hydrogen in their daily routine. This hazardous substance can burn-freeze human tissues by direct contact. Additionally, due to a very low operating temperature, the hydrogen tank needs heavy insulation which adds weight to the system making this technology suffer from a low energy-to-weight ratio.

Some metals are capable of absorbing hydrogen to form a more stable compound under normal pressure and temperature such as iron, titanium, manganese, nickel, and the alloys of these metals. These metal hydrides can be carried on-board as solid fuels and later decomposed by a supply of heat to give out hydrogen when needed. The general form of such reaction is given in Equation (1.9), where M stands for metal [10].

$$M + H_2 \leftrightarrow MH_2 \tag{1.9}$$

The use of carbon nanofibre was reported in 1998 by Chambers et al. [12]. This graphite-based material was thought to be an excellent alternative to metals with superior energy density. However, carbon nanofibre technology is still in its early stage and therefore requires more time and research effort before it can find its use in a practical fuel cell car.

Clearly, the issue of hydrogen distribution infrastructure is also in the mainstream interests and should be addressed. This is, however, a very broad topic covering all aspects from technical/engineering advancement, environmental impact, city planning, and national energy policy which is far beyond the scope of this thesis. It is therefore omitted.

It is evident that all of the technologies discussed above still require further improvement. In the meanwhile more technologies are being researched and demonstrated in many initiative programs. It will take some time for automotive designers and engineers to achieve adequate advancement in such technologies. Once public awareness of the adverse effects of fossil fuels has been achieved and the safety and comparable performance of hydrogen fuel to fossil fuels has successfully gained public acceptance, this will mark the new era of mankind which is the start of the hydrogen economy.

1.2 Fuel Cells Technology

1.2.1 Fuel Cell at a Glance

For a very brief definition, a fuel cell is a galvanic cell. It generates electricity from chemical substances called a fuel and oxidant via an electrochemical reaction shown as a "black box" in Figure 1.8.

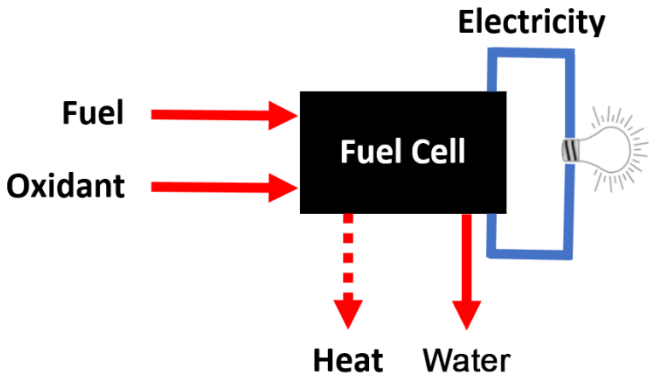

Figure 1.8 Schematic diagram showing fuel cell as a "black box".

A fuel cell is very similar to a battery in the way they both generate electricity from chemical substances. However, once the chemicals which are stored inside a battery are used up, it is said to be fully discharged and needs to be disposed of if it is a primary battery or recharged in case of a secondary battery. A fuel cell, on the other hand, can never discharge

as long as a constant supply of fuel and oxidant is maintained. Since fuel and oxidant are carried on-board a vehicle in tanks just like petrol or diesel in a conventional car, the fuel supply and subsequently cruising range are only limited by the size of these tanks. Typically, a fuel cell engine provides a much longer range than a battery module with equivalent weight. Additionally, fuel and oxidant can be refilled within a much shorter time, in minutes rather than hours, compared to the recharging of a battery module. This is a great advantage which makes a fuel cell favourable over a battery.

1.2.2 A Very Brief History of Fuel Cells

A man who should be accredited for demonstrating the principle of a fuel cell for the first time in 1839 was an English lawyer and scientist Sir William Robert Grove [13] which he then called it a "gas voltaic battery". However, the concept of a fuel cell remained as a scientific curiosity for almost a century [14] before it was re-introduced to the scientific community by another English engineer named Francis Thomas Bacon. Being fascinated by Grove's discovery, Bacon started working on fuel cells in 1937 until he successfully developed the first practical fuel cell capable of producing 6 kW output power in 1959. This Bacon's Cell, which was the forerunner of alkaline fuel cells (AFCs), operated on hydrogen and oxygen with an aqueous alkaline solution, potassium hydroxide (KOH), as electrolyte in contrast to an acid electrolyte used in Grove's early works. In addition, Bacon used the porous gas-diffusion electrode in his cell instead of a solid electrode used in Grove's cells.

In the early 1960s, fuel cell technology found its first application in space exploration. NASA used the new type of fuel cell, the polymer electrolyte membrane (PEM) fuel cell, which was developed by General Electric on the Gemini Earth orbit space capsule. Subsequently, Pratt and Whitney won the contract from NASA to manufacture a fuel cell to be used in their moon-landing Project Apollo in 1970s. An alkaline fuel cell (AFC) was developed based on the cell which they had licensed from Bacon's design to supply electricity for electrical appliances in the space shuttle. Since the only product is water, it was said that the generated water was clean such that it was used as drinking water for the crews during their mission and this AFC remains as the standard fuel cell for aerospace application.

Throughout 1970s and 1980s, fuel cell technology found its way back to Earth where research efforts were shifted towards the application on road vehicles. At present, many research efforts and fundings have been put into fuel cell technology as can be seen in car manufacturers' laboratories, private companies, or leading academic research institutions. A notable contributor that successfully developed the first marketable fuel cell powered vehicle

[15] and ensured a certain future of commercial PEM fuel cells is a Vancouver-based company called Ballard Power Systems. They are the major motive forces in PEM fuel cell business with over 500 patents [16].

1.2.3 The Fuel Cell Family

Like any other technologies, different types of fuel cell exist and each of these variation is suitable for a certain application than others. Fuel cells are normally categorised by their electrolyte and a very good illustration showing major types of fuel cells together with their electrolyte, fuel and oxidant, and operating temperature range is given in Figure 1.9.

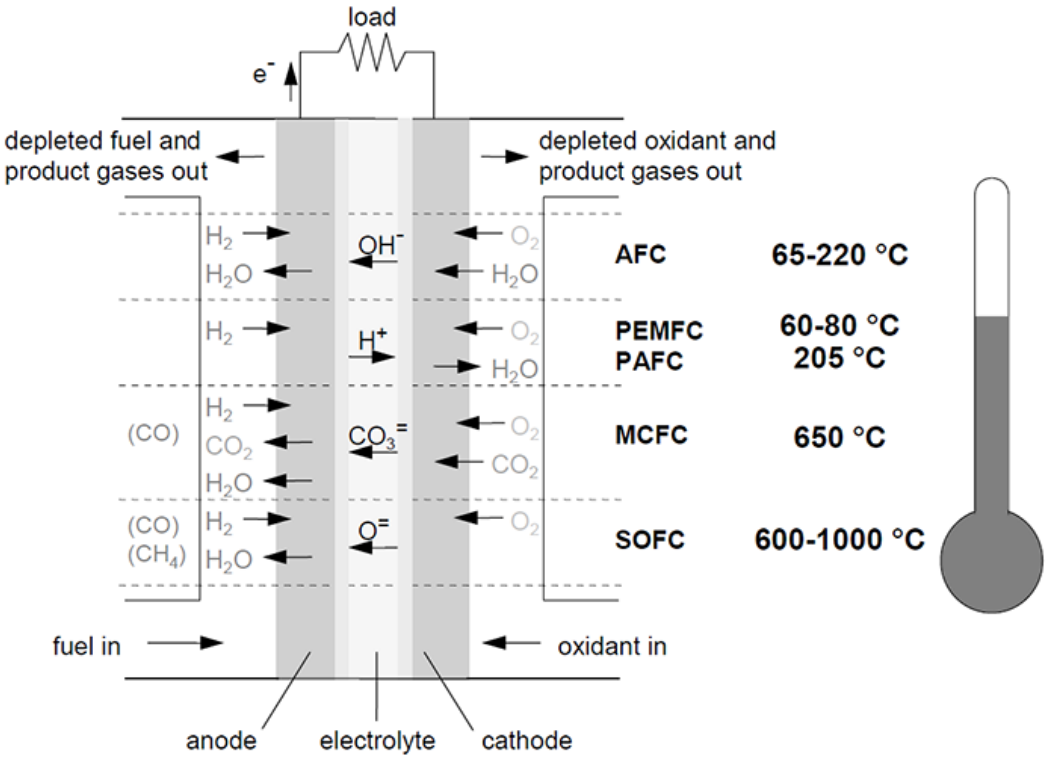

Figure 1.9 Major types of fuel cell showing their electrolyte, fuel and oxidant, and operating temperature range [14].

Alkaline Fuel Cell (AFC)

As mentioned previously, alkaline fuel cells found their first use in space exploration since 1960s. It has been a standard fuel cell for NASA space programs and therefore can be regarded as a mature technology from this perspective. The unique feature of this type of fuel cell is that it can be operated over a wide range of temperature (80-230 °C) and pressure (2.2-45 atm) [17].

As the name implies, an AFC uses alkaline solutions such as sodium hydroxide (NaOH) and preferably potassium hydroxide (KOH) as electrolytes. This makes the transfer of ions between the two electrodes different from other acid-based electrolyte fuel cells such as a PEM fuel cell in which the hydroxide ion (OH^-) is carried instead of hydrogen ion (H^+). Consequently, water is produced at the anode electrode while it is consumed by the reaction at the cathode. This usually causes a cathode-side membrane to dry out and the solution to this is to prevent water from leaking out by making an electrode waterproof [3]. However, even an AFC uses cheap catalyst and electrolyte, it suffers from corrosion in its electrolyte as well as carbon dioxide poisoning to its catalyst.

Polymer Electrolyte Membrane Fuel Cell (PEMFC)

Since the main focus of this thesis is on this type of fuel cell, it will be discussed in detail in a separate section. A PEM fuel cell at a glance is the most mature fuel cell technology for road vehicle application and a very promising candidate that will replace internal combustion engines in the near future. This is attributable to its high energy density, fast response, and low operating temperature which are particularly beneficial to an automobile.

It uses a solid but porous polymer electrolyte membrane to transfer hydrogen ion (H^+) or proton between its electrodes hence it is given various names such as solid polymer electrolyte fuel cell (SPEFC), proton exchange membrane fuel cell (PEMFC), or just polymer electrolyte fuel cell (PEFC). However, some technical barriers need to be overcome before its commercialisation becomes viability. These includes a high loading of precious catalyst material such as platinum and the poisoning of the catalyst due to the presence of carbon monoxide in the fuel.

Direct-methanol Fuel Cell (DMFC)

Unlike other fuel cells which require pure hydrogen, liquid methanol is supplied directly to a DMFC which is in turn converted to electricity. Because of this, there is no need to integrate the bulky internal reformer into the vehicle so that the overall system energy density can be improved. As an additional benefit, there is little need for the modification to the already available distribution infrastructures. Methanol can be refilled at the fuel station just like conventional petrol or diesel. In fact, as a fuel for vehicles, methanol is more common than hydrogen. It can be produced economically in a large scale from coal, natural gas, or even sugar canes. All of the above reasons make DMFC a very attractive technology particularly for transportation.

Nevertheless, this DMFC is much less advanced in terms of automotive application compared to a PEMFC [18]. Even though they are more efficient under high operating temperature and pressure, however, due to the lack of effective system integration, the whole system suffers from more loss than the gain. Therefore it is not practical to operate a DMFC at any higher point other than its normal operating temperature of 50-100 °C and atmospheric pressure [19]. At present, DMFCs are considered the least mature technology among its cousins [3].

Phosphoric Acid Fuel Cell (PAFC)

A PAFC is the first fuel cell to achieve commercialisation [3]. Similar to a PEM fuel cell, the electrolyte of this type of fuel cell is an acidic solution, phosphoric acid (H_3PO_4). With an operating temperature of just above 200 °C, this fuel cell benefits from a faster start-up characteristics than other high-temperature fuel cells and makes it favourable among designers in small-scale stationary power generating application. It can be used to generate electricity to power electrical appliances in a house. However, this fuel cell technology also suffers from technical issues similar to those found in PEMFCs such as expensive platinum as a catalyst material and carbon monoxide poisoning to the catalyst.

Molten Carbonate Fuel Cell (MCFC)

The MCFC is considered a high-temperature fuel cell that has an operating temperature of 500-800 °C. It uses molten carbonate salts such as lithium-potassium carbonate or lithium-sodium carbonate as an electrolyte to conduct carbonate ions (CO_3^{2-}). In fact, pure hydrogen gas is not necessary, this fuel cell can directly utilise any conventional hydrocarbon fuels. Its operating temperature is sufficiently high to decompose the fuel internally and give out hydrogen molecules. Such ability offers some benefits to automotive designers in which the vehicle equipped with this type of fuel cell may not need to carry the bulky hydrogen tank nor an on-board reformer. However, because of a high operating temperature, it takes considerable amount of time from start to reach this temperature and an effective cooling system is required for this technology to be used in a vehicle.

Solid Oxide Fuel Cell (SOFC)

SOFCs use ceramics as an electrolyte and operate at very high temperature (1000-1200 °C). At this temperature, other ceramics become conductive to hydrogen ion but the yttrium-stabilised zirconia (YSZ) used in SOFCs conducts oxygen ions (O^{2-}). Due to a very high

operating temperature, it dissipates large amount of heat to the surroundings. This high-grade heat can be harvested and re-introduced to power other balance of plant components which makes the overall efficiency of a typical SOFC system very high. Moreover, carbon monoxide has virtually no poisoning effect on the catalyst.

From an automotive viewpoint, however, the start-up time and transient response are appreciably slow due to a very high operating temperature similar to MCFC. Additionally, its size and weight also pose some challenges to engineers if this system is to be integrated onto a vehicle. On the other hand, SOFC has found its place in the distributed power generation around the world. It is an established technology found in many large-scale stationary power generating modules where system size and weight are less important. A comprehensive chart which summarises the application range for each of the fuel cell technologies discussed above can be seen in Figure 1.10.

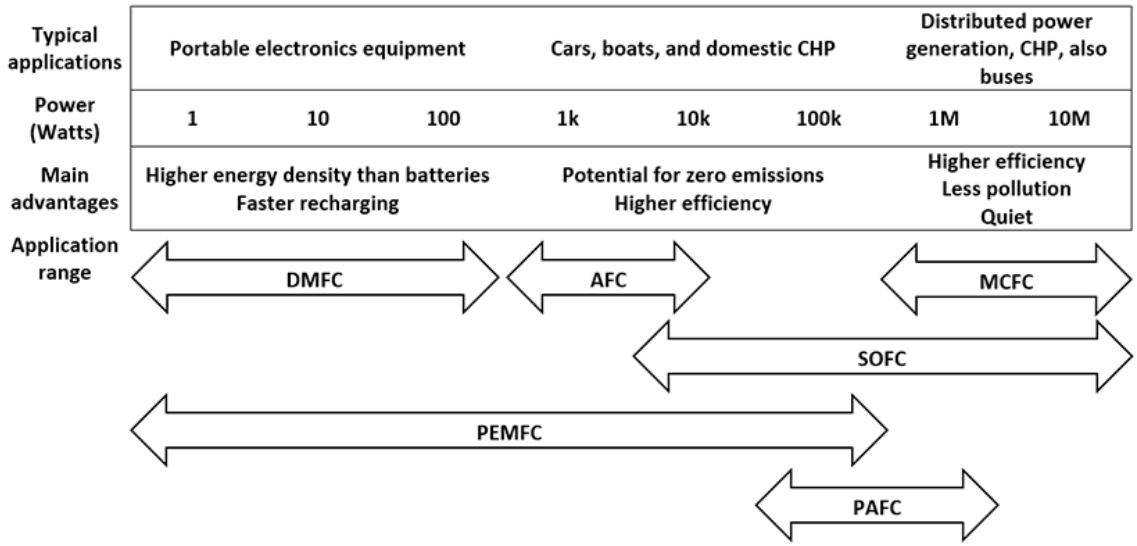

Figure 1.10 Summary of applications of different types of fuel cells with main advantages and range of power output (reproduced from [18]).

1.3 The Polymer Electrolyte Membrane Fuel Cell

1.3.1 Operating Principles

A PEM fuel cell is an electrochemical device that generates electricity from hydrogen and oxygen via a chemical, or more technically correct electrochemical, reaction. In fact, the electrochemical reaction inside a fuel cell can be thought of as a reverse process of electrolysis of water in which hydrogen atoms combine with oxygen atoms under the existing potential difference between the two electrodes to form water. This results in the flow of electron (or electricity) and heat of reaction which is dissipated to the surroundings as by-products.

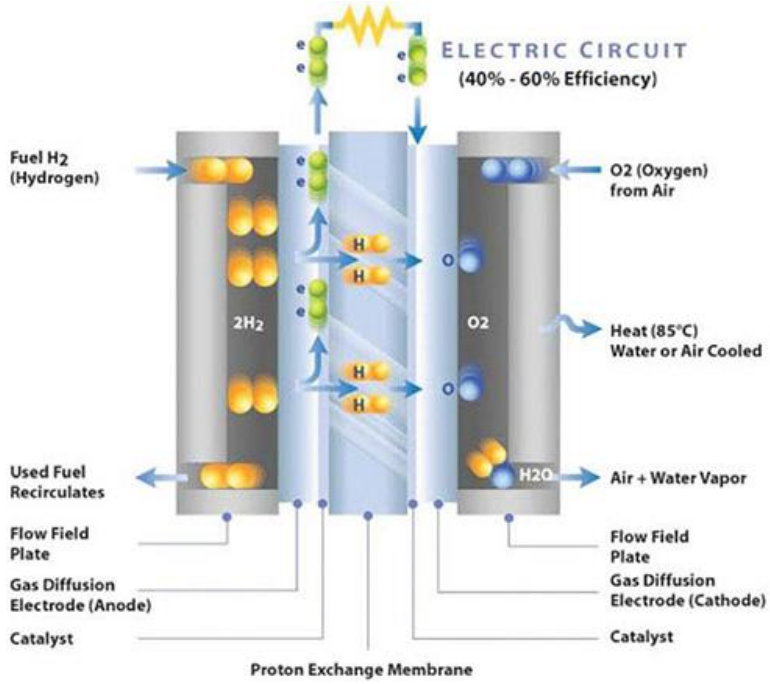

Figure 1.11 Diagram showing how electricity is produced in a typical PEM fuel cell [20].

Figure 1.11 demonstrates how electricity is generated in a PEM fuel cell. It relies on the two half-cell reactions which are known as hydrogen oxidation reaction (HOR) and oxygen reduction reaction (ORR) at the anode and cathode electrodes, respectively. At the anode, hydrogen is oxidised in which an electron is stripped off from a hydrogen atom resulting in one free electron and hydrogen ion (H^+) or proton according to;

$$H_2 \rightarrow 2H^+ + 2e^- \tag{1.10}$$

The polymer electrolyte is a selective membrane, therefore only proton is able to move across the membrane to the cathode while electron has to travel to the cathode by means of an external circuit before reuniting with proton at the other side. This flow of electron through the circuit can be extracted as useful electricity. At the cathode, oxygen is reduced by proton and electron coming from the anode and water is formed according to;

$$O_2 + 4H^+ + 4e^- \rightarrow 2H_2O \tag{1.11}$$

The overall reaction creates only water with electricity and heat as by-products as;

$$2H_2 + O_2 \rightarrow 2H_2O + electricity + heat \tag{1.12}$$

It should be emphasised that water is generated at the cathode and tends to clog up the pores in the porous media. This prevents oxygen from reaching the active site especially at high current operations and such a phenomenon is known as liquid water flooding. The water thus needs to be removed by effective water management which, up to the present, remains as a major challenge to PEM fuel cell technology.

1.3.2 PEM Fuel Cell Components

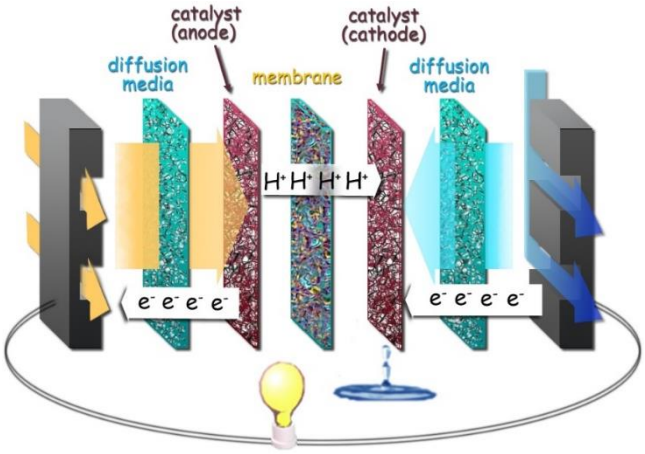

Figure 1.12 Schematic diagram of a single PEM fuel cell showing its components [21].

For demonstration purposes, a single unit of a typical PEM fuel cell with its components exposed is shown in Figure 1.12. From the figure, a PEM fuel cell is nothing but an assembly of seven different layers. These layers are, from left to right, anode current collector with hydrogen flow channels embedded on it, anode gas-diffusion layer (GDL_{an}), anode catalyst layer (CL_{an}), polymer electrolyte membrane (PEM), cathode catalyst layer (CL_{ca}), cathode gas-diffusion layer (GDL_{ca}), and lastly cathode current collector with embedded oxygen (or air) flow channel. Each of these layers has its own unique property and function which is discussed separately as follows.

Current Collector and Flow-field

The current collectors (also known as flow-field plates) are the two outermost layers, usually made from graphite, of a single cell. They provide four main functions in the operation of a cell. Firstly, they are the most rigid component in the cell used to support the entire structure. Secondly, they conduct the free electrons out of the anode and then back into the cathode thus completing the electrical circuit. Thirdly, they conduct the heat out of the cell in addition to the cell cooling system. Lastly, they provide a path or a flow-field for the reactant stream to flow over an entire active area.

The flow-field is a network of connected, usually elongated, channels which are grooved into the surface of the current collector. It plays a major role in the distribution of reactant species over the active area and water management hence determines the cell performance. Though variations of the shape of channel's cross-section are reported and investigated, the most commonly used shapes in commercial cells are a rectangle or square

and the dimensions of their cross-section are in the order of 1 mm. Similar to the shape of the cross-section, there exist variations in flow-field configurations such as the straight-parallel, single-serpentine, multi-serpentine, interdigitated, or the combination of more than one designs as shown in Figure 1.13. Each configuration has its own pros and cons which can be found in the literature therefore they are not repeated here.

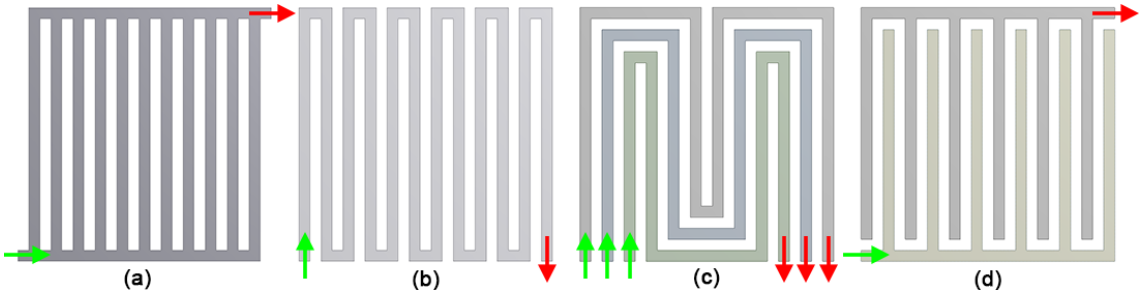

Figure 1.13 Common flow-fields: (a) Straight-parallel (b) Single-serpentine (c) Multiple-serpentine (triple) and (d) Interdigitated. Green arrow – inlet, red arrow – outlet.

In practise, it is not unusual to have different flow-field designs or same design but with different orientations in the same cell. Such arrangements are called co-flow (0°), transverse flow (90° or 270°), or counter flow (180°). A typical PEM fuel cell stack comprises of repeated cell units connected in series. In this case the current collector also acts as a separator between the two adjacent cells. A flow-field is cut into both sides of a current collector to accommodate the flow of hydrogen on one side and oxygen on the other side. The current collector is thus sometimes referred to as a bipolar plate (BPP).

The current collector accounts for more than 60% and 30% of the total weight and cost of a stack [22]. This offers a potential research area for improving the stack specific power ($kWkg^{-1}$) and cost-to-power ratio ($\$kW^{-1}$). An ideal current collector needs to be capable of uniformly distributing reactant species over the active area while using less material. The researches on a current collector covering the choice of materials, flow-field configurations, and optimal flow channels dimensions and are reviewed in the next chapter.

Gas Diffusion Layer (GDL)

Moving further towards the centre of the cell, the next layer is known as gas diffusion layer (GDL) that typically measures 200-500 microns in thickness. It is made from a porous material, most commonly carbon cloth or carbon paper. It consists of an electronically conductive solid matrix with interconnected void spaces known as pores which acts as a path for gaseous and liquid species to flow as seen in Figure 1.14.

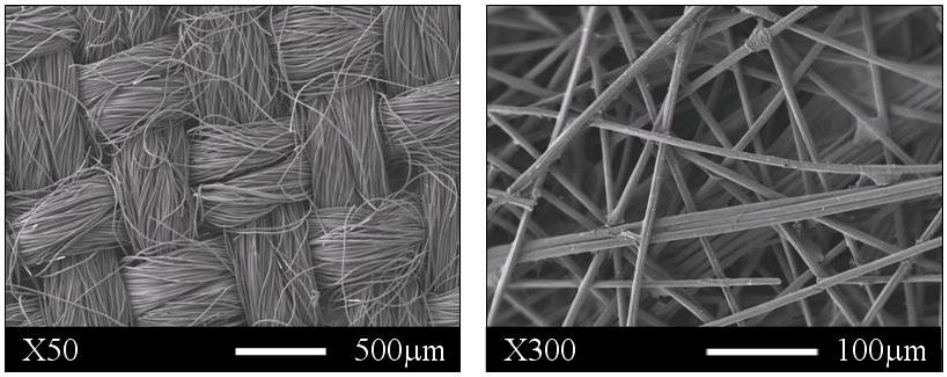

Figure 1.14 Typical GDL material: AvCarb™ 1071HCB woven carbon cloth (left) and TGP-H-060 hydrophobic carbon paper (right) [23].

A GDL has three main functions. Firstly, it helps promote a uniform distribution of reactant species over the active area. Without the GDL, it would be difficult for the reactant species to diffuse to the region in the active site that is directly underneath the current collector rib. This would result in a non-uniform local current generation and consequently thermal and mechanical stresses could develop on the fragile membrane which is highly undesirable. Having a fibrous structure, it is considered as anisotropic and thus its in-plane and through-plane properties are different. However, most research works on a PEM fuel cell, especially numerical ones, treat the GDL as a homogeneous and isotropic material.

The second function involves the removal of product water. The GDL provides a passage for liquid water to be removed from the cathode catalyst, where it is produced, to the flow channel mainly by means of capillary effect. Once emerged into the flow channel as droplets or liquid films, these water are then expelled out of the cell at the channel outlet by the incoming cathode stream. Because of this, the GDL is usually coated with hydrophobic polytetrafluoroethylene (PTFE) or Teflon to aid in the water removal.

Lastly, the GDL provides a path for electron between the anode catalyst layer where it is produced and the current collector so that it can travel to the external circuit. Similarly, the GDL provides the path for electron between the current collector and cathode catalyst layer where it is consumed in the ORR. The important properties of the GDL are its thickness, porosity, permeability to gaseous species, and thermal and electronic conductivity.

Catalyst Layer (CL)

The catalyst layer (CL) is the porous region where the half-cell reaction takes place – the HOR takes place in the anode catalyst layer while the ORR takes place in the cathode catalyst layer. It is the thinnest layer in a single cell unit having a thickness of 10-30 microns. The

precious metal, platinum, is known to be the best catalyst for a PEM fuel cell. These small platinum particles are deposited onto a larger electronically conductive carbon particle and such a structure is called carbon-supported platinum (Pt/C) catalyst as shown in a rather idealised form in Figure 1.15. Early PEM fuel cells used a very high platinum loading of 28 $mgcm^{-2}$ which made this technology too expensive for a commercial implementation. However, with extensive research effort on this issue, the state-of-the-art PEM fuel cell now operates with a much less platinum loading of 0.2 $mgcm^{-2}$.

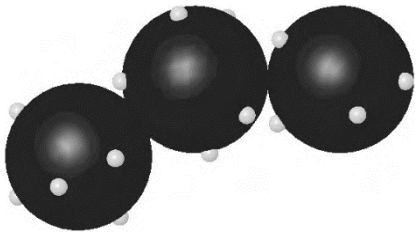

Figure 1.15 Idealised structure of carbon-supported platinum (Pt/C) catalysts [10].

The catalyst layer ensures that all ingredients of an electrochemical reaction including hydrogen, oxygen, proton, and electron can meet up. The carbon-supported platinum catalysts have to be interconnected to the electronically conductive solid matrix of the GDL to provide the path for electron, the electrolyte material for an access of proton, and the gas species via the pores as shown in Figure 1.16. Due to the mutual presence of reactant species, catalyst particle, and electrolyte, this region is also known as the triple-phase zone (TPZ) or triple-phase boundary (TPB) which is a critical condition for the half-cell reaction to occur.

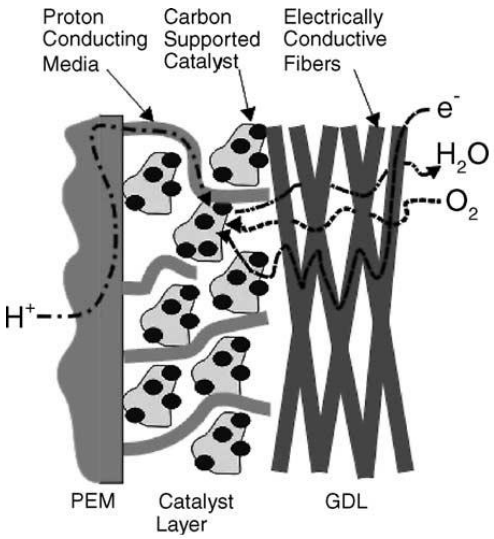

Figure 1.16 Schematic diagram showing a structure of catalyst layer [24].

Polymer Electrolyte Membrane (PEM)

At the heart of a PEM fuel cell, there exists a polymer electrolyte membrane. This porous layer, with a thickness of 100-200 microns, is sandwiched between anode and cathode catalyst layers forming the so-called membrane electrode assembly (MEA). It is a selectively permeable membrane in which only proton (H^+) is allowed to move across the membrane from anode to cathode while the electron is not allowed to pass through.

The backbone of the electrolyte is the hydrophobic polytetrafluoroethylene (PTFE), also known as Teflon. The structure of PTFE and its monomer, the tetrafluoroethylene are shown in Figure 1.17. It is the modified polyethylene by means of perfluorination process which replaces each hydrogen atom by a carbon atom in its basic unit (ethylene, shown in Figure 1.18). The resulting perfluorinated monomer is called tetrafluoroethylene. Here, the word "tetra" indicates that all four hydrogen atoms have been substituted by fluorine atoms.

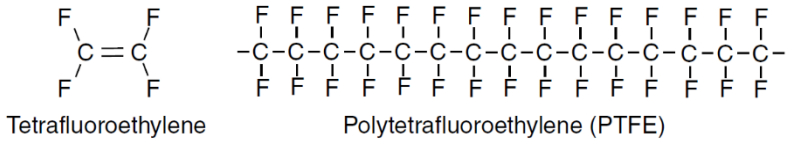

Figure 1.17 Structure of polytetrafluoroethylene (PTFE) and its monomer [10].

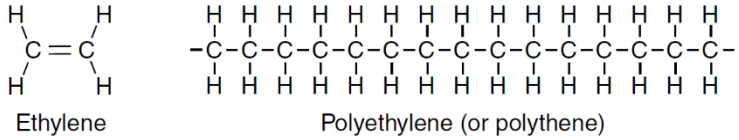

Figure 1.18 Structure of polyethylene and its monomer [10].

Then the sulphonic acid (HSO_3) side chain is added to the basic unit of PTFE which results in the presence of SO_3^- and H^+ ions at the end of the side chain as seen in Figure 1.19. Because of the highly hydrophilic property of the sulphonic acid, it tends to absorb water molecule and is capable of increasing the dry weight of the membrane by up to 50% [10]. With the presence of water in this region, the attraction between the two ions are weakened and therefore the H^+ ions are able to move freely within the electrolyte.

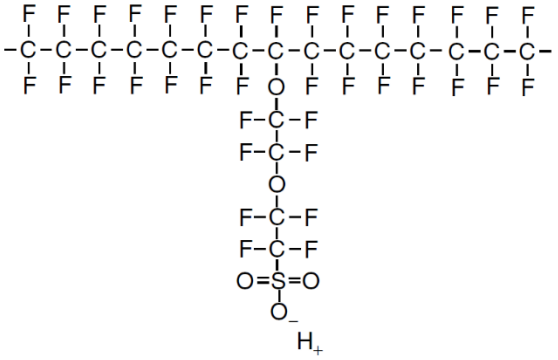

Figure 1.19 Example of sulphonated fluoroethylene structure [10].

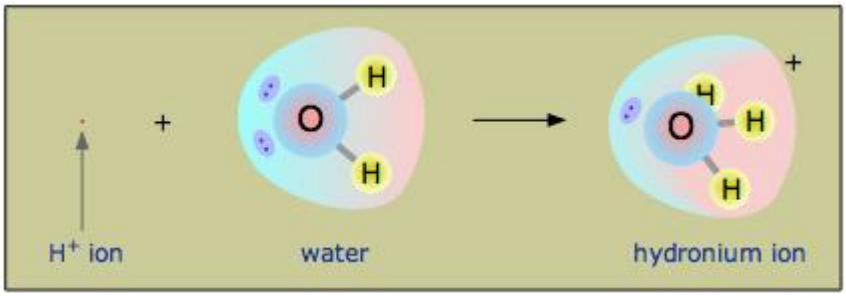

Figure 1.20 Illustration on how hydronium ion is formed [25].

It should be pointed out that a hydrogen ion cannot survive as a free ion in a solution. It has to combine with a water molecule to form the hydronium ion (H_3O^+) as is illustrated in Figure 1.20. In fact, the proton does not stick to a certain water molecule, but rather keeps changing its host forming the new hydronium ion as it hops from one water molecule to another within the electrolyte solution. The result is the transport of proton across the membrane as if these hydronium ions themselves were moving. Clearly, water is extremely important for the function of a membrane and the condition of good membrane hydration must always be ensured.

1.3.3 PEM Fuel Cell Thermodynamics

Even though a PEM fuel cell converts chemical energy into electrical energy directly, not all of this chemical energy is transformed into electricity and there are some irreversible losses in this process according to the second law of thermodynamics. During the electrochemical reaction, entropy is formed and the difference between the enthalpy and the product of temperature and this entropy defines the maximum energy that can be extracted from an electrochemical device. This is known as Gibbs free energy and is expressed mathematically in Equation (1.13);

$$\Delta G = \Delta H - T \cdot \Delta S \tag{1.13}$$

where ΔG is the change in Gibbs free energy, ΔH is the change in enthalpy, T is temperature, and ΔS is the change in entropy. At the reference condition where T = 25 °C, atmospheric pressure, and using hydrogen as a fuel, the total energy takes the value of 286.02 kJmol^{-1} and the portion that can be converted to electricity takes the value of 237.34 kJmol^{-1}. This means that 48.68 kJmol^{-1} of energy will be lost into heat during the process.

From this, the theoretical potential of a PEM fuel cell at normal condition can be calculated according to Equation (1.14);

$$E = \frac{-\Delta G}{nF} = \frac{237\,340\ [Jmol^{-1}]}{2 \times 96\,485\ [Cmol^{-1}]} = 1.23\ V \tag{1.14}$$

where n is the number of electrons transferred for each hydrogen molecule which is 2. It should be emphasised that this value represents the cell potential at standard condition. However, practical PEM fuel cells are operated at temperature and pressure other than the standard value and hence the theoretical cell potential will be less than 1.23 V.

The efficiency of a thermodynamic system is defined as a ratio of the output energy to the input energy according to Equation (1.15);

$$\eta = \frac{output}{input} \times 100\% \tag{1.15}$$

For a PEM fuel cell, the theoretical maximum output energy is equivalent to Gibbs free energy while the input energy is equivalent to the heating value of hydrogen. Dividing the two terms by nF, the maximum efficiency is expressed in terms of cell potential as;

$$\eta = \frac{\Delta G}{\Delta H_{HHV}} = \frac{\frac{\Delta G}{nF}}{\frac{\Delta H_{HHV}}{nF}} = \frac{1.23}{1.482} \times 100\% = 83\% \tag{1.16}$$

The higher heating value (HHV) of hydrogen in Equation (1.16) takes the value of 285.84 kJmol^{-1} [10] and the resulting cell potential corresponding to this value is called the thermoneutral potential. If the lower heating value (LHV) of hydrogen, which has the value of -241.83 kJmol^{-1} [10], is used, then the theoretical maximum efficiency becomes;

$$\eta = \frac{\Delta G}{\Delta H_{LHV}} = \frac{237340}{241830} \times 100\% = 98\% \tag{1.17}$$

It seems that the theoretical maximum efficiencies calculated above are attractively high. However, in a real operation, the fuel cell stack cannot operate on its own. It needs to interact with other auxiliary systems such as fuel delivery, air blower, humidification, and cooling sub-systems. Each of these devices introduces additional loss to the whole system and hence the overall efficiency of a PEM fuel cell engine will be lower.

1.3.4 The Polarisation Curve

A polarisation curve is a plot of averaged current density in the x-axis against cell's operating potential in the y-axis. It is the most important indicator of cell performance and very effective tool to compare the performances of PEM fuel cells of any size, designs, or any operating conditions. The typical polarisation curve is give in Figure 1.21.

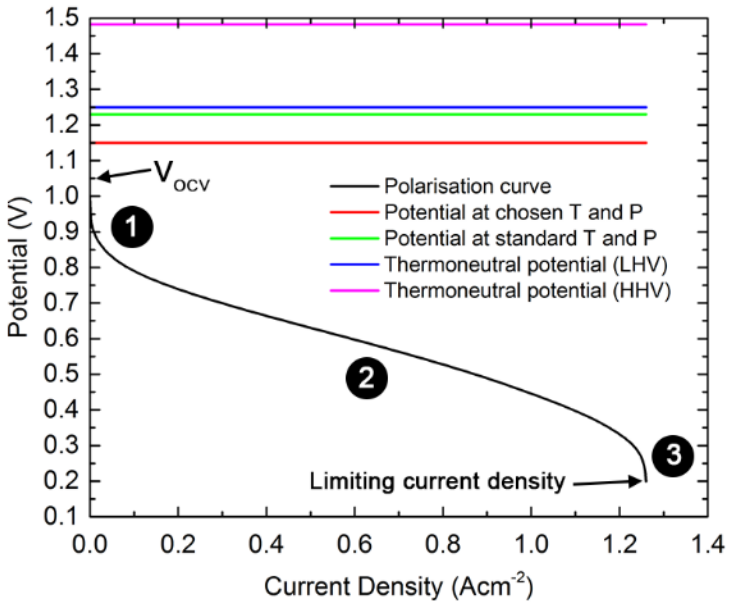

Figure 1.21 Typical polarisation curve of PEM fuel cell.

An ideal voltage source is capable of maintaining its operating voltage at a fixed value regardless of how much current is being drawn. In fact, such an ideal voltage source does not exist and therefore the potential will change with current accordingly. When no current is drawn, the cell is said to be in equilibrium and the corresponding potential is called open-circuit voltage. This open-circuit voltage is not equal to the theoretical voltage. In fact it is lower than the theoretical potential due to the internal resistance inside the cell even the current is not flowing. When the current is drawn from the cell, some irreversible losses occur and the cell is said to be polarised. This results in a decrease of cell potential as the current density increases as seen in the figure.

Depending on the dominating loss mechanism, the polarisation curve can be divided into three distinct regions as labelled in the figure. In order for the electrochemical reaction to occur, some energy is required to overcome an energy barrier and this results in a sharp decline of cell potential seen in the first region. This loss is known as activation overpotential and prevails over low-current operations. Oxygen reduction reaction (ORR) is known to be much more sluggish than hydrogen oxidation reaction (HOR), therefore the cathode

activation overpotential is much larger than the anode activation overpotential. As a consequence, the anode activation potential is therefore neglected in some numerical studies. This loss can be alleviated by increasing the operating temperature and catalyst surface area.

The loss associated with the linear decline of cell potential in the second region is known as ohmic overpotential. It is caused by the resistance to the flows of electron and proton during the operation. The resistance to the flow of electron is present in all electronically conductive components such as current collector, solid matrix in the GDLs, cell interconnects, or the wires in the external circuit while the resistance to the flow of proton only exists in the membrane. The use of a material with greater electrical conductivity, a thinner membrane, and humidified reactant streams can minimise this loss.

The last type of loss is responsible for the sharp drop of cell potential in the third region. It is called mass transport overpotential which dominates under high current density operations. This loss is associated with the concentration of reactant species at the active sites especially oxygen. Hydrogen, on the other hand, is much lighter with higher mass diffusivity than oxygen, therefore its mass transport overpotential is much smaller. Water flooding in the GDLs might be another cause of this loss since liquid water will clog up the pores in the GDLs preventing oxygen from reaching the catalyst layer. This loss can be reduced by using higher operating pressure, higher reactant species stoichiometry or inlet velocity, and better water removal.

As seen in the figure, when cell potential decreases, the current density increases and vice versa. In fact, the current density will only increase up to a certain point where a further increase in current only decreases the cell potential to zero. The current density at this point is called the limiting current density. The occurrence of this limiting current density can be delayed by the same methods on how to reduce the mass transport overpotential.

It should be emphasised that these three overpotentials exist mutually throughout the entire current density range. Applying a method to minimise a certain overpotential might have an adverse effect on another overpotential. For example, to minimise the mass transport overpotential, higher stoichiometry for both reactant streams is used. As a consequence, the higher gas velocity can dry out the membrane which results in higher ohmic overpotential. Finally, it is essential that PEM fuel cell designers are able to read and interpret information from the polarisation curve. In such a way, any loss that limits the performance of the cell can be pin-pointed and eliminated.

1.4 Research Objectives & Scope of Research

This research aims at developing a comprehensive, three-dimensional model of an automotive PEM fuel cell under a transient operation using computational fluid dynamics (CFD) as a tool to investigate the two major aspects;

1) To investigate the cell's current density response to various voltage change patterns representing the change in power demand in a typical automotive operation. A wide range of different initial voltages and excitation amplitudes are used so that all possible current response patterns can be detected and, if at all possible, categorised.
2) To investigate those current responses with the presence of significant current overshoot/undershoot and subsequently establish the relationship between these irregularities and flow-field configuration. The proposed relationship can be used as a criterion to compare the transient performance of cells with different flow-field designs and to develop a better transient performance-specific PEM fuel cell for use in an automobile.

It should be emphasised that this research is restricted to the cell-level analysis meaning the interaction between cells in the fuel cell stack and between the stack and its fuel supply, air blower, humidifier, and cooling systems are assumed to be ideal with 100% efficiency and hence discarded. Two different computational domains are used, the straight single-channel cell and the square cell, in order to address each of the two objectives, respectively. They represent a fully working cell comprising of all major components, anode and cathode flow-fields, gas-diffusion layers, catalyst layers, and membrane, except the current collector plates. Even though these segmented domains are partial replicas of a practical cell, their active areas and other dimensions are carefully chosen to ensure physically meaningful results while such characteristics of the actual cell is also preserved.

In terms of the transient excitation, where those driving cycles proposed by legalised automotive-related organisations such as NEDC, EUDC, or FTP-75 are preferred by automakers, four different voltage change patterns are used instead. These, however, are sufficient to cover all possible power demand patterns met on a typical road trip.

1.5 Thesis Outline

This thesis is organised in seven chapters as summarised in Table 1.1.

Chapter 1	The oncoming hydrogen economy and its challenges are introduced. Fuel cells technology and its variations, with particular attention on PEM fuel cells, are discussed. The working principles, applications, and criteria for examining its performance are also given. The chapter ends with the research objectives and thesis outline.
Chapter 2	This chapter reviews several major PEMFC research works found in the literature. The notable ones that serve as the cornerstone of PEM fuel cell modelling and ongoing researches are discussed. This leads to the research question at the end of the chapter.
Chapter 3	Mathematical formulation of the model is given.
Chapter 4	Important numerical aspects of the proposed model are discussed. The grid and time-step size independency studies are given which are then followed by the steady-state and transient model validations.
Chapter 5 & Chapter 6	These chapters discuss the steady-state and transient performances of the straight single-channel and square cells, respectively.
Chapter 7	A conclusion to this thesis is drawn with the discussion on difficulties the author came across during the research and some suggestions for future work.

Table 1.1 Thesis outline with description for each chapter.

Chapter 2
Literature Review

"Fools make researches and wise men exploit them."
H.G. Wells

A literature survey on PEMFC-related studies is given in this chapter. This forms an essential part of the thesis and hence was done in an early step in order to avoid reinventing the wheel which is not the purpose of such a doctoral thesis. Despite the fact that PEMFC is a rather new technology compared to batteries or internal combustion engines, PEMFC research is a multidisciplinary field that offers a wide range of potential research topics and therefore a large amount of written work, covering its entire spectrum, have already been reported. This means that addressing every single work in detail, if at all possible, is hence not an easy task.

To avoid such an unnecessary and laborious task, an inverted pyramid approach as illustrated in Figure 2.1 is used in which PEMFC research at its broadest sense is discussed briefly at the beginning in order to equip the readers with useful background information regarding all aspects of PEMFC research. The discussion then narrows down its scope as it moves towards the tip of the pyramid where those works that are relevant to the thesis objective are addressed in more details. Finally, the research question which serves as the backbone of this thesis is discussed at the end of the chapter.

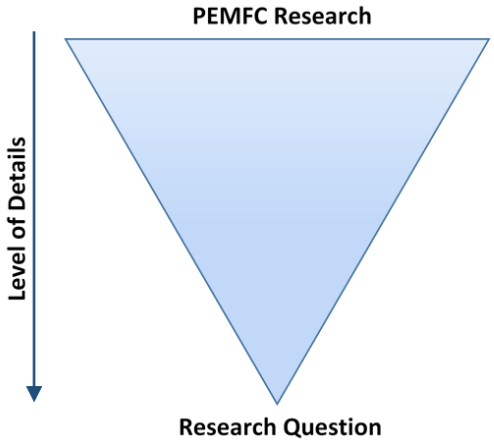

Figure 2.1 A diagram illustrating an inverted pyramid approach.

2.1 PEM Fuel Cell Commercialisation

PEM fuel cell research is a multi-disciplinary topic involving mass and heat transport, electrochemistry, power electronics, material sciences, manufacturing, to name but a few. Therefore researchers can choose to improve the cell performance in many aspects depending on their interests and expertise. As a result, many PEM fuel cell-related research works exist in the literature and it is impossible to categorise them using a single set of criteria. Nonetheless, all research work do share common objectives – increasing the cell performance, extending lifetime, and reducing manufacturing cost, in order to make this a marketable technology alongside other power-generating technologies and this is known as PEM fuel cell commercialsation.

The United States seems to be the most active country in bringing commercialisation to PEM fuel cells. This is evident since many joint-ventures and collaborations between the U.S. Government, research institutions both public and private, and industries are announced while such project reports can be accessed over the internet. A report from the U.S. Department of Energy (DoE) [26] confirms that hydrogen is the solution for America to reduce the dependence on imported oil and Green House effect gases (GHGs) and the transition to hydrogen economy has already begun. However, they are facing the "chicken-and-egg" problem in which safe and efficient hydrogen infrastructures must be built before fuel cell vehicles gain public acceptance. Finally, they stress the importance of a consistent support from the government at the energy policy level. An overview of the strategy towards the hydrogen economy is shown in Figure 2.2.

Another report from the U.S. DoE [27] addresses the challenges to the transition to hydrogen economy in four aspects; cost reduction, hydrogen production methods, efficient on-board hydrogen storage, and safe and efficient hydrogen infrastructures. The U.S. government also provides funding opportunities on various PEM fuel cell-related projects as can be seen in [28] where the 2015 target for PEM fuel cell system for transportation application is set and shown in Figure 2.3. This is widely accepted as the performance target for an automotive PEM fuel cell among the research community.

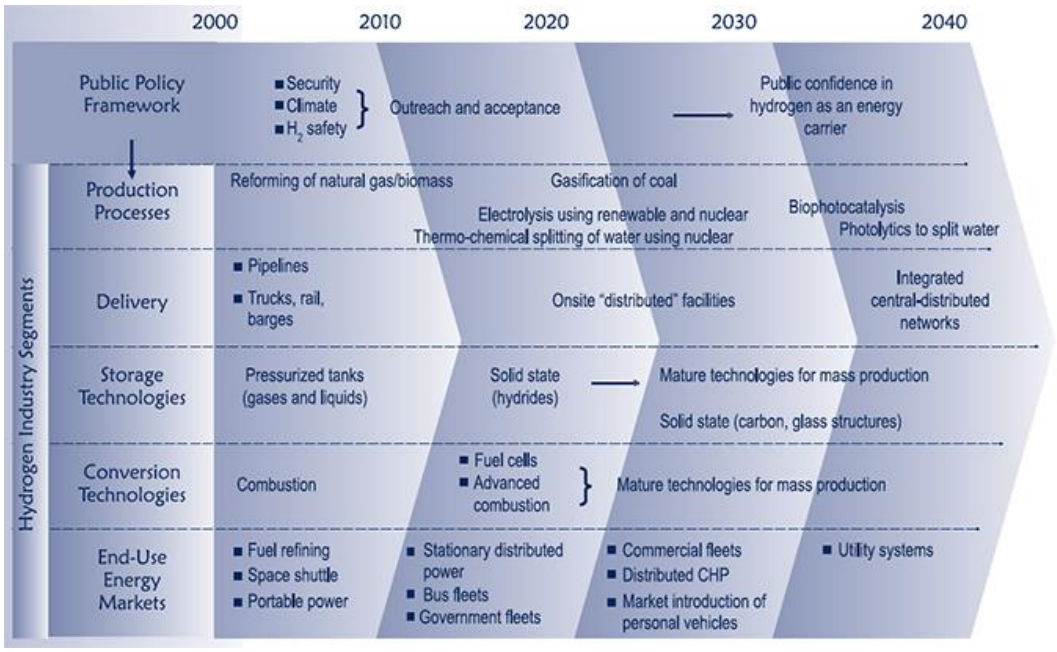

Figure 2.2 Overview of America's transition to the hydrogen economy.

Characteristic	Units	Target 2015
Energy efficiency @ 25% of rated power [b]	%	60
Energy efficiency @ rated power	%	50
Power density	W / L	650
Specific power	W / kg	650
Cost [c]	$ / kW_e	30
Transient response (time from 10% to 90% of rated power)	s	1
Cold start up time to 50% of rated power @–20°C ambient temperature @+20°C ambient temperature	 s s	 30 5
Start up and shut down energy [d] from -20°C ambient temperature from +20°C ambient temperature	 MJ MJ	 5 1
Durability with cycling	hours	5,000 [e]
Unassisted start from low temperatures [f]	°C	-40

[a] Targets exclude hydrogen storage, power electronics and electric drive.
[b] Ratio of DC output energy to the lower heating value (LHV) of the input fuel (hydrogen). Peak efficiency occurs at about 25% rated power.
[c] Based on 2002 dollars and cost projected to high-volume production (500,000 systems per year).
[d] Includes electrical energy and the hydrogen used during the start-up and shut-down procedures.
[e] Based on test protocols in Appendix D.
[f] 8-hour soak at stated temperature must not impact subsequent achievement of targets.

Figure 2.3 The 2015 technical targets for automotive applications: 80 kW_e (net) integrated transportation fuel cell power systems operating on direct hydrogen[a] [28]

To move towards such commercialisation, many aspects of the PEM fuel cells require extensive research. A review given by Wang et al. [29] addressed important challenges to the PEM fuel cell researches in stationary, transportation, and portable electronics applications. They perceived PEM fuel cell commercialisation as having three major aspects – durability, manufacturing cost, and performance, which can be improved through effective heat and water management and advanced materials research. Another good review by Martin et al. [30] also treated the PEM fuel cell commercialisation in the same three aspects as [29] with a detailed review on advanced materials research for catalyst layers and electrolyte membrane, in particular.

As discussed in Chapter 1 that PEM fuel cells possess a very promising characteristics to be used in vehicles, several reviews on PEM fuel cell research trends for transportation application, in particular, can be found. These include a review by Ahluwalia and Wang [31] which discussed state-of-the-art ongoing research taking into account the U.S. DoE 2015 performance targets. They concluded that the 2015 targets were very tight, and with current advancement, these could only be achieved by operating the cell on elevated temperature up to 120 °C without pressurisation nor reactant streams humidification. This, however, requires a new type of membrane that can withstand a temperature as high as 95 °C. Erdinc and Uzunoglu [32] confirmed, in their review, that PEM fuel cells are superior to other fuel cells in the transportation application while they examined various hybrid configurations implemented on a car in terms of the complexity of control system versus performance. They concluded that in order for a PEM fuel cell car to have a comparable performance to a conventional ICE-powered car, a PEM fuel cell needs to be hybridised with an auxiliary power storage device. An interesting comparison between an all-electric PEM fuel cell vehicle and other partially-electric hybrid vehicles from Thomas [33] was reported. In his study, a numerical model was developed to compare the societal effect of each hybrid configuration such as mass, volume, cost, green house gases, refuelling time, and efficiency over a 100-year timeframe. They found that all-electric vehicles such as PEM fuel cell vehicles (PEM-FCVs) and battery-electric vehicles (BEVs) are the only options if the goal of pollution reduction is to be met in the near future and they are superior to any ICE-based hybrid electric vehicles (HEVs) even biofuels are used.

In an attempt to understand the aging mechanism of a PEM fuel cell, many experimental studies have been reported either on single-cells [34], scaled-down stacks with small number of cells [35], or commercial-scale PEM fuel cell stacks under stationary or transient automotive operations [36]–[39]. The findings from these studies suggest that the

durability of an electrolyte membrane determines the cell's lifetime which varies considerably depending on the operating conditions and loading cycles. This is in agreement with the work published by Pei and Chen [40]. In addition, another review on durability issues with state-of-the-art conditioning and monitoring approaches can be found in the work of Knowles et al. [41]. Moreover, a PEM fuel cell stack under automotive load cycle tends to have a shorter lifespan than the one operated under a stationary operation and the variation in current density between cells in the stack exists in the same way it does in a single cell where the cells near the outlet tend to fail due to the effect of liquid water flooding. In addition, a numerical approach has also been used in understanding the degradation mechanism of the polymer electrolyte membrane at a molecular level and such a model is proposed in the work of Shah et al. [42] while some other degradation models are reviewed in reference [43].

The performance of a PEM fuel cell can also be improved through the electrochemistry aspect. Advancements in materials and interfacial sciences on the catalyst layers and PEM membrane, where electrochemical reaction takes place, are therefore needed. However, this is beyond the scope of the thesis thus only relevant examples are given here. As an example, Parthasarathy and Srinivasan [44] studied the effect of oxygen pressure at the catalyst/electrolyte interface on oxygen reduction kinetics from an electrochemistry viewpoint. They found that the diffusion coefficient of oxygen was lower when air was used as the cathode gas stream instead of pure oxygen. An attempt to better understand the complex behaviour of the catalyst layer can be seen both experimentally [45], where an environmental scanning electron microscopy (ESEM) was used for the first time to obtain the local distribution of micro-contact angle inside the catalyst layer, and numerically, where a model of a single catalyst particle was used to confirm that size of platinum particle and its loading play a major role in the performance of the cell in the work of Yan and Wu [46]. Similarly, the electrolyte membrane used in power generating devices was modelled at a molecular level in the work of Balbuena et al. [47].

Lastly, cost reduction of a PEM fuel cell system can be achieved through a more economical manufacturing method that saves the cost while keeping manufacturing defects to a minimum. Manufacturing methods and alternative options for each component of an automotive PEM fuel cell are reviewed in [48]. The bi-polar plate, in particular, is known to contribute to a large portion of the total cost in a fuel cell stack therefore receives much attention from the research community. The research trends on this specific component are reviewed and discussed in [49], [50] while the latter focuses on material selection for those bi-polar plates made from the stamping process.

2.2 PEM Fuel Cell Research by Scopes

It should be re-emphasised here that the commercialisation of a PEM fuel cell could be achieved through increasing the performance of a PEM fuel cell. However, all the works mentioned in the previous section involved in materials and electrochemistry aspects which are out of the scope of this thesis. Besides, such power/energy density and steady-state/transient response of the cell can be improved through effective cell components design, appropriate operating conditions, and intelligent integration between a PEM fuel cell engine and other sub-systems in the vehicle's powertrain together with robust control algorithms, which are regarded as the most active topics in PEM fuel cell research.

In this section, only the works that are relevant to the above topics are reviewed. Using the scope of study as a criterion, these works can be categorised into three major groups as shown in Figure 2.4 where the linkage between them is illustrated. These are known as, from top to bottom, system-level, stack-level, and cell-level study.

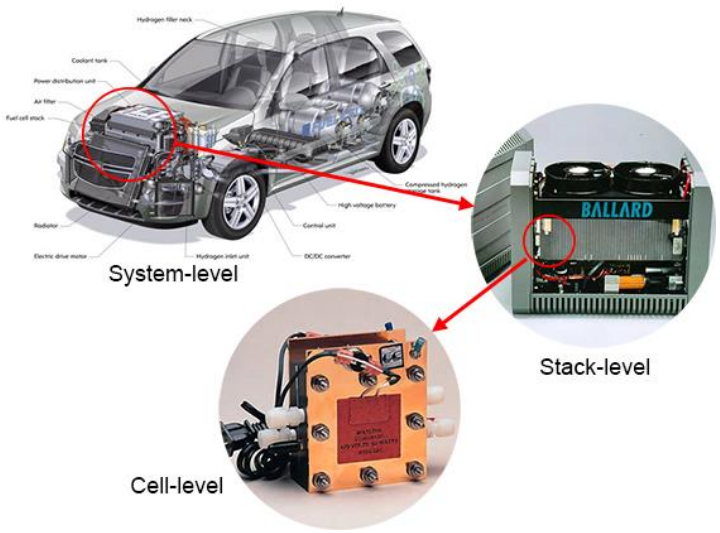

Figure 2.4 Depending on the scope of the study, published works in the literature can be grouped as system-, stack-, and cell-level studies (reproduced from [51]–[53]).

2.2.1 System-level Study

Most system-level studies focus on the interaction between the PEM fuel cell engine and other sub-systems in the vehicle's powertrain where the efficiency, fuel economy, and ability to deliver the required power are of prime importance. Additional performance targets and dynamic requirements for a fuel cell engine from a powertrain viewpoint have been systematically analysed in the work of Pischinger et al. [54] which can be used as a good starting point for a system-level PEM fuel cell research.

Successful implementation of a PEM fuel cell engine on a ground vehicle under real driving conditions has been reported. The Green Car, for example, which is claimed to be the world's first PEM fuel cell car, has been reported [55] to successfully operate on a PEM fuel cell engine with the aid of a lead-acid battery bank to provide peak power during acceleration. Other successful demonstration programs on a light-vehicle [56], a three-wheeler [57], and a scooter [58] have also been reported.

Typically, a PEM fuel cell engine is not the only source of power in the powertrain. An energy storage device such as battery or ultra-capacitor is also included in order to account for high power surge during acceleration, hill-climbing, or cruising at high speed. This is commonly known as hybridisation. Such characteristics and performance of a vehicle under hard and mild hybrid configurations are discussed in the works of Corbo et al. [59]. Moreover, it is more common to operate the PEM fuel cell engine in a load-levelled mode rather than a load-following mode in order to achieve higher efficiency from the fuel cell system as reported in [60]–[62].

To conclude, with current advancement in PEM fuel cell technology, a satisfactory performance that is comparable to a conventional powertrain can only be achieved by hybridising a PEM fuel cell with an energy storage device. As a consequence, various possible hybrid configurations exist which still require considerable research effort to seek for efficient powertrain system integration and robust control algorithms.

2.2.2 Stack-level Study

In comparison to system-level studies, a stack-level study tackles the problem by;

1. Treating a fuel cell stack as an ideal stack having no performance variation of individual cells within the stack in order to investigate an interaction between the fuel cell stack and its auxiliary sub-systems such as fuel delivery, air compressor, humidifier, or cell cooling sub-system. This approach aims at finding the best control strategy in order to achieve desire performance from the fuel cell stack in terms of both stack power and response.
2. Taking into account the variation of important parameters such as voltage, current density, temperature, and pressure drop between individual cells. In contrast to the first approach, the interaction between the stack and other sub-systems is often neglected or assumed ideal with 100% efficiency to simplify the situation. This allows the study to focus on why such variation occurs and how to achieve the uniformity, or at least reduce non-uniformity, of these parameters.

One of the most important performance indicators used in most stack-level studies is the stack voltage. Since many, typically several hundreds, individual cells are connected in series in a fuel cell stack, voltage variation of each cell within the stack has been observed. This has an adverse effect on the fuel cell system and should be avoided. An effective voltage monitoring method is thus needed as discussed in the work of Webb and Moller-Holst [63] where a low-cost, light-weight, fast, and accurate method is proposed. Moreover, Shen et al. [64] found that this voltage variation is also affected by magnitude of operating current in which greater current density induces more non-uniformity of the voltage within the stack. Corbo et al. [65] also reported that this voltage variation was enlarged under a transient operation. Using their self-derived coefficient of variation, C_V, to quantify the uniformity of stack voltage where the value of 2% was claimed acceptable for a reliable stack operation, they found that the stack tested was able to survive the two European driving cycles and the faster load commutation induces larger voltage variation.

Efficiency of the fuel cell system can also be improved through better fuel utilisation which requires effective fuel delivery system. In fact, such a system can be broken down to the fuel (hydrogen) and oxidant (oxygen) delivery lines. For the fuel side, it is common to make use of the exiting unused hydrogen stream and re-introduce it to the anode flow-field, known as hydrogen recirculation and a novel control strategy is proposed by He et al. [66]. However, Han et al. [67] claimed that hydrogen recirculation system requires pumps or ejectors which introduce additional parasitic power to the system and suggested an innovative stack design that can achieve high fuel utilisation without the need for hydrogen recirculation. Instead of using pure hydrogen stored in a tank, an on-board reformer feeding on petrol has been investigated as an alternative by Mitchell et al. [68] where it is found that the response of the fuel cell system is strongly affected by the fuel processor response time.

It is known that the flow of oxidant is critical in achieving high current density. This is especially true in an automotive fuel cell system where the use of ambient air, which has much lower oxygen content, is more practical than pure oxygen from a tank. The air delivery system, particularly the compressor, thus receives much more attention from the research community compared to the fuel delivery system. Important requirements and design approaches for a compressor in the air feeding system are reviewed and discussed in the work of De Francesco and Arato [69] with particular attention on the system start-up. The most common trend of regulating the air compressor is to operate it under the load-following mode where improvement in stack voltage uniformity and system efficiency was evidenced in [70], [71].

In addition to keeping the stack temperature within a designated range, another important objective of the heat management system is to promote uniform temperature within the stack through a dedicated cell cooling system. As an introduction to this research area, interested readers are advised to consult the work of Kandlikar and Lu [72] where important issues and ongoing researches regarding heat management of a fuel cell stack are addressed. Another heat management-related publication by Zhang and Kandlikar [73] puts emphasis on stack cooling where the current cooling techniques are categorised into four main methods – (i) conductive cooling using heat spreaders, (ii) convective air cooling, (iii) convective cooling by liquid water or coolant, and (iv) evaporative cooling.

A PEM fuel cell operates at around 80-100 °C, which is much lower temperature compared to conventional ICEs or high-temperature fuel cells, therefore the requirement for heat removal by the cooling system is not as critical. This makes air cooling the most popular method. A study from Adzakpa et al. [74] reveals that large temperature variation not only exists in a single cell (5 °C), but also within a stack, which is even more significant (8 °C), suggesting the need for a proper air cooling strategy. A novel method is proposed by Sasmito et al. [75] using the "flow reversal technique." By intermittently reversing the direction of the flow of cooling air, the issue of a higher stack temperature at the outlet which is caused by the cooling air picks up the heat and heats up along the path can be eliminated. Even though improvement in stack temperature uniformity and reduction of maximum stack temperature are claimed, this design requires the second cooling fan which incurs additional system complexity and cost. This leaves a question whether the proposed design is practical. Finally, an attempt to design a more effective dedicated cooling plate can be seen in [76], [77].

Water management is a complex issue involving sophisticated two-phase transport of water and membrane water absorption/desorption. This suggests the need to investigate such issue at a smaller level – macroscopic scale. Therefore, stack-level studies on water management are less plentiful than the cell-level studies. As a result, most stack-level water management studies concentrate on finding the best method to monitor or detect liquid water flooding in the stack. An attempt to correlate the already available anode/cathode pressure drop data to the degree of flooding can be seen in [78], [79].

As a main power source for an automobile, the most important specification of a PEM fuel cell stack is its response under the real automotive operation. Such stack responses in terms of voltage or current density to the applied dynamic loads representing the engine startup, shut down, and driving cycles are extensively investigated both experimentally [80]–[82] and numerically [83]–[88]. It is found that the PEM fuel cell stack has a fast response to

all load commutations tested confirming the eligibility of a PEM fuel cell as a replacement to the conventional internal combustion engines. Additionally, an interesting transient behaviour of the output current is reported in which the current overshoot and undershoot have been detected when the stack voltage is decreased and increased, respectively. These current overshoot and undershoot, however, are undesirable and thus need special attention.

On the other hand, the cell-level study has gained most attention from the research community among the three. It deserves a separate section in which the related publications are discussed.

2.3 PEM Fuel Cell Research at Macroscopic Scale (Cell-level Study)

As more stringent regulations on road vehicles become active, the performance targets have to be set inevitably higher. The system- and stack-level studies seem too coarse to achieve such new goals necessitating the need to understand the PEM fuel cell from a more fundamental perspective – a cell-level study. Compared to the system- and stack-level studies, the scope of a cell-level study is narrowed down to within a unitary cell hence isolating it from the effect of non-ideal sub-systems such as fuel delivery system, stack cooling, battery banks, electric motor, or even other unitary cells in the same stack. From this macroscopic viewpoint, an insight to the transport phenomena and electrochemistry inside the cell and effect of operating parameters on the cell performance are the main objectives.

As mentioned previously in Chapter 1 that a current collector and the flow-field grooved onto it plays an important role in achieving high performance. Therefore, only cell-level studies which are relevant to the flow-field configuration are discussed in this section. The readers should be informed that a similar review regarding this aspect has been addressed briefly in the author's previous works [89], [90]. Here, its structure is maintained while additional materials are added for a more comprehensive review.

Due to the fact that the a typical length scale of a PEM fuel cell is in a range of a few microns to millimetres, this poses challenges to experimenters in which sophisticated measuring devices, if at all available, and great skills are required. Moreover, Djilali [24] and Wang et al. [29] have emphasised in their work that an insight into the highly coupled and non-linear phenomenon between species transport and electrochemistry is critical in achieving a better performance of a cell. This explains why PEM fuel cell modelling dominates PEM fuel cell experiments. An excellent work addressing all aspects of PEM fuel cell modelling from fundamental principles to the current issues is given by Wang [91] while comparisons on different modelling approaches can be seen in [92]–[94].

Early attempts to numerically study the PEM fuel cell can be seen in the works of Springer et al. [95] and Bernadi et al. [96], [97]. In these works, mechanistic equations are used to describe the transport of reactant species and electrochemical reaction inside the cell. The transport of water inside the membrane, on the other hand, is much more sophisticated hence an empirical relation was used to describe the crucial membrane water content, λ, as a function of water vapour activity on the membrane. It should be noted that even though this empirical relation has been derived from experimental data of Zawodzinski [98], which is limited to the Nafion-family membranes, particularly Nafion 117, it remains as the "standard" membrane water content model used in most numerical studies until present. A generic model that can be used with all membranes is still lacking. In spite of being one-dimensional in nature, these early works provided basic concepts to cell-level PEM fuel cell modelling and served as a framework in which later multi-dimensional models are built upon.

The use of a single-domain approach on the modelling of electrochemical systems has been reported in [99], [100]. Gurau et al. [101] used this same method to develop their two-dimensional PEM fuel cell model which allowed computational fluid dynamics (CFD) to be deployed on fuel cell modelling for the first time. The use of this single-domain approach eliminates the need to define the boundary condition for the internal interfaces between different sub-regions because they all share the same set of governing equations. Rather, only external boundaries need treatment which reduces researcher's effort during the pre-processing stage considerably. Other two-dimensional modelling works which focus on different aspects of a PEM fuel cell such as water and heat management [102]–[104] or effect of flow-field geometry [105], [106] are also reported.

As the highly three-dimensional characteristics of species transport and electrochemistry inside the cell has been realised through the discrepancy between experimental data and numerically predicted results from one- and two-dimensional models, a full three-dimensional model is needed. By extending their previous two-dimensional works, Dutta et al. [107] proposed, for the first time, a three-dimensional CFD model to study the straight single-channel cell. In their model, a commercial CFD code was modified to account for the consumption/production of reactant species while the two catalyst layers was treated as an interface with no thickness. This CFCD technique has stimulated a surge in new research interest in which CFD is used to investigate the effect of flow-field configurations and geometries on the cell performance which remains as one of the most active topics in PEM fuel cell modelling. Such works can be found in [108]–[118].

2.4 Chapter Summery and Research Question

It is evident that the mainstream interest focuses on the steady-state performance of a PEM fuel cell in which the effect of operating parameters and flow-field configurations on the steady-state performance has been well-established. In a contrary, much less research attention has been put into the transient performance which is of paramount importance for an automotive PEM fuel cell.

The transient responses of a cell under dynamic loading has been investigated both experimentally [119]–[122] and numerically [123]–[140]. Even though the cell current density has been reported to respond sufficiently fast to the voltage change, the undesirable current overshoot and undershoot have been also detected. Some studies have been carried out to investigate such phenomenon in order to establish the relationship between the magnitude or characteristics of these current overshoot/undershoot and operating temperature [123], [138] or cell humidification [127], [130], [137], for example, while the effect of flow-field geometry on the current response is barely touched.

However, remarkable works on transient analysis of a PEM fuel cell under dynamic loading have been published by Shimpalee et al. [128], [129], [131], [141]. An interesting conclusion has been drawn from these works in which the occurrence of current overshoot and undershoot is closely coupled to the non-uniformity of local current density over the cell's active area which is caused by the redistribution of reactant species as the cell adjusts itself to the new equilibrium stage. Since the flow-field design has been known to be the major player in determining the uniformity of reactant species and in turn local current density, this suggests that such current overshoot/undershoot must be affected by the flow-field design to some extent. This leaves the author with a research question as follows;

"Since flow-field design has a strong influence on the steady-state performance of a PEM fuel cell, to what extent, and how does it affect the transient response in terms of current overshoot and undershoot?"

Chapter 3
Model Development

"All models are wrong, but some models are useful."
George P. E. Box

A PEM fuel cell has a very simple geometry in which it comprises solely of orthogonal components without any curvature. Despite its researcher-friendly appearance, the underlying physics inside the cell is complex and highly non-linear. Computational Fluid Dynamics (CFD) is chosen to be a tool in the analysis of PEM fuel cells, often the method is known as Computational Fuel Cell Dynamics (CFCD). Theoretically, this gives unlimited spatial and temporal resolutions which makes possible the local distribution of flow-fields variables that are critical to the design process. This is particularly essential for understanding the effect of flow-field geometries on the distribution of flow-field variables and in turn the cell performance, which is the objective of this thesis.

This chapter addresses how a numerical model is developed, which is organised into four parts:

1) Fundamental and auxiliary equations embedded in the model.
2) The two computational domains used for the analyses.
3) Boundary conditions and initial conditions.
4) Model input parameters.

3.1 Governing Equations

The governing partial differential equations (P.D.E.s) are the heart and soul of a PEM fuel cell model. They represent the underlying physics inside a PEM fuel cell, which can be thought of as a coupled system of

1) Gas species transport,
2) Heterogeneous electrochemical reaction, and
3) Transport of electron (or electric current).

The governing equations for the above physical phenomena are based on the fundamental principles in physics, without the presence of nuclear reaction, these are:

1) Mass is conserved.
2) Linear momentum is conserved (Newton's Second Law).
3) Energy is conserved (First Law of Thermodynamics).
4) Electric charge is conserved.

All equations are structured around a so-called unified-domain approach, which means that an entire computational domain is governed by the same set of equations. However, the physics specific to each sub-domain is not lost as they will manifest themselves as source and sink terms in their corresponding transport equations.

3.1.1 Assumptions

The validity of CFCD results is, at best, as good as their embedded mathematical equations, and, at worst, as good as their simplification. While ensuring that the physical characteristics of the cell are retained, some assumptions are made to simplify the calculation as follow;

1) Effect of gravity is ignored.
2) All gas-phase species behave as an ideal gas.
3) Anode reactant gas is pure hydrogen so there is no contamination effect.
4) Cathode reactant gas is air with an oxygen to nitrogen ratio of 21:79, by volume.
5) Both reactant streams are humidified and the relative humidity (RH%) varies depending on the objective of each analysis.
6) The flow of reactant gases are laminar throughout the operation range.
7) The flow of reactant gases are treated as incompressible flow.
8) Multiphase flow is present both in the flow channel and porous media.
9) The membrane is impermeable to gas species.
10) Porous media are isotropic and homogeneous.

11) Due to a high electric conductivity of the current collector, potential drop across the terminal surface is neglected and therefore a uniform potential is assumed.
12) Current collector is said to only introduce additional resistance to the flow of electron in the circuit, which is negligible. Hence it is excluded from the model.
13) Water is assumed to be in either liquid or vapour state only. It does not exist as a dissolved state.
14) Product water from the reaction is assumed to be in a vapour state.
15) There is no interaction between gas-phase species and liquid water.
16) The cooling of the cell is assumed to be highly effective hence all external boundaries have a constant and uniform temperature which is equal to the cell's operating temperature.

3.1.2 Multiphase Flow

The typical operating temperature for a PEM fuel cell is around 100 °C which is sufficiently low for water vapour to condense into liquid. This liquid tends to block the pores in porous media preventing reactant species from reaching the active site. As a consequence, the overall performance will be decreased. In fact, multiphase flow is inevitable in practical cells under normal operations. A numerical model should therefore take into account the physics of multiphase flow if a proper water management in the cell is to be addressed. In addition to its physical aspect, the numerical aspect of a multiphase flow should be discussed before moving on to the derivation of governing equations since it determines the approach used in formulating the governing equations that follow.

The formulation for a multiphase flow used in the numerical model in this thesis is centred around a so-called multiphase mixture method (M^2) which was developed by Wang and Cheng [142]. In their approach, the flow is treated as a single fluid consisting of diffusing constituents or phases [143]. The M^2 formulation is based on a mixture basis in which all phases in the mixture share the same continuity, velocity, and pressure fields. The characteristics of the flow are described in terms of the mixture properties. However, explicit relations such as volume of fraction for each phase and relative velocity (velocity slip) between phases are introduced which would then be used to derive back the properties for each individual phase. This is to ensure that their physical characteristics is not lost.

Liquid water is assumed to exist in all porous layer except in the membrane. Liquid water is condensed from water vapour present in these layers, due to humidification of the reactant gas and chemical reaction, depending on the local saturation level and it is removed

from the porous layers to the channel by means of capillary effect. This liquid water is assumed to emerge as small droplets and be uniformly dispersed in the gas flow once it has reached the flow channel. The velocity of liquid water is assumed to be equal to the gas velocity according to a mist flow assumption. The flow in the channels is then treated as a homogeneous multiphase flow.

As oppose to the model proposed in the work of Wu [144], where water is produced and transported across the membrane in a dissolved form. The water in this thesis is assumed to be transported by electro-osmosis and back-diffusion in the vapour form. They will emerge as source and sink terms in the conservation of water vapour equation. Though this may violate the gas-impermeable assumption of the membrane, realistic results were obtained without losing much accuracy as is evident in the model validation section.

3.1.3 Conservation of Mass

The conservation of mass states that mass can neither be created nor destroyed. The time-dependent mass conservation equation in the entire domain takes the form;

$$\frac{\partial(\varepsilon\rho)}{\partial t} + \nabla \cdot (\varepsilon\rho \boldsymbol{V}) = S_m \tag{3.1}$$

Equation (3.1) is also known as the continuity equation, where ρ is the mixture density and ε is the porosity of a porous region which takes the value of unity in the flow channels. The flow in all sub-domains, except the membrane, is both multicomponent and multiphase. The gas-phase species are hydrogen, oxygen, and water vapour while the only liquid-phase species is liquid water. The source term, S_m represents the consumption or generation rate of these species which is different from region to region as summarised in Equation (3.2).

$$S_m = \begin{cases} S_{H_2} + S_{H_2O,an} + S_{liq} & anode\ channel, GDL, CL \\ S_{O_2} + S_{H_2O,ca} + S_{liq} & cathode\ channel, GDL, CL \\ 0 & membrane \end{cases} \tag{3.2}$$

The source terms for hydrogen gas, oxygen gas, anode and cathode water vapour, and liquid water are addressed in the next section. As mentioned previously in Sections 3.1.1-3.1.2, the transport of water due to electro-osmosis and back-diffusion is assumed to take place in a vapour form and liquid water condensation does not occur in the membrane. No species is therefore consumed or produced in the membrane thus a zero source term is used.

3.1.4 Conservation of Species

For the gas-phase i-th species, the governing equation takes the form;

$$\frac{\partial(\varepsilon\rho w_i)}{\partial t} + \nabla\cdot(\rho w_i \boldsymbol{V}) = -\nabla\cdot\boldsymbol{J_i} + S_i \tag{3.3}$$

where mass fraction of the i-th species, w_i, is the ratio between its mass to total mass of the mixture. The flux of the i-th species into the elementary volume, $\boldsymbol{J_i}$ ($kgm^{-2}s^{-1}$), is written as;

$$\boldsymbol{J_i} = -\rho D_{ij}\nabla w_i - D_{T,i}\frac{\nabla T}{T} \tag{3.4}$$

The first term in Equation (3.4) represents the Fickian diffusion due to concentration gradient while the second term represents the mass flux due to Soret effect which is caused by a temperature gradient. The thermo-diffusion coefficient, D_{T_i}, has units of $kgm^{-1}s^{-1}$. Since the cell temperature is effectively uniform throughout the operation range, the mass flux due to the Soret effect is very small and can be neglected in most cases.

The diffusion coefficient, D_{ij}, is calculated using a Stefan-Maxwell model. Though this method is more computationally intense, it gives accurate local species distributions which are critical to the determination of local current density especially in the porous media where diffusion is the dominating mode of transport. The tortuosity of the porous media is also taken into account through the use of the so-called Bruggeman correction equation;

$$D_{ij}^{eff} = \varepsilon^{\tau} D_{ij} \tag{3.5}$$

where D_{ij} is calculated from Stefan-Maxwell model and the tortuosity, τ, takes the value of 1.5 which is the typical value used in the literature [145].

The transport of liquid water in the flow channels is governed by a local volume-fraction of liquid water or water saturation equation;

$$\frac{\partial(\varepsilon\rho_{liq}s)}{\partial t} + \nabla\cdot(\rho_{liq}s\acute{\nu}\boldsymbol{V}) = S_{liq} \tag{3.6}$$

Water saturation, s, is defined as the ratio of volume in the pore occupied by liquid water to the total pore volume. The slip velocity between liquid-phase and gas-phase species, $\acute{\nu}$ is unity as all phases share the same velocity fields. Inside porous layers where flow velocity is very small due to high flow resistance, the convective term in Equation (3.6**)** is replaced by a new diffusion term which is caused by capillary action. The resulting equation thus becomes;

$$\frac{\partial(\varepsilon\rho_{liq}s)}{\partial t} + \nabla\cdot\left(-\rho_{liq}\frac{ks^3}{\mu_{liq}}\frac{dp_c}{ds}\nabla s\right) = S_{liq} \tag{3.7}$$

Using Leverette function, the capillary pressure, p_c, is a function of s and can be calculated from;

$$p_c = \begin{cases} \dfrac{\sigma \cos\theta_c}{\sqrt{\dfrac{k}{\varepsilon}}}(1.417(1-s) - 2.12(1-s)^2 + 1.263(1-s)^3) & \theta_c < 90° \\ \dfrac{\sigma \cos\theta_c}{\sqrt{\dfrac{k}{\varepsilon}}}(1.417s - 2.12s^2 + 1.263s^3) & \theta_c > 90° \end{cases} \quad (3.8)$$

where σ is surface tension (Nm^{-1}), θ_c is contact angle, and k is absolute permeability (m^2).

The model assumes an equilibrium phase change between liquid water and water vapour throughout the domain which is the only mechanism that consumes or generates liquid water. When condensation occurs, the source term, S_{liq} ($kgm^{-3}s^{-1}$), in Equations (3.6**)** and (3.7**)** has a positive value indicating that more liquid water is added into the domain. The amount of water in the water vapour equation, Equation (3.3**)**, which is lost through phase change will be equal to the amount of liquid water gained from condensation.

To simplify the calculation, the condensation and evaporation rates are assumed to be equal in this model. The condensation source term, S_{liq}, in the liquid water equations is a function of local partial pressure of water vapour and saturation pressure as;

$$S_{liq} = k_c(1-s)\frac{P_{wv} - P_{sat}}{RT}M_{H_2O} \quad (3.9)$$

where k_c is the condensation/evaporation rate and takes a constant value of 100 s^{-1}. The $-S_{liq}$ term is added to water vapour equation as a sink term.

The consumption of hydrogen at the anode catalyst layer is derived from the fact that $\frac{1}{2}$ moles of hydrogen is consumed in order to produce 1 mole of electrons, therefore;

$$S_{H_2} = -\frac{R_{an}}{2F}M_{H_2} \quad (3.10)$$

Similarly, $\frac{1}{4}$ moles of oxygen is needed to produce a mole of electrons;

$$S_{O_2} = -\frac{R_{ca}}{4F}M_{O_2} \quad (3.11)$$

Finally, the generation of water vapour from the reaction is calculated in the same way;

$$S_{wv,gen} = \frac{R_{ca}}{2F}M_{H_2O} \quad (3.12)$$

where R_{an} and R_{ca} are transfer current discussed in Section 3.1.7. The fluxes of water vapour due to electro-osmosis and back-diffusion $\boldsymbol{J_{osm}}$ and $\boldsymbol{J_{diff}}$, respectively, are described in Section 3.1.8. The source terms for each species are summarised in Table 3.1.

$(kgm^{-3}s^{-1})$	S_{H_2}	$S_{H_2O,an}$	S_{O_2}	$S_{H_2O,ca}$	S_{liq}
$\mathrm{Channel_{an}}$	-	$-S_{liq}$	-	-	$k_c(1-s)\frac{P_{wv}-P_{sat}}{RT}M_{H_2O}$
$\mathrm{GDL_{an}}$	-	$-S_{liq}$	-	-	$k_c(1-s)\frac{P_{wv}-P_{sat}}{RT}M_{H_2O}$
$\mathrm{CL_{an}}$	$-\frac{R_{an}}{2F}M_{H_2}$	$-\nabla\cdot\boldsymbol{J_{osm}}+\nabla\cdot\boldsymbol{J_{diff}}-S_{liq}$	-	-	$k_c(1-s)\frac{P_{wv}-P_{sat}}{RT}M_{H_2O}$
PEM	-	-	-	-	-
$\mathrm{CL_{ca}}$	-	-	$-\frac{R_{ca}}{4F}M_{O_2}$	$\frac{R_{ca}}{2F}M_{H_2O}+\nabla\cdot\boldsymbol{J_{osm}}$ $-\nabla\cdot\boldsymbol{J_{diff}}-S_{liq}$	$k_c(1-s)\frac{P_{wv}-P_{sat}}{RT}M_{H_2O}$
$\mathrm{GDL_{ca}}$	-	-	-	$-S_{liq}$	$k_c(1-s)\frac{P_{wv}-P_{sat}}{RT}M_{H_2O}$
$\mathrm{Channel_{ca}}$	-	-	-	$-S_{liq}$	$k_c(1-s)\frac{P_{wv}-P_{sat}}{RT}M_{H_2O}$

Table 3.1 Species sources in different sub-regions.

3.1.5 Conservation of Momentum

The velocity field is governed by, in a vector form;

$$\frac{1}{\varepsilon}\frac{\partial(\rho \boldsymbol{V})}{\partial t}+\frac{1}{\varepsilon^2}\nabla\cdot(\rho \boldsymbol{V}\boldsymbol{V})=-\nabla p+\nabla\cdot\bar{\bar{\boldsymbol{\tau}}}+S_{pj} \tag{3.13}$$

where $\bar{\bar{\boldsymbol{\tau}}}$ is a stress tensor.

Due to additional resistance in the porous layers, momentum is lost and the pressure drop is increased. Using Darcy's law for flow in a porous medium, the sink term, S_{pj}, is only active in the porous layers and modelled as, where j represents x-, y-, and z-coordinates;

$$S_{px}=-\frac{\mu}{k_x}u\,,\qquad S_{py}=-\frac{\mu}{k_y}v\,,\qquad S_{pz}=-\frac{\mu}{k_z}w \tag{3.14}$$

where μ is dynamic viscosity (Pa·s) and β is permeability (m^2). Since porous media are assumed to be isotropic therefore $k_x=k_y=k_z=k$ unless specified otherwise.

3.1.6 Conservation of Energy

Even though the temperature variation is small in typical PEM fuel cells, heat transfer in the cell is still important, particularly, in determining the properties of reactant species which are temperature-dependent. Additionally, the water phase change is also strongly dependent on the temperature field. By enabling the energy equation in the model, an accurate distribution of local liquid water in porous layers which is a critical parameter in flow-field design can be obtained. The energy equation is;

$$\frac{\partial(\varepsilon\rho E)}{\partial t}+\nabla\cdot[(\rho E+p)\boldsymbol{V}]=\nabla\cdot\left[k\nabla T-\sum_i h_i\boldsymbol{J_i}+(\bar{\bar{\boldsymbol{\tau}}}\cdot\boldsymbol{V})\right]+S_h \tag{3.15}$$

where E is the specific total energy in Jkg^{-1}, k is thermal conductivity in $Wm^{-1}K^{-1}$.The three terms in squared brackets on the right hand side represent energy fluxes due to heat conduction, Dufour effect due to species diffusion (in contrast to Soret effect, last term in Equation (3.4**)**), and viscous dissipation.

The source term, S_h represents the addition of heat into the system due to various reversible/irreversible mechanisms. In this model, the heat source comprises of, from left to right, heat released from the electrochemical reaction, irreversible activation heat at catalyst layers, ohmic heating, and latent heat from equilibrium phase change of water. It should be noted that these heats have the same units of $Jm^{-3}s^{-1}$. In anode catalyst layer, the heat source term takes the form;

$$S_h=h_{react}+|R_{an}\eta_{an}|+(\boldsymbol{J_s^2}\rho_s+\boldsymbol{J_m^2}\rho_m)+h_{latent} \tag{3.16}$$

Heat of electrochemical reaction in the anode catalyst layer is denoted by the first term on the right hand side of Equation (3.16**)**. It should be noted that majority of numerical models ignore this term due to a much larger reference exchange current density for the anode. However when the reference exchange current densities at the two electrodes are close, it cannot be ignored and therefore is retained in the equation. According to Equation (1.10**)**, the hydrogen oxidation reaction (HOR) absorbs heat. Therefore this term has a negative value indicating a heat sink. The second term represents heat generated due to activation overpotential which is the product of transfer current, R_{an} and overpotential, η_{an}. The third term in brackets, ohmic heating, is the product of a square of charge flux and resistivity. It is the combination of fluxes of charge through electronically and protonically conductive matrices in the porous catalyst layer and is denoted by $\boldsymbol{J_s^2}\rho_s$ and $\boldsymbol{J_m^2}\rho_m$, respectively, where resistivity has the units of ohm-metre (Ωm).

The source term in the cathode catalyst layer is formulated in a similar manner. The heat of reaction now takes a positive value since the oxygen reduction reaction (ORR) in Equation (1.11**)** is exothermic.

$$S_h = h_{react} + |R_{ca}\eta_{ca}| + (\boldsymbol{J_s^2}\rho_s + \boldsymbol{J_m^2}\rho_m) + h_{latent} \tag{3.17}$$

The heat sources in other regions are summarised in Table **3.2**;

Region	$S_h\ (Jm^{-3}s^{-1})$
$\mathrm{Channel_{an}}$	h_{latent}
$\mathrm{GDL_{an}}$	$\boldsymbol{J_s^2}\rho_s + h_{latent}$
PEM	$\boldsymbol{J_m^2}\rho_m$
$\mathrm{GDL_{ca}}$	$\boldsymbol{J_s^2}\rho_s + h_{latent}$
$\mathrm{Channel_{ca}}$	h_{latent}

Table 3.2 Heat sources in different sub-regions.

3.1.7 Conservation of Charge

Under electroneutrality, the continuity of charge states that;

$$\nabla \cdot \boldsymbol{J} = 0 \tag{3.18}$$

where $\boldsymbol{J}$ is the charge flux in $Cm^{-2}s^{-1}$. In PEM fuel cell analysis, it is often referred as a current density, i (Am^{-2}). When this occurs in a porous medium, two simultaneous components of charge fluxes result. One component represents a flux of charge through the electronically conductive solid region, denoted by $\boldsymbol{J_s}$. The other component represents a flux of charge through the protonically conductive electrolyte region, denoted by $\boldsymbol{J_m}$.

They have to satisfy

$$\nabla \cdot \boldsymbol{J_s} + \nabla \cdot \boldsymbol{J_m} = 0 \tag{3.19}$$

This can best be demonstrated by Figure 3.1 which is reproduced from the work of [146].

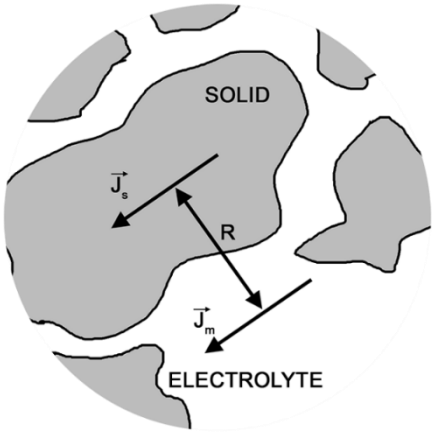

Figure 3.1 Diagram showing components of charge flux in porous medium.

The charge carrier in the solid phase is an electron while the charge carrier in the membrane phase is a proton. The driving force for electrochemical reaction is known as overpotential, η, which is the difference between an electric potential of a solid phase, ϕ_s (V), and membrane phase, ϕ_m (V), according to;

$$\eta_{an} = \phi_s - \phi_m \tag{3.20}$$

$$\eta_{ca} = \phi_s - \phi_m - V_{oc} \tag{3.21}$$

where V_{oc} is the open-circuit voltage of a cell.

It is assumed that there exists an electric potential field for each of the phase in the electrode [146]. By applying Ohm's law, the governing equation for electron transport can be written as;

$$\nabla \cdot \boldsymbol{J_s} = \nabla \cdot (\sigma_s \nabla \phi_s) = S_{\phi,s} \tag{3.22}$$

where σ_s is electronic conductivity in Sm^{-1}. Electrons are generated in the anode catalyst layer, the source term, $S_{\phi,s}$ becomes;

$$S_{\phi,s} = R_{an} \tag{3.23}$$

In the cathode catalyst layer, electrons are consumed in the ORR, hence;

$$S_{\phi,s} = -R_{ca} \tag{3.24}$$

In other regions, there is no consumption or generation of electron and therefore a zero source term is applied.

Similarly, the governing equation for proton transport is;

$$\nabla \cdot \boldsymbol{J_m} = \nabla \cdot (\sigma_m \nabla \phi_m) = -S_{\phi,m} \tag{3.25}$$

where σ_m is protonic conductivity of membrane in Sm^{-1}. Protons are generated in the anode catalyst layer, the source term, $S_{\phi,m}$ becomes;

$$S_{\phi,m} = R_{an} \tag{3.26}$$

In the cathode catalyst layer, protons are consumed in the ORR, hence;

$$S_{\phi,m} = -R_{ca} \tag{3.27}$$

A zero source term is applied in other regions where there is no electrochemical reaction.

The source terms, R_{an} and R_{ca} are known as transfer currents. They are calculated from the famous Butler-Volmer equation for electrochemical kinetics which are;

$$R_{an} = a j_{an,0}^{ref} \left(\frac{C_{H_2}}{C_{H_2,0}^{ref}} \right)^{\gamma_{an}} \left(e^{\frac{\alpha_{an} F \eta_{an}}{RT}} - e^{\frac{-\alpha_{ca} F \eta_{an}}{RT}} \right) \tag{3.28}$$

$$R_{ca} = a j_{ca,0}^{ref} \left(\frac{C_{O_2}}{C_{O_2,0}^{ref}} \right)^{\gamma_{ca}} \left(-e^{\frac{\alpha_{an} F \eta_{ca}}{RT}} + e^{\frac{-\alpha_{ca} F \eta_{ca}}{RT}} \right) \tag{3.29}$$

where a = specific active surface area of catalyst layer (m^{-1})

j_0^{ref} = reference exchange current density (Am^{-2})

$C_{i,0}^{ref}$ = reference concentration of i-th species ($kmolm^{-3}$)

$\gamma_{an,ca}$ = exponent of concentration

$\alpha_{an,ca}$ = transfer coefficients for anodic and cathodic reaction, respectively

F = Faraday constant, 96 487 $Cmol^{-1}$

3.1.8 Transport in Membrane

The most important property of a membrane is its membrane water content, λ, which is defined as the number water molecules per sulphonic acid group in the membrane;

$$\lambda = \frac{water\ molecules}{SO_3H} \tag{3.30}$$

Springer and his colleagues [95] suggested the use of an empirical correlation [98] between water content of Nafion family membranes and water activity as;

$$\lambda = \begin{cases} 0.043 + 17.18a - 39.85a^2 + 36a^3 & (0 < a \leq 1) \\ 14 + 1.4(a-1) & (1 \leq a \leq 3) \end{cases} \tag{3.31}$$

where a, the activity of water vapour is defined as;

$$a = \frac{p_{wv}}{p_{sat}} + 2s \tag{3.32}$$

It is known that the membrane has to be sufficiently hydrated in order for the transport of proton to take place. The membrane-phase conductivity is strongly dependent on the membrane water content according to;

$$\sigma_m = e^{1268\left(\frac{1}{303}-\frac{1}{T}\right)}(0.514\lambda - 0.326) \tag{3.33}$$

Under the presence of an electric field, protons move across the membrane from anode to cathode. When travel, each proton will also drag water molecules to the cathode which is known as electro-osmosis. The electro-osmosis drag coefficient is defined as;

$$n_d = \lambda \frac{2.5}{22} \tag{3.34}$$

The flux of water vapour due to electro-osmosis is therefore;

$$\boldsymbol{J_{osm}} = \frac{n_d}{F}\boldsymbol{J_m} M_{H_2O} \tag{3.35}$$

The negative sign indicates that this flux only travels from anode to cathode which introduces a consumption of water vapour in the anode catalyst layer.

Depending on the concentration gradient of water vapour across the membrane, back diffusion can occur in either direction. The water diffusion flux is calculated from;

$$\boldsymbol{J_{diff}} = -\frac{\rho_m}{M_m} M_{H_2O} D_{liq} \nabla\lambda \tag{3.36}$$

where the density and molar mass of a dry polymer electrolyte membrane are denoted by ρ_m and M_m, respectively. The diffusion coefficient of liquid water in the membrane, D_{liq}, is also a function of membrane water content given as;

$$D_{liq} = \lambda e^{2416\left(\frac{1}{303}-\frac{1}{T}\right)} \tag{3.37}$$

3.2 Comments on Computational Domains

Two types of computational domains are used in this thesis; the single-channel and full-cell type domains. The significance and detailed dimensions of each domain together with the corresponding simulation results are discussed separately in Chapter 5 and Chapter 6, respectively. However, the common features of the two are discussed here.

The thesis can be classified as a cell-level analysis in which a unitary cell is the domain of interest. In comparison to cell stack-level, electric powertrain-level, or electric hybrid vehicle analysis, a single cell domain can give an insight into the simultaneous effect of flow-field geometries and operating conditions on the cell performance at a local level.

A discussion with ANSYS support engineers suggests that current collector can be safely neglected if cell cooling was not the main objective. In this regard, they only introduce

additional electrical resistance to the flow of current. Additionally, most current collectors are made from highly conductive materials such as aluminium or graphite so that the current lost is expected to be insignificant. It should be noted that most numerical studies, except the ones which addressed cell cooling, also discarded these current collectors.

The meshing strategy is discussed in details in the next chapter but if we follow the strategy given in Chapter 4, mesh elements in current collectors must be hexahedral and at least as small as the ones in flow channels if conformal mesh and zero skewness are to be maintained. Figure **3.2** demonstrates three possible approaches on how to deal with this.

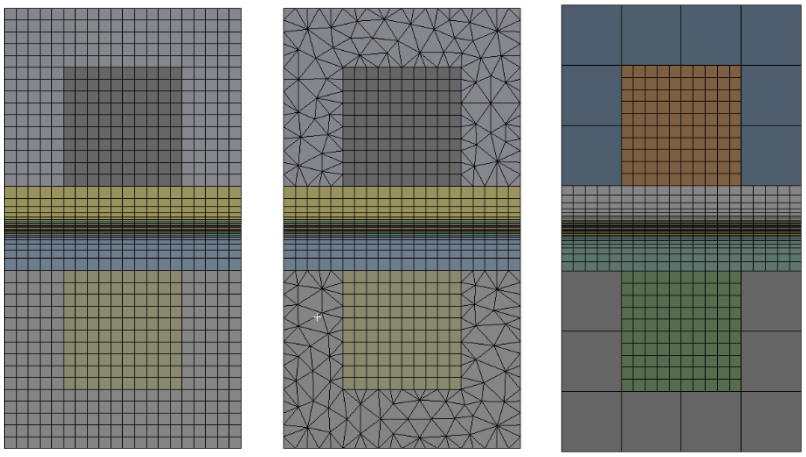

Figure 3.2 Three approaches on meshing the current collectors.

The left mesh was obtained through a conformal mesh approach with zero element skewness. As a result, the total number of elements is increased by approximately 50% compared to the original value when current collectors were excluded. The mesh in these regions is unnecessarily dense since only temperature and current density fields are present and they are expected to have negligible variation. The middle mesh employed tetrahedral elements in the current collectors. Though being conformal, the resulting mesh has more number of elements than the left one with high skewness in a large number of elements. In the right mesh, the meshes on the two sides of an interface between flow channel walls and current collectors are separated. They were treated as two separate topologies and hence meshed independently. The nominal element size in current collector is 0.50 mm which is sufficient to resolve the temperature field. Even though cell skewness was kept at zero but this is the non-conformal mesh which should be avoided unless necessary.

From the above discussion, both anode and cathode current collectors were therefore excluded from all analyses in order to reduce the total number of elements in the mesh keeping simulation time and results to a manageable level.

3.3 Boundary Conditions and Initial Conditions

Whether it is the flow in the River Thames in London, Chao Phra Ya River in Bangkok, flow in water park slides, or open-channel flow in irrigation ducts, they all are governed by the same set of equations. Clearly, they are different problems with completely different flow-fields. What distinguish each of them from the others are the boundary conditions.

One of the advantages of utilising a unified-domain approach is that it allows the boundary conditions to be applied only on the external boundaries. Internal boundaries between sub-domains are treated with an interface-type boundary condition which greatly reduces the amount of work required in the pre-processing stage. The application of boundary conditions and its corresponding location are demonstrated in Figure 3.3.

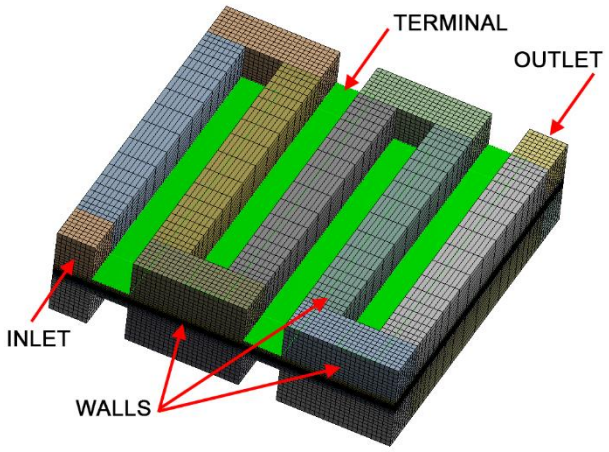

Figure 3.3 Application of boundary layers on computational domain.

At the two inlets, a velocity boundary condition is used. Species flow rates are input into the domain via flow velocity, species mole fractions, and temperature. In case of humidified reactant gases, this temperature corresponds to the humidification temperature.

$$inlet_{an} = \begin{cases} v_{in,an} \\ x_{H_2}, x_{H_2O} \\ T_{in} \\ s_{in} = 0 \end{cases} \tag{3.38}$$

$$inlet_{ca} = \begin{cases} v_{in,ca} \\ x_{O_2}, x_{H_2O} \\ T_{in} \\ s_{in} = 0 \end{cases} \tag{3.39}$$

Because the cell is operated under a pressurised condition therefore the pressure at the outlets is known a priori. A pressure outlet boundary condition is thus used. In addition, a reversed flow at the outlet is likely to occur under a high fuel utilisation operation which poses difficulty to convergence. This pressure outlet B.C. gives a faster convergence rate than

outflow B.C. should a reversed flow occurs. Since the flow is assumed fully developed at the outlet, the gradient of any flow variable across the outlet is also zero.

$$outlet_{an,ca} = \begin{cases} p\ (gauge) \\ \dfrac{d\phi}{d\vec{n}} = 0 \\ x_i\ (reversed\ flow) \\ T_{in}\ (reversed\ flow) \\ s_{in}\ (reversed\ flow) \end{cases} \tag{3.40}$$

It is assumed that cooling of the cell is very efficient that temperature variation throughout the cell is small, especially on the external surfaces. A fixed temperature was used on all external boundaries and is equal to the cell operating temperature.

$$T_{wall}, T_{terminal} = T_{cell} \tag{3.41}$$

Since current collectors are discarded, the exposed current collector/GDL interface is hence treated as a terminal surface where a potentiostatic (fixed voltage) B.C. is applied. As a reference electrode, a zero solid-phase potential is specified at the anode terminal whereas the operating voltage is used at the cathode terminal;

$$\phi_{s,terminal} = \begin{cases} \phi_{s,an-term} = 0 \\ \phi_{s,ca-term} = V_{cell} \end{cases} \tag{3.42}$$

Similar to boundary conditions, an initial condition is required to start the transient simulations. Depending on the starting point, the corresponding steady-state solution is used.

3.4 Model Input Parameters

PEM fuel cell modelling involves many parameters which can be grouped into electrochemical properties, physical and thermal properties, and operating conditions. The first two groups are given in Table 3.3-3.4, respectively.

Parameter	Value
Anode reference exchange current density, $j_{an,0}^{ref}$ (Am^{-2})	10
Cathode reference exchange current density, $j_{ca,0}^{ref}$ (Am^{-2})	2.90×10^{-2}
Hydrogen reference concentration, $C_{H_2,0}^{ref}$ ($kmolm^{-3}$) [96]	5.64×10^{-2}
Oxygen reference concentration, $C_{O_2,0}^{ref}$ ($kmolm^{-3}$) [96]	3.39×10^{-3}
Exponential of hydrogen concentration, γ_{an} [144]	0.50
Exponential of oxygen concentration, γ_{ca} [144]	1
Transfer coefficient for anodic reaction, α_{an} [144]	0.50
Transfer coefficient for cathodic reaction, α_{ca} [144]	0.50

Table 3.3 Electrochemical properties.

Parameter	Value
GDL density, ρ_{GDL} (kgm^{-3}) [147]	440
GDL porosity, ε_{GDL} [147]	0.78
GDL electric conductivity, $\sigma_{s,GDL}$ (Sm^{-1}) [147]	1250
GDL thermal conductivity, k_{GDL} (Wm^{-1}K^{-1}) [147]	23
CL density, ρ_{CL} (kgm^{-3})	440*
CL porosity, ε_{CL}	0.30*
CL electric conductivity, $\sigma_{s,CL}$ (Sm^{-1})	1250*
CL thermal conductivity, k_{CL} (Wm^{-1}K^{-1}) [148]	0.8725
Dry membrane density, ρ_m (kgm^{-3}) [144]	1980
Molar mass of dry membrane, M_m (kgkmol^{-1}) [144]	1100
Membrane thermal conductivity, k_m (Wm^{-1}K^{-1}) [148]	0.445*
Porous media specific active surface, a (m^{-1}) [144]	2×10^{7}
Permeability of porous media, k (m^2) [149]	1.12×10^{-14}
Contact angle, θ_c (°) [144]	110°

Table 3.4 Physical and thermal properties (*typical value).

Two computational domains are used in this thesis with an entire chapter being dedicated to each of them. The operating conditions are different depending on the objectives of each analysis and therefore not tabulated together.

A saturation pressure of water vapour (atm) is calculated as [95];

$$\log_{10} P_{sat} = -2.1794 + 0.02953(T - 273.15) - 9.1837 \times 10^{-5}(T - 273.15)^2 + 1.4454 \times 10^{-7}(T - 273.15)^3 \quad (3.43)$$

If a reactant gas is fully humidified then the partial pressure of water vapour in the gas mixture is equal to the saturation pressure. The mole fraction of water vapour in anode gas mixture is;

$$x_{H_2O,an} = \frac{100\% \times P_{sat}}{P_{an}} \quad (3.44)$$

where P_{an} is the total pressure of anode gas in Pascal (Pa). It should be noted that the saturation pressure in this expression also has a unit of Pa.

The mole fraction of hydrogen is found from the relation;

$$\sum x_{an,i} = x_{H_2} + x_{H_2O,an} = 1 \quad (3.45)$$

On the cathode side, mole fraction of oxygen is calculated from;

$$x_{O_2} = \left(1 - x_{H_2O,ca}\right)\frac{21}{100} \quad (3.46)$$

Knowing partial pressures of hydrogen and oxygen gases in atm, the open-circuit voltage is calculated as [18];

$$V_{oc} = 1.229 - 0.83 \times 10^{-3}(T - 298.15) + 4.3085 \times 10^{-5} T \ln\left(p_{H_2} p_{O_2}^{0.5}\right) \tag{3.47}$$

Finally, inlet velocity for anode and cathode gases are calculated as [18];

$$u_{an} = \xi_{an} \frac{i_{ref}}{2F} \frac{A_{mea}}{A_{ch}} \frac{RT_{an}}{x_{H_2} p_{an}} \tag{3.48}$$

$$u_{ca} = \xi_{ca} \frac{i_{ref}}{4F} \frac{A_{mea}}{A_{ch}} \frac{RT_{ca}}{x_{O_2} p_{ca}} \tag{3.49}$$

where ξ = stoichiometric ratio

i_{ref} = reference current density, 1 Acm^{-2}

A_{mea} = cell active area (m^2)

A_{ch} = cross sectional area of flow channel (m^2)

R = universal gas constant, 8.314 $Jmol^{-1}K^{-1}$

T = inlet gas temperature (K)

p = inlet gas pressure (Pa)

x_i = mole fraction of reactant species

3.5 Chapter Summary

In this chapter, the conservation principles of physical quantities in which all governing equations are built upon are described together with auxiliary relations which are used to close the system of equations. The common features of the two computational domains are discussed with reasons on the exclusion of current collectors. Finally, electrochemical, physical, and thermal parameters necessary to run the models are presented.

Chapter 4
Numerical Method

"In theory, there is no difference between theory and practice. But, in practice, there is."
Jan L. A. van de Snepscheut

A numerical study does not end just after the geometry is created, model parameters are input, and clicking the "solve" button and wait for the solutions to come out. Oftentimes, in many engineering problems involving complex geometries and extreme operating conditions, the calculation will, unfortunately, stop at some point even the solving algorithm and its corresponding parameters are chosen carefully. This is known as divergence. Therefore considerable amount of effort are required, still, to regulate the simulation and ensure that the calculation proceeds towards a convergent solution.

This chapter addresses the numerical aspects of the model developed in Chapter 3 covering the following three aspects;

1) Solver and its settings including the spatial and temporal discretisation schemes, pressure-velocity coupling scheme, and convergence criteria.
2) Grid-independence and time-step-size-independence studies.
3) Steady-state and transient model validations with experimental data.

4.1 Solver and Its Settings

Each solving algorithm and its settings have a different characteristics that are suitable for certain problems – one solver that is successfully applied to one problem does not guarantee a success should it be applied to another problem. Hence it is a priority, when choosing the solver, to have an insight to the flow problem and characteristics of each solving algorithm so that the simulation will be treated numerically appropriately.

All PEM fuel cell flow problems are practically laminar and therefore all numerical studies, to the best of the author's knowledge, treat them as laminar flow. Unlike in super- or hypersonic flows where the presence of turbulence, shocks, and high density variation are typical, the density variation in a PEM fuel cell is negligible and the flow can safely be treated as an incompressible flow. This is beneficial as it greatly simplifies the calculation.

4.1.1 Segregated versus Coupled Solver

The segregated solver, which is a default solver in ANSYS FLUENT, is favoured over its counterpart, the coupled solver, for incompressible calculation and has been used in all studies in this thesis. Despite the fact that the coupled solver gives more accurate solutions, it requires more memory and computation time. In addition, this solver is less stable which means it is more difficult for the solutions to converge.

Unlike the coupled solver where pressure and velocity fields are solved simultaneously, the segregated solver, as the name implies, decouples each governing equation from the rest and solve them one after another in a sequential manner which results in a faster calculation time and better convergence rate. Starting with a guessed flow-field, the continuity equation in a form of a pressure-correction equation is solved and then the three momentum equations are updated accordingly. The species, temperature, and other scalar equations that are dependent on the velocity fields are solved consequently. The procedure repeats until the solutions are fully converged. The convergence criteria are described in the next section.

4.1.2 Discretisation Schemes

An effective discretisation scheme will keep the residuals to a minimum throughout the domain and aid in convergence. The 2nd-order Upwind Scheme was used for momentum, species, temperature, and other scalar equations to ensure both accuracy and stability.

As recommended by ANSYS, the 1st-order Implicit was selected for a temporal discretisation scheme since it gives good results in most problems. Using the implicit scheme means that it uses both nodes from the previous and current time steps in the calculation. Unlike the explicit scheme, the maximum time-step size is not limited by the spatial mesh. As a consequence, the spatial mesh and temporal resolution can be refined or coarsened independently and this gives great flexibility in the pre-processing stage.

4.1.3 Pressure-velocity Coupling

Having treated the flow as an incompressible flow also poses a problem in the numerical perspective. In an incompressible flow, the density is constant. This implies that the density terms in the continuity equation, Equation (3.1), can slip off from the divergence operators and the equation reduces to;

$$\frac{\partial u}{\partial x}+\frac{\partial v}{\partial y}+\frac{\partial w}{\partial z}=0 \tag{4.1}$$

Clearly, Equation (4.1) can no longer be used as a transport equation to solve for the density filed. Therefore the pressure is said to be "disconnected" from density and cannot be calculated using the state relation; $p=p(\rho,T)$. In order to solve these system of equations, a special algorithm must be applied. By looking at the coupling between pressure and velocity in the three momentum equations, one can deduce an extra condition that must be met; if a correct pressure field is applied in the momentum equations, then the resulting velocity field should satisfy the continuity equation [150].

The most commonly used pressure-velocity coupling scheme SIMPLE was proposed by Patankar and Spalding in 1972 [151] and such the algorithm can best be described by the diagram given in Figure 4.1. It should be noted that the diagram describes the solving algorithm of two-dimensional problems. However, the algorithm can be easily extended to deal with three-dimensional problems.

The algorithm starts with initially guessed fields of all variables as indicated by an asterisk. These field variables are then input to momentum equations to calculate an updated velocity field. In the second step, the pressure correction equation, which is the modified form of the continuity equation, uses the updated velocity field to obtain the pressure

corrector. The pressure and velocity fields are then corrected by the pressure corrector, $\acute{p}$ in the third step. In the last step, the corrected pressure and velocity fields are used to solve for other transport equations. The convergence is checked after that and if it is not met, the calculated fields are then re-used as initial fields in the first step. The procedure repeats until convergence is achieved. Though its variants such as SIMPLEC or SIMPLER schemes are claimed to have a better convergence rate in some problems, SIMPLE has proved to be economical in terms of solution time and convergence rate for steady-state PEM fuel cell simulations and it was used in all steady-state runs in the author's publications [152], [153] and in this thesis.

The PISO algorithm is recommended for all transient simulations by ANSYS. From the SIMPLE algorithm viewpoint, it performs an additional pressure correction step to speed up the convergence. As a result, PISO is known to take longer time per iteration compared to SIMPLE-transient or SIMPLEC-transient. However, PISO is preferred if a large time-step size is to be used and the scheme is stable even the under-relaxation factors of momentum and pressure equations are close to unity, though in this thesis the URF's of 0.9 and 0.7, respectively are used. This accelerates convergence considerably and hence the overall computation time is reduced. Both PISO and SIMPLEC-transient were used for transient simulations in this thesis depending on which one gives a better convergence rate – PISO was the default scheme unless specified otherwise.

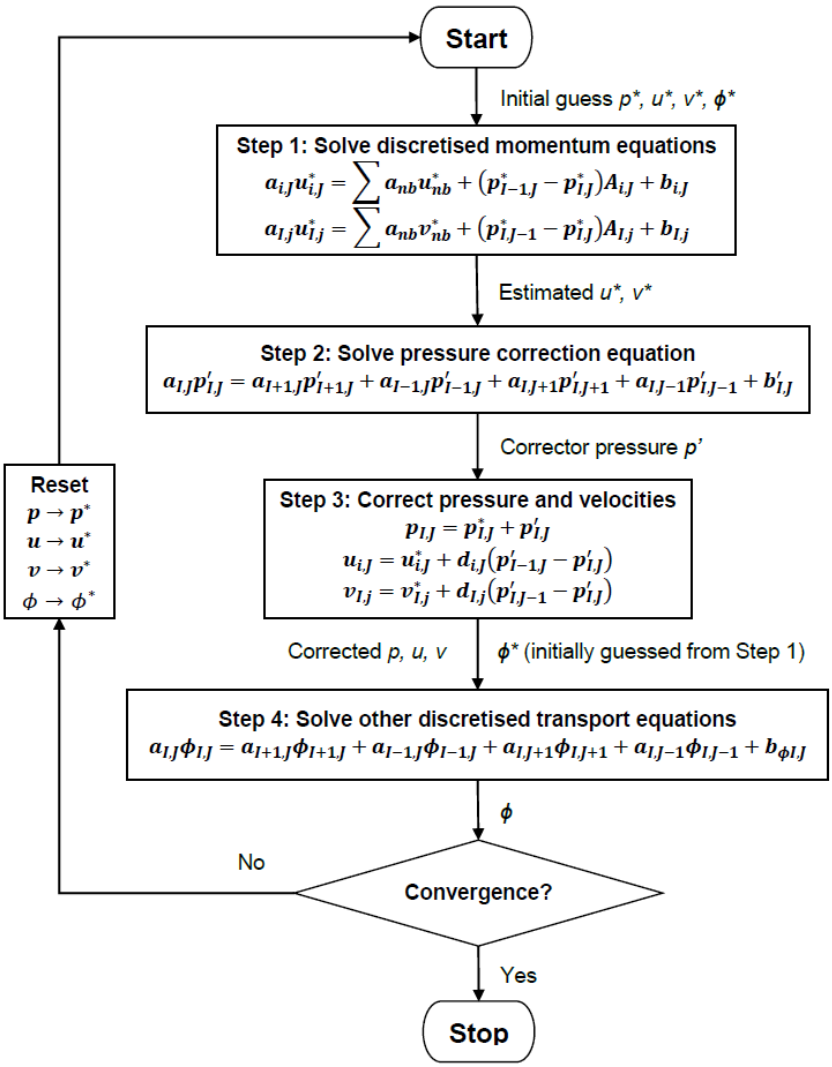

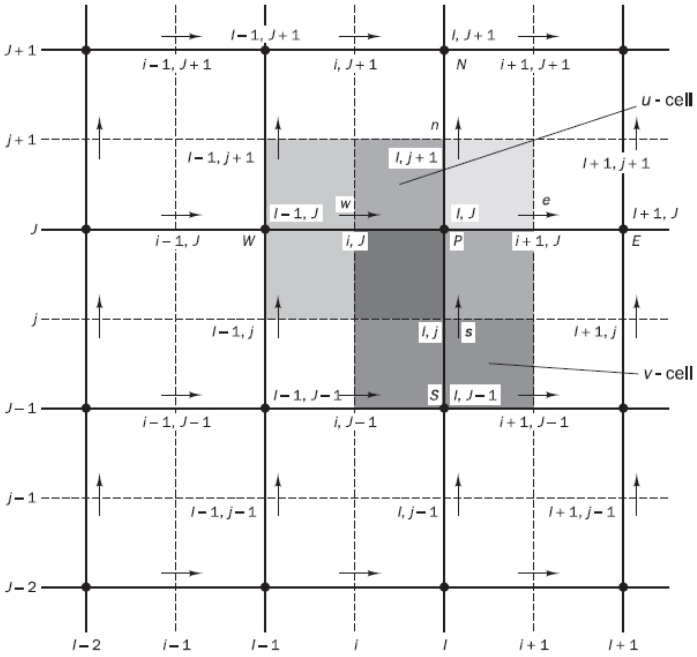

Figure 4.1 SIMPLE Algorithm (top) as reproduced from [150], the computational cells for velocity fields and other scalar variables are also shown (bottom).

4.1.4 Convergence Criteria

CFD solutions are usually solved by an iterative approach. As a comparison to the direct method, for example, if Gaussian elimination is used to solve a system of n equations with n unknowns, it involves at least n^3 calculation steps and a large memory is required to store n^2 coefficients. The iterative method, on the other hand, requires much less memory, especially when the number of elements of 10^6-10^7 in PEM fuel cell CFD modelling is typical, and it has proved to be an effective method to solve CFCD problems.

In the calculation procedure, the solution changes from one iteration to another approaching the final, in theory, exact solution thus the difference between two consecutive iterations should decrease as the iteration proceeds. At the point where the difference reduces to zero, the solution no longer changes with iteration and it is said to converge.

In some cases, instead of having an absolute zero value, the difference never reach zero regardless of the number of iterations but rather a negligibly small value. Then the solution appears to freeze or fluctuate around a certain value with very small amplitude and it can be considered as being converged. It is the operator's responsibility to exercise his/her own engineering judgment on whether the iteration should continue. This section describes essential criteria for judging convergence that were used in this thesis.

Residuals

After the transport equation has been discretised, an algebraic expression of the conserved quantity, ϕ, in an elementary cell P can be represented as [154];

$$a_P \phi_P = \sum_{nb} a_{nb} \phi_{nb} + b \tag{4.2}$$

where a_p is the coefficient for Cell P and a_{nb}'s are coefficients for cells surrounding Cell P. The constant b comes from the constant part of the linearised source term, S_c ($S = S_c + S_{P\phi}$) and the contribution from boundary conditions that emerge as a source term during the formulation.

The residual of a conserved quantity (ϕ), R^{ϕ}, is defined by FLUENT as the imbalance in Equation (4.2) summed over all the cells according to, for pressure-based solver;

$$R^{\phi} = \sum_{cells\ P} \left| \sum_{nb} a_{nb} \phi_{nb} + b - a_P \phi_P \right| \tag{4.3}$$

The above R^{ϕ} is regarded as the unscaled or absolute residual. However, this is impractical to be used in judging convergence and hence some scaling factors are applied. The resulting

residual is known as the scaled residual and can be used to compare the convergence between different problems, for example, a PEM fuel cell operated under different reactant flow rates. For more details regarding the scaling method, the reader should refer to [154].

The residual of each conserved quantity is reported after each iteration showing how convergence evolves through the calculation process. Theoretically, residuals should decrease to zero if the solution has converged. In practice, they decay to a small value and eventually level out. As a rule of thumb, a drop by three orders of magnitude is a good indicator that convergence might be reached but this is not always the case, however. A typical residuals plot for steady-state PEM fuel cell runs is shown in Figure 4.2.

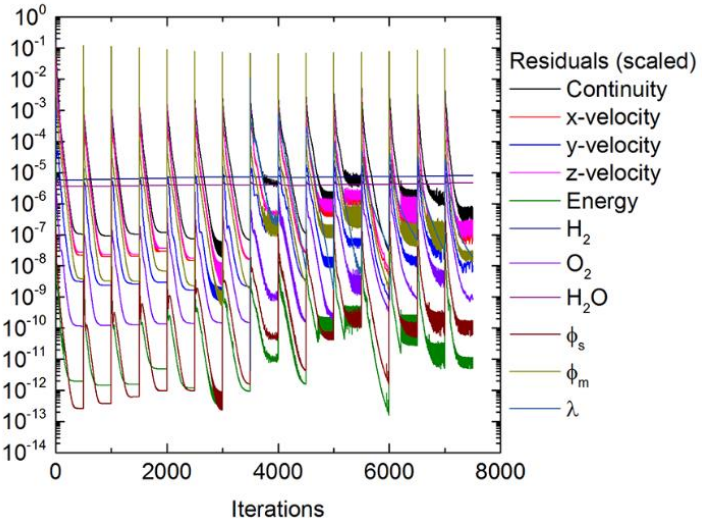

Figure 4.2 Typical residuals plot in PEMFC steady-state modelling.

Sudden jumps in residuals can be seen in the plot. These occurred each time a new boundary condition was applied to the model, in this case the cell potential at the cathode electrode was varied potentiostatically from 0.90 V down to 0.20 V with a 0.05 V increment.

Observations through many steady-state runs suggest that the rate of decrease of residuals not only depend on Under Relaxation Factors (URFs), but also the operating current, operating conditions, and cell geometry. At a high current operation, where all other conditions are kept the same, residuals decrease more slowly with a smaller negative gradient and they level out at a higher value and vice versa. This also applies to a larger cell with multi-channel, complex flow-field configuration, or a cell with very large inlet flow rates.

Therefore the threshold value of 10^{-6} is set for all residuals under normal conditions. Under extreme conditions where the value 10^{-6} is difficult to achieve, the threshold was relaxed and the higher threshold value was used in conjunction with other criteria.

Point, Surface, and Volume Monitors

FLUENT provides a tool for monitoring the evolution of variables of interest as the calculation proceeds. When the cell has reached an equilibrium, the flow-field and all variables should be near constant or at least show a cyclic behaviour having fluctuated around a certain value. These can be used as an indicator of convergence.

As an example, the time-histories of velocity at a random point in the flow channel, area-weighted averaged membrane hydration, λ on the interface between membrane and anode CL, and transfer current in the cathode CL are shown in Figure 4.3. It is seen from the figure that all variables evolve through iterations. Some variables may reach its constant value before the other. After certain iterations, however, all variables level out indicating that an equilibrium has been reached. The solution is then said to be fully converged.

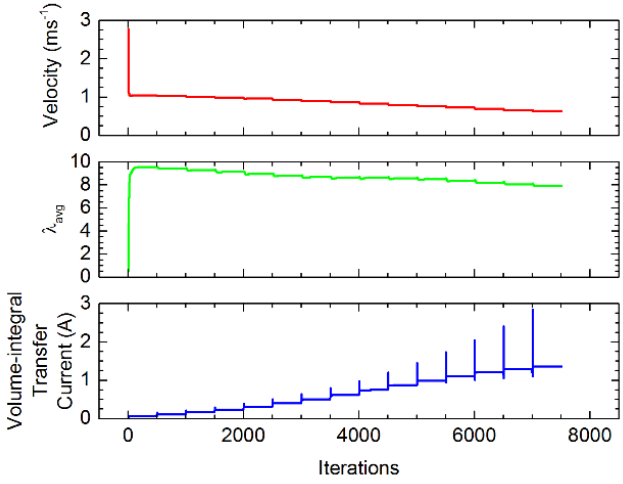

Figure 4.3 Examples of point monitor, surface monitor, and volume monitor.

For all simulations presented in this thesis, important variables such as velocity, pressure, species mass fraction, water saturation, and current density in appropriate regions were monitored as additional criteria.

Conservation of Charge

One of the most important variables in PEM fuel cell analysis is the averaged current density, i, which is, by convention, reported in amperes per unit active area of the cell (Acm^{-2}). FLUENT reports the averaged current densities from both sides of the membrane at the end of each iteration together with the difference between the two, di_{mea}, according to;

$$di_{mea} = i_{anode} - i_{cathode} \tag{4.4}$$

The conservation of charge states that an electric charge can neither be created nor destroyed therefore the total amount of charge must be conserved. On the other hand, it is true to state that the magnitude of electric current density at the PEM/CL_{an} interface due to the flux of electron leaving the anode active site must be equal to the current density at PEM/CL_{ca} interface due to the flux of electron entering the cathode active site or;

$$i_{anode} = i_{cathode} \tag{4.5}$$

This requires that di_{mea} must be zero if the conservation of charge is to be satisfied.

Similar to residuals, it is difficult for di_{mea} to reduce to zero under certain circumstances even after considerable iterations have been performed. It is not economical to continue the simulation and a non-zero di_{mea}, under certain circumstances, can be considered sufficient. Wu et al. [155] suggested the difference within ±1% to be acceptable. However, if the operating current is in the order of 1 Acm^{-2}, this means that the value of ±0.010000 Acm^{-2} for di_{mea} is considered acceptable. Clearly, the cell's current density at this stage is far from a converged value and this constant 1% threshold would result in a highly distorted solution especially at high current operations. A constant threshold value of ±0.000010 Acm^{-2} for maximum di_{mea} was therefore used in all simulations in this thesis regardless of magnitude of the nominal current density.

Conservation of Reacting Species

If no nuclear reaction is involved, mass can neither be created or destroyed. Therefore mass is conserved in PEM fuel cell modelling. This implies that the imbalance of oxygen influx and efflux is attributable to the oxygen reduction reaction (ORR) according to;

$$\dot{m}_{O_2,in} = \dot{m}_{O_2,consumed} + \dot{m}_{O_2,out} \tag{4.6}$$

FLUENT can report an imbalance of oxygen inflow and outflow rates which is corresponding to an oxygen consumption rate. Using Equation (4.7) [156], the current generated can be calculated as;

$$I_1 = \frac{\dot{m}_{O_2,net} zF}{M_{O_2}} \tag{4.7}$$

where z = 4 since 4 kmol of electron is consumed when 1 kmol of oxygen is reduced. Molar mass of oxygen gas, $M_{O_2} = 31.9988$ kg kmol^{-1}.

The current density reported after each iteration, however, is calculated by averaging the local current over the entire active area. Reversing its definition, the total current generated can be calculated as, where A is the cell's active area;

$$I_2 = iA \tag{4.8}$$

Equations (4.7) and (4.8) suggest that in order to ensure that mass conservation is maintained, the two currents, I_1 and I_2 must be equal or very close.

Convergence in Transient Simulations

In a transient run, it is essential that convergence must be obtained at each time step. This is to ensure that the solution of one time step is used as a correct initial boundary condition of the next time step. Experiences suggest that it is more economical to use a small time-step size so that convergence is achieved within small number of inner iterations rather than using a large time-step size with many inner iterations in each time step. The determination of an appropriate time-step size is discussed in Section 4.2.2. For all transient runs, the time-step size was chosen so that the solution converged within 20-30 iterations.

In conclusion, it should be emphasised that residuals are usually misunderstood as an indicator of a converged solution and therefore it should not be used solely as a judging criterion for convergence. The criteria explained above should be used in combination with one another in order to obtain a fully converged solution, reducing numerical errors that can be introduced to the analysis as much as possible. Finally, the threshold value of each criterion can be relaxed depending on the problem geometry and operating condition. Therefore the knowledge of the physics inside the cell and its behaviour is very crucial in choosing these criteria and the corresponding thresholds.

4.2 Mesh-independent Solution and Time-step Size-independent Solution

4.2.1 Mesh Generation Strategy

In numerical studies, often, considerable amount of time is spent on pre-processing the problem which involves model creation, mesh generation, and applying boundary conditions and this could take up to 50% of the total time spent on the project [150]. In a CFD simulation, in particular, the process of dividing the computational domain into smaller, non-overlapping cells or elements is called meshing. This mesh generation step is very essential to the success of the simulation.

Theoretically, smaller cells (hence denser grid) will lead to a more accurate solution and ideally if each cell is infinitesimally small then the exact solution will be achieved. In practice, however, computational resources such as computation time, memory, and storage space are usually not unlimited and not all problems require exact solutions. This is the case

in most engineering problems and therefore a compromise between the appropriate number of cells and acceptable degree of accuracy of the solution must be met.

Conventionally, an initial mesh is selected based on prior experience to similar problems. The mesh will then undergo a series of mesh refinement process until the results change no further even more elements are used. At this stage, the solution is said to be mesh-independent and should be ensured prior to commencing any CFD simulation.

A mesh can be refined in two ways; global refinement and local refinement. Providing that the computational resources are unlimited, which is usually not the case, the global refinement is the easiest method where a single element size is specified and will be applied to the entire domain. As a consequence, this results in a very large number of element and very large file which in turn requires prohibitively long time to compute. By locally refining the mesh, on the other hand, different sizes are applied to the elements depending on their location in the domain. An area where there exists large variation of flow field variables, or more technically high gradient, will have more elements or denser mesh while a mesh can be relaxed in areas where the variation is not as large. Even though the latter method requires more treatment to the mesh but it is thought to be more effective than the former one in a long run as the number of elements can be reduced significantly which prevents unnecessarily large files and computation time.

Ideally, the modelling of an entire cell is favoured over a segmented or single-channel models due to three aspects. Firstly, a fuel cell is said to be highly 3-dimensional in nature. A typical cell will comprise of several flow channels that run over a square active area and this means that a single channel or scaled-down cells normally used in laboratories and early PEMFC numerical studies cannot accurately represent the performance of a commercial-sized cell in spite of a simple, repeatable, and symmetric appearance of its flow channels.

Secondly, the size of an active area of the cell under study varies considerably ranging from 1 cm^2-900 cm^2 while the thickness of porous layers and channel dimensions remain the same in 10-500 μm and 1 mm, respectively, as demonstrated in Figure 4.4 where the nominal size of each cell is different while the dimensions of their porous layers and channel are the same. Obviously, these cells will exhibit different characteristics at local level and unlike a wind-tunnel experiment, there is no such scaling rule that will relate the performance of a scaled-down cell to a practical cell to the best of the author's knowledge.

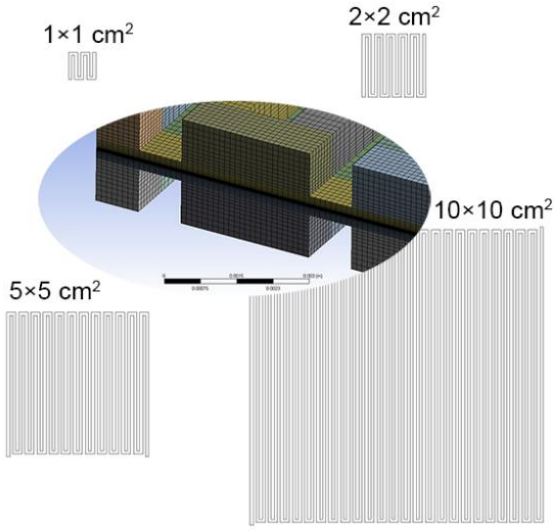

Figure 4.4 Cell active areas in research community vary vastly but channel dimensions are basically the same.

Lastly, most commercial codes with PEMFC modelling capability are developed based on a non-segmented MEA [157] and therefore a model that only accounts for a fraction of the MEA may be subject to some errors. All of the points addressed above suggest that if accurate predictions are to be obtained, an entire cell having the same size as the cell of interest should be used. As a consequence the number of elements present in the mesh will increase drastically signifying the need for a good and effective meshing strategy.

Methodology

Herein, the orientation convention specific to PEMFC modelling in reference to the Cartesian coordinate system will be established and used throughout this thesis.

1) The x-axis is referred to as the lateral or in-plane direction in which cross flows (secondary flow) underneath the rib between adjacent channels take place.
2) The y-axis is referred to as the along-the-channel or axial direction corresponding to direction of the primary flow.
3) The z-axis is referred to as the through-plane direction. The transport in this direction is highly non-uniform and critical to the cell's electrochemistry.

The most commonly used mesh among the research community is selected as a guidance where the mesh in each dimension will then be investigated and refined separately. By analysing the resulting flow-fields and effect of mesh fineness in each direction in a systematic manner, the final meshing strategy will be proposed. It is noteworthy to state the criteria that apply to all of the meshes in this study;

- The flow is viscous-dominated and hence considered laminar. The use of prism mesh elements in near-wall regions is not necessary.
- Low or zero cell skewness wherever possible to avoid divergence.
- Cell aspect ratio is kept below 200 (1 000 is claimed to be acceptable by ANSYS).
- A high jump in cell size of adjacent cells is avoided wherever possible.
- A conformal mesh is used at all interfaces.
- A structured, conformal, and hexahedral mesh is used throughout the domain.

A single 180-degree bend representing a portion of a serpentine flow-field is chosen to keep the simulation time to a minimum as shown in Figure 4.5. Even though the cell should be treated as non-isothermal, the temperature does not vary significantly due to a very small geometry and hence temperature variation can be safely discarded. The cell is operated under a single-phase flow assumption while cell parameters and operating conditions are tabulated in Table 4.2 and Table 4.3, respectively. For clarification purposes, the coordinates for those lines in Figure 4.5 are given in Table 4.1.

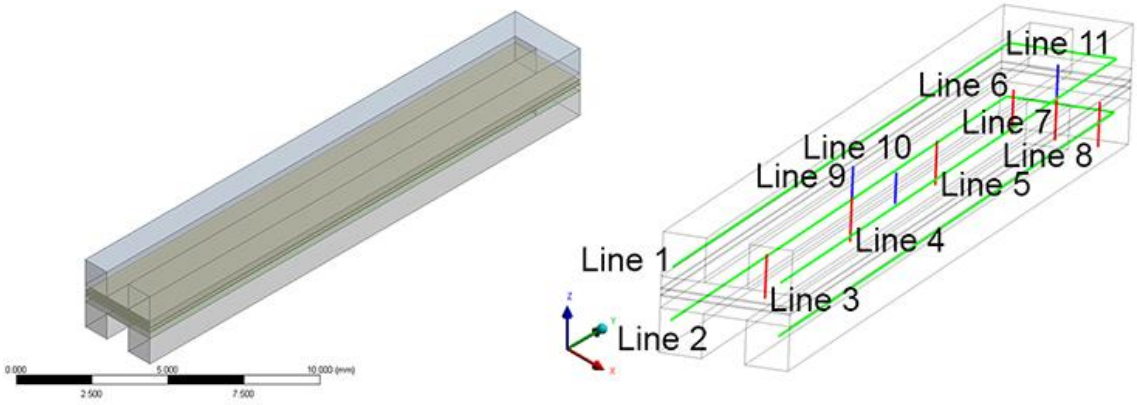

Figure 4.5 A 180-degree U-bend and Lines used in visualisation of the results.

Line Number	Starting Point (mm)	Endpoint (mm)
3	(0.5, 5, 0)	(0.5, 5, 1)
4	(0.5, 10, 0)	(0.5, 10, 1)
5	(0.5, 15, 0)	(0.5, 15, 1)
6	(0.5, 19.5, 0)	(0.5, 19.5, 1)
7	(1.5, 19.5, 0)	(1.5, 19.5, 1)
8	(2.5, 19.5, 0)	(2.5, 19.5, 1)
9	(0.5, 10, 1)	(0.5, 10, 1.703)
10	(1.5, 10, 1)	(1.5, 10, 1.703)
11	(1.5, 19.5, 1)	(1.5, 19.5, 1.703)

Table 4.1 Coordinates of some of the visualisation lines used in the discussion.

Parameter	Value
Channel width (mm)	1
Channel depth (mm)	1
Rib width (mm)	1
Channel length (from inlet to bend, mm)	20
Active area (cm^2)	0.6
GDLs thickness (μm)	260
CLs thickness (μm)	28
PEM (Nafion 115) thickness (μm)	127
GDLs porosity	0.5
CLs porosity	0.82
Specific surface area of CLs (m^{-1})	1.25×10^7

Table 4.2 Cell dimensions and other structural properties.

Parameter	Value
Operating temperature (°C)	80
Operating pressure, absolute (atm)	1
Relative humidity for anode gas (RH%)	100
Relative humidity for cathode gas (RH%)	100
Anode gas stoichiometry	3
Cathode gas stoichiometry	3
Anode inlet velocity (ms^{-1})	0.507
Corresponding Reynolds number for anode gas	17
Cathode inlet velocity (ms^{-1})	1.207
Hydrogen/water vapour mole fractions for anode gas	0.533/0.467
Corresponding Reynolds number for cathode gas	47
Oxygen/water vapour mole fractions for cathode gas	0.112/0.467
Open circuit voltage (V)	1.16

Table 4.3 Operating conditions.

Study 1: Through-plane (z-direction) Mesh

As previously mentioned, mass transport in this direction is very critical in which all early 1D models were built upon. In these models, the flow-field is assumed to vary along this direction from the gas channel wall down to the catalyst layers where electrochemistry takes place whereas the flow variables in other two directions are assumed constant. A good start in the meshing process is the flow channel as this is the first area where reactant gases enter the computational domain. Accurately solving for the flow-filed in this area ensures correct species concentration distribution and in turn accurate local current density.

In laboratory and commercial cells, a 1×1 mm^2 flow channel is most typical and usually divided into smaller 0.10×0.10 mm^2 elements over the cross section in a CFD analysis. However, as a reference mesh, it is refined further so that each elementary volume in the channels is 0.05×0.05×0.05 mm^3. This should be noted that this mesh is purposely made unnecessarily fine for comparison and hence cannot be seen anywhere else. Depending on the functions and physics inside, each porous layer has different thicknesses and hence requires different mesh in this through-plane direction, they will not be meshed totally independently, however. Rather, all porous layers are meshed and refined simultaneously. Porous layers in anode and cathode sides will have the same grid density while the transfer of mesh from one layer to an adjacent one is only restricted by a minimum jump in cell size.

Keeping the lateral and along-the-channel meshes the same and only varying the grid density in the through-plane direction, the resulting four meshes are shown in Figure 4.6 and the only difference among them is the number of elements in the porous layers. Statistical properties of Meshes 1-4 can be seen in Table 4.4.

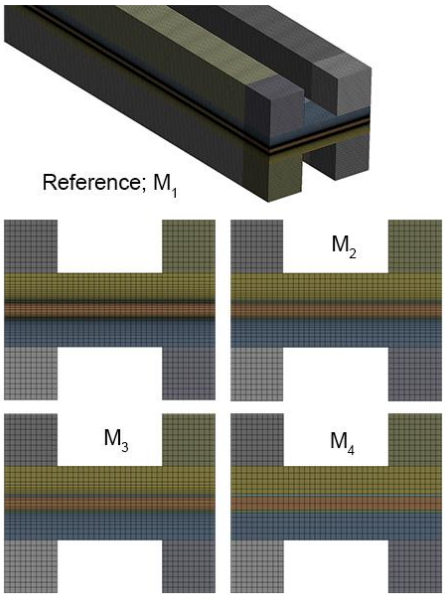

Figure 4.6 The four meshes with different grid density in the through-plane (z) direction.

Mesh	Element	Orthogonal Quality (avg)	Skewness (avg)	Aspect Ratio (max/avg)
M_1	1 904 000	1	0	12/4
M_2	1 520 000	1	0	7/3
M_3	1 328 000	1	0	5/2
M_4	992 000	1	0	2/1

Table 4.4 Statistics of Meshes 1-4.

The polarisation curves are shown in Figure 4.7. The percentage errors, defined in Equation (4.12) as the difference between the average current density obtained from the particular mesh to the reference mesh, are also superimposed in the plot.

$$\%Err = \frac{i - i_{M_1}}{i_{M_1}} \times 100\% \tag{4.9}$$

The percentage errors of the three meshes show similar characteristics having low values at low operating current and increase with the operating current. It is interesting to see that the errors peak at a mid-current operation corresponding to the ohmic region. This suggests that the elements present in the mesh are not sufficient to accurately resolve the transport of electron in the electronically conductive portion of the porous layers. Mesh 4, in particular, has only one element in the through-plane direction in both catalyst layers hence highest deviation from the reference mesh results. This means that the early models which treated the catalyst layers as an interface with zero thickness are not a proper representation of a real catalyst layer and thus should be avoided.

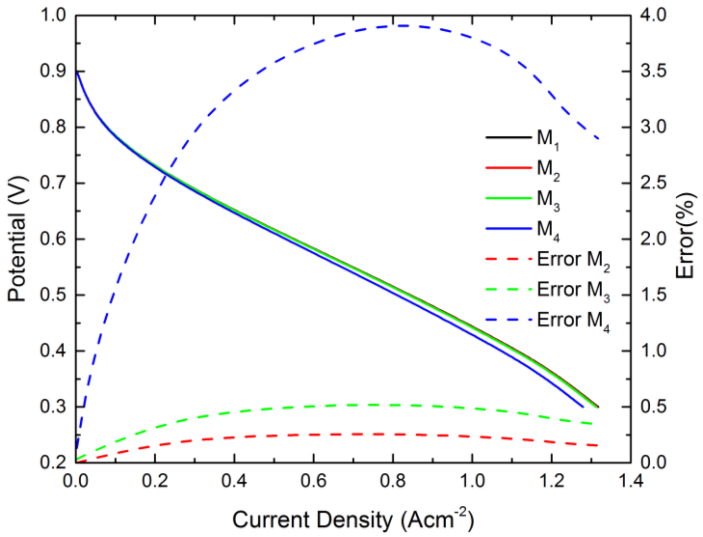

Figure 4.7 Polarisation curves and corresponding percentage errors of Study 1.

The source of error is investigated further. For ease of comparison, the operating voltage which corresponds to the highest percentage error, 0.30 V, is chosen. Firstly, the effect of through-plane mesh is examined by looking at the local distribution of flow-fields in flow channels. Since the electrochemical reaction only takes place in the catalyst layers, having different mesh densities across these layers might result in different local reaction rate and hence local flow-field variables are expected to vary to some extent. Two along-the-channel lines (Lines 1 and 2 in Figure 4.5) will be used to visualise such variables.

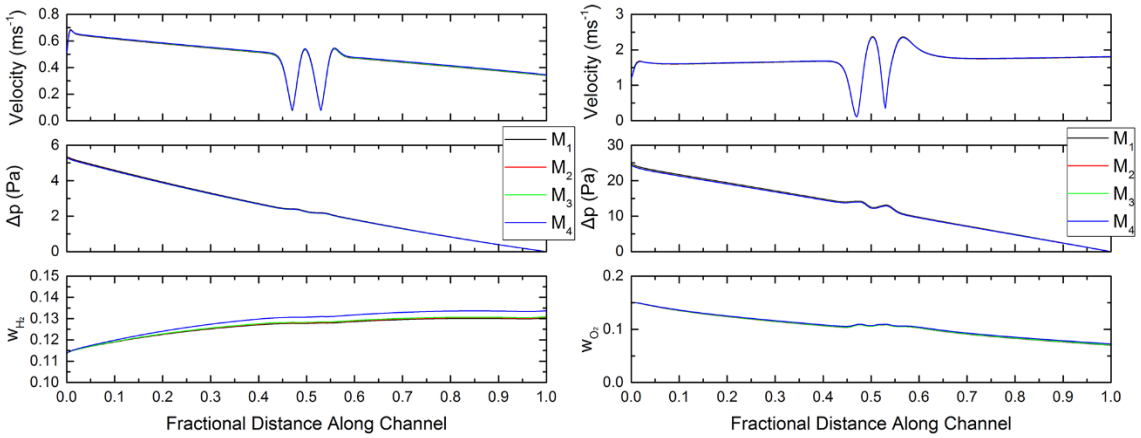

Figure 4.8 Flow-field variables along anode (left) and cathode (right) channels.

As can be seen from Figure 4.8, the deviation of velocity from the reference mesh is very small and this is true for both channels. A large velocity fluctuation inside the bend region indicates that the flow undergoes separation which can be captured by all four meshes. The pressure drop in the cathode channel is much higher than the anode channel as expected due to the presence of heavier oxygen gas and liquid water. Negligible difference in pressure drop between the four meshes is seen in both channels.

Looking at hydrogen and oxygen mass fractions in the anode and cathode channels, respectively, it is clear that the effect of through-plane mesh is more pronounced and the deviation increases along the channel. This is the result of a non-uniform local reaction rate which varies along the flow path. The deviation not only occurs in the through-plane direction but also in the direction where the flow propagates and it adds up resulting in a higher deviation of the species mass fraction near the channel exit.

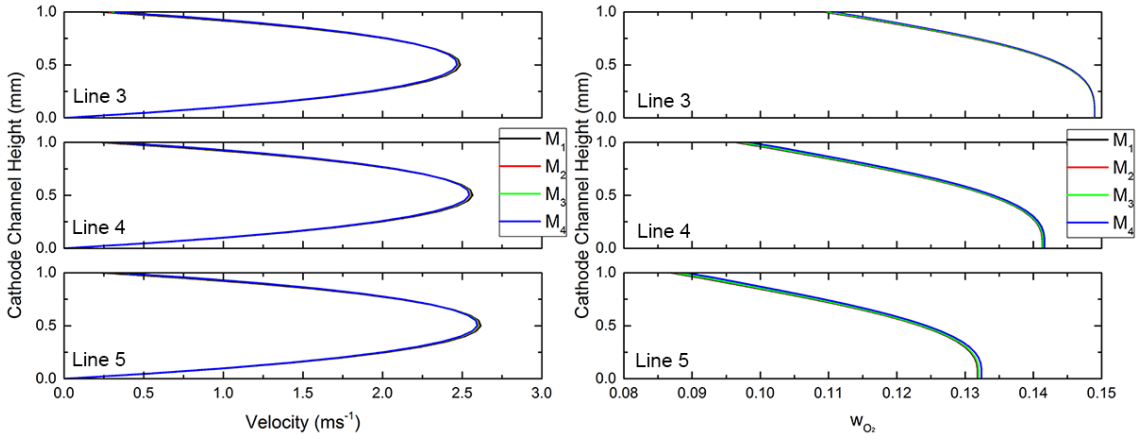

Figure 4.9 Velocity and oxygen mass fraction across cathode channel in the channel region.

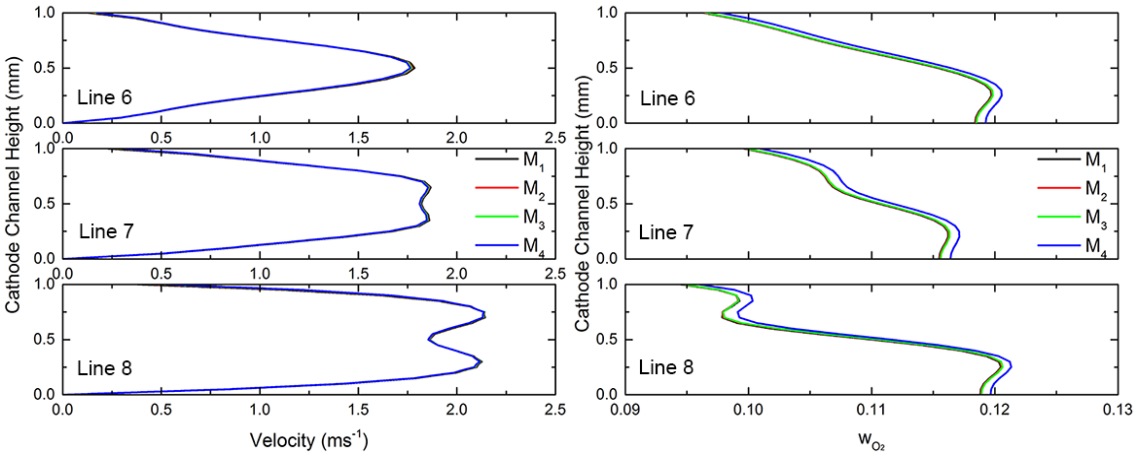

Figure 4.10 Velocity and oxygen mass fraction across cathode channel in the bend region.

The velocity profiles of cathode gas across the channel height at different locations are shown in Figure 4.9 and Figure 4.10. As can be seen that the velocity profiles either in the channel or bend regions show the same characteristics having negligible deviation among different meshes. However, the asymmetry of the velocity profile about the flow channel axis can be clearly seen which is caused by different boundary conditions between the bottom and top of the channel. The non-zero velocity at the top wall represents the species flux across this interface into the porous cathode GDL as opposed to a zero velocity at the bottom solid wall where a no-slip boundary condition applies.

From Figure 4.9, the maximum velocity can be found at the channel's mid-height whereas this same velocity profile is not seen in the bend region. A drastic 180-degree turn inside the bend causes the flow to detach from the wall forming eddies and vortices. Because these flow features are highly three-dimensional, the flow field in the bend region is thus chaotic and inhomogeneous which explains the occurrence of the double-peak profile found in Lines 7 and 8 of Figure 4.10.

The oxygen mass fraction has the same behaviour as other two variables but the deviation increases slightly further downstream. Clearly, it can be seen that oxygen is consumed in the porous region therefore there exists oxygen mass fraction gradient in both the through-plane and downstream directions. Nevertheless, the effect of through-plane mesh to the flow-field in the channels is very small and hence the channels can be safely discarded in the next discussions.

The effect of the mesh is investigated further by creating three additional lines extending through the porous layers from cathode GDL to anode GDL (refer to Figure 4.5 as Lines 9, 10, and 11). Local distributions of velocity, pressure, hydrogen and oxygen mass fractions, and current density along each line are given in Figure 4.11.

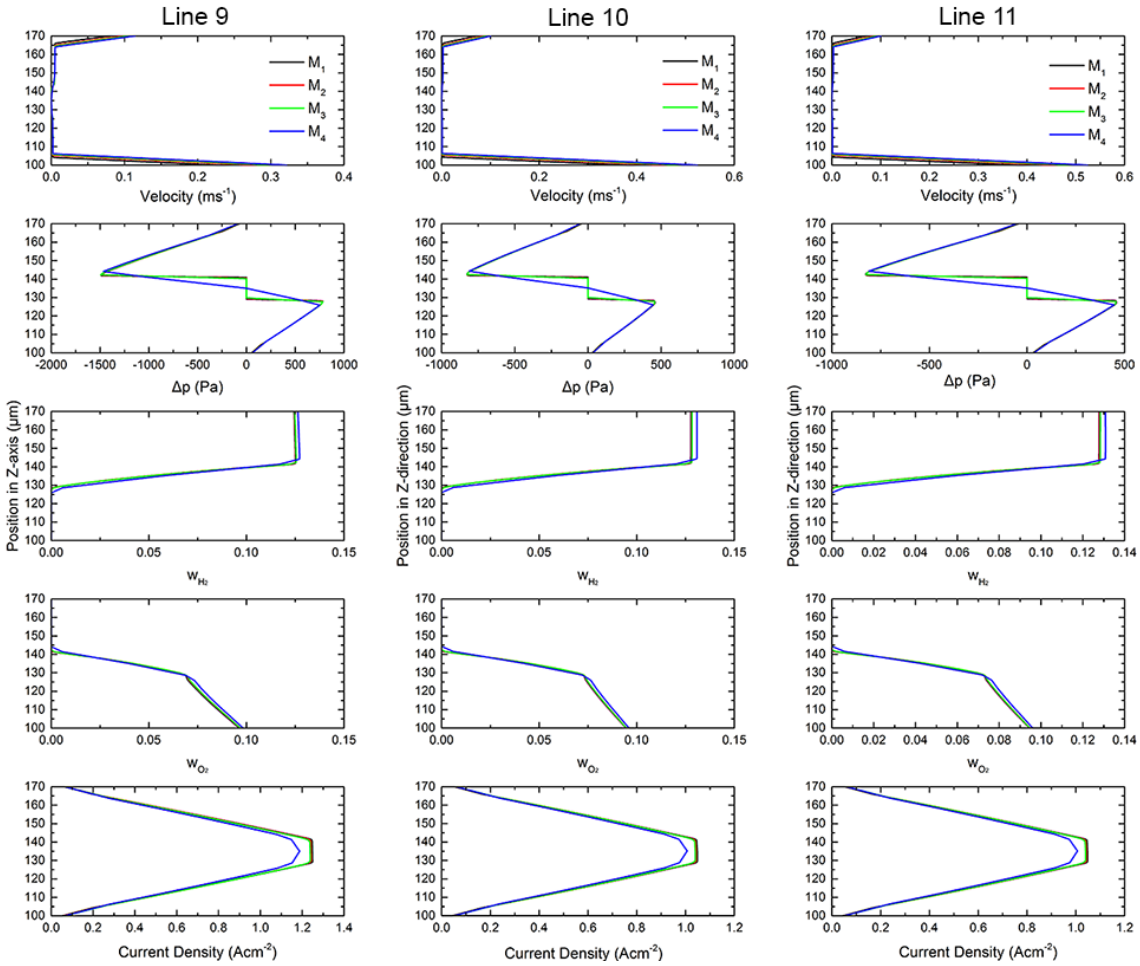

Figure 4.11 Flow-field variables profiles across the porous layers (GDLs, CLs, and PEM).

The smaller velocity in Figure 4.11 indicates that diffusion dominates the mass transport in the porous layer in contrast to convection-dominated flow-field in the channels and clearly due to a very thin structure of each porous layer, the difference of velocity, pressure, and hydrogen and oxygen mass fractions are very small even the catalyst layers are treated as an interface in Mesh 4.

The current density, on the other hand, is not a function of reactant concentrations alone and therefore differs significantly among the four meshes despite similar reactant species distributions. This can be confirmed by observing an electron-transport-related variable like local overpotential as shown in Figure 4.12. Clearly, insufficient elements in the porous layers cannot accurately resolve the overpotential and other electron-transport related parameters. This is amplified by discrepancies in species distributions and results in a large current deviation as seen in Figure 4.7.

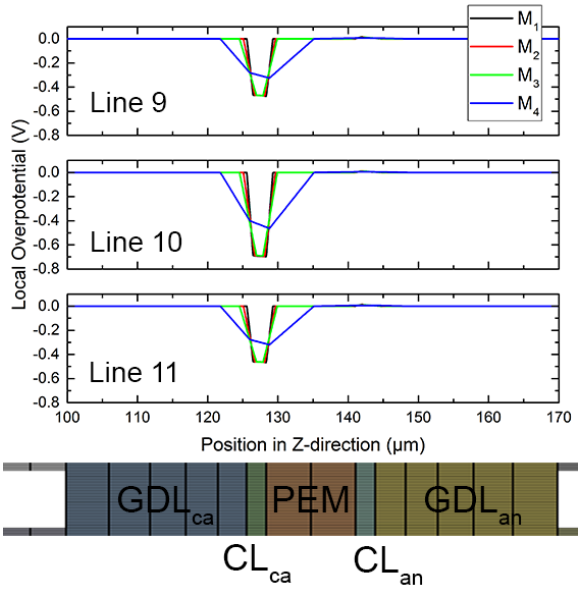

Figure 4.12 Overpotential profile across porous layers.

In conclusion, even though the percentage errors are under 4%, these, however, cannot be considered insignificant especially when the number of elements in each mesh is taken into account. It is clear from Table 4.4 that the element numbers in Meshes 2, 3, and 4 are reduced only slightly with 20%, 30%, and 48% element reduction, respectively. The through-plane mesh is therefore said to have a profound effect to the accuracy of the solution and should be treated with great attention.

Finally, treating the catalyst layer as a zero-thickness interface can only give acceptable solutions of flow-field variables such as velocity, pressure, or species mass fraction. However, the current density and other electron-transfer-related parameters are notably inaccurate and hence this should be avoided in a CFCD simulation where detailed distribution of current density is required.

Study 2: In-plane (x-direction) Mesh

In this section, the main focus is the flow-field at the bend, a small portion in the cell where the flow undergoes a drastic 180-degree change in direction. Here, the primary flow is aligned with the x-axis where the mesh is coarsened and hence high deviations of flow-field variables due to different meshes are expected.

Having Mesh 1 as a reference, the effect of the mesh across the width of the cell is investigated by increasing the size of the mesh in this direction to 0.100, 0.125, 0.200, and 0.500 mm and the four meshes are referred to as Meshes 5, 6, 7, and 8, respectively as shown in Figure 4.13. The mesh properties are given in Table 4.5.

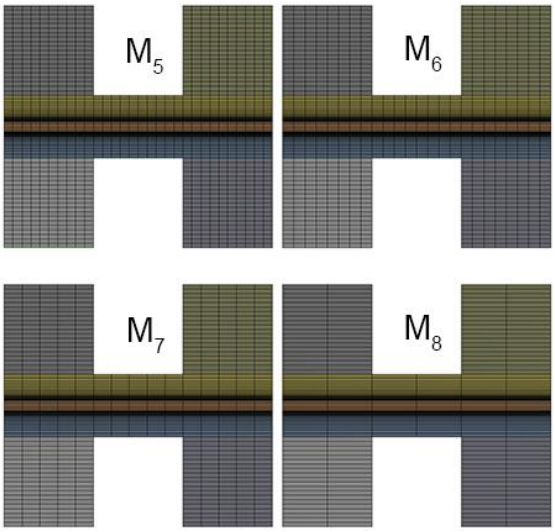

Figure 4.13 The four meshes with different grid density in the lateral (x) direction.

Mesh	Element	Orthogonal Quality (avg)	Skewness (avg)	Aspect Ratio (max/avg)
M_5	952 000	1	0	23/9
M_6	761 600	1	0	29/11
M_7	476 000	1	0	46/18
M_8	190 400	1	0	116/44

Table 4.5 Statistics of Meshes 5-8.

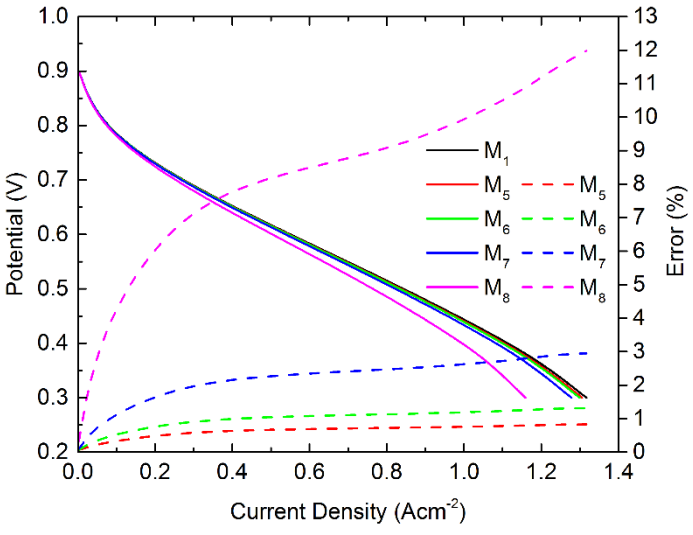

Figure 4.14 Polarisation curves and corresponding percentage errors of Study 2.

The polarisation and percentage error curves of all five meshes are shown in Figure 4.14. Compared to the first study, the errors are slightly larger with these meshes but it should be noted that the number of elements used and hence computation time is much

smaller. All error curves are different from those found in Study 1 in which they continually rise with the operating current and peak at the mass transfer region with the values of 0.8%, 1.3%, 3%, and 12% for Meshes 5, 6, 7, and 8, respectively. The solution to the flow-field at 0.30 V operating voltage is, again, chosen.

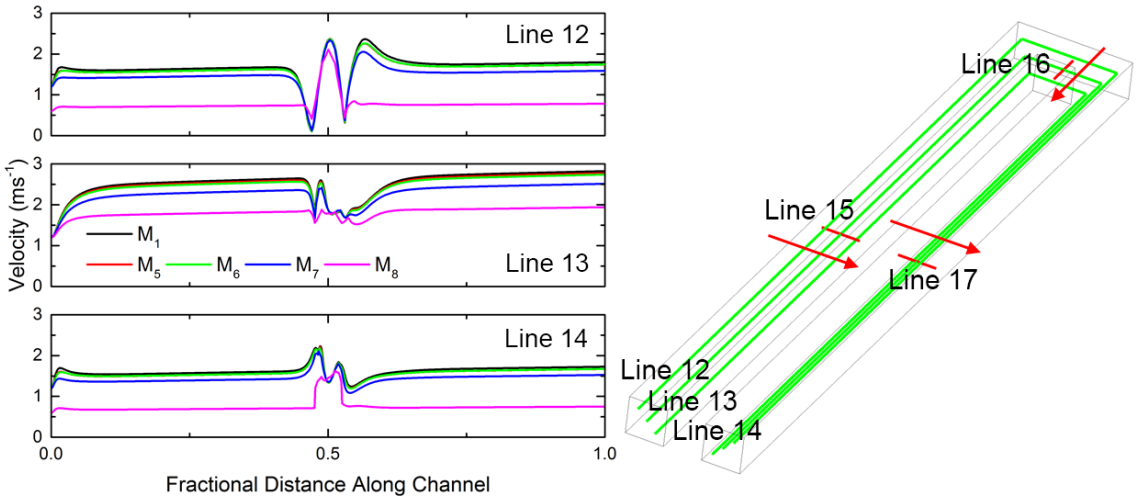

Figure 4.15 Velocity profiles along the cathode channel (a red arrow indicates the direction from one channel wall to the other as a reference for the velocity profile plot).

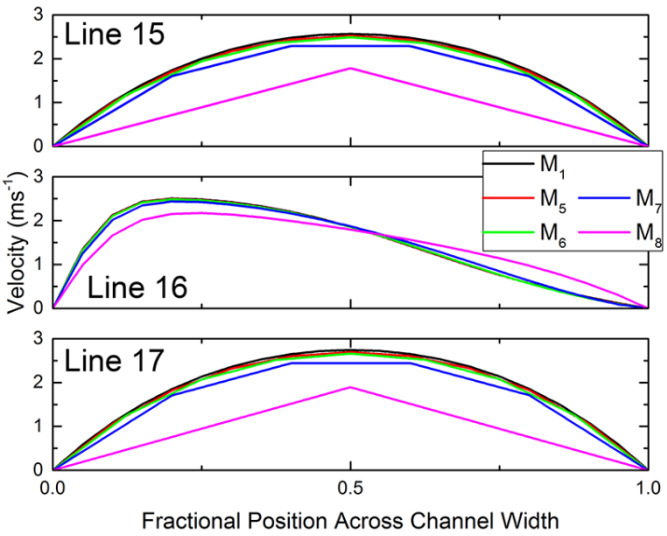

Figure 4.16 Velocity profiles across the channel width.

Figure 4.15 shows cathode gas velocity along the three lines as defined in the same figure. Surprisingly, there is negligible difference between the velocity curves in the bend region whereas the velocity curves in the channel region differ considerably. This is due to an insufficient number of elements near the channel wall which cannot accurately resolve the boundary layer in the channel region since the mesh in this area has been coarsened. The

mesh in the bend region has been coarsened in the same direction as in the channel region, however, the direction of the primary flow is now changed and therefore the boundary layer is now aligned with the y-axis where the mesh is unchanged and very fine as shown in Figure 4.17. The resulting velocity fields then show a large deviation in the channel region but not in the bend. It should be noted that the small discrepancies between the velocity curves exist and these are caused by the coarser mesh in the channel close to the upstream and downstream of the bend.

Figure 4.16 confirms the above explanation showing the velocity profiles across the cathode channel's cross section at three different locations corresponding to Lines 15-17 along the flow path. It is evident that the deficiency of element near the channel wall causes a large deviation in velocity profiles across the channel especially in the channel regions.

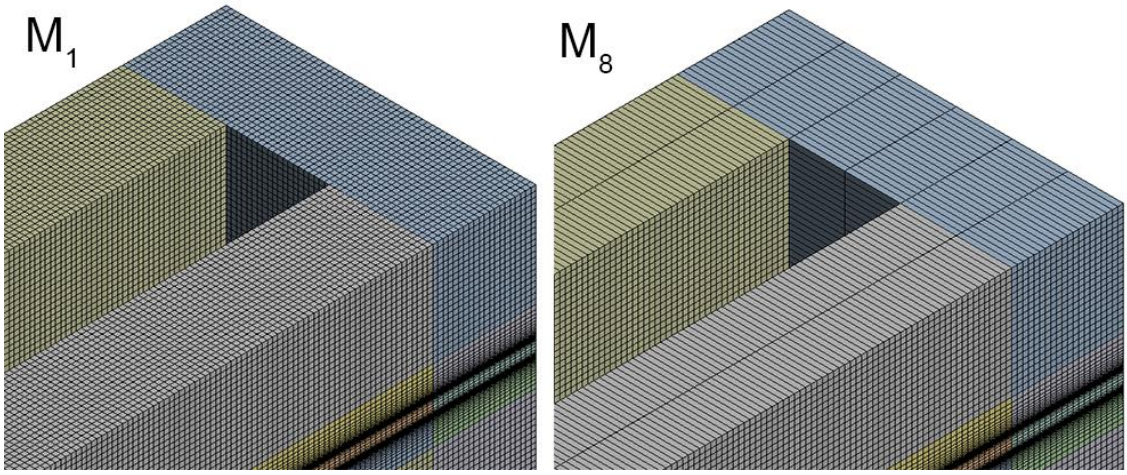

Figure 4.17 Comparison of grid in the bend region of Meshes 1 and 8.

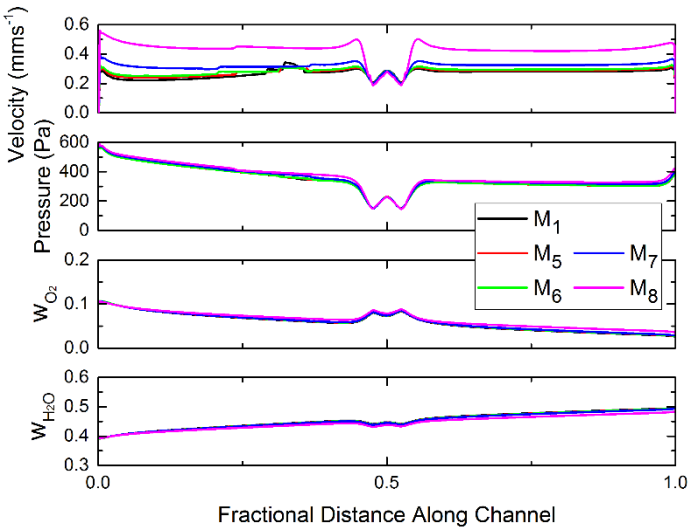

Figure 4.18 Flow-field variables profiles at the interface between PEM/CL_{ca}.

The effect of a lateral mesh on the flow-field in the porous region is shown in Figure 4.18. In the figure, velocity, pressure, and cathode species mass fraction profiles along a line similar to Lines 12-14, but created on the interface between cathode catalyst layer and membrane, are shown. As seen from the figure, the velocity is significantly lower than in the channel whereas pressure drop is very high due to the porous structure which introduces additional resistance to the flow. Both variables, however, have the same characteristics in which the large deviation between the meshes exists in the channel region than in the bend.

Nevertheless, it is not distinguishable whether the deviations in channel or bend is larger in the case of oxygen and water vapour mass fractions since the species transport in porous media is dominated by diffusion which is driven by species concentrations but not by the velocity field. The calculation of the pressure field, in contrast, is closely coupled to the velocity field as described in the preceding section on SIMPLE algorithm and hence it has the same characteristic as seen in the figure.

It is interesting that the major source of error from this meshing scheme stems from the channel region, not the bend as hypothesised. This reveals the importance of accurately resolving the boundary layer at wall channels which occupy most of the computation domain even though the flow is laminar and the region near the wall channels should always be given sufficient mesh elements following the primary flow regardless of x-, y-, or z-direction.

Study 3: Along-the-channel (y-axis) Mesh

In this section, the mesh in the direction of the flow channel which covers most of the cell is investigated. Similarly, Mesh 1 is used as a reference and only the mesh in y-direction is relaxed having sizes of 0.100, 0.125, 0.200, and 0.500 mm and referred as Meshes 9, 10, 11, and 12, respectively. The four meshes and their corresponding properties are presented in Figure 4.19 and Table 4.6, respectively. Here, the maximum size is limited to 0.500 mm as used in Mesh 12 in order to maintain the cell aspect ratio below 200.

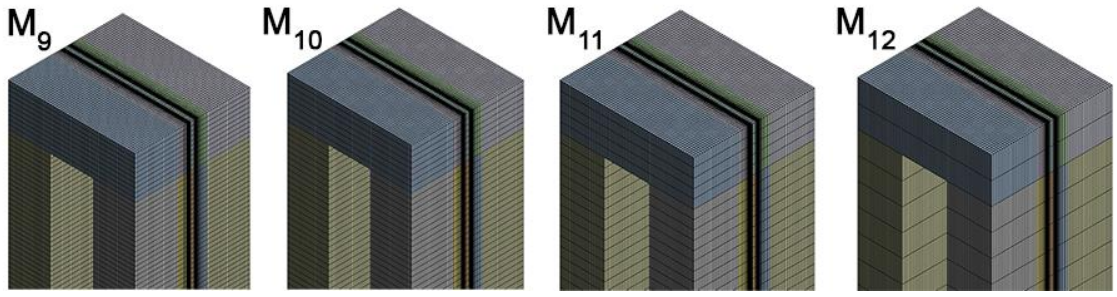

Figure 4.19 The four meshes with different grid density in along-the-channel (y) direction.

Mesh	Element	Orthogonal Quality (avg)	Skewness (avg)	Aspect Ratio (max/avg)
M_9	952 000	1	0	23/9
M_{10}	761 600	1	0	29/11
M_{11}	476 000	1	0	46/18
M_{12}	190 400	1	0	116/44

Table 4.6 Statistics of Meshes 9-12.

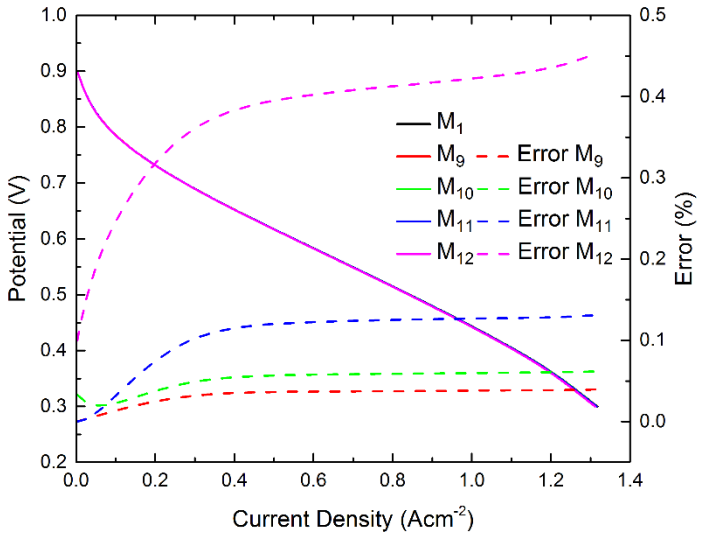

Figure 4.20 Polarisation curves and corresponding percentage errors of Study 3.

The polarisation and percentage error curves are shown in Figure 4.20. This along-the-channel meshing scheme produces impressive results as the percentage error of the four meshes are much smaller compared to Meshes 5, 6, 7, and 8 even with the same number of elements. The polarisation curves deviate more as the current density increases while the largest deviation, which is found in Mesh 12, is under 0.5%.

The finding in Study 2 suggests that since the y-direction mesh is elongated in the bend region and is responsible for the boundary layer near the walls at the bend, a large discrepancy of flow-field variables among the meshes in this region are expected and this is confirmed in Figure 4.21 which shows the velocity profiles along Lines 12-14 when the cell is operated at 0.30 V. In contrast to the velocity curves in Figure 4.15 in Study 2, a large deviation in velocity occurs in the bend region as expected. This is also true for the variables along Line 21 at and interface between CL_{ca} and membrane shown in Figure 4.22. Clearly, the source of error comes from the bend region where the mesh in the boundary layer is not sufficiently fine.

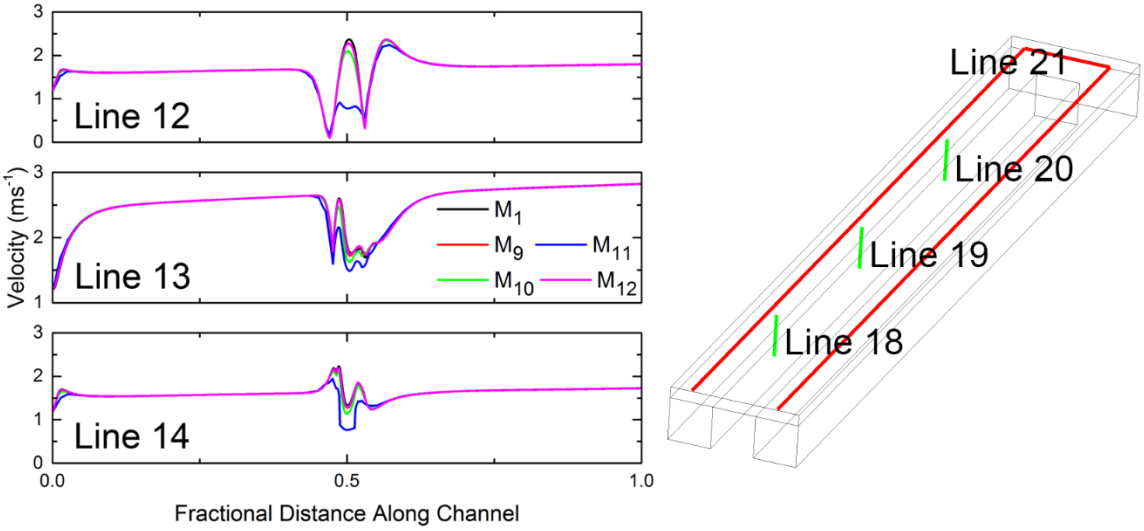

Figure 4.21 Velocity profile along the cathode channel.

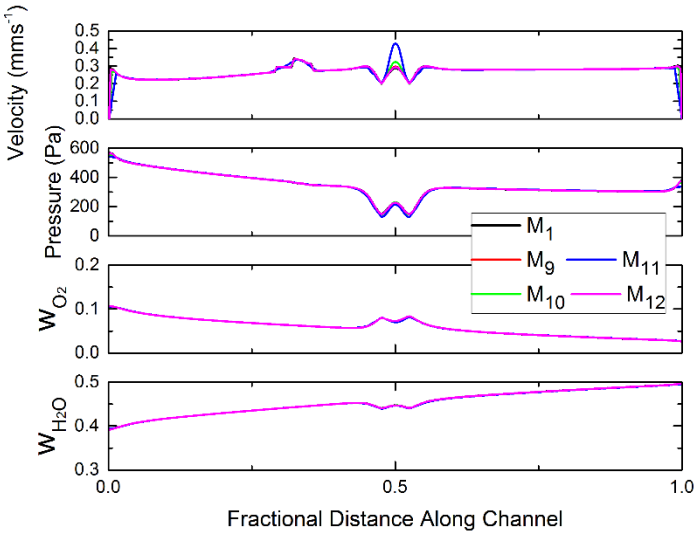

Figure 4.22 Flow-field variables profiles along Line 21.

It is evident that the along-the-channel mesh has very little effect on the solutions and it should be investigated further. The possible explanation is that since the flow is laminar which means that the velocity field is not high and hence the flow reaches the fully-developed stage only at a relatively short distance from the entrance and from the bend exit. In a fully developed flow, by definition, the velocity field will remain constant regardless of the distance the flow has propagated and hence the fineness of the mesh in this direction makes no difference as is evident in Figure 4.23 where velocity profiles across the flow channel of the four meshes are effectively the same regardless of their location along the channel.

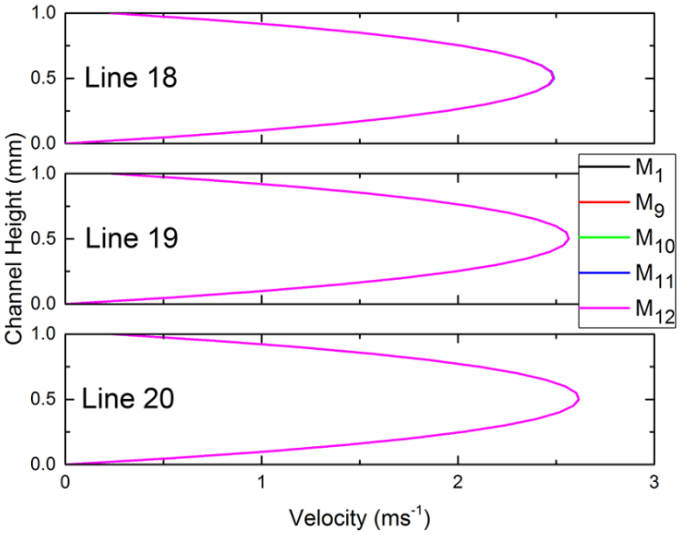

Figure 4.23 Velocity profiles across cathode channel height at different locations.

To summarise, under typical range of flow velocity, the along-the-channel mesh has little effect to the accuracy of the solution compared to the other two directions as the flow becomes fully developed in most region of the channel. This is of great benefit since the mesh along this direction can be relaxed which reduces the number of elements in the mesh considerably. Finally, it should be noted that the mesh in this direction cannot be coarsened independently. The reactant gas flow rate, stoichiometric ratio, and other operating conditions play an important role in determining the flow velocity in the channels and hence limit the coarseness of the mesh.

Study 4: Proposed Meshing Strategy

Using the findings from previous studies which suggest that if the mesh schemes in all three dimensions are combined in a proper way, the number of elements can be reduced further while keeping the percentage error to an acceptable level. An effective mesh generation strategy is proposed and used to generate three additional meshes which will then be tested in this section.

Due to a good balance between mesh density in the through-plane direction and degree of accuracy, Mesh 3 is chosen as the base mesh in which modification in the along-the-channel and in-plane directions will be made. From this, an averaged thickness of the sub-layer in each porous layer can be approximated as 10, 20, and 30 μm for CLs, PEM, and GDLs, respectively.

The lateral mesh is the one used in Mesh 6 because even the highest percentage error from this mesh (1.3%) is acceptably low thus the value of 0.125 mm is used throughout the

domain. The axial mesh, nevertheless, is not uniform having more grid density at the channel inlet and outlet and at the bend while the mesh in channel region is less dense. The benefit of doing this is two-fold. Firstly, at regions where the primary flow undergoes acceleration and deceleration such as inlet, outlet, and bend entrance or exit, a denser grid will help resolve the flow-field in these regions with greater accuracy. The second benefit is seen in the bend region where the primary flow is rotated by 90 degrees and hence the boundary layers now extend in the y-direction which can be resolved with sufficient elements. The use of thicker through-plane elements in porous layers allows the axial mesh to be elongated further so that the resulting new Meshes 13, 14, and 15 will have the longest cells of 0.50, 1.00, and 1.77 mm, respectively as shown in Figure 4.24 and Table 4.7.

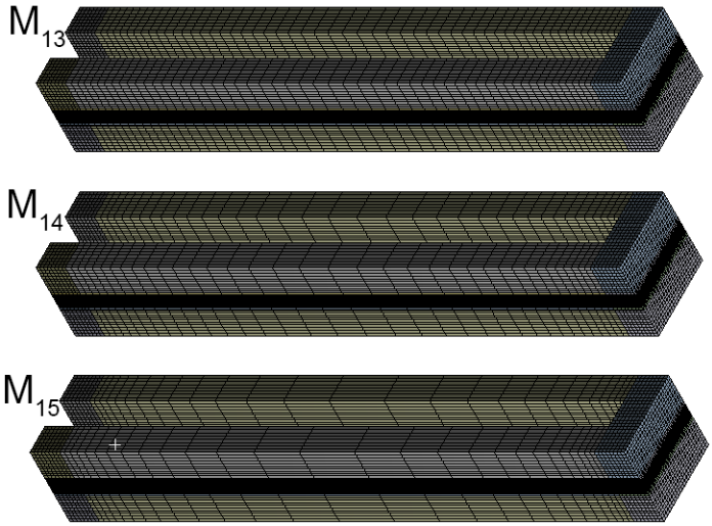

Figure 4.24 Three meshes generated by the proposed meshing scheme.

Mesh	Element	Orthogonal Quality (avg)	Skewness (avg)	Aspect Ratio (max/avg)
M_{13}	70 720	1	0	54/12
M_{14}	52 864	1	0	107/16
M_{15}	43 936	1	0	199/19

Table 4.7 Statistics of Meshes 13-15.

The polarisation and percentage error curves are shown in Figure 4.25. In spite of the same behaviour, these errors are higher than the ones in Study 3. This was expected, however, since the number of elements are significantly less. Flow-field variables in the mid-cathode channel along Lines 13 and 21 (defined in Figure 4.15 and Figure 4.21, respectively) are shown in Figure 4.26. It is evident that the proposed meshes is able to capture the profiles

from Mesh 1 reasonably well without the presence of large deviation in neither channel nor bend regions.

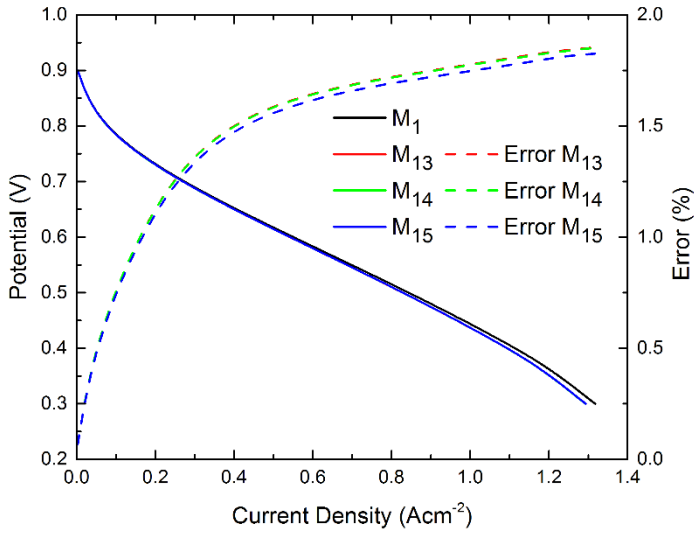

Figure 4.25 Polarisation curves and corresponding percentage errors of Study 4.

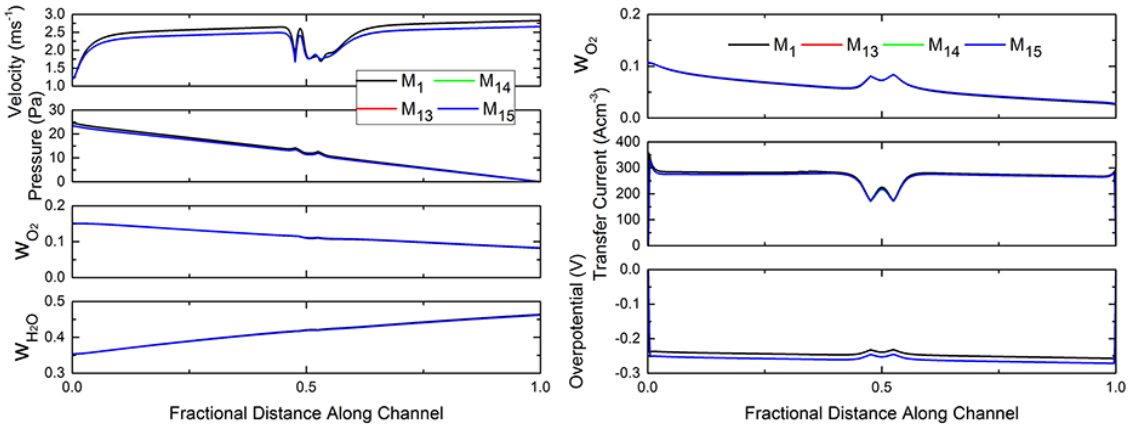

Figure 4.26 Flow-field variables along Line 13 (left) and 21 (right).

Even though the three meshes result in a slight decrease in accuracy, if the number of elements in the mesh is taken into account, for example, the reduction of Mesh 15 from Mesh 1 is;

$$\frac{n_{M1}}{n_{M15}} = \frac{1\,904\,000}{43\,936} \times 100\% = 4333\%$$

which uses 43 times less elements while the error is under 2% throughout the operating range. Obviously, it can be said that the proposed meshes perform very satisfactorily and the maximum element length in the axial direction below 2 mm can safely be used.

Study 5: Range of Application

In the first part of this study, the U-turn model is expanded to form a square cell with an active area of 21×21 mm^2. The single-serpentine flow-field is maintained in order to verify that the proposed meshing strategy is valid regardless of the cell size. To make a comparison, the cell is meshed using three different meshing schemes as used in Meshes 1 (reference), 4 (through-plane, zero-thickness CLs), and 15 (proposed mesh) resulting in 13 028 800, 6 317 200, and 310 144 elements and are referred to as Grids 1, 2, and 3, respectively.

The polarisation and percentage error of the three grids are present in Figure 4.27. Each of the error curves follows its characteristics found in the previous studies despite the use of a new cell geometry. The error of Grid 2 is large in the ohmic region where the error of Grid 3 increases with current density but stays well within an acceptable range throughout the operation. It should be noted that the error from Grid 3 is increased slightly from Mesh 15 as expected due to a larger computational domain.

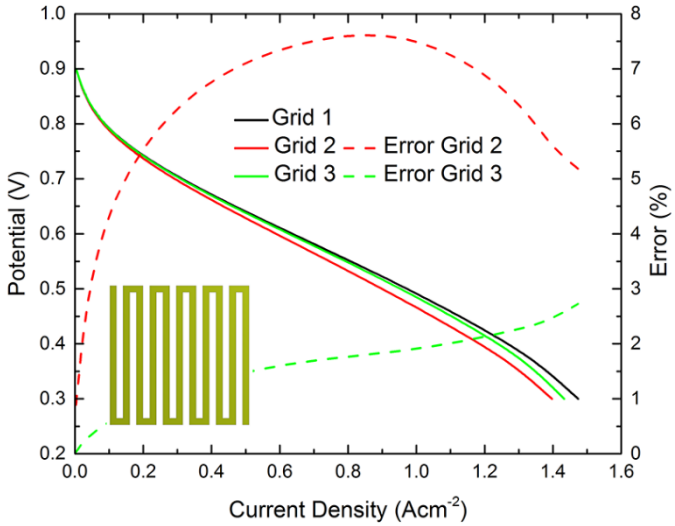

Figure 4.27 Polarisation curves and corresponding percentage errors of three grids.

It is interesting to see that the maximum error from Gird 3 is almost four times lower than that of Grid 2 even the number of elements is much less indicating that a denser mesh does not always guarantee a more accurate solution if those extra elements are not placed in the correct regions.

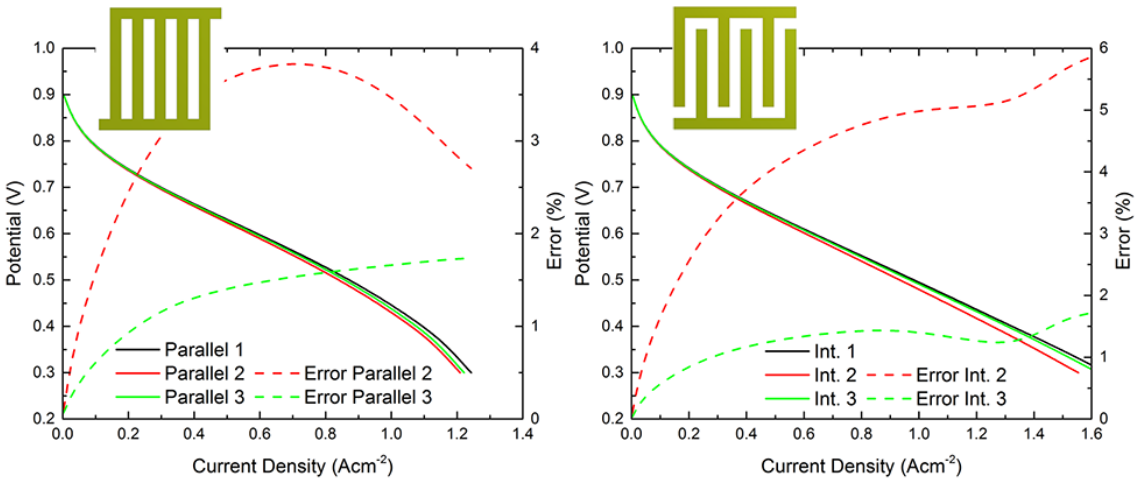

Figure 4.28 Polarisation curves and corresponding percentage errors of parallel (left) and interdigitated (right) cells.

The validity of the proposed mesh on different flow-field configurations is tested in this second part and presented in Figure 4.28 which show the polarisation and percentage error curves of parallel and interdigitated cells both having an 11×11 mm^2 active area, respectively. Similarly, the error from each meshing scheme follows its unique pattern regardless of the flow-field being used and stays acceptably low. This can be concluded that the proposed meshing strategy is valid regardless of cell size or flow-field configuration.

Concluding Remarks

It is clear that a CFCD modelling, which is a highly 3-dimensional simulation, involving heat and mass transports in different spatial and temporal scales requires a large number of elements. A good mesh not only gives great degree of accuracy within a manageable timeframe but also helps avoid divergence in the calculation process.

The through-plane mesh, though the cell has the least dimension in this direction, has the strongest effect on the solution especially in the determination of current density and other electron transfer related variables. Great attention must be paid to the mesh in this direction especially in the porous media and hence it is advisable to always treat the catalyst layers as a porous layer with a finite thickness.

The in-plane mesh coincides with the direction which boundary layers near channel walls develop perpendicular to the primary flow and covers major parts of the cell. The in-plane mesh therefore has a moderate effect on the solution accuracy and the boundary layers, regardless of direction of the primary flow, should always have sufficient elements even though the flow is laminar in all operating conditions.

The axial mesh, on the other hand, has little effect on the solution accuracy because the flow is fully developed in most parts of flow channels. This offers a great advantage in which the number of elements in this direction and consequently total mesh elements can be reduced drastically. However, it should be done in such a way that the mesh in the regions where the flow undergoes acceleration and deceleration is denser and the mesh is relaxed in the middle region of the channel where the flow has reached the fully developed stage.

In summary, the proposed mesh comprises of structured, non-uniform hexahedral mesh elements having all surfaces at 90 degrees to each other and zero skewness. The cubic elementary volumes will exist in channel entrance, exit, and bend regions while elongated ones are present in the channel regions occupying most part of the cell. The mesh has been shown to perform very satisfactorily offering a good balance between manageable number of mesh elements, computation time, accuracy of polarisation curve, and most important the local distribution of flow-field variables which are essential in a PEMFC analysis.

It should be pointed out that a smaller number of elements used in the proposed mesh not only reduced the calculation time for each iteration, but also accelerated the convergence significantly as demonstrated in Figure 4.29 where the residuals from Meshes 1 and 15 are presented. Both cells started off under the same initial condition, solver settings, and under-relaxation factors (URFs) and then iterated under two potentiostatic conditions of 0.50 V and 0.40 V given the same iterations number of 500.

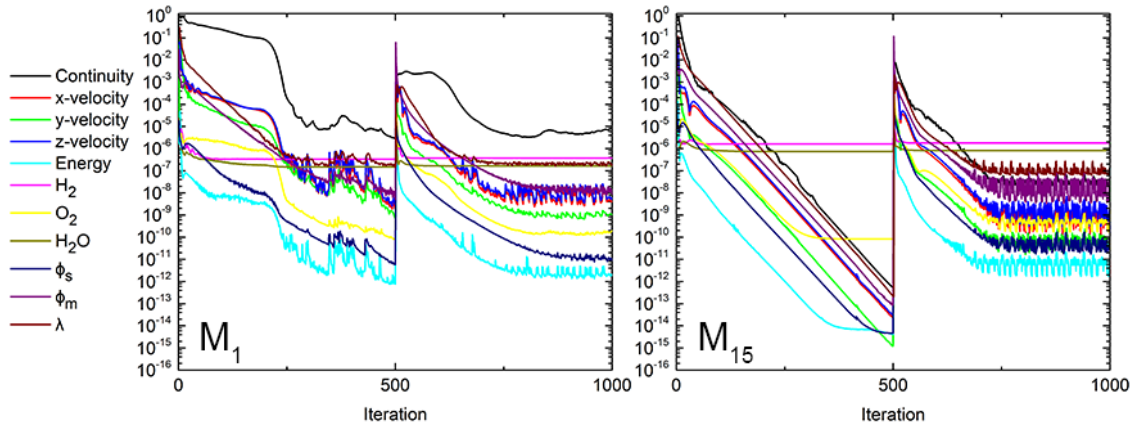

Figure 4.29 Residuals plots of Meshes 1 and 15 showing effect of grid fineness.

Clearly, Mesh 15 already reached a converged solution after 500 iterations whereas the residuals of Mesh 1 were still struggling to settle down. It took one hour and forty minutes for Mesh 1 compared to two and a half minutes for Mesh 15 to complete 500 iterations. This 4000% reduction is significant and should not be overlooked especially when commercial-

sized cells are used. The corresponding evolution histories of velocity, oxygen mass fraction, and current density at a random point in the cathode channel are shown in Figure 4.30 which indicates that it took less iterations for each variable in Mesh 15 to become stable.

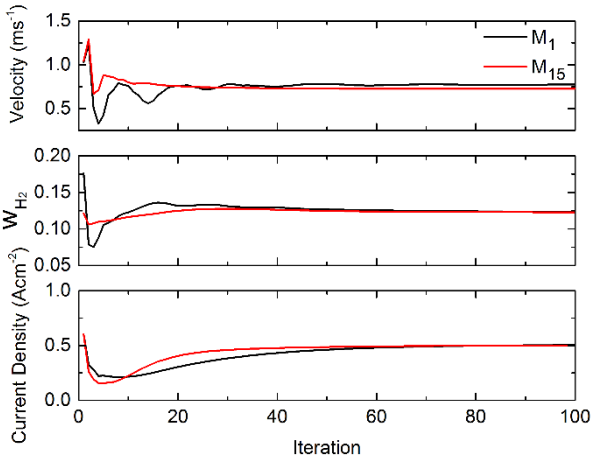

Figure 4.30 Time histories of sampling variables which evolved with iterations.

This can be explained by examining the velocity vector field at the middle plane of the cathode channel after the number of iterations was increased so that convergence was achieved in both meshes shown in Figure 4.31.

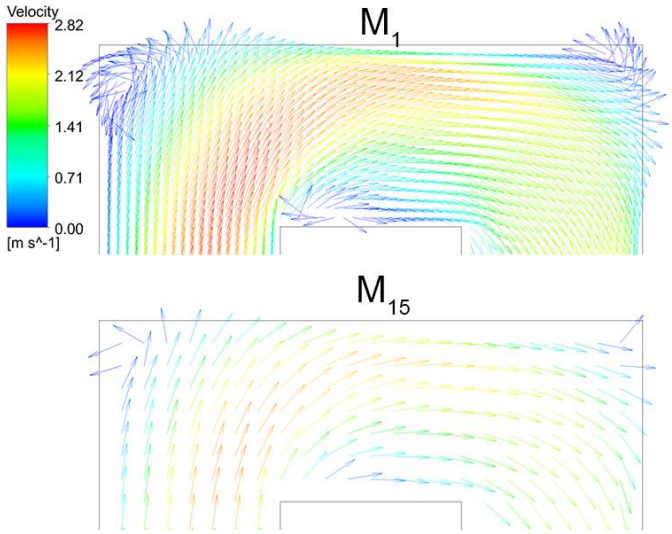

Figure 4.31 Velocity vector field at bend region under 0.50 V operating potential.

The finer grid used in Mesh 1 could capture flow features such as flow separations and re-circulations around the bend as seen in the figure. The sudden change of flow variables in these regions has a direct effect on the stability of calculation and affects the

global residual values and rate of convergence. However, as it has been shown through the previous studies that all flow-field variables are effectively the same with negligible error and hence these flow features can be safely ignored. Using a coarser grid like Mesh 15 will smooth out such flow separations and speed up the convergence giving a good compromise between calculation time and accuracy.

Finally, the proposed mesh generation strategy is proved to be valid under PEM fuel cell typical operating conditions regardless of cell size or flow-field configuration and this meshing scheme is applied to all studies presented in this thesis.

4.2.2 Time-step Size Independence Study

The main focus of this thesis is the analysis of an automotive PEM fuel cell where its transient response is of particular importance to engineers and researchers. The transient behaviour of a cell is achieved by running a dynamic simulation that seeks for time-dependent solutions as the cell operates through time.

The time-step size, Δt, defined at each time step, tells the calculation algorithm how further ahead the next point in time is. For example, if the current time step at time = 10 second is defined as t_1 and the time-step size is chosen to be Δt = 0.5 s, then the next time step, t_2 is an instant when time = 10+0.5 = 10.5 s. Any solution at any time between t_1 and t_2 for example, at time = 10.1, 10.25, or 10.495 s is not calculated and hence not exist.

In analogy to the element size in x-, y-, and z-coordinates, the time-step size can be visualised as the size of a mesh element in the fourth coordinate along the time-axis. Clearly, a large temporal size will contribute some inaccuracies in the solution fields just like a large spatial size does and therefore it is important to select a proper time-step size.

Determination of Time-step Size

Figure 4.32 gives a comprehensive illustration diagram [158] of the characteristic time-scales of transient mechanisms occurring in the cell. There exist three important mechanisms, however, that are worth the attention since they are known to influence the cell dynamics. The knowledge of characteristic time-scales of these three mechanisms is helpful in the determination of a time-step size to be used in the transient run and are discussed in this section.

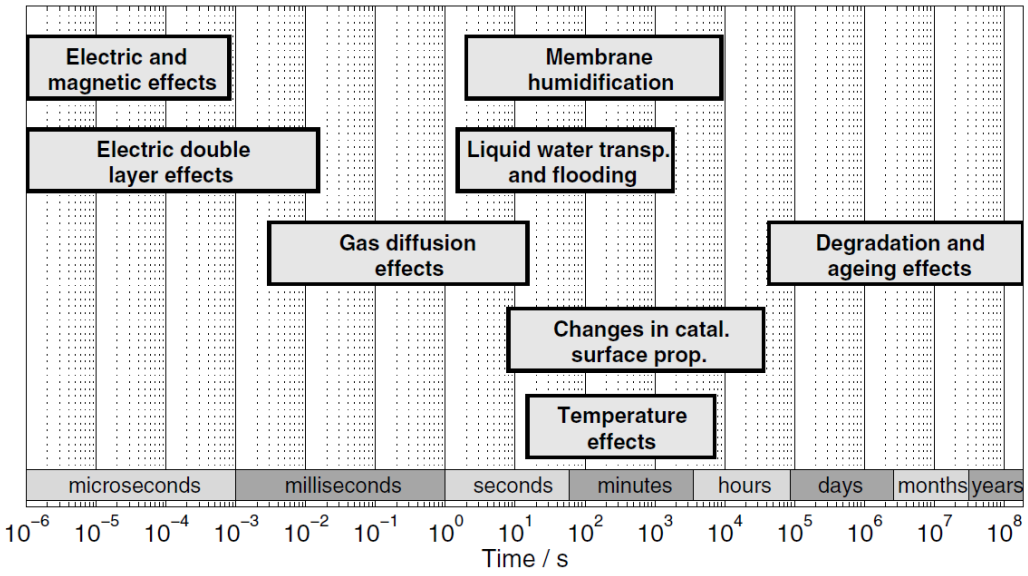

Figure 4.32 Dynamic processes in PEM fuel cells [158].

Wu et al. [127] suggested that the characteristic time-scale of the charge double layer mechanism could be calculated as;

$$\tau_{dl} = \delta_{CL}^2 aC\left(\frac{1}{k}+\frac{1}{\sigma}\right) \tag{4.10}$$

where most of the symbols are already defined in the Nomenclatures, the typical value for capacity, C = 0.2 Fm^{-2}, the specific area, a = 10^5 m^{-1}, the thickness of a catalyst layer is in the order of 10 microns, k = 10 Sm^{-1}, and σ = 5000 Sm^{-1} and these give the time-scale, τ_{dl} = 0.2 microseconds. This suggests that the charging/discharging (though they may differ) occur almost instantaneously and therefore this mechanism can be safely discarded like in most CFCD transient models.

Many studies, both experimental and numerical, have revealed that the time for membrane hydration/dehydration to take place is in the order of 10^1 to 10^2 seconds and the value can be theoretically estimated [127] as;

$$\tau_{PEM} = \frac{\rho\sigma_{PEM}\Delta\lambda}{EW}\times\frac{I}{2F} \tag{4.11}$$

For Nafion® family membranes, their membrane water content when fully-hydrated, $\Delta\lambda$ = 14. The thickness of a Nafion® 115 membrane = 127 microns and taking I = 1 Acm^{-2}, the characteristic time-scale is worked out as τ_{PEM} = 60 seconds. This is the dominating mechanism which influences the cell dynamics over a long period of time and its effect can only be seen if the simulation time is sufficiently large.

The time-scale of species transport in the porous region can be approximated by a simple expression [127] as;

$$\tau_k = \frac{\delta_{GDL}^2}{D_g^{eff}} \tag{4.12}$$

Typical GDL thickness is in the range of 300-500 microns and using the effective diffusion coefficient of a gas-phase species of 10^{-5}, thus the characteristic time-scale is approximately 0.01 seconds. This value is much smaller than τ_{PEM} but sufficiently large so that its effect can be seen and hence it cannot be ignored.

The time-step size, Δt, has to be smaller than τ_k if the dynamics of species transport is to be captured correctly. The value greater than τ_k will tend to smear out the species transport dynamics as if it does not exist which results in highly inaccurate solutions.

This poses a challenge to the choosing of time-step size, however. If the time-step size has to be smaller than τ_k whereas the total physical time has to be around 10^2 seconds to see the effect of membrane hydration/dehydration, a simple calculation suggests that, if Δt is kept constant at 10^{-2} seconds, at least $\frac{10^2}{10^{-2}} = 10\,000$ time steps are required to be solved for. The simulation time might be even prohibitive if the problems of interest involve larger and more complex cell geometries with large number of mesh elements.

Additionally, under certain circumstances when the change in operating condition is extreme, such as a step change in cell voltage, which occurs within a very tiny fraction of a second and will be accompanied by a drastically sharp increase/decrease in corresponding current density, a much smaller time-step size than 10^{-2} second may be needed. This is illustrated in Figure 4.33 where a voltage step-up was applied to the cell, the cell current responses were reported using different time-step sizes.

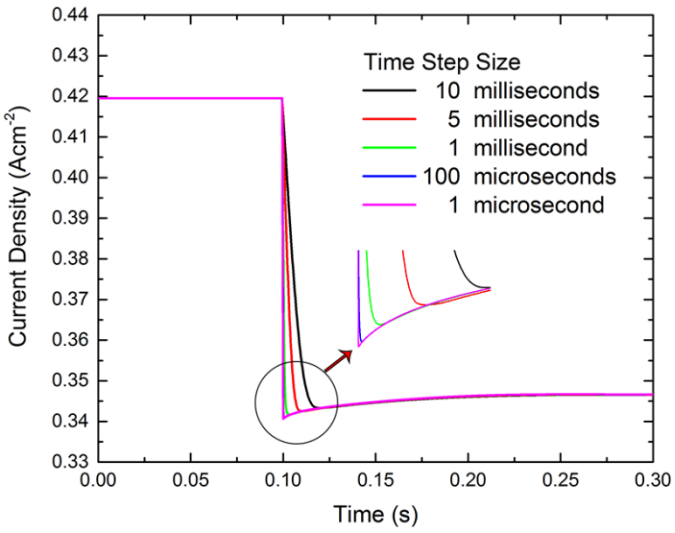

Figure 4.33 Effect of different time-step sizes on solution under a sudden change.

The cell responded with a sharp decrease in cell current density followed by a relaxation period where the current gradually adjusted to its new final value due to a slower species transport dynamics in the porous layer. It is obvious that even a time-step size as small as 5 milliseconds could not accurately capture the current response and hence a time-step size as small as 10 microseconds might be needed and a larger Δt can be used outside this sudden change window.

The best practise is to use a non-uniform time-step size – Δt will be varied as the calculation proceeds. A sufficiently small Δt will be used when the species transport dynamics is known to dominate and then Δt can be relaxed at later times analogous to locally refining the mesh in the areas where the flow-field undergoes sudden changes.

Finally, in addition to the meshing scheme proposed in the previous section, varying time-step sizes, ranging from 10^{-4}-10^{0} seconds unless stated otherwise, are used in all transient simulations in this thesis and it will be adjusted manually as the simulation proceeds. Although, this is a more tedious method as opposed to a more common Adaptive Time Stepping used in many transient studies, it offers more flexibility when judging convergence by using a more physically meaningful convergence criteria than just a truncation error with tolerance and this could sometimes be more effective and faster if used properly.

4.3 Model Validation

In order to ensure the validity of the developed model, it needs to be validated against experimental data obtained from the real operating cell. Since the main focus of this research is the transient operation of a PEM fuel cell, the model is validated in both steady and transient operating regimes and will be described separately. For the meshing process, the meshing strategy that is proposed in the preceding section is employed to demonstrate its universal applicability regardless of cell active areas or channel dimensions.

4.3.1 Steady-state Operation

The most common method to experimentally validate the fuel cell model is to obtain the so-called polarisation curve either galvanostatically or potentiostatically and compare it with the experimental data of a real operating cell. However, the thorough understanding of the transport phenomena inside the fuel cell requires that the local distribution of important performance-indicating variables such as current density or hydrogen and oxygen mass/mole fractions to be known and therefore a good numerical model should be able to predict these

with a good degree of accuracy in addition to an averaged current density over the entire active area of the cell in the form of polarisation curve.

As suggested in the study of Ju and Wang [149] that the polarisation curve alone is not sufficient to verify the validity of a numerical model. Using a numerical model developed by the group based on a Gore-Select 18 μm membrane under the same operating voltage of 0.70 Volts and 80 °C cell temperature, they demonstrated that the two totally different cases having fundamentally different assumptions and hence characteristics can predict exactly the same current density by manipulating only two parameters which are electronic resistance of catalyst layer and kinetic constant of oxygen reduction reaction. This emphasises the need to validate the simulated data against the local distribution data.

An experiment reported by Mench et al. [157] is selected as a reference since it allows for the polarisation data as well as local distribution of current density to be compared. This single cell is of practical size with an active area of 50 cm^2 and has an identical single-serpentine flow-field for both anode and cathode sides but they are aligned in a 180° so that the two flow-fields provide a counter-flow configuration for the reactant gases. The cell comprises of a Nafion 112 membrane sandwiched by the two ELAT anode and cathode GDLs with a catalyst loading of 0.5 mg cm^{-2} in the catalyst layers. The operating temperature and pressure are 80 °C and 1.5 atm (absolute), respectively. The anode gas is high-purity hydrogen and the cathode gas is commercial-grade air, both fully humidified. Only two cases corresponding to cathode stoichiometries of 1.5 and 2.25 Acm^{-2} equivalent are selected. The relatively high anode stoichiometry of 1.875 Acm^{-2} equivalent, however, is kept constant throughout the experiment in order to eliminate the mass transport limit at the anode side.

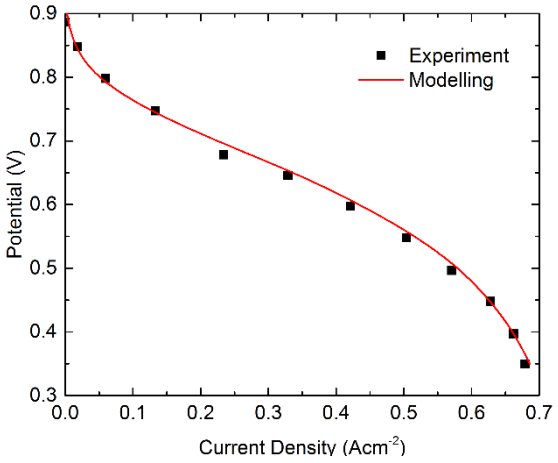

Figure 4.34 Comparison of polarisation curves for Case 1.

For the lower cathode gas flow rate case, its polarisation is compared with the predicted result from the present model is shown in Figure 4.34. It is clear that the predicted result agrees well with the experiment.

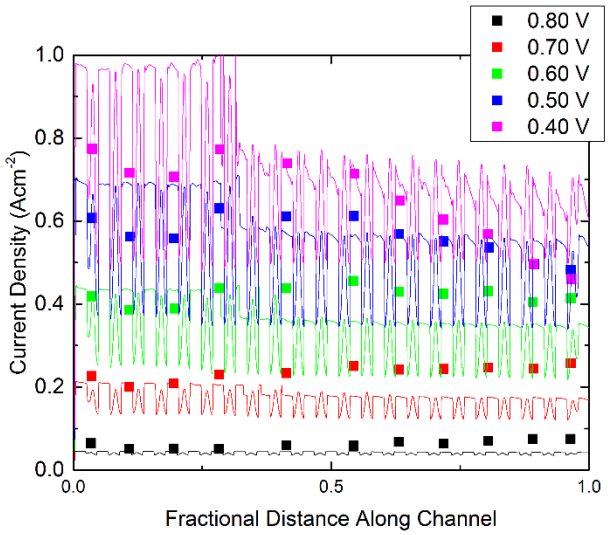

Figure 4.35 Local current density distribution along line at CL_{ca}/PEM interface which follows flow channel path for Case 1.

The comparison between the numerical and experimental data of local distribution of current density along the channel length is shown in Figure 4.35. The rapid-scan technique was employed in order to isolate the effect of cathode stoichiometry from other influencing factors. Nevertheless, the predicted results look rather oscillating showing the peaks and valleys which correspond to the current density at channel mid-length and channel-bend regions, respectively. This is clearly the benefit from a numerical approach where it can theoretically provide unlimited spatial resolution to any variable of interest. Though not quantitatively, however, the predicted results show that the current density decreases along the channel path and the non-uniformity of the current density becomes more pronounced at higher operating current.

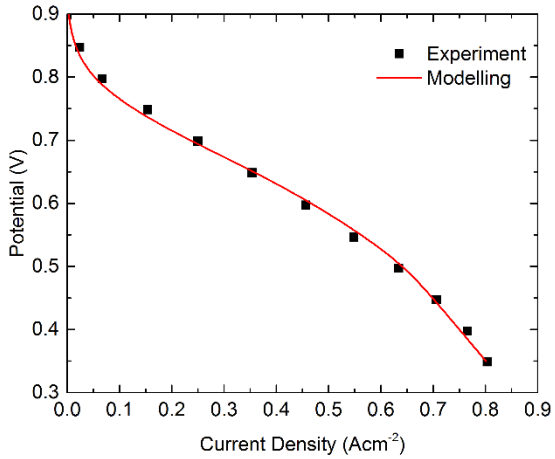

Figure 4.36 Comparison of polarisation curves for Case 2.

When the higher cathode stoichiometry of 2.25 Acm^{-2} equivalent is used, the model could also accurately predict the polarisation curve as shown in Figure 4.36. An interesting phenomenon of using a higher flow rate where the cell benefitted from a better water removal becomes evident which manifested itself as delayed occurrence of limiting current density compared to Figure 4.34 and this was also captured by the model.

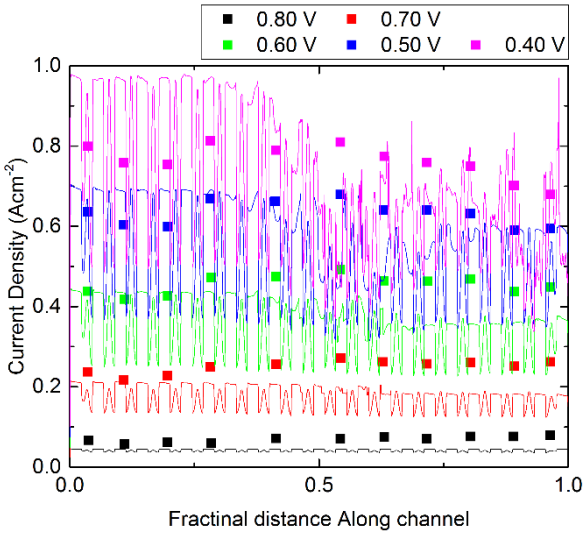

Figure 4.37 Local current density distribution along line at CL_{ca}/PEM interface which follows flow channel path for Case 2.

Similarly, the model agrees qualitatively well with the rapid-scan data as shown in Figure 4.37. It should be emphasised here that the rapid-scan technique does not allow sufficient time for flooding to occur and hence the cell cannot be said to be in a complete equilibrium as in the case for a numerical simulation where the fully converged solution

represents the final current density of a cell at a complete equilibrium taking into account all phenomena regardless of what time scale. The present PEM fuel cell model is said to be capable of predicting the performance of practical cell to a high level of accuracy. However, since the main focus of this research is the transience of a PEM fuel cell, the model should also prove its validity when predicting a performance of a cell under dynamic operations as presented in the next section.

4.3.2 Transient Operation

The main focus of this thesis is the transient response of an automotive cell, therefore the model must be validated dynamically to ensure the validity of the proposed model. The transient model was validated against a linear sweep voltammetry experiment by Yu et al. [159] and a voltage step change experiment by Wu [144].

Linear Sweep Voltammetry

In the first part, the model is validated against experimental data as reported by Yu et al. [159] where a 1 cm^2 single-serpentine cell was operated under partially dry reactant gases. A voltage sweep rate of 10 mVs^{-1} was used so that the entire sweep took 160 seconds to complete. A uniform time-step size of 5 milliseconds is used throughout the simulation which results in 32 000 time steps. Thirty inner iterations is used to ensure good convergence after each time step. The threshold, defined as the point of intersection of forwards and backwards current curves, due to the hysteresis of membrane water content was observed as seen in Figure 4.38. The polarisation obtained from a steady-state analysis is also superimposed on the graph to demonstrate that for any PEM fuel cell, the transient performance is completely different from its steady-state performance.

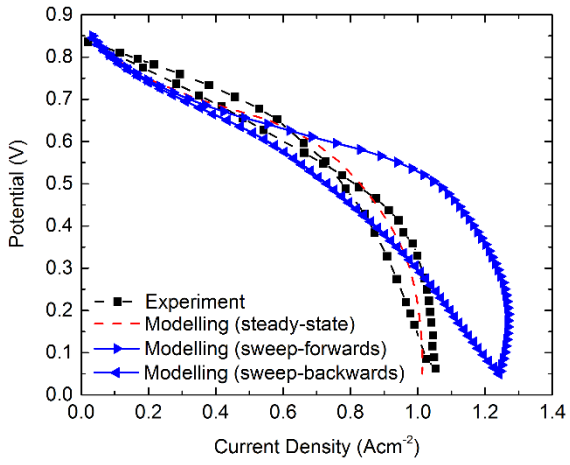

Figure 4.38 Comparison of linear sweep voltammetry and modelling results.

The predicted current does not agree very well with the experimental data mainly due to the lack of cell properties especially flow-field dimensions which is known to have a strong influence on cell performance. The most common channel dimensions of 1×1 mm^2 cross section and 1 mm rib width were assumed. Other model parameters were estimated from typical values from the literature since very little details are given.

The model shows that the forwards sweep current response are different from the backwards one which is a unique behaviour of a cell operated under a dynamic condition. Interestingly, the backwards sweep current is lower than the forwards one confirming the experiment which claimed that the cell was suffering from water flooding in the porous medium which is the result from higher water generation rate from the forwards sweep. Liquid water could not be removed from the porous regions in time compared to a much faster voltage sweep rate and therefore the current obtained was lower in the backwards sweep. The author believes that if more parameters were provided, the current curves would have been matched more closely. The transient model is tested further in the next section.

Voltage Step-change Experiment

Experimental data from Wu's work [144] was used to validate the transient model in this section. In his experiment, a step-change in voltage between 0.60V → 0.65V → 0.60V was applied to a 100 cm^2 cell. A single channel model was created to reduce the computation time while other model parameters were taken from his other publications.

The model required a parameter fitting on the reference exchange current densities in order to replicate the current response as shown in Figure 4.39. The reference exchange current densities for anode and cathode were decreased from 500 000 Am^{-2} and 0.65 Am^{-2} to 10 Am^{-2} and 0.029 Am^{-2}, respectively.

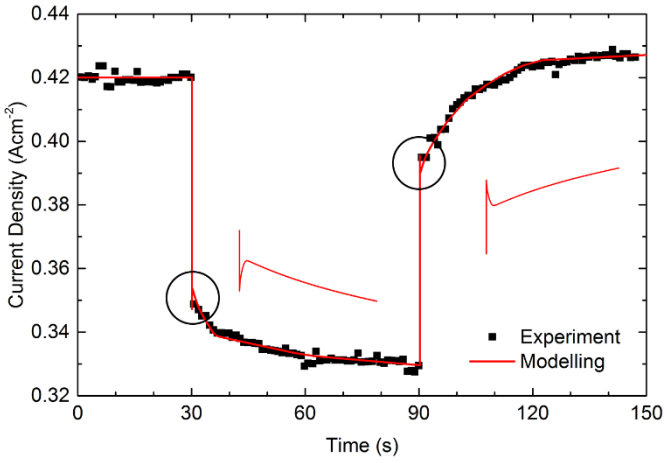

Figure 4.39 Transient model validation against experimental data given in Wu's work [144].

The model has proved to be able to predict results of practical cells under both steady-state and dynamic operations therefore it can be used to provide reliable results for PEM fuel cell analysis.

4.4 Chapter Summary

Essential numerical aspects of PEM fuel cell simulations have been addressed in detail. The choices for solvers and its corresponding settings were discussed together with criteria for judging convergence in order to ensure a fully converged solution.

A method for selecting the best meshing strategy was presented in a systematic manner before a conclusion was drawn to propose the mesh that has been used in every analyses presented in this thesis. The mesh was proved to be valid over a typical PEM fuel cell operating range. In addition, it has been shown to provide high degree of accuracy with considerable reduction in calculation time allowing the analyses to be done within a manageable time frame.

Finally, the model was validated against both steady-state and transient experiments. It was found that the model predicted results which agreed well with experimental data while important transient feature such as hysteresis and current over-/undershoot were also captured successfully. The model is said to give realistic predictions for practical PEM fuel cells and therefore eligible for PEM fuel cell analysis.

Chapter 5
Results: Single-channel Cell

"The purpose of computing is insight, not numbers."
Richard Hamming

The outcome of any experiment are obviously measurement readings. Normally, it is decided prior to commencing the experiment on which parameters are needed. Accordingly, certain measurements are then carried out first-hand by the experimenter. From this perspective, the experimenter is always reminded that such certain readings will be used to gain an insight into the problem which is the ultimate goal of any study regardless of the approach.

The output of a numerical model, on the other hand, is a very large array of numbers, some are relevant and useful to the analysis while some are not. Being buried in massively large amount of results that are solely numerics and therefore less intuitive, unexperienced users are prone to be misled and believe that these are what they are looking for, which are obviously not. Besides, a numerical model should be perceived as an alternative tool to investigate a problem of interest. Its numeric output does not signify that the analysis is completed therefore the hidden meaning it conveys must be extracted and interpreted.

Two types of computational domain were used in this thesis and a separate chapter has been designated to each of them. This chapter addresses the first of the two, a straight single-channel domain. Starting with the description of the dimensions, operating parameters used in the analysis are then presented. The responses of the cell under both steady-state and transient operations are discussed next followed by a summary. The discussion of a full-cell domain is organised in the same manner and given in Chapter 6.

5.1 Problem Description

5.1.1 Computational Domain

This numerical study was designed to be a comprehensive analysis aiming at categorising the current response of the cell to various voltage change patterns. It involved in a large number of sub-cases to be simulated and computation cost was therefore the most critical criterion in choosing the size of a computational domain. It has to be sufficiently large so that the results are physically meaningful and comparable to practical cells while keeping the number of cell elements to a minimum.

The author's experience in PEM fuel cell modelling suggests that an increase in computation time is not linearly proportional to an increase in the size of a computational domain, unfortunately. This means that it usually takes more than twice as long to obtain a converged solution for a problem that has its size doubled. In a larger computational domain, not only more cell elements are present, the existence of more flow channels and bends also adds complications to the flow-field which slows down the convergence rate and requires more iterations.

In contrast to the steady-state simulation, a transient run is much more time-consuming since the solution process has to march in the time-coordinate in addition to the three spatial coordinates. Moreover, because the solution of a previous time step is used as an initial condition for the next time step, a transient simulation is more convergence-sensitive and it is critical that convergence must be reached at each time step. A non-converged solution will result in a wrong solution for each subsequent time step which deviates more and more from the correct one until it eventually arrives at a completely wrong solution like a snowball effect.

Taking all these considerations into account, a single-channel domain was chosen. Its practicality has been proved by many numerical models in the literature. The straight channel ensures that the solution can converge easily within 30 iterations for each time step with minimal solver settings adjustment. The domain is shown in Figure 5.1 and its dimensions are given in Table 5.1. It should be noted that the mesh strategy developed in Chapter 4 is used for all simulations presented in this chapter whereas the initial and boundary conditions are the same as those presented in Chapter 3.

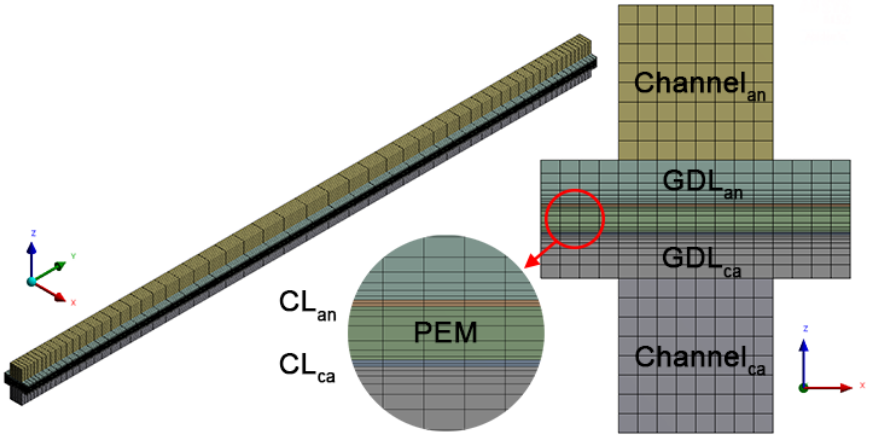

Figure 5.1 Straight single-channel computational domain.

Parameter	Value
Channel width (mm)	1*
Channel depth (mm)	1*
Rib width (mm)	1*
Channel length (mm)	50
Active area (cm^2)	1
GDLs thickness (Toray Carbon Paper, T-090), δ_{GDL} (μm) [147]	280
CLs thickness, δ_{CL} (μm)	20*
PEM thickness (Nafion 115), δ_{PEM} (μm) [160]	164
GDLs porosity [147]	0.78
CLs porosity	0.3*
Specific surface area of CLs (m^{-1}) [144]	2×10^7

Table 5.1 Dimensions of the single-channel computational domain (*typical value).

5.1.2 Operating Conditions

The main objective of the studies in this chapter is the response of the cell to various voltage change patterns. Therefore most operating parameters are fixed except the operating voltage. Assuming a very effective cooling system and high thermal conductivity of the current collectors, the cell is operated under a constant operating temperature and atmospheric pressure.

Membrane hydration is known to play an important role in the response of the cell under transient voltage changes. In order to investigate this, two different reactant gases humidity conditions were used which are referred as wet cell and dry cell hereafter. The anode gas was fully and partially humidified in the former and latter cases. There was no humidification of the cathode gas, however, in order to represent an ambient air as is usually the case for a vehicle, the relative humidity was kept at 50% for both cases.

Finally, to ensure that the response of the cell is solely caused by different voltage change patterns, the effect of mass transport limit was eliminated by using an excessive stoichiometric ratio for both reactant gases. The operating conditions for wet and dry cases are summarised in Table 5.2 and Table 5.3, respectively.

Parameter	Value
Operating pressure (atm)	1
Operating temperature (°C)	80
Saturation pressure at operating pressure (atm)	0.4669
Relative humidity of anode/cathode streams (%)	100/50
Stoichiometry of anode/cathode streams	3/2
Anode gas inlet velocity (ms^{-1})	0.845
Anode gas inlet Reynolds number	27.8
Hydrogen/water vapour mole fractions	0.533/0.467
Cathode gas inlet velocity (ms^{-1})	0.933
Cathode gas inlet Reynolds number	39.9
Oxygen/water vapour mole fractions	0.161/0.233
Open-circuit voltage, V_{oc} (V)	1.159

Table 5.2 Operating conditions for wet case.

Parameter	Value
Operating pressure (atm)	1
Operating temperature (°C)	80
Saturation pressure at operating pressure (atm)	0.4669
Relative humidity of anode/cathode streams (%)	50/50
Stoichiometry of anode/cathode streams	3/2
Anode gas inlet velocity (ms^{-1})	0.588
Anode gas inlet Reynolds number	11.7
Hydrogen/water vapour mole fractions	0.767/0.233
Cathode gas inlet velocity (ms^{-1})	0.933
Cathode gas inlet Reynolds number	39.9
Oxygen/water vapour mole fractions	0.161/0.233
Open-circuit voltage, V_{oc} (V)	1.165

Table 5.3 Operating conditions for dry case.

5.2 Steady-state Polarisation Curve

The polarisation curves under wet and dry operations can be seen in Figure 5.2 while the corresponding current densities are tabulated in Table 5.4. As expected, the current density

was higher when the cell was operated under the wet condition indicating that wet reactant gases improved cell performance.

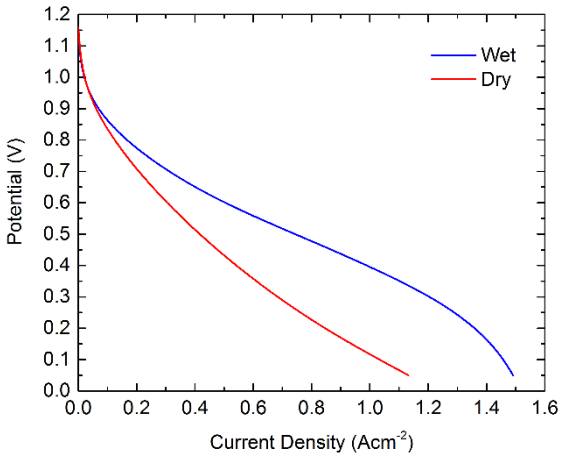

Figure 5.2 Steady-state polarisation curves of wet and dry cases.

Voltage (V)	Current Density, Wet (Acm^{-2})	Current Density, Dry (Acm^{-2})
1.16 (V_{OC})	0	0
1.10	0.004	0.004
1.05	0.009	0.010
1.00	0.019	0.021
0.95	0.038	0.037
0.90	0.068	0.060
0.85	0.110	0.090
0.80	0.166	0.124
0.75	0.232	0.164
0.70	0.310	0.207
0.65	0.400	0.254
0.60	0.502	0.305
0.55	0.618	0.359
0.50	0.744	0.416
0.45	0.869	0.477
0.40	0.990	0.542
0.35	1.104	0.610
0.30	1.207	0.683
0.25	1.292	0.762
0.20	1.362	0.846
0.15	1.416	0.936
0.10	1.459	1.033
0.05	1.491	1.133

Table 5.4 Steady-state current densities for wet and dry cells at different operating voltages.

Considering the performance in the ohmic region which is seen as a straight portion in both curves, the cell benefited from wet reactant gases because more water vapour was present in the gas stream. Membrane hydration is known to have a significant effect on the steady-state performance of a cell because more protons can be transported across the membrane to the active site on the cathode. Dry reactant gases, on the other hand, dried out the membrane causing high resistance to the flow of protons. The effect was too strong so that even higher hydrogen and oxygen concentrations in the dry anode and cathode streams, respectively, could not compensate this. The cell under a dry condition suffered from high proton resistivity and can be seen from a straight line being steeper.

This is confirmed by Figure 5.3 where the local distributions of oxygen and water vapour mass fractions, protonic conductivity, and current density at the CL_{ca}/PEM interface from both cells under an operating voltage of 0.50 V are reported. As can be seen from the figure that more oxygen are present at the active site for the dry case, it could not compensate a very low membrane protonic conductivity and hence the resulting averaged current densities are 0.744 Acm^{-2} and 0.416 Acm^{-2} for the wet and dry cases, respectively.

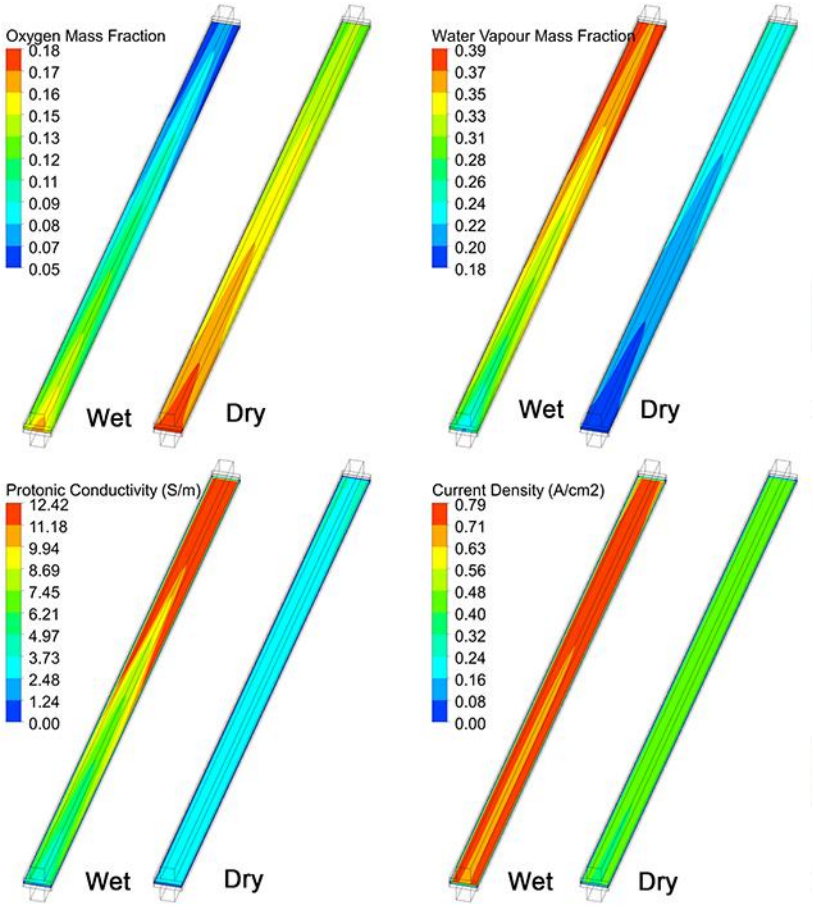

Figure 5.3 Local distribution of flow-field parameters at the CL_{ca}/PEM interface.

It is common to restrict the operation of an electronic device under a certain current or voltage range. Practical PEM fuel cells are normally operated between 0.50-0.80 V in order to avoid permanently damaging the membrane and this range is also used in most numerical studies though a voltage as low as 0.20 V can be seen in some studies. Interestingly, both cells did not suffer from mass transport limit even at the operating voltage of 0.30 V. The cells were therefore polarised further down to 0.05 V to see if the limiting current density would occur and it should be noted that this was done for demonstration purposes only. This shows the advantage of a numerical model over an experiment because a practical cell would fail to operate at this operating voltage.

Finally, the effect of mass transport limit started to occur in the wet cell and can be traced from 0.10 V. Though the existence of a limiting current density is not obvious, it is evident that the wet cell suffered from mass transport limit in this region which is seen as a sudden drop in cell potential as current density increases. This was not found in the dry cell, nonetheless. The contours of water saturation and oxygen mass fraction along the channel when the cell was operated at 0.05 V can be used as an indicator of water flooding as shown in Figure 5.4 and Figure 5.5, respectively. The length of the channel is scaled down by 90% for clarity in Figure 5.4. It is seen that much more liquid water are present in the wet cell, especially in the gas diffusion layer, while this region stays almost completely dry for the cell operated under dry reactant gases.

This liquid water, as shown in Figure 5.5, prevents oxygen from reaching the active site. The oxygen mass fraction of the wet cell almost reaches zero value indicating the presence of severe water flooding caused by excessive liquid water in the cathode GDL. It should be pointed out that even though the wet cell is suffering from severe water flooding, its membrane is better hydrate thus giving higher output current density than the dry cell.

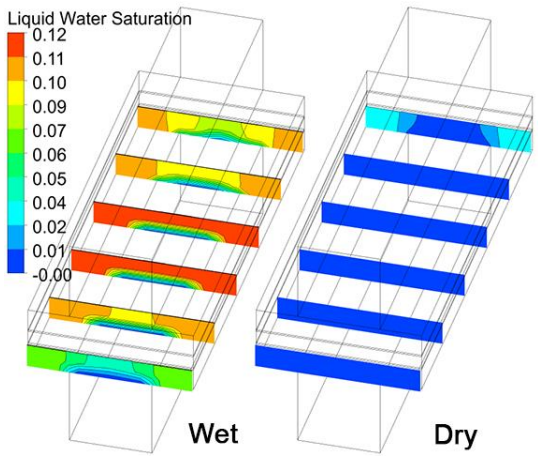

Figure 5.4 Liquid water saturation in cathode GDL and CL (length scaled to 10%).

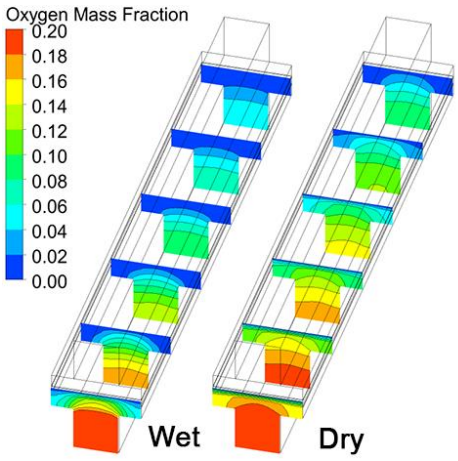

Figure 5.5 Oxygen mass fraction in cathode channel, GDL, and CL (length scaled to 25%).

In practical cells, the limiting current density occurs when the operating voltage drops to around 0.30 V regardless of cell size or flow-field configuration. The delayed occurrence of limiting current density of the two cells is attributable to its single-channel geometry. When a full-cell is operated at low voltage, the reaction becomes more intense and water is generated rapidly. The product water tends to accumulate in the regions where convective flow is weak such as the portions of GDL directly underneath the ribs or the sharp corners of the bend. In a single-channel geometry, however, these regions are much less and therefore the water flooding effect is less severe as is evident in Figure 5.2 that the limiting current density for the wet cell starts to appear at much lower voltage than 0.30 V.

Even though the main objective of the studies in this chapter is a transient response of a cell, these steady-state polarisation curves are important and therefore were determined first. Each point on the polarisation curve represents the equilibrium current density under a specific set of operating condition. They are used to normalise the current response curves of different cases in order to make a comparison between them possible.

5.3 Linear Voltage Sweep

According to Figure 4.32, the transience of membrane hydration extends over the range of 10^0-10^4 seconds, several minutes, or even hours. Clearly, this has a strong influence on the cell's transient response especially when a cell undergoes a change in operating voltage over a long period of time as is typically met in an electric vehicle. In order to investigate this prolonged effect, the operating voltage was swept back and forth between two terminal voltages, 0.8V↔0.3V, to compare the forwards and backwards current responses of the cells.

Three different sweep rates representing a slow, moderate, and fast sweep were used and the corresponding statistics for each case is reported in Table 5.5.

Case	Sweep Rate (mVs^{-1})	Forwards Sweep 0.8V→0.3V (s)	Backwards Sweep 0.3V→0.8V (s)	Total Swept Time (s)
Sweep 1	10	50	50	100
Sweep 2	50	10	10	20
Sweep 3	100	5	5	10

Table 5.5 Three sweep rates and corresponding statistics.

5.3.1 Effect of Sweep Rate

The time-history of current response for both cells under three sweep rates are given in Figure 5.6. The time-history of voltage sweep, shown as the black dashed line, is also superimposed in the graph so that the two current responses during forwards and backwards sweeps can be easily distinguished.

Both cells responded to all voltage sweeps in the same manner. When voltage was swept down, current gradually increased until it reached the maximum value corresponding to an instant when the lower terminal voltage was reach. In the backwards sweep, the current decreased back and almost reached the initial current density at the end of the sweep. Since the values of all current responses are very close and they behaved very similarly, the effect of voltage sweep rates cannot be explicitly seen from the figure. For this reason, transient polarisation curves of both cells as seen in Figure 5.7 are examined.

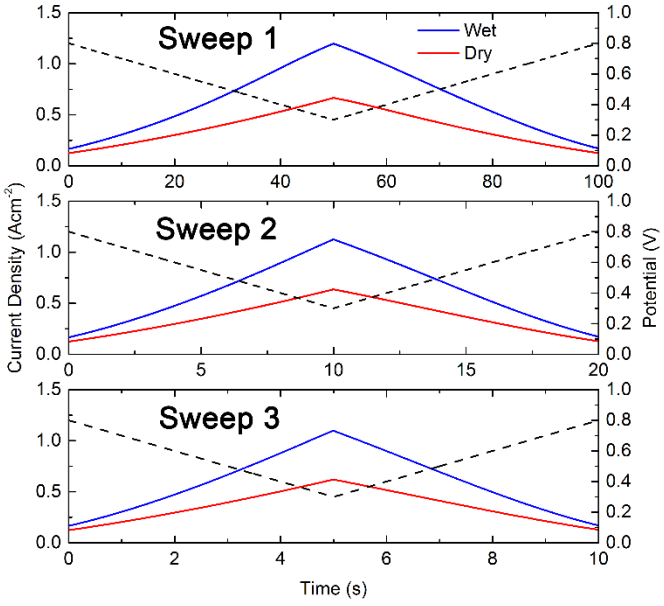

Figure 5.6 Time-history of current response to the three linear voltage sweep rates.

In Figure 5.7, the polarisation curve during a forwards sweep is plotted by a solid line whereas a backwards sweep is plotted by a dashed line for clarity. A black solid line is also inserted in the plot which denotes the steady-state polarisation curve. It is used as a reference upon which discussion and comparison are made.

It is evident that the hysteresis effect is present during the voltage sweep because forwards and backwards polarisation curves differ and neither of them coincides with the steady-state polarisation curve. This is expected since all transport mechanisms in the cell have now become time-dependent under a transient operation therefore the output current is strongly influenced by voltage change rate and initial conditions. This suggests that the output current of a PEM fuel cell operated under varying voltage can differ significantly from its steady-state current.

Moreover, the effect of voltage sweep rate becomes evident in this figure. It can be seen that the discrepancy between the transient and steady-state polarisation curves becomes larger as the sweep rate increases. Though forwards and backwards curves do not coincide in any case, both curves are very close to the steady-state polarisation curve in Sweep 1. As the sweep rate is increased in Sweep 2 and Sweep 3, the forwards and backwards curves deviate more and more from the steady-state curve. To demonstrate this, the current densities at 0.30 V for all cases are compared in Table 5.6.

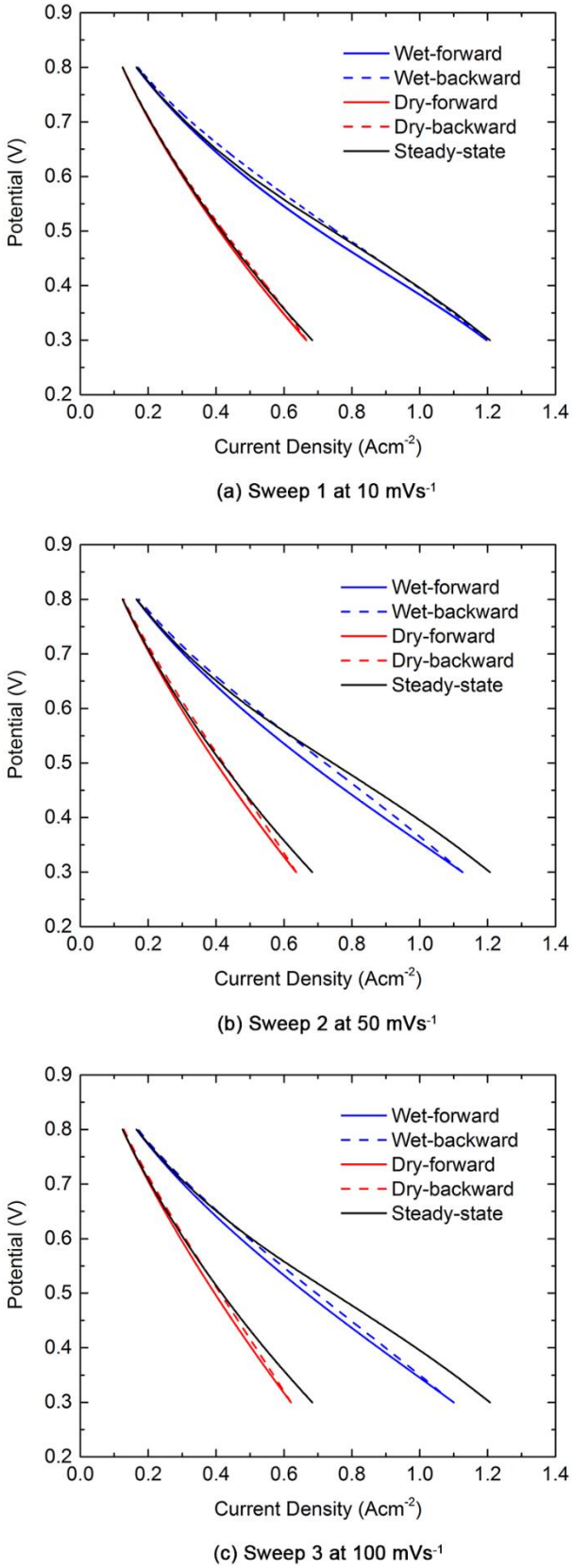

Figure 5.7 Transient polarisation curves under the three linear voltage sweep rates.

Cell	Sweep Case	Current Density (Acm^{-2})	Deviation (%)
Wet	Steady-state	1.207	-
	Sweep 1 @ 10 mVs^{-1}	1.197	-0.80%
	Sweep 2 @ 50 mVs^{-1}	1.126	-6.69%
	Sweep 3 @ 100 mVs^{-1}	1.100	-8.84%
Dry	Steady-state	0.683	-
	Sweep 1 @ 10 mVs^{-1}	0.666	-2.57%
	Sweep 2 @ 50 mVs^{-1}	0.636	-6.97%
	Sweep 3 @ 100 mVs^{-1}	0.621	-9.18%

Table 5.6 Current densities of both cells under the three voltage sweep rates when operating voltage reached 0.30 V.

This is attributable to the difference in time scales of membrane hydration transience and voltage sweep rate. At 0.30 V operating voltage, more water is generated due to a faster reaction kinetics. If a cell is operated under a steady-state operation, it can be said that the time allowed for membrane to soak up these product water and reach the equilibrium value is infinity. For a cell undergoing the slowest voltage sweep rate, however, the entire sweep test only took 100 seconds and therefore less water could be absorbed by the membrane due to a much slower membrane hydration mechanism. At this instant, the membrane was therefore less hydrated and less protonically conductive resulting in lower current density.

The effect of voltage sweep rate on the hysteresis of the cell can be explained by examining the plots in Figure 5.8 where averaged membrane water content on both sides of the membrane and the volume-averaged membrane protonic conductivity over the operating current range are shown. The same convention is used here where forwards and backwards curves are represented by the solid and dashed lines, respectively. During the forwards sweep, more current was being generated as the voltage was swept down. Water vapour was transported from anode to cathode due to electro-osmosis. This is seen as a decrease of the anode-side membrane water content and an increase of the cathode-side membrane water content. In addition to the electro-osmosis effect, more water is also generated due to higher reaction rate. As a consequence, the membrane becomes better hydrated as seen by an increase in protonic conductivity.

It should be noted that both cells perform better during a backwards sweep regardless of the sweep rate. During the backwards sweep, the cell operated at higher voltages and therefore less water is generated. This suggests that the membrane must undergo water desorption in order to adjust to its new and lower equilibrium membrane water content. However, the membrane water transport could not keep up with a faster voltage sweep,

therefore the membrane water content and in turn its protonic conductivity, remained high which resulted in higher current density than the forwards sweep.

Comparing Figure 5.8a, c, and e, the hysteresis effect becomes weaker as the sweep rate increases. A faster rate means less time for water transport mechanisms in the membrane to occur and therefore the difference between the forwards and backwards curves is reduced.

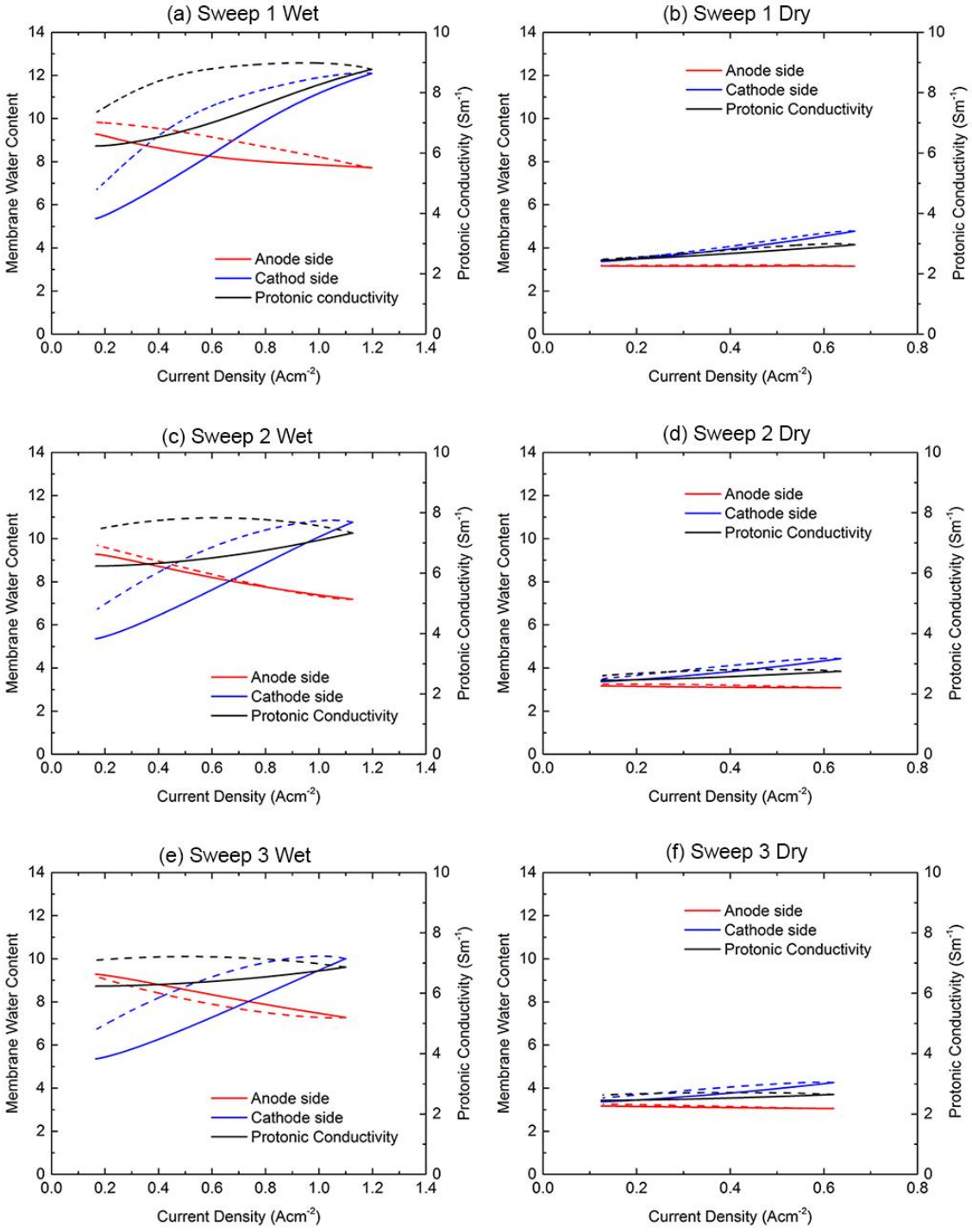

Figure 5.8 Membrane water content and protonic conductivity under the three sweep rates.

5.3.2 Effect of Reactant Gas Humidity

Under wet reactant gas streams the performance of the cell is improved considerably due to enhanced membrane hydration as is evident in Figure 5.2 and Figure 5.6-5.8. The current density from the wet cell is higher than the dry cell throughout its operating range in all cases.

The effect of gas relative humidity can be seen by comparing transient polarisation curves of the wet and dry cells in Figure 5.7a-c. For the dry cell, the difference between its forwards and backwards curves is smaller. This is even more evident in Figure 5.8. Due to relatively dry gas streams used in the dry cell, most regions remains dry with minimum water activity. The water generation rate stays low even the cell is polarised to as low as 0.30 V. There is not much water to be absorbed by the membrane therefore its hydration remains relatively constant. All curves in Figure 5.8b, d, and f demonstrate this as they stay relatively flat over the entire current range where the forwards and backwards curves almost coincide.

5.3.3 Concluding Remarks

Even though the current does not respond perfectly linearly to the voltage sweep, the cells respond well at all three sweep rates. It has been found that the deviation of current response from its steady-state value diminishes as the sweep rate decreases. If this is to be prevented totally, the sweep rate has to be infinitesimally slow approaching a steady-state operation. This is, however, impractical for an automotive fuel cell because it is subjected to varying power demand throughout its operation. Therefore it can be concluded that such current deviation from the steady-state value in an automotive PEM fuel cell under transient operations will always be present. It cannot be completely eliminated but can be weakened by a slower sweep rate or milder change in power demand.

It is interesting to say that the presence of current overshoot or undershoot which are well-known characteristics of an electronic device, including PEM fuel cells, under a transient operation have not been found in this analysis. Nonetheless, these behaviours only occur under a sufficiently fast voltage change which are investigated through a specifically designed series of analyses in the next sections.

5.4 Sinusoidal Voltage Sweep

In this analysis, a voltage was sinusoidally swept up and down around a certain value while current response was recorded and investigated in a similar manner to the linear voltage sweep. Instead of a single upwards followed by a downwards path, the voltage excitation was repeatedly oscillating between two values known as lower and upper margins. This was to imitate a vehicle under an urban operation where it has to intermittently accelerate and decelerate between traffic lights or in a traffic congestion during the rush hour. The current response can be used to investigate the repeatability and reproducibility of a cell whether it would be able to successfully follow this on-and-off power demand throughout its operation.

Since the ideal operating voltage range of a typical cell is between 0.8 V and 0.6 V, the voltage was swept back and forth between these two margins and the initial voltage of 0.7 V was chosen. This sine-wave excitation voltage is expressed mathematically as;

$$V_{cell} = 0.7 + 0.1\sin(2\pi f t) \tag{5.1}$$

Where V_{cell} is the operating voltage (Volt) applied at the cathode terminal. The frequency, f, is in Hertz and the time, t, is in seconds. In this analysis, three frequencies were used – 10, 1, and 0.1 Hz. As an example, the excitation voltage of 1 Hz is given in Figure 5.9 whereas the corresponding statistical detail of each case is summarised in Table 5.7.

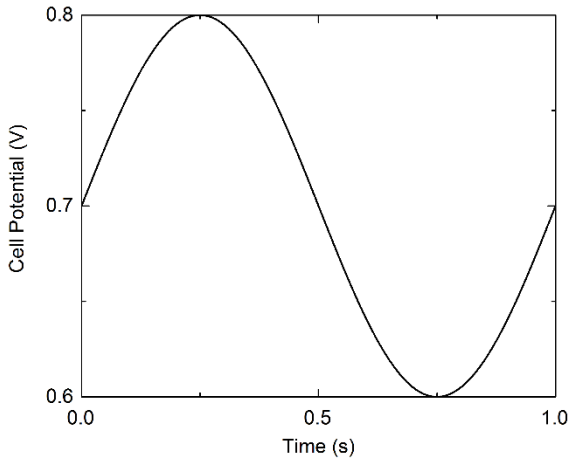

Figure 5.9 Example of the 1-Hertz sinusoidal excitation voltage.

Case	Frequency (Hz)	Time to Complete 1 Wave (s)	Averaged Voltage Change Rate, (Vs^{-1}) (0.7→0.8→0.7→0.6→0.7; ΔV = 0.40 V)
Sine 1	10.0	0.1	4.00
Sine 2	1.0	1.0	0.40
Sine 3	0.1	10.0	0.04

Table 5.7 Three sinusoidal sweep rates and corresponding statistics.

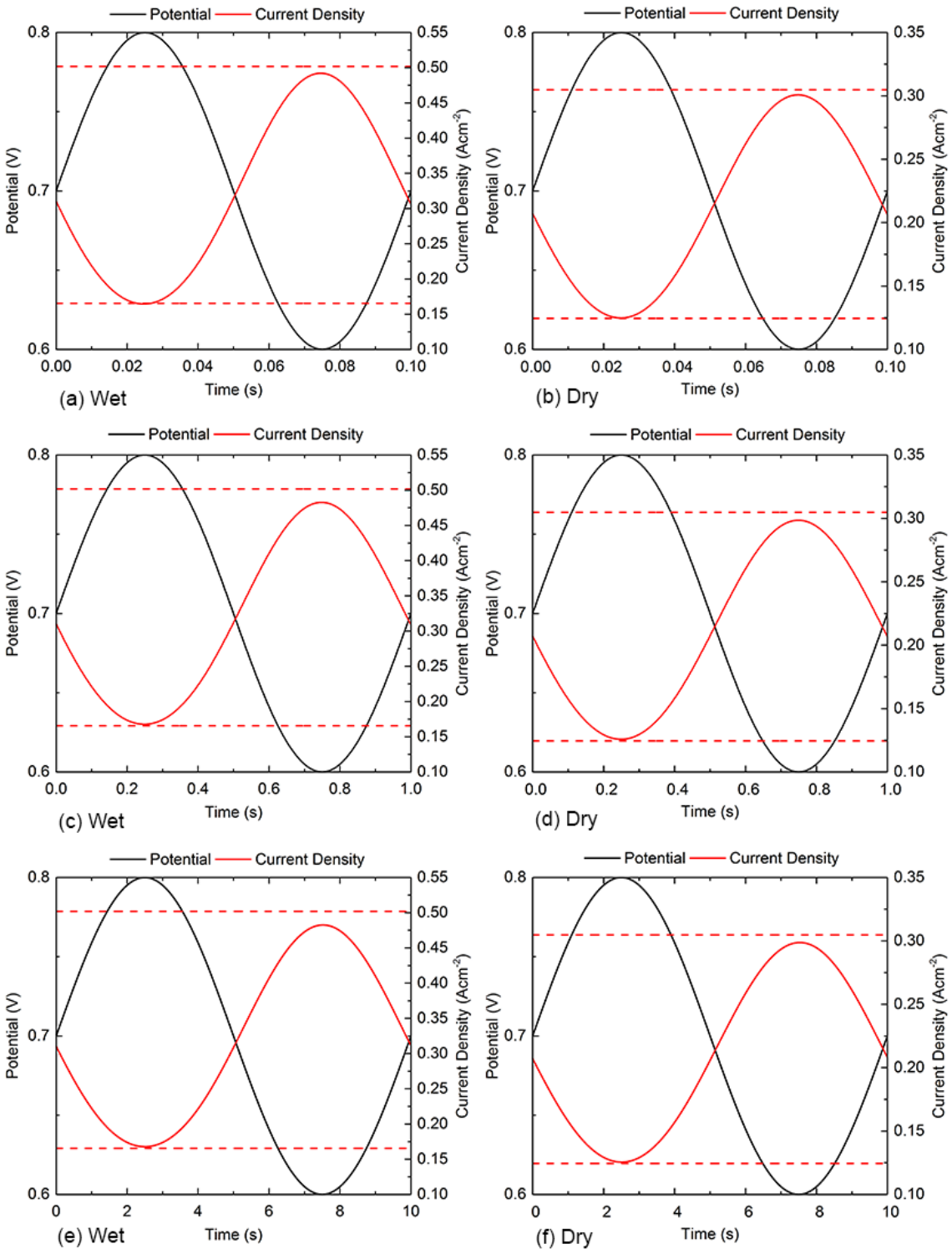

Figure 5.10 Current responses of wet (left) and dry (right) cells to sinusoidal voltage sweep under three excitation frequencies of 10 (top), 1 (middle), and 0.1 (bottom) Hz.

5.4.1 Effect of Excitation Frequency

The current responses of both wet and dry cells to a voltage sweep are present in Figure 5.10 where the excitation voltage, denoted by a black solid line, is also given as a reference. In order for the hysteresis effect to become evident and easy comparison between cases with different excitation frequencies, two red dashed lines are plotted to represent the steady-state current densities at the two margins. These current densities are 0.161 and 0.502 Acm^{-2}, respectively, for the wet cell and 0.124 and 0.305 Acm^{-2}, respectively, for the dry cell.

It can be seen from the figure that the current responds to the voltage in the form of a sinewave curve. A close inspection at the peak and trough on the current response curve reveals that they occur at an instant when the voltage reaches its lower and upper margins, respectively, suggesting that the current response curve is shifted by the exact 180°.

For a comparison between different frequencies used, the three response curves are plotted against a common normalised time axis as shown in Figure 5.11. The three curves almost coincide and the difference between them can hardly be detected except at their peak currents. Nevertheless, none of these peaks coincides with the steady-state value which indicates there also existed a weak but noticeable hysteresis effect under this sinusoidal voltage change that prevents the peak current from reaching its equilibrium value. On the other hand, the troughs are much closer to the steady-state value in all cases.

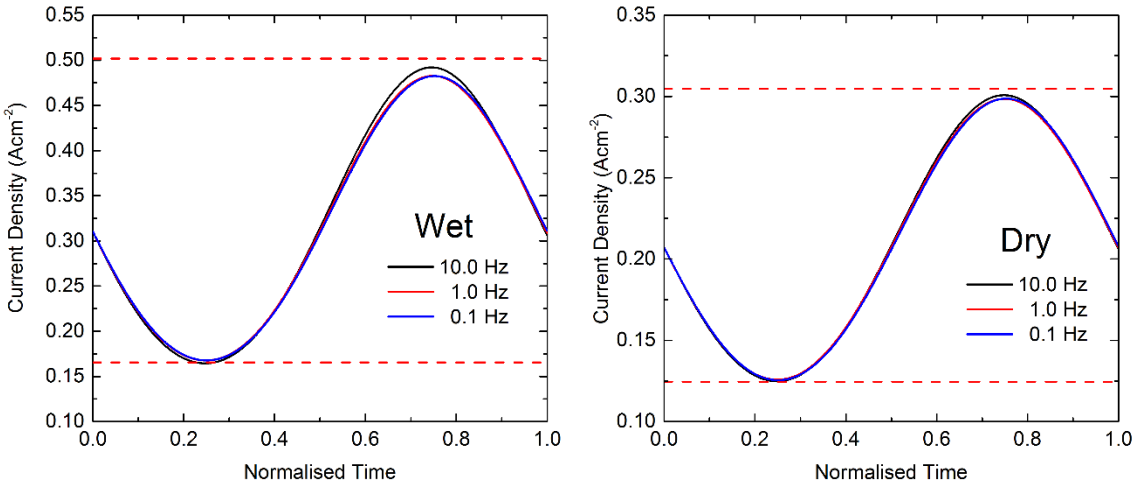

Figure 5.11 Comparison between three frequencies used for wet (left) and dry (right) cells.

This is most likely caused by the discrepancy between the characteristic time scales of various mechanisms in the cell to reach the equilibrium state. Since the local overpotential responses very fast to the voltage and Ohm's law is assumed to take place instantaneously, the current rises promptly with no lag. The temperature and protonic conductivity, on the other hand, take much longer to adjust to the new equilibrium therefore restricting the current peaks and troughs from coinciding with their equilibrium values.

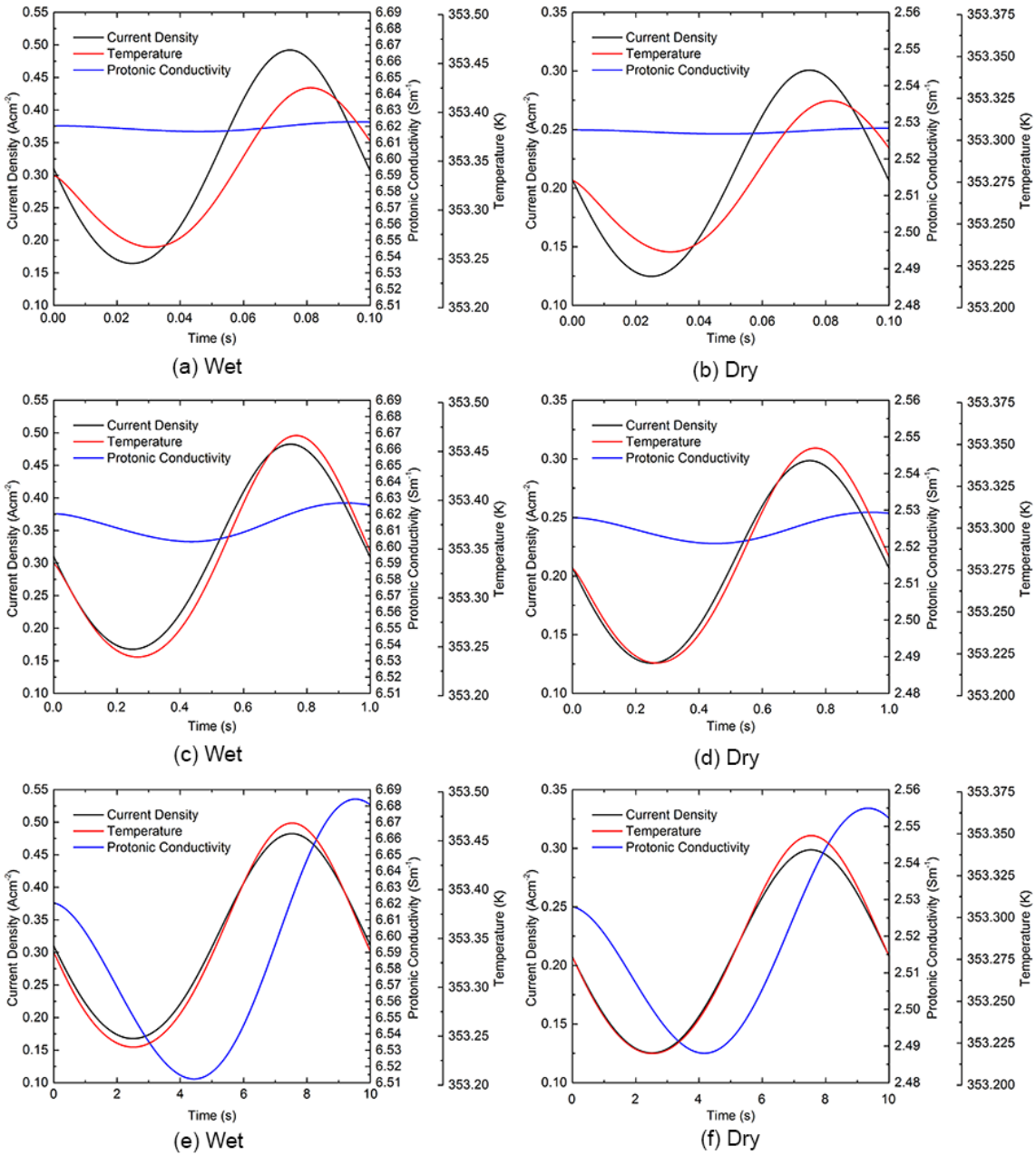

Figure 5.12 Time histories of current density, cathode CL temperature, and membrane protonic conductivity of wet (left) and dry (right) cell under sinusoidal voltage sweep with three excitation frequencies of 10 (top), 1 (middle), and 0.1 (bottom) Hz.

The above explanation can be confirmed by examining the time history of volume-averaged temperature in the cathode catalyst layer and membrane protonic conductivity during the sinusoidal sweep as shown in Figure 5.12. The phase shifts between the three variables can be seen explicitly. During a high excitation frequency of 10 Hz, the voltage and consequently overpotential are changing too fast. It only takes 0.10 seconds for the whole sweep to complete which means that the sluggish membrane hydration process could not absorb or desorb much water during this tiny fraction of a second. Therefore its membrane water content and in turn protonic conductivity remain effectively constant over time as seen in Figure 5.12a-b. The temperature, however, is much faster than membrane hydration process and therefore it lags the current by a much smaller degree.

Once the frequency was decreased to 1 Hz, the sweep process took one second to complete. Clearly, this was ten times longer in contrast to the 10 Hz-sweep and thus more time was allowed for membrane water absorption/desorption. As a result, the peak and trough on the protonic conductivity curves in Figure 5.12c-d became apparent. The phase lag of temperature improved considerably as it became almost in phase with the current density with only a small degree phase shift under this frequency.

Interestingly, at 0.1 Hz, the phase shift between current and temperature almost disappear indicating that the characteristics time scale for the temperature field is in the range of 10^0-10^1 seconds, which is consistent to the diagram in Figure 4.32. Additionally, it suggests that if the excitation frequency is reduced further, the phase lag between protonic conductivity and current and temperature can also be reduced and eventually eliminated hence revealing its characteristics time scale which is much larger than ten seconds.

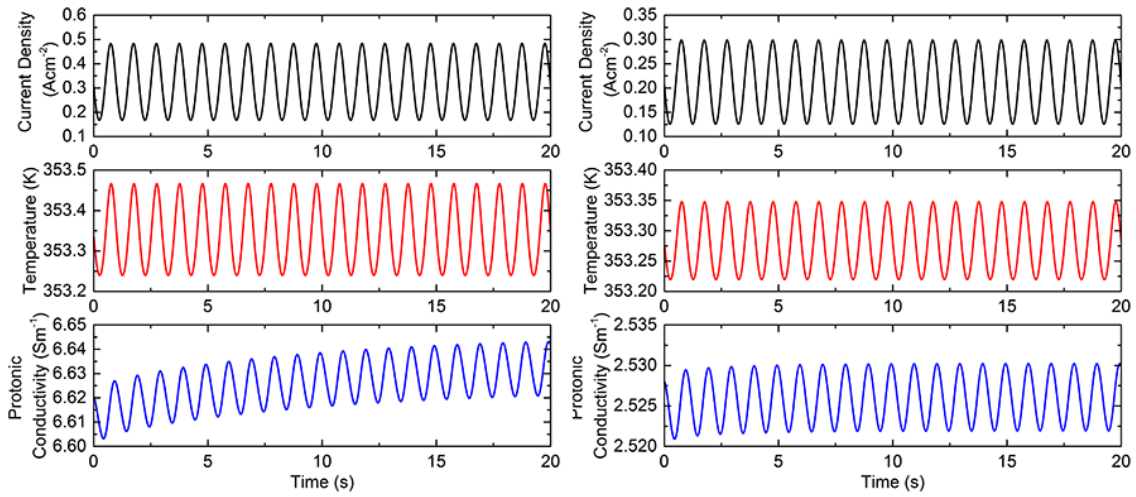

Figure 5.13 Extended response curves of current density, volume-averaged cathode catalyst temperature, and volume-averaged membrane protonic conductivity of wet (left) and dry (right) cells under 1 Hz excitation frequency.

To investigate the repeatability of the current response whether it would be able to follow this on-and-off power demand throughout its operation in a consistent manner, the physical time for the cases Sine 2 wet and dry cell with an excitation frequency of 1 Hz was extended to twenty seconds. The current density, averaged temperature at cathode catalyst, and the membrane protonic conductivity for the wet and dry cells are given in Figure 5.13.

The current was able to follow to the voltage change pattern satisfactorily while maintaining its peak and trough values over a long period of time in both cells hence proving its repeatability. The temperature had no difficulty in reaching its equilibrium under this frequency as discussed previously. Even though the membrane was losing and gaining water periodically according to the voltage change pattern, the net effect was the gain of water content in the membrane which was reflected by an improvement of membrane protonic conductivity over time as seen in the figure.

5.4.2 Concluding Remarks

In this analysis, the current response under a sinusoidal voltage sweep and its repeatability have been investigated. It is found that the current responds satisfactorily to the applied voltage change pattern in terms of the time response and its magnitude. Though hysteresis has been found, its effect is weak and only detectable at the peak currents.

Using various frequencies, the characteristics time scale of a certain transient mechanism can be extracted and it is found that this is in the range of 10^0-10^1 seconds for cell temperature which is consistent to the diagram in Figure 4.32. It can be said that if the frequency is reduced further, the characteristics time scale of the protonic conductivity can be determined. Finally, the current response is highly repeatable as it is able to withhold its response pattern and magnitude throughout a long operation.

5.5 Linear Voltage Change

In this analysis, the voltage was decreased and increased linearly on both wet and dry cells under a fixed rate of 1 Vs^{-1}. They will be referred to as the downwards and upwards path, respectively, in the discussion. This fixed rate was chosen to replicate a relatively fast change in power demand that a vehicle can experience such as during acceleration or deceleration.

Three voltage change amplitudes as defined in Equation (5.2), were applied. These were ±0.10 V, ±0.20 V, and ±0.50 V. The negative sign indicates a down path where the final voltage is lower than initial voltage and vice versa.

$$\Delta V = V_{final} - V_{initial} \tag{5.2}$$

In addition, even under the same change amplitude, different values of initial and final voltages between 0.3V↔0.8V, inclusive, were used including those voltages that are outside the normal operating range to make this analysis comprehensive.

5.5.1 The Downwards Path

The main interest for this analysis was current response during the presence of voltage change which only took place within the first half of the first second, the physical time for each simulation case was decided to be five seconds in order to keep computational time to a minimum. Within this duration, the current was expected to approach its new equilibrium value like those given in Table 5.4 and no significant change in either magnitude or behaviour should occur beyond this point. Hence we may assume, without loss of generality, that the first five-second current response is sufficient for the investigation and generalisation of the cell response and any response later than five seconds can be safely discarded.

Before proceeding, the labelling convention and details of each simulation case which is used throughout the analysis is introduced. Table 5.8 shows these information together with the current density at time = 5 seconds grouped by their excitation amplitude. The results show that all currents fall well within the 10% lower margin of the equilibrium current which proves the above assumption.

Amplitude	Path (V)	Time (s)	Label	i_{wet} (Acm^{-2})	Deviation (%)	i_{dry} (Acm^{-2})	Deviation (%)
-0.10 V	0.4→0.3	0.1	Down-A	1.200	-0.56%	0.670	-1.96%
	0.5→0.4	0.1	Down-B	0.974	-1.65%	0.534	-1.44%
	0.6→0.5	0.1	Down-C	0.716	-3.76%	0.412	-1.01%
	0.7→0.6	0.1	Down-D	0.489	-2.56%	0.302	-0.91%
	0.8→0.7	0.1	Down-E	0.306	-1.43%	0.206	-0.58%
-0.20 V	0.5→0.3	0.2	Down-F	1.190	-1.39%	0.660	-3.43%
	0.6→0.4	0.2	Down-G	0.947	-4.37%	0.528	-2.54%
	0.7→0.5	0.2	Down-H	0.697	-6.31%	0.408	-1.97%
	0.8→0.6	0.2	Down-I	0.481	-4.15%	0.301	-1.24%
-0.50 V	0.8→0.3	0.5	Down-J	1.130	-6.36%	0.641	-6.21%

Table 5.8 Labelling convention used in the downwards path analysis and current density after five seconds.

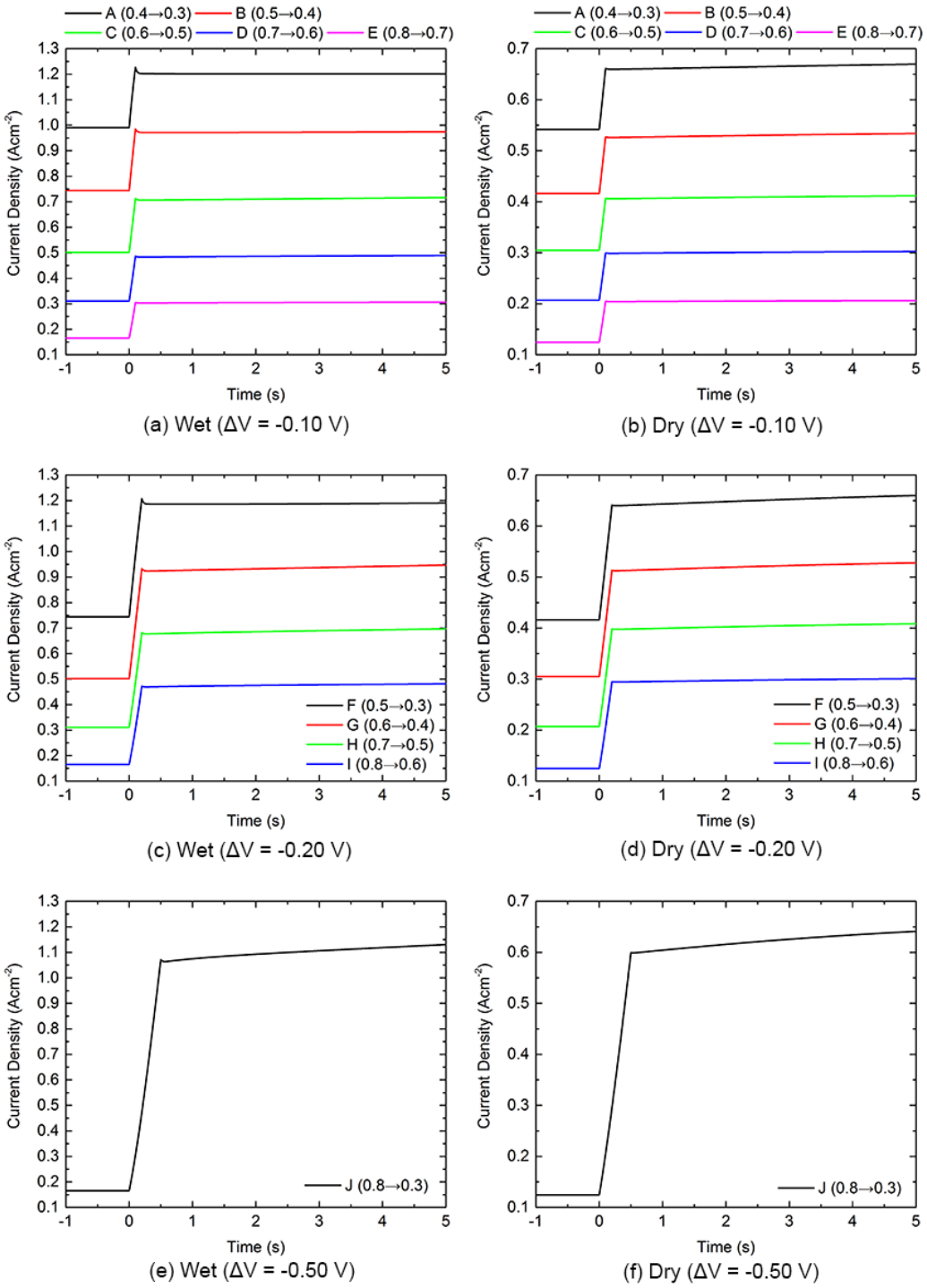

Figure 5.14 Current responses under the 1 Vs^{-1} linear voltage decrease.

The current responses to a downwards voltage change for all cases are shown in Figure **5.14**. It can be seen that the current does not reach the equilibrium current in the first place. In fact, it rises sharply up to a certain point and then increase gradually to the equilibrium value over a much longer period of time. This is due to the discrepancy in time scales among various transport mechanisms while adjusting to a new equilibrium state.

Ideally, if all transport mechanisms were independent of time in which they occurred instantaneously, at the time when the final voltage was reached, all parameters would have reached its equilibrium and the current would coincide with the equilibrium value. In reality, unfortunately, different mechanisms take a different time to reach the new equilibrium.

Generally, the path to the equilibrium current of these curves can be thought of as being composed of three distinct sub-regions. These are the primary response, followed by the relaxation period, and finally the secondary response. The primary response is responsible for an initial rise of current density seen in the curve which occur immediately at the start of the downwards voltage change process. As the voltage is decreased, this causes a local overpotential to increase and in turn alleviates the reaction kinetics. The surplus supplies of reactant species at the reactive sites, referred to as species reservoirs, that are originally available due to a higher initial voltage are then consumed promptly resulting in a sharp increase in current. Hence, the rise of current during this primary response can be mainly attributable to the increased overpotential and the availability of the species reservoirs.

A close inspection on each current response curve reveals that during the rise, the current increases almost linearly and reaches a maximum at the end of the voltage process marking the end of the primary response. These maxima are lower than their corresponding equilibrium value except that in Case A wet cell.

At this instant, it is evident that there must be a mechanism that prevents these maxima from reaching this equilibrium value. The overpotential changes almost instantaneously with voltage thus it reaches the equilibrium value almost immediately after the final voltage has been reached. The membrane hydration, on the other hand, is achieved through water absorption/desorption which is a much slower process. Since the voltage change only occurs within a fraction of a second, the membrane hydration and its protonic conductivity could not improve much therefore remained effectively constant at its initial value throughout this period. Compared to the equilibrium state, the protonic conductivity at this instant is lower therefore restricting the current from reaching the equilibrium value.

This can be demonstrated by examining the evolution of cathode overpotential, protonic conductivity, and oxygen mass fraction of Case A wet cell, for example, over time as given in Figure **5.15**. Since the change rate is large, it only takes place within the first 0.10 seconds to decrease from 0.40 V down to 0.30 V. From the figure, the only parameter that can follow the voltage and reach its equilibrium value at the same time when the final voltage of 0.30 V is reached is the cathode overpotential. It can be seen that after 0.10 seconds, the cathode overpotential, shown as a negative value by definition, barely changes.

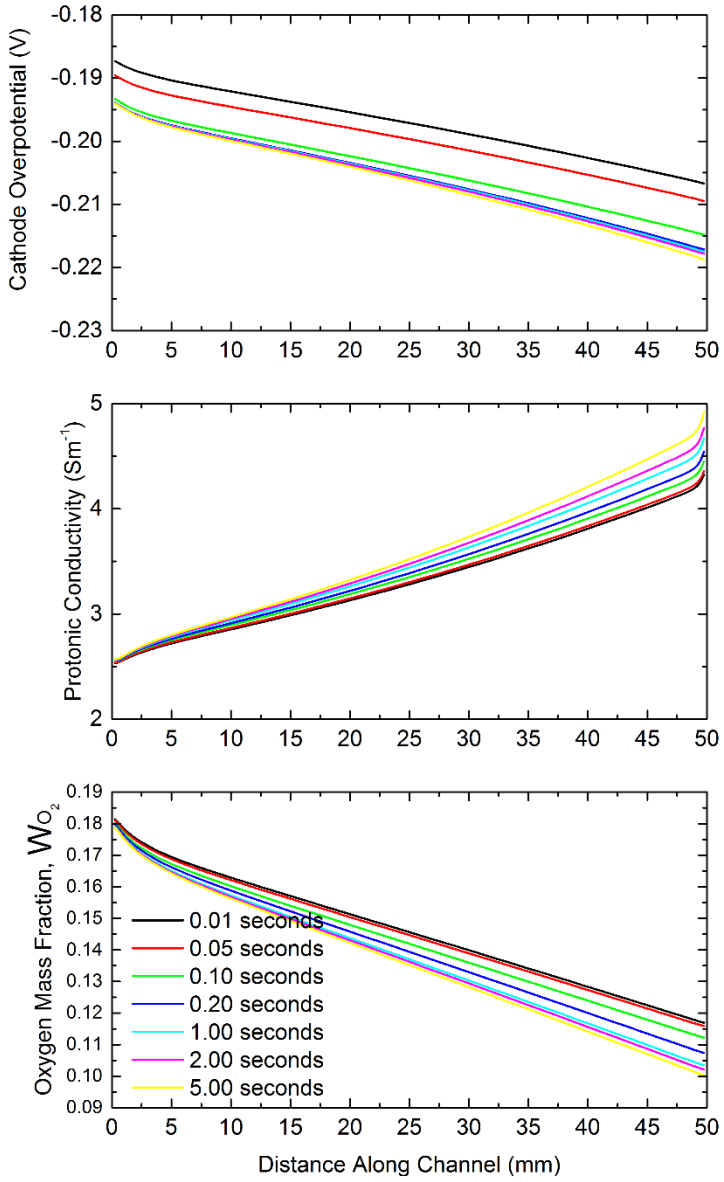

Figure 5.15 Cathode overpotential, membrane protonic conductivity, and oxygen mass fraction profile for Case A of wet cell on CL_{ca}/PEM interface at various instants.

The transport of oxygen to the reactive site is achieved mainly by diffusion which is slower and therefore it takes approximately one second for oxygen to reach the equilibrium. As discussed previously in Chapter 4, membrane hydration is one of the slowest mechanisms in a PEM fuel cell that spans over several minutes. The membrane productivity therefore keeps evolving through time and does not reach an equilibrium even after five seconds as is evident in the figure. Both numerical and experimental studies in the literature suggest that this would take place over a much longer period of time.

Immediately after the maximum current has been reached at the end of the primary response, there exists a relaxation period when the current relaxes and declines sharply forming a current spike. The relaxation of current in this region is the net effect between the depleting reactant reservoirs which tends to decrease the current and enhanced membrane hydration which tends to increase the current. Since the reaction kinetics is already at its highest value, the incoming species fluxes could not keep up with the increased oxygen consumption rate. This gradually depletes the oxygen reserve in the cathode catalyst layer. Because the reaction kinetics also depends on the reactant species concentration at the reactive site, the current generation is reduced.

The tendency to increase the current due to better membrane hydration, on the other hand, is more pronounced in this relaxation period despite the fact that it is neglected in the primary response. This is because the response time of membrane hydration is closer to the oxygen diffusion compared to that of the cathode overpotential which occur almost instantaneously. During the first stage of the relaxation period, oxygen depletes faster therefore it overwhelms the effect of better membrane hydration and resulted in a sharp decline of current density.

The oxygen reservoir continues to adjust to the new equilibrium state as time progresses until an instant when the incoming reactant fluxes could balance the consumption rates, the current drop then decelerates and levels off. At this point, all mechanisms have effectively reached equilibrium except the membrane hydration mechanism. The membrane protonic conductivity overpowers the oxygen diffusion and is in charge of any change in current density after this. Since protonic conductivity is still slowly improving, the current then gradually increases again. At the point where this second rise occurs, a current trough is formed marking the starting point of the secondary response. During this secondary response, which extends over a long period of time, the current would continue to rise and eventually approach the new equilibrium value.

The relationship between protonic conductivity and current density in the secondary response can be seen by examining their time histories over an extended period. The averaged membrane protonic conductivity and current density for Cases A, G, and J of the wet cell are shown in Figure **5.16**. These cases are specifically chosen for a clear comparison. Clearly, these two parameters are closely coupled and therefore behaved similarly. For Case A, its protonic conductivity does not vary much hence its secondary current remains relatively stable. On the other hand, when the change in protonic conductivity is moderate and drastic, the current increases moderately and drastically in Cases G and J, respectively.

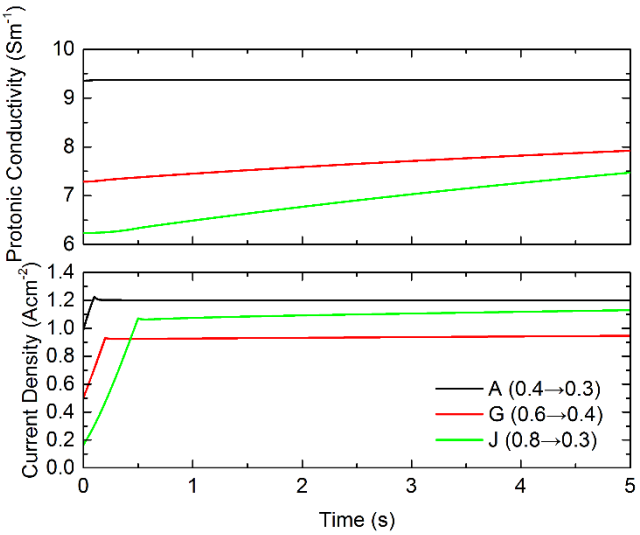

Figure 5.16 Time-history of protonic conductivity and current density for Cases A, G, and J of wet cell.

Clearly, the secondary response is relatively simple and predictable without any undesirable irregularities. Therefore it is said to be of less concern in a system design perspective and discarded henceforth. The primary response, on the other hand, occurs during the voltage change which is the period of interest and its final magnitude is a result of a complex interplay between different transient mechanisms which is more difficult to predict and classified. Additionally, the change in voltage is dramatic over a short period of time therefore the presence of current spikes can be seen in the response curve which requires special attention. Nevertheless, it is not obvious whether these current spikes will have a negative effect on the cell. In order to discuss this, a special treatment is applied to these current response curves as described in the next section.

Effect of Initial Voltage

As can be seen from Figure 5.14, the initial and final voltages are different in each case therefore the equilibrium currents are also different which makes comparison difficult. Nevertheless, the main interests in this analysis are the primary response and its spikes, the absolute magnitude of equilibrium current is therefore irrelevant. Depending on the final voltage, the corresponding steady-state current as given in Table 5.4 is used to normalise its current response curve. In order to make the curves, especially in the region where current spikes occurs, easily distinguishable, each curve is shifted by 0.50 seconds along the time axis from the previous curve. It should be reminded that the physical time is five seconds for all cases. The modified current responses are shown through Figure 5.17-5.19.

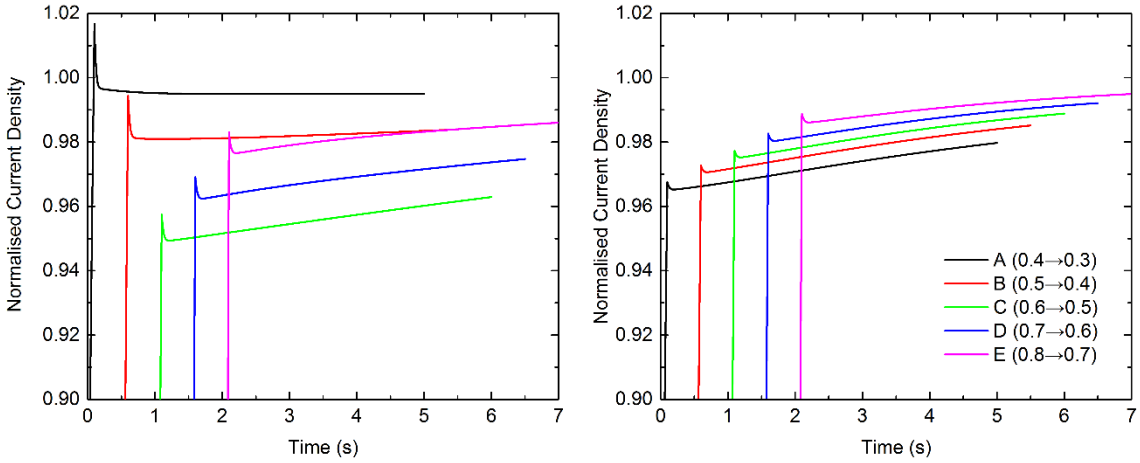

Figure 5.17 Normalised current response of wet (left) and dry (right) cells (ΔV = -0.10 V).

By normalising the current responses, any current spike that is invisible in Figure 5.14 is now revealed. It suggests that, under the present voltage change rate of 1 Vs^{-1}, current spike is present in all cases regardless of the change amplitude, initial voltage, or reactant streams humidification. The current overshoot is defined in Equation (4.12) as the difference between the peak current and new equilibrium current;

$$i_{overshoot} = i_{peak} - i_{equilibrium} \tag{5.3}$$

With this definition, the current overshoot is distinguished from current spikes. Clearly, current overshoot is undesirable since the current at that instant is outside the prescribed operating range. In an uncontrolled cell, an overly excessive overshoot can cause local hotspots which permanently damage the membrane.

Subsequently, the normalised current density greater than unity indicates a current overshoot as is seen in Case A of the wet cell in Figure 5.17. However, the magnitude of this current overshoot is close to unity therefore its effect on the cell can be neglected. In all other cases, their current spikes do not exceed the corresponding final value therefore are not considered as current overshoots.

Considering the response during the relaxation period of all curves given in Figure 5.17-5.19, two distinct types of behaviour can be identified. The first-type behaviour is seen in Cases A and B wet cell. Even though their current spikes are very close to unity, their relaxation time is large. After a sharp drop, the current continues to level off very slowly which makes it difficult to identify the current trough which is the starting point of the secondary response. Throughout the rest of the simulation time, the current remains relatively constant for a long period before the secondary response takes place in Case B wet cell. However, this cannot be seen in Case A wet cell where the current is still decreasing

very slowly therefore its current trough cannot be seen in the first five seconds. The remaining cases, Cases C, D, and E wet cell and all cases of the dry cell, fall into the second category. They have a much shorter relaxation time and the current trough can be easily identified despite the fact that their current spikes are much lower than unity.

Figure 5.18 and Figure 5.19 show the normalised responses under the change amplitudes of -0.20 and -0.50 V, respectively. Clearly, all curves fall into the two categories described above. It can be seen that Case F wet cell is the only case that falls into the first category while all other cases fall into the second category.

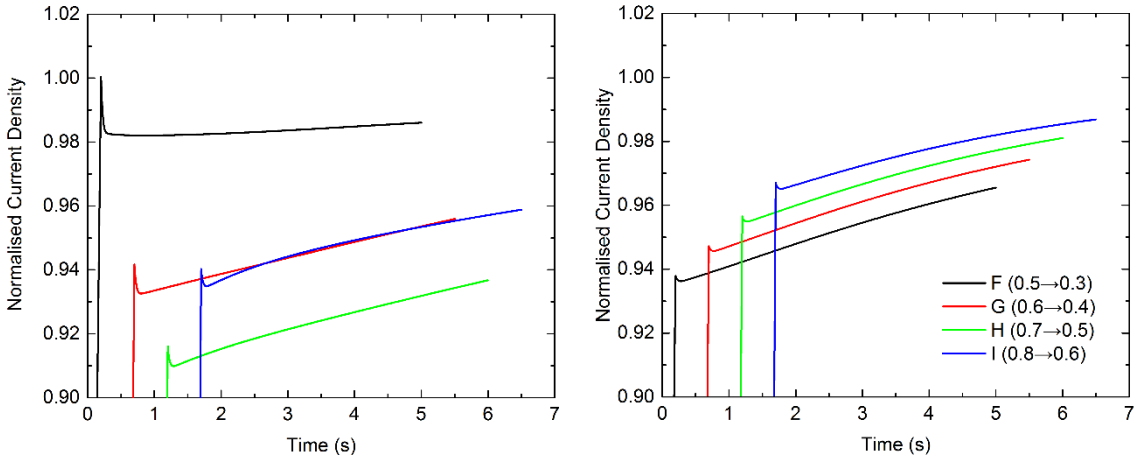

Figure 5.18 Normalised current response of wet (left) and dry (right) cell (ΔV = -0.20 V).

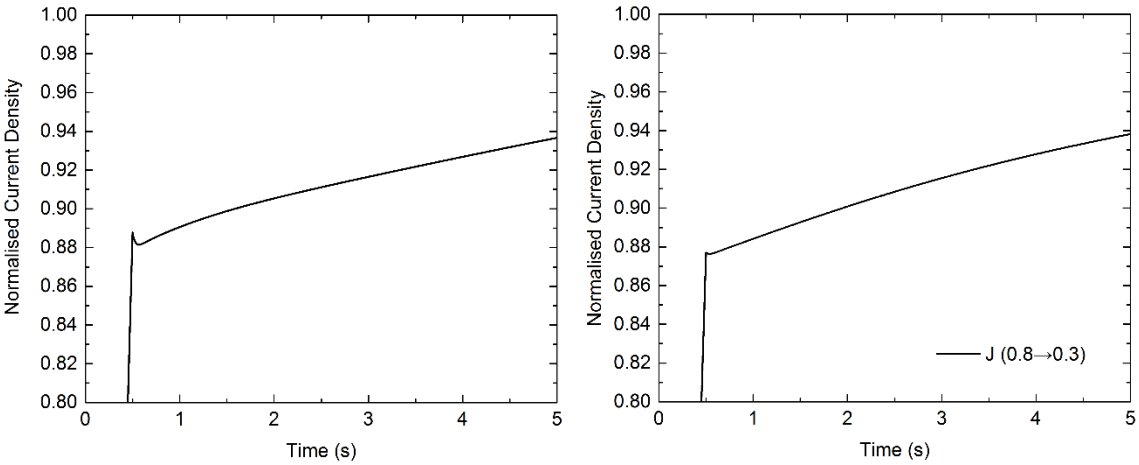

Figure 5.19 Normalised current response of wet (left) and dry (right) cell (ΔV = -0.50 V).

This is caused by a complex interplay between electro-osmosis and water back-diffusion which affects the membrane water content on both sides of the membrane. To demonstrate this, the time histories of normalised current, averaged anode- and cathode-side membrane water content, and averaged membrane protonic conductivity of Case A wet cell

and Case A dry cell are given in Figure 5.20 and Figure 5.21, respectively. The former represents the first-type behaviour while the latter represents the second-type behaviour.

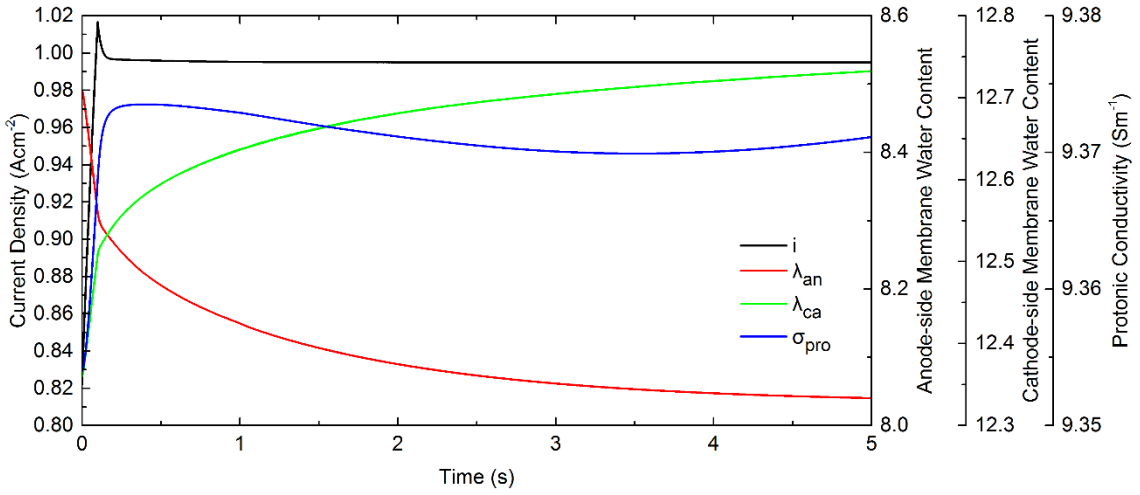

Figure 5.20 Representative case of the first-type behaviour (Case A wet cell).

It is known that the transport of proton across the membrane only occurs if the membrane is sufficiently well hydrated. This is true for Case A wet cell where membrane hydration is close to its full-hydration state due to the humid reactant gas streams used and low operating voltage of 0.40 V. Once the voltage has reached 0.30 V, the hydrogen oxidation reaction (HOR) becomes more intense and more protons are generated at the anode. The initially well hydrated membrane hence allows these protons to move across the membrane with minimum resistance. Each proton that moves across the membrane to the cathode also drags some water molecules with it which results in the loss of water from the anode-side membrane known as electro-osmosis.

It should be noted that, due to the existence of water concentration gradient across the membrane, some water also diffuses back to the anode seeking for an equilibrium between the two sides. Nevertheless, the electro-osmosis is so intense in this first-type behaviour such that it dominates back diffusion. The anode-side membrane is losing more water due to electro-osmosis than gaining water from back diffusion and hence said to be drying out. This is seen as a continuous drop of anode-side membrane water content, shown as the red solid line, over a long period of time without the sign of recovery. In the contrary, more water is present at the cathode due to the combined effect of electro-osmosis from the anode and more water generation rate which manifests itself as an increase in membrane water content at the cathode side denoted by a green solid line in Figure 5.20.

However, the anode-side membrane dry-out effect not only causes membrane protonic conductivity to decrease, but also lower proton transport and consequently current generation. This combined effect prolongs the relaxation period and hence the occurrence of the secondary response is delayed as seen in the figure.

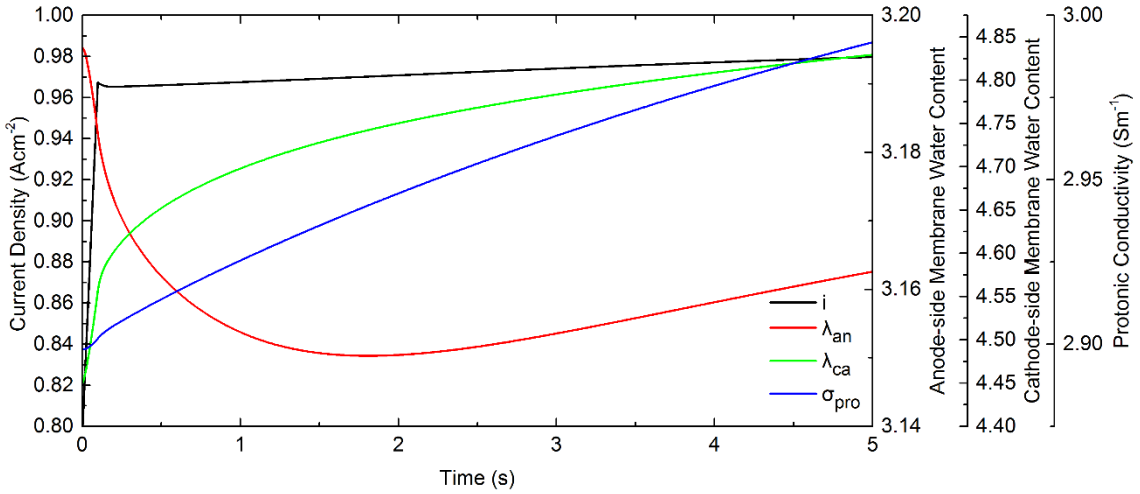

Figure 5.21 Representative case of the second-type behaviour (Case A dry cell).

Compared to the first-type behaviour, all cases in the second category is operated under a much drier condition. Their membrane, especially the anode-side, is far from being fully hydrated and therefore the effect of electro-osmosis is easily counteracted by the back diffusion. The anode-side membrane is initially losing water due to electro-osmosis until an instant when more water diffuses back and eventually overwhelms this loss of water. This is seen as an initially declining curve followed by a gradual rise indicating the membrane on this side is gaining more water than losing. As a consequence, the membrane protonic conductivity improves more rapidly than the one in the first-type behaviour. The occurrence of a current trough is therefore early and can be easily identified.

To summarise, the absolute value of the initial voltage at the start of the voltage change is not the main factor in dictating the type of behaviour of the current response. In fact, it is the initial membrane hydration status that dictates the current response behaviour. If the voltage change starts off with a sufficiently low initial voltage and good membrane hydration, its current would respond with a first-type behaviour. On the other hand, a cell with a low initial voltage but dry membrane would respond with the second-type behaviour. This explains why Cases A and B wet cell falls into the first category while Cases A and B dry cell falls into the second category despite the fact that they started off with the same initial voltages.

Effect of Voltage Change Amplitude

If the initial voltage is the same, a larger change amplitude means a lower final voltage and therefore gives a larger current spike at the end of the primary response. However, if the current response is normalised, the above observation is no longer valid. In order for the effect of change amplitude to become visible, the normalised responses are re-grouped according to their initial voltage as shown in Figure 5.22. It can be seen that the change amplitude only affects the magnitude of normalised current spike.

A larger change amplitude results in a smaller normalised current spike and therefore takes longer to reach the desired value. This is caused by the relative difference between initial and final membrane hydration levels among the cases. Since the initial voltage is the same, a larger amplitude means a larger difference between initial and final membrane hydration.

Considering Figure 5.22g and Figure 5.22h, for example, since the protonic conductivity at 0.80 V is very close to the value at 0.70 V, the normalised spike immediately after the voltage has reached 0.70 V in Case E was therefore close to unity. On the other hand, in Case J, the protonic conductivity at 0.70 V is much lower than the value at 0.30 V. Even its voltage has already reached 0.30 V and water is generated faster, this is not sufficiently fast to improve membrane hydration. During the primary response, however, the protonic conductivity remains effectively constant at its initial value and therefore restricts the normalised spike to a much lower value than unity as seen in the figure.

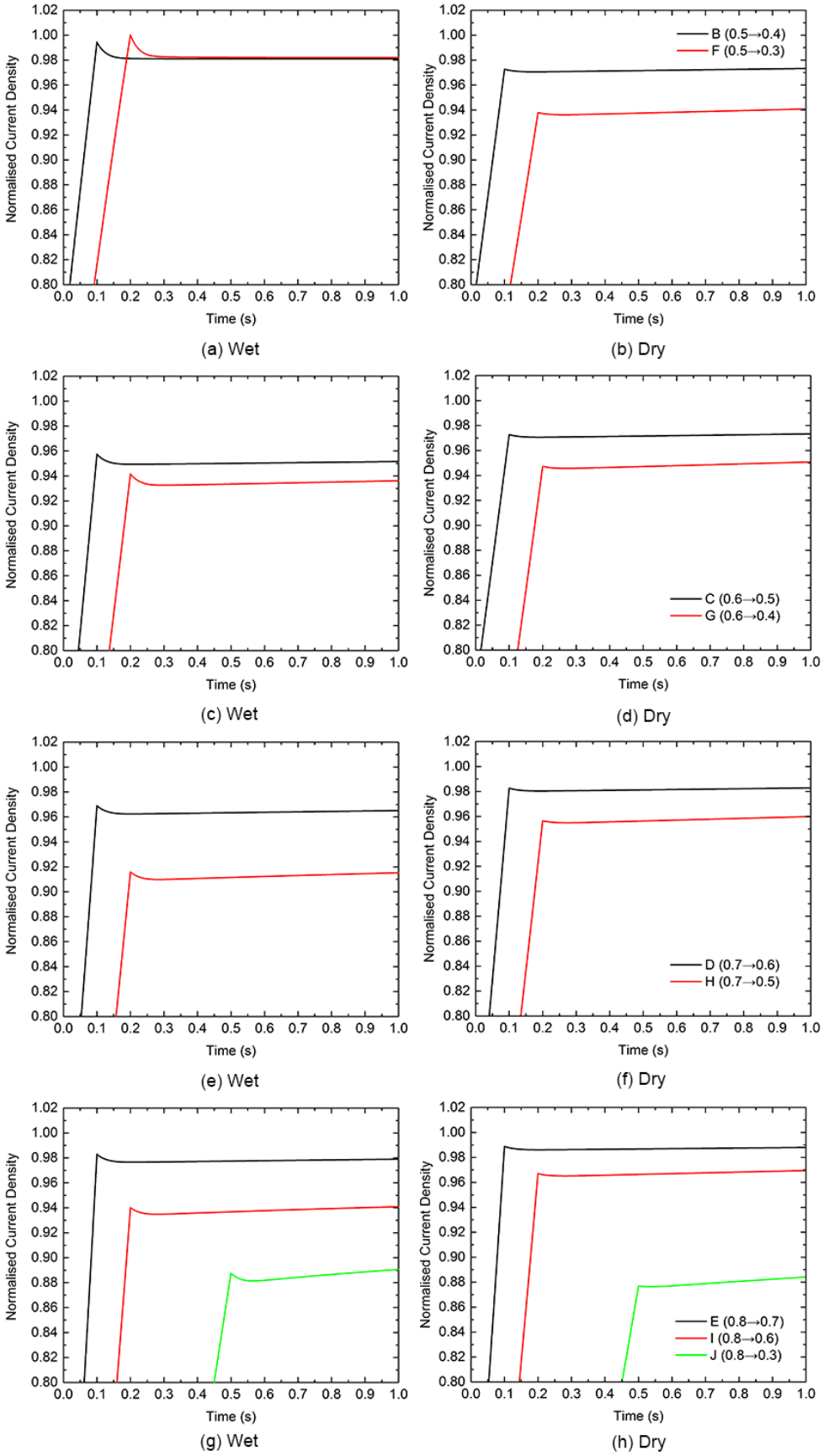

Figure 5.22 Normalised current responses for wet (left) and dry (right) cells under downwards voltage change grouped by initial voltage.

5.5.2 The Upwards Path

Similar to Section 5.5.1, the labelling convention and details of each simulation case are given in Table 5.9. As expected, since voltage is increased, the overpotential is decreased which then reduces the reaction kinetics. Both cells respond with a decrease in current density as shown in Figure 5.23. In contrast to the response under the downwards voltage change, an irregularity exists which is seen as a sharp trough on the response curve. Compared to the spikes in Section 5.5.1, the magnitude of these troughs are much smaller so that they are almost invisible from the figure.

After the trough, current increases to a certain value and stays relatively stable. This makes it difficult to judge whether the secondary response exists. However, the information given in Table 5.9 reveals that at time = 5 seconds the current is higher than its equilibrium value. This suggests that current is approaching the final value from above and proves the existence of a secondary response. Therefore, it can be said that the three-step response also exists under the upwards voltage change. However, during the secondary response, the current approaches the equilibrium value at a much slower rate than that found in the downwards voltage change analysis.

Amplitude	Path (V)	Time (s)	Label	i_{wet} (Acm^{-2})	Deviation (%)	i_{dry} (Acm^{-2})	Deviation (%)
0.10 V	0.3→0.4	0.1	Up-A	0.998	0.82%	0.551	1.70%
	0.4→0.5	0.1	Up-B	0.760	2.13%	0.421	1.18%
	0.5→0.6	0.1	Up-C	0.523	4.17%	0.307	0.82%
	0.6→0.7	0.1	Up-D	0.317	2.12%	0.208	0.54%
	0.7→0.8	0.1	Up-E	0.167	0.99%	0.125	0.31%
0.20 V	0.3→0.5	0.2	Up-F	0.768	3.20%	0.429	2.96%
	0.4→0.6	0.2	Up-G	0.535	6.58%	0.311	2.04%
	0.5→0.7	0.2	Up-H	0.328	5.50%	0.210	1.35%
	0.6→0.8	0.2	Up-I	0.170	2.54%	0.125	0.79%
0.50 V	03→0.8	0.5	Up-J	0.171	3.01%	0.129	3.47%

Table 5.9 Labelling convention used in the upwards path analysis and current density after five seconds.

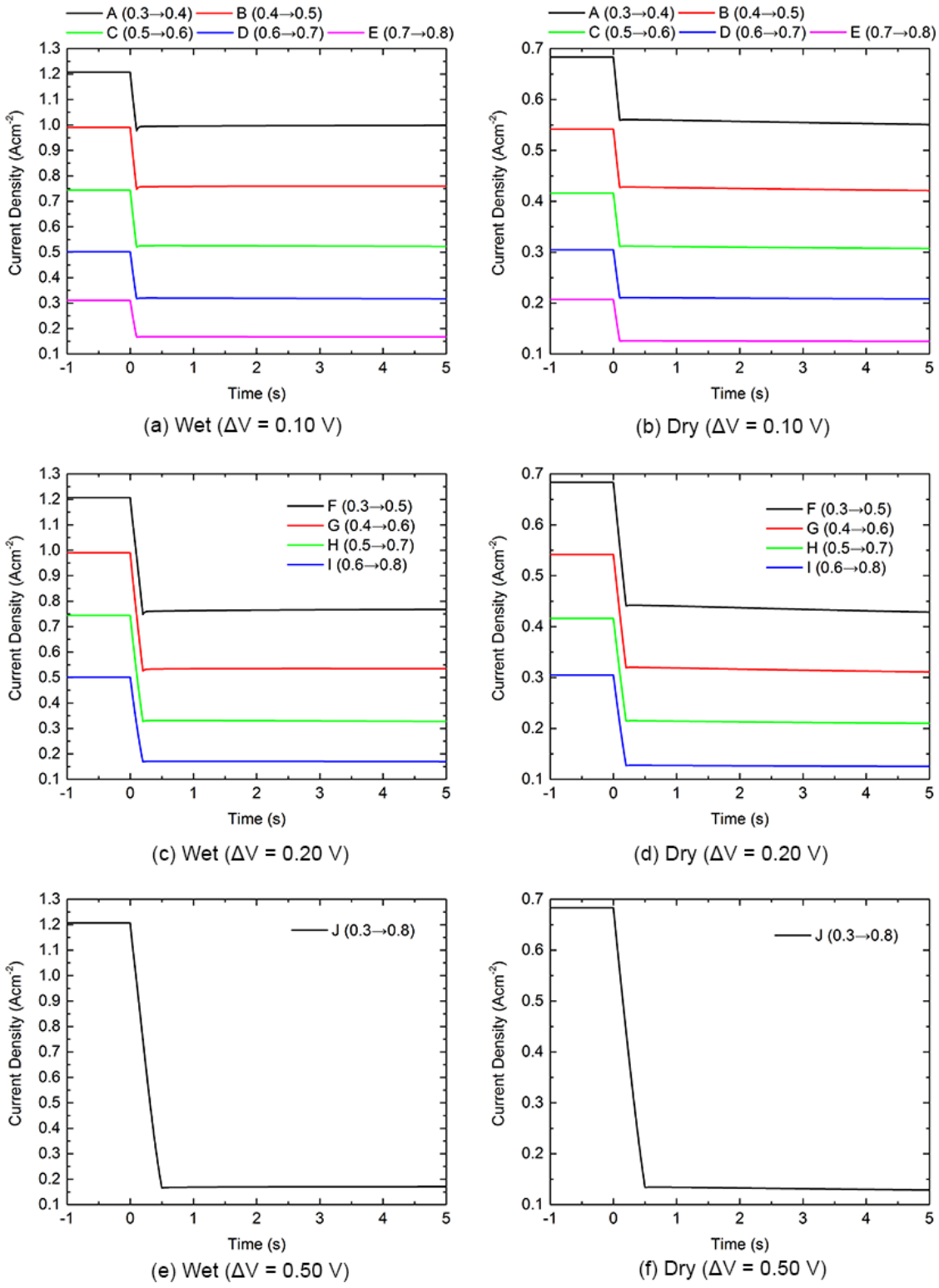

Figure 5.23 Current responses under the 1 Vs^{-1} linear voltage increase.

In order to distinguish the three responses from each other, the current response curves are normalised and grouped in the same manner as in the previous section. They are presented in Figure 5.24-5.26.

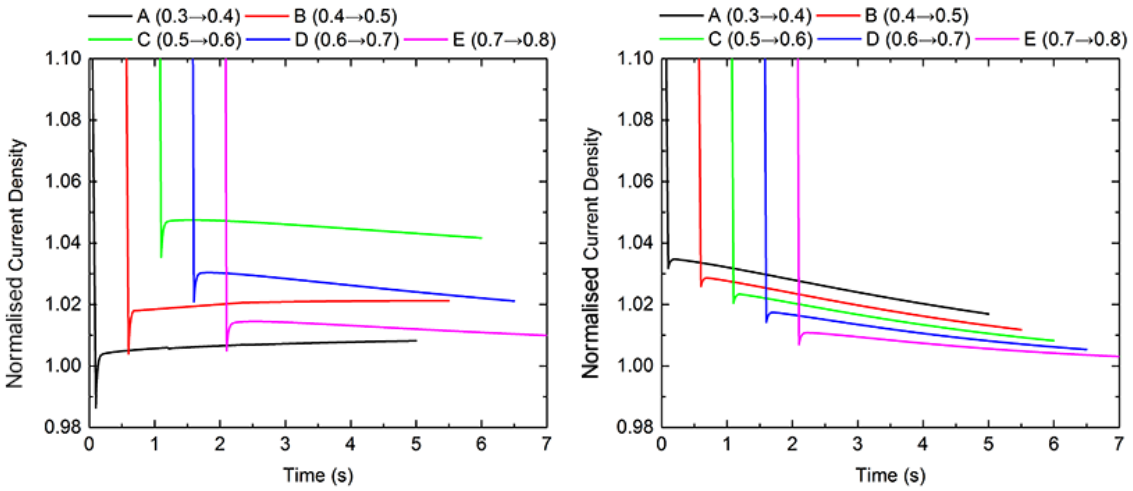

Figure 5.24 Normalised current response of wet (left) and dry (right) cell (ΔV = 0.10 V).

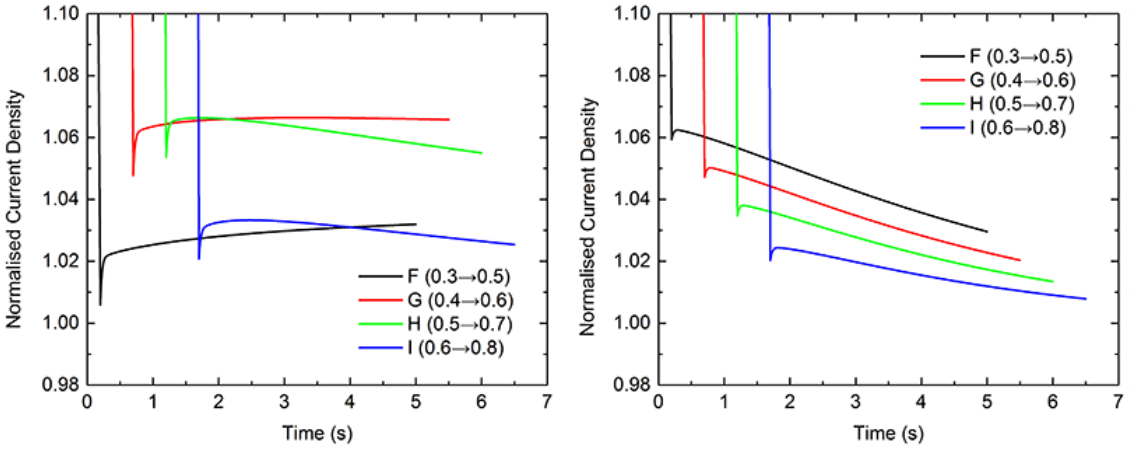

Figure 5.25 Normalised current response of wet (left) and dry (right) cell (ΔV = 0.20 V).

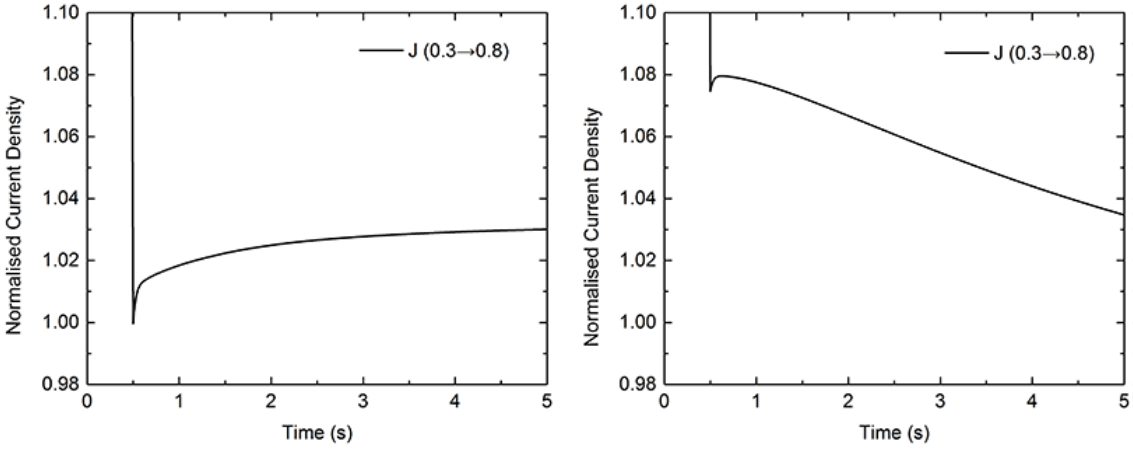

Figure 5.26 Normalised current response of wet (left) and dry (right) cell (ΔV = 0.50 V).

From the above figures, the three regions on each response curve have now become easily identifiable. The primary response occurs during an increase of voltage and is seen as a sharp drop in current density. Nevertheless, the current could not reach the equilibrium value during this primary response. This is due to the difference in the time responses of reaction kinetics and membrane hydration. In an attempt to explain this, Case A wet cell is chosen. Its local distribution of overpotential, membrane protonic conductivity, and oxygen mass fraction along channel length at different instants are shown in Figure 5.27. It should be noted that the cathode overpotential is negative by definition.

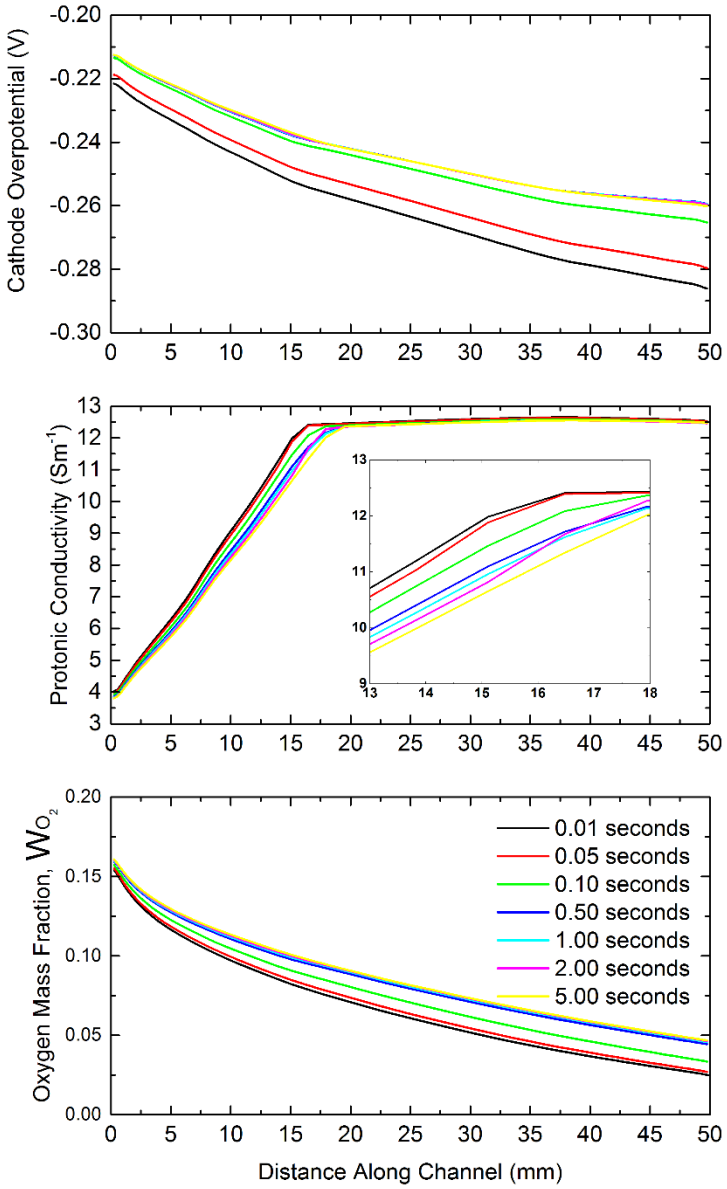

Figure 5.27 Cathode overpotential, membrane protonic conductivity, and oxygen mass fraction profile for Case A of wet cell on CL_{ca}/PEM interface at various instants.

At time = 0.10 seconds, which corresponds to the end of the primary response, the overpotential profile hardly changes indicating that the reaction kinetics is already at the new equilibrium. The membrane hydration, on the other hand, is still evolving very slowly. Its protonic conductivity therefore stays effectively constant during this period. This means that, compared to the new equilibrium state, the membrane at this instant is better hydrated and hence protonic conductivity is higher which restricts the primary current response from dropping to the equilibrium value. It is evident that protonic conductivity has not reached the equilibrium value even after five seconds and would continue to evolve.

After the primary response, the cell arrives at the relaxation period where reaction kinetics stays at its lower rate except the slowly evolving membrane hydration and oxygen diffusion. During this period, the current response is controlled by the combined effect of oxygen transport to the cathode reactive site and membrane water desorption. Combining with the fact that the inlet flow rate of oxygen is constant, the initially depleted oxygen reservoir is therefore being replenished by the incoming flux. More oxygen becomes available at the cathode reactive site as time progresses which is seen as an increase of oxygen mass fraction over time. By examining the oxygen mass fraction, it can be concluded that the oxygen reserve at the reactive site has reached the equilibrium at time = 0.50 seconds. This higher oxygen concentration causes reaction kinetics to increase and in turn tends to increase the current density.

On the other hand, membrane desorption is much slower than the oxygen transport. The figure shows that membrane protonic conductivity is still decreasing very slowly even after five seconds therefore staying the same as the initial value during this period. This means that the faster replenishment of oxygen dominates the slower membrane dehydration at the first stage of the relaxation period which is seen as an increase in current density immediately after the trough.

The cell continues to benefit from this combined effect of initially high membrane protonic conductivity and improved reaction kinetics for a certain period therefore the current keeps on rising. In the meanwhile, the membrane keeps on losing its water on its path to the new equilibrium and this mechanism is gradually taking control over the current response. At the point where the effect of membrane protonic conductivity reduction becomes sufficiently large to overpower oxygen transport, the current flattens out and starts to decrease again.

This marks the beginning of a secondary response where the current response is controlled solely by the decreasing membrane hydration. During this, the current continues to decrease until it eventually reaches the equilibrium value at a much later time.

Effect of Initial Voltage

Similar to current overshoot, the current undershoot is defined in the same way and is given in Equation (5.4) as;

$$i_{undershoot} = i_{equilibrium} - i_{trough} \tag{5.4}$$

By re-examining the normalised current response curves in Figure 5.24-5.26, and using the above definition, current undershoot can be extracted. It can be seen that even a current trough exists in all cases, not all of them are current undershoots. In fact, only the trough that is below unity can be considered as a current undershoot similar to how a current overshoot is judged in Section 5.5.1. From this criterion, current undershoot is only present in Cases A and J for the wet cell. In the remaining cases, current troughs exist but their magnitude exceeds the equilibrium value and therefore not considered a current undershoot.

However, these current undershoots are negligibly small such that it will not have any negative effect to the cell, therefore they can be safely discarded from the discussion. On the other hand, the characteristics of the response as a whole is of more concern. Using the concept of relaxation time as in the previous section, two distinct behaviours are noticed. The first category is seen in Cases A, B, F, G, and J of the wet cell. They have a large relaxation period and the starting point of the secondary response cannot be seen within five seconds. The remaining cases fall into the second category. Their relaxation time is small and the starting point of the secondary response can be noticed easily.

In Section 5.5.1, it has been shown that the decrease in current during this relaxation period is caused by the drying out of the anode-side membrane. This limits the transfer of proton across the membrane to the cathode and in turn reduces the current generation at the cathode. In this upwards voltage change case, the rise of current in this period is also caused by the status of anode-side membrane water content but in the opposite manner.

To explain this, the time histories of normalised current, averaged anode- and cathode-side membrane water content, and averaged membrane protonic conductivity of Case J wet cell and Case J dry cell are given in Figure 5.28 and Figure 5.29, respectively. The former represents the first-type behaviour while the latter represents the second-type behaviour.

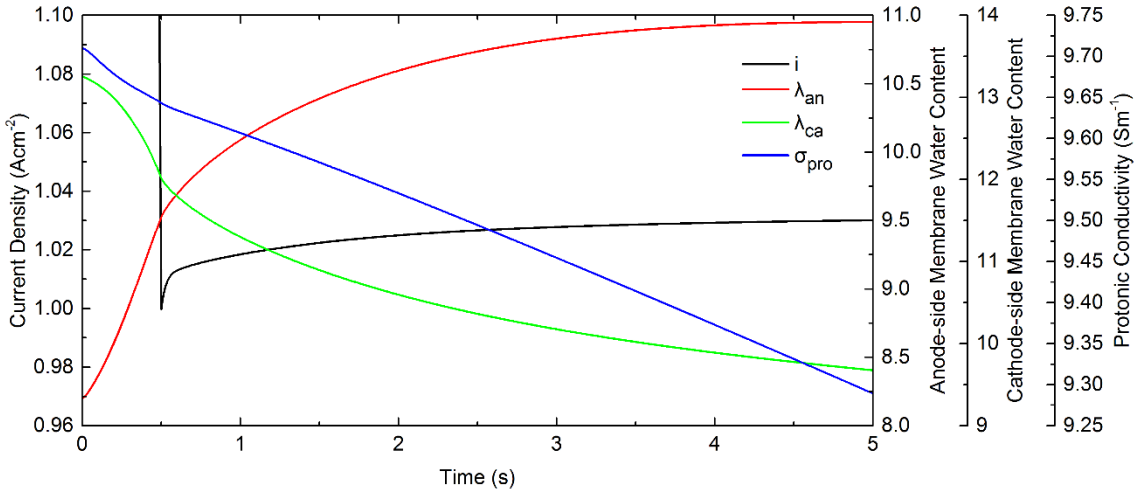

Figure 5.28 Representative case of the first-type behaviour (Case J wet cell).

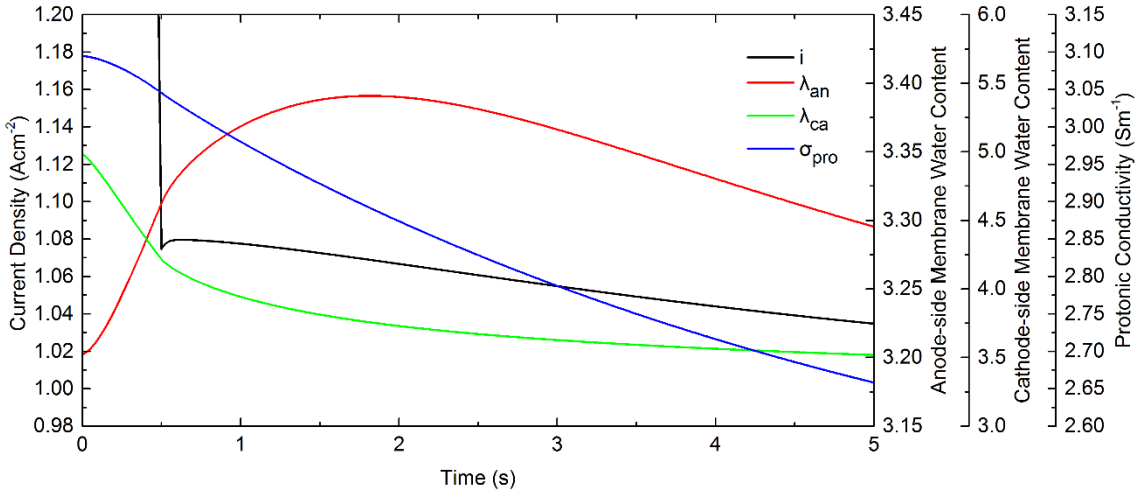

Figure 5.29 Representative case of the second-type behaviour (Case J dry cell).

It is evident from both figures that membrane water content is increasing at the anode side. The cathode-side membrane, on the other hand, is losing water indicating that more water molecules diffuse back to the anode dominating the gain of water from electro-osmosis. This is due to a low initial operating voltage combined with high humidity reactant streams which results in a large amount of water at the cathode and high water concentration gradient between the two sides. As a consequence, the membrane becomes better hydrated at its anodes side. This enhances the transport of protons across the membrane that involve in the oxygen reduction reaction (ORR) at the cathode catalyst layer. Combining with an increasing oxygen reserve as explained in the previous section, more current is generated as seen in the figures.

A comparison between these two figures suggests why they fall into different category. It is clear that Case A wet cell in Figure 5.28, the amount of water at the cathode is excessively large and therefore the effect of back diffusion is sufficiently large to prolong the gain in water at the anode-side membrane. This in turn delays the starting point of anode-side membrane drying out and consequently the starting point of the secondary response.

For the second-type behaviour, the cell operates under partially humidified reactant streams therefore the cathode is much drier. The back diffusion effect is not sufficiently strong to rehydrate the anode-side membrane for a long period. This is why its water content, shown as a red solid line, only increases during a certain period before it levels off and starts to decrease again. The second decline is caused by membrane desorption mechanism due to a higher operating voltage.

Even though the primary current in the first category is much closer to unity, a cell with this behaviour might not be considered superior than the one with the second category behaviour if the time taken to reach the exact equilibrium value is of concern. This can be seen clearly in Case J wet and dry cells shown in Figure 5.26. Evidently, even after five seconds, the current is still increasing in the wet cell on the left whereas the current of the dry cell on the right has already started declining. This suggests that it would take much longer time for the wet cell to reach the new equilibrium value.

Effect of Voltage Change Amplitude

Similarly, in order for the effect of voltage change amplitude to become visible, the normalised responses are re-grouped according to their initial voltage and are shown in Figure 5.30. It can be seen that the change amplitude only affects the magnitude of normalised trough of the primary response.

Similar to what is explained in the downwards voltage change analysis, the same principle applies here. Due to the relative difference between the initial and equilibrium value of membrane proton conductivity, the case with a larger excitation amplitude therefore has a higher normalised current trough.

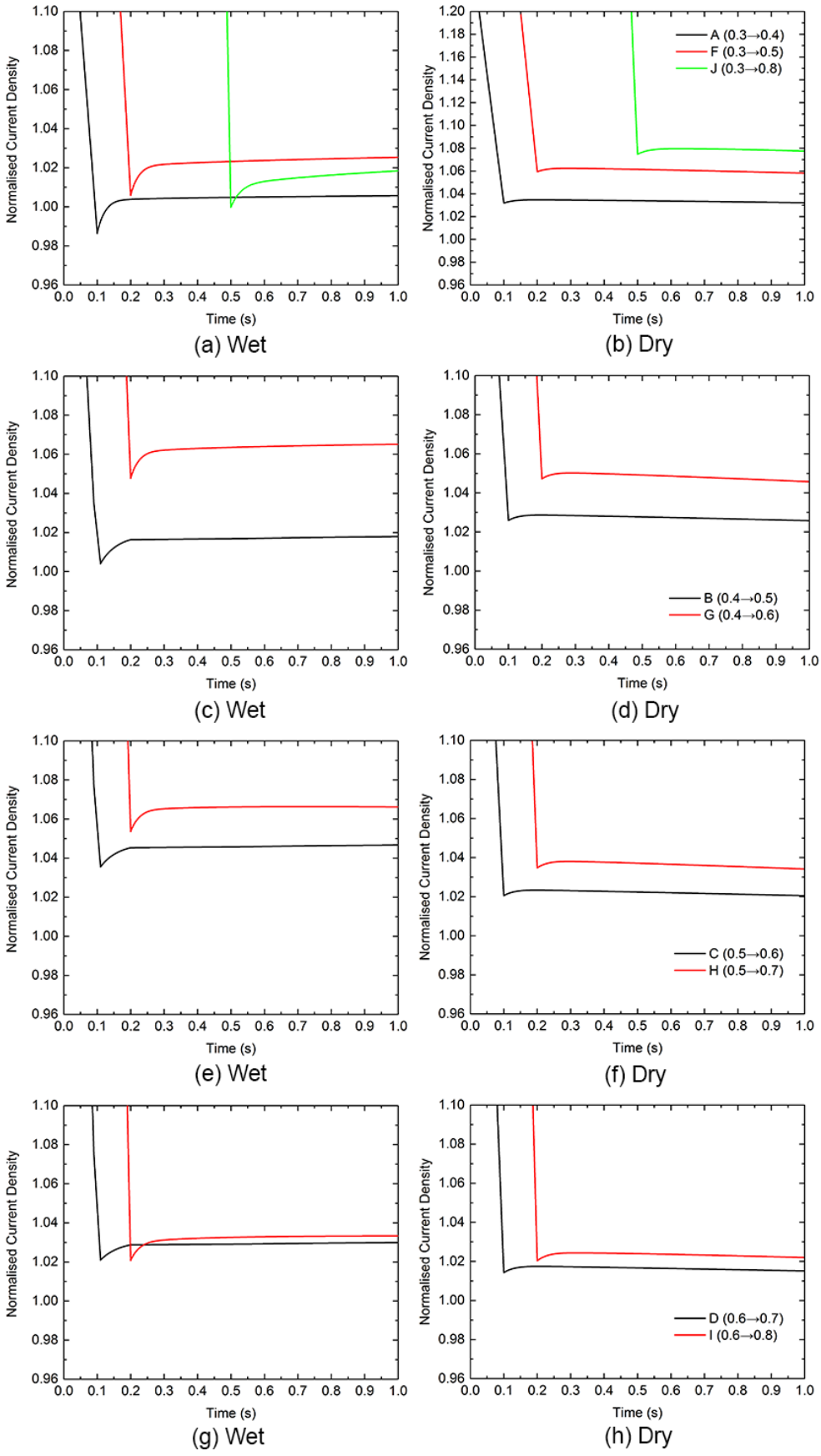

Figure 5.30 Normalised current responses for wet (left) and dry (right) cells under upwards voltage change grouped by initial voltage.

5.5.3 Concluding Remarks

It is clear that this analysis is very comprehensive in which it takes both downwards and upwards change paths into consideration. Its range of applicability is large and covers different initial voltages between 0.80 V ↔ 0.30 V which is the range a typical cell is subjected to under a normal operation. Moreover, the effect of change amplitude size under the same initial voltage is also discussed.

Even though the current density could not reach the equilibrium value immediately at the end of the change, it is very close to the desired value. This value is well within the ±10% margins after five seconds which is considered acceptable. Therefore it is said that the cell responds satisfactorily under the present change rate of 1 Vs^{-1}. Additionally, the rate used is sufficiently fast to deduce the irregularity seen as a spike or trough on the current response curve. Once normalised, the current overshoot or undershoot are revealed and they only exist in very few cases with negligible magnitude.

The current responds to the voltage change in three steps in an attempt to reach the new equilibrium value. These are known as the primary response, relaxation period, and secondary response. The secondary response is solely controlled by the slow membrane hydration mechanism which results in a gradual increase or decrease of current over a long period of time and therefore it is discarded from the discussion.

However, the primary and relaxation responses occur during the change process and are much more complex and therefore receive special attention. It has been found that during the primary response, the rise or decline of current is caused by the instantaneous change of overpotential and its final value is dictated by the initial membrane protonic conductivity at the start of the change process. The current response in the relaxation period, on the other hand, is controlled by the net effect between reactant species transport and the anode-side membrane hydration which is in turn the net effect between electro-osmosis and back diffusion across the membrane. It is shown that depending on the hydration status of the anode-side membrane, two distinct behaviours of the response curve exist.

Additionally, the absolute value of the initial voltage does not explicitly effect the current response. It is the operating region in which this initial voltage falls into, whether it is in the activation, ohmic, or mass transport limit region, combined with the humidification level of the reactant streams that dictate the behaviour of the response current. Besides, the voltage change amplitude is found to determine how close the current spike/trough at the end of the primary response is to the equilibrium value. The larger voltage jump or drop, the further the peak/trough from its new equilibrium value.

5.6 Voltage Step Change

As can be seen from the previous analysis that once the voltage change rate is increased, irregularity in the current response in the form of current spikes and troughs becomes more pronounced. In this analysis, downwards and upwards step changes in voltage are applied on the cells in order to replicate the sudden change in power demand in which a vehicle is subjected to during an engine start-up or engine shut-down, respectively. Therefore, larger current overshoot and undershoot are expected.

It should be pointed out that since this sudden change in voltage takes place within an infinitesimally small period of time, an infinitesimally small time step size is required. The computation time could become prohibitively long and therefore is impractical. To resolve this, the step change is approximated by a very fast linear change of voltage between its initial and final voltages. On the other hand, this voltage step change can be thought of as an extreme case of a linear voltage change with a very fast rate. Therefore, the rate of 100 Vs^{-1} is chosen and this requires a smaller time-step size than that used in the previous analyses. A microsecond is used as the lower limit of time-step size to correctly capture the current response and therefore the total physical time is shortened to two seconds in order to save the computation time.

5.6.1 The Downwards Path

In this analysis, the voltage change takes place between 0.8 V and 0.3 V with three excitation amplitudes of ±0.10 V, ±0.20 V, and ±0.50 V similar to those used in Section 5.5. The details of each sub-case and its current density after two seconds are given in Table 5.10 while the current response curves are shown in Figure 5.31.

Despite the fact that the voltage changes extremely fast, the current, however, responds very satisfactorily as it is able to reach within 90% of the equilibrium current even after two seconds. To aid in the comparison, a current response curve under a 1 Vs^{-1} linear voltage change from the previous analysis, shown as a dashed line, is also superimposed in the plot of Figure 5.31. The three-step characteristics of the current response can be detected in all cases. For each case, its secondary response coincides exactly with the secondary response of its 1 Vs^{-1} counterpart. The only difference is the magnitude of current spike which is increased significantly as expected. By normalising the current response with the equilibrium value and using the definition in Equation (5.3), the current overshoots are seen in Cases A, B, and F wet cell as shown in Figure 5.32. It should be noted that the current in these cases overshoots the equilibrium value by a significant 10%.

Amplitude	Path (V)	Time (s)	Label	i_{wet} (Acm^{-2})	Deviation (%)	i_{dry} (Acm^{-2})	Deviation (%)
-0.10 V	0.4→0.3	0.001	Down-A	1.199	-0.61%	0.664	-2.90%
	0.5→0.4	0.001	Down-B	0.972	-1.84%	0.529	-2.32%
	0.6→0.5	0.001	Down-C	0.710	-4.53%	0.408	-1.85%
	0.7→0.6	0.001	Down-D	0.486	-3.18%	0.301	-1.40%
	0.8→0.7	0.001	Down-E	0.305	-1.85%	0.205	-0.96%
-0.20 V	0.5→0.3	0.002	Down-F	1.186	-1.76%	0.648	-5.14%
	0.6→0.4	0.002	Down-G	0.933	-5.82%	0.519	-4.15%
	0.7→0.5	0.002	Down-H	0.686	-7.79%	0.403	-3.28%
	0.8→0.6	0.002	Down-I	0.475	-5.25%	0.297	-2.43%
-0.50 V	0.8→0.3	0.005	Down-J	1.097	-9.12%	0.618	-9.52%

Table 5.10 Labelling convention used in downwards path analysis and current density after two seconds.

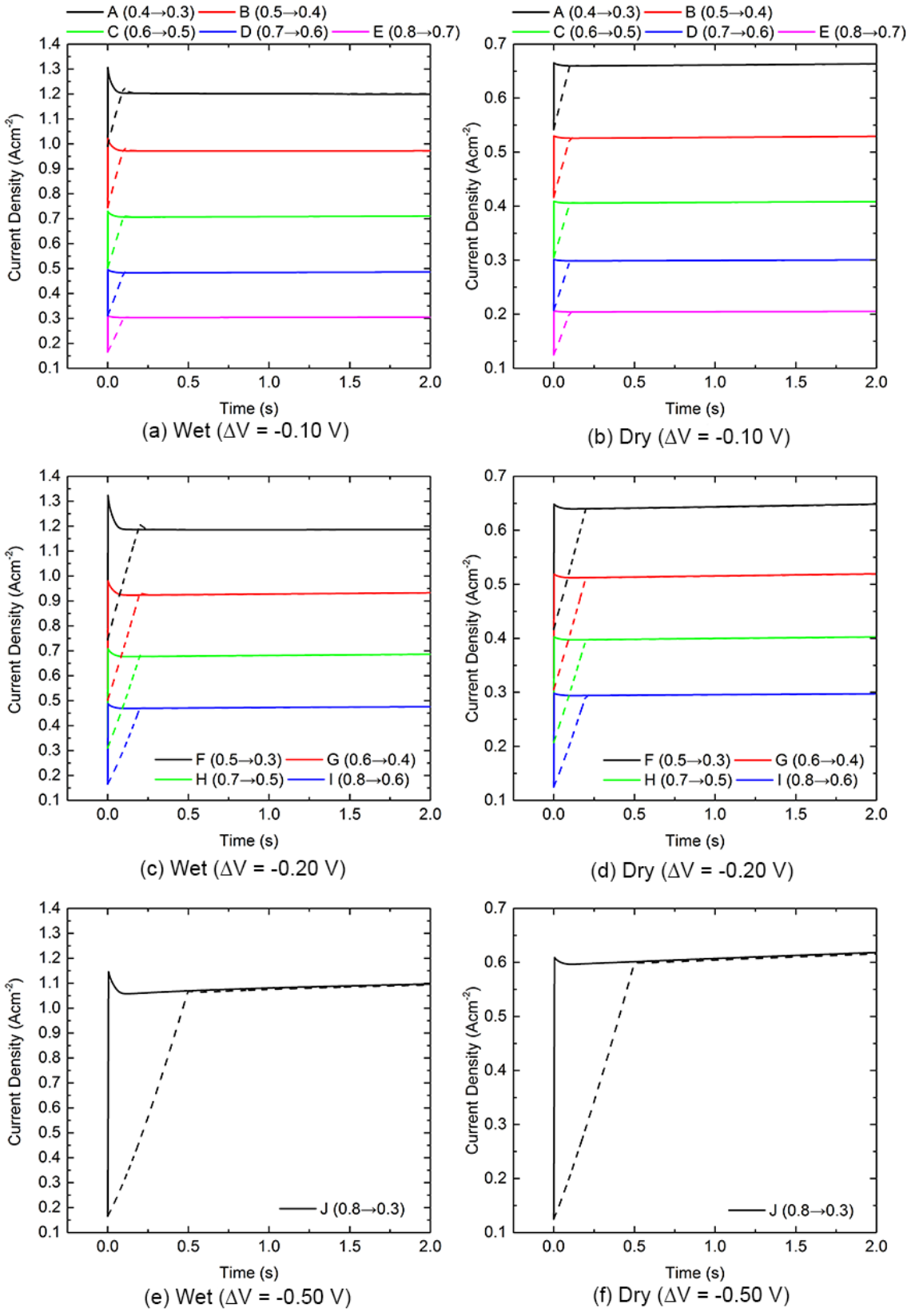

Figure 5.31 Current responses under the voltage step-down.

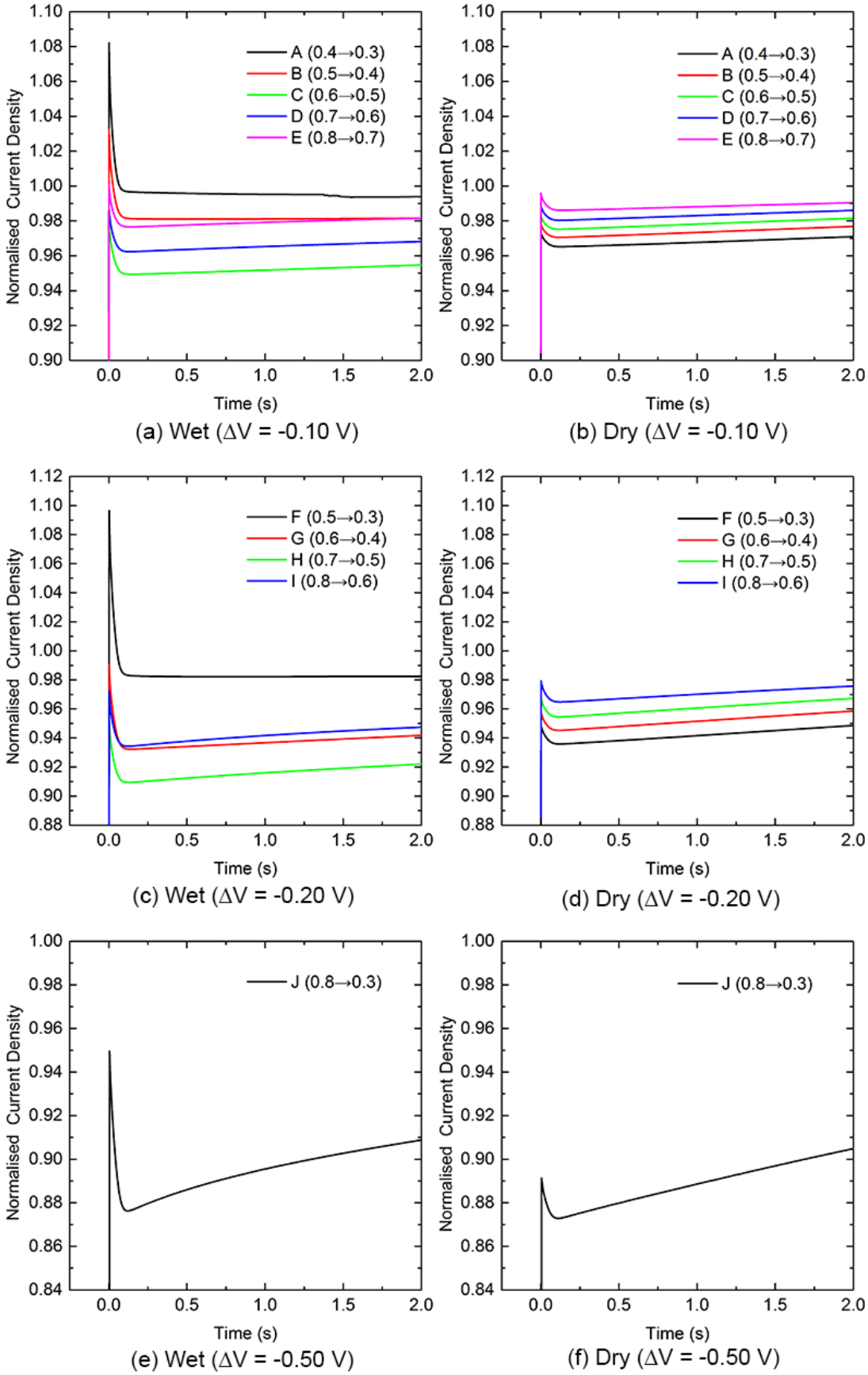

Figure 5.32 Normalised current responses under the voltage step-down.

5.6.2 The Upwards Path

Similar to the voltage step-down analysis, various initial and final voltages are used in this voltage step-up analysis as summarised in Table 5.11 while the current response curves are presented in Figure 5.33.

It is evident that current troughs are much more pronounced in all cases similar to those found in the previous section. Using Equation (5.4), the current undershoots are extracted from current troughs on the normalised current response curves as shown in Figure 5.34. It is interesting that these current undershoots are found in most cases and the largest undershoot is found in Case J wet cell where the current undershoots its equilibrium value by almost 40%.

5.6.3 Concluding Remarks

The current response to a step change in voltage has been investigated. Such a step change is approximated by a linear voltage change with an excessively large rate of 100 Vs^{-1}. As expected, the current responds to this extremely fast voltage change with a three-step response behaviour. It has been found that the magnitude of current spikes and troughs at the end of the primary response increase significantly under this much faster change rate.

Because of these higher current spikes and lower current troughs, current overshoots or undershoots are detected in majority of the cases and some of them are sufficiently large to cause problems to the operation of the cell. However, the relationship between the increased voltage change rate and enlarged current spikes/troughs could not be established in this analysis.

Amplitude	Path (V)	Time (s)	Label	i_{wet} (Acm^{-2})	Deviation (%)	i_{dry} (Acm^{-2})	Deviation (%)
0.10 V	0.3→0.4	0.001	Up-A	0.997	0.69%	0.557	2.79%
	0.4→0.5	0.001	Up-B	0.759	2.07%	0.425	2.16%
	0.5→0.6	0.001	Up-C	0.525	4.61%	0.310	1.66%
	0.6→0.7	0.001	Up-D	0.319	2.73%	0.210	1.19%
	0.7→0.8	0.001	Up -E	0.168	1.31%	0.125	0.73%
0.20 V	0.3→0.5	0.002	Up -F	0.765	2.82%	0.437	4.97%
	0.4→0.6	0.002	Up -G	0.535	6.62%	0.316	3.77%
	0.5→0.7	0.002	Up -H	0.330	6.37%	0.213	2.72%
	0.6→0.8	0.002	Up -I	0.171	3.18%	0.127	1.72%
0.50 V	0.3→0.8	0.005	Up -J	0.170	2.58%	0.132	6.39%

Table 5.11 Labelling convention used in upwards path analysis and current density after two seconds.

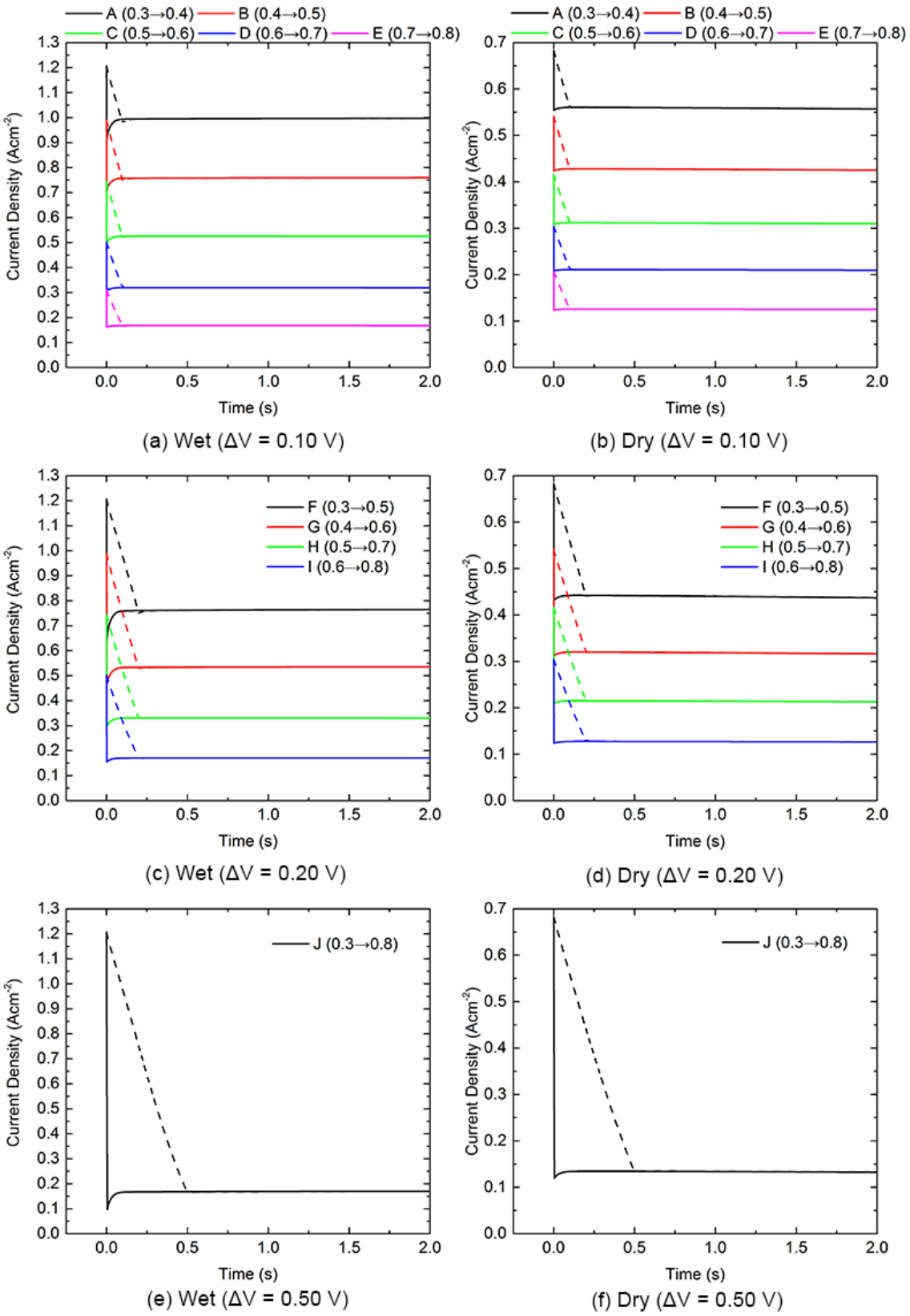

Figure 5.33 Current responses under voltage step-up.

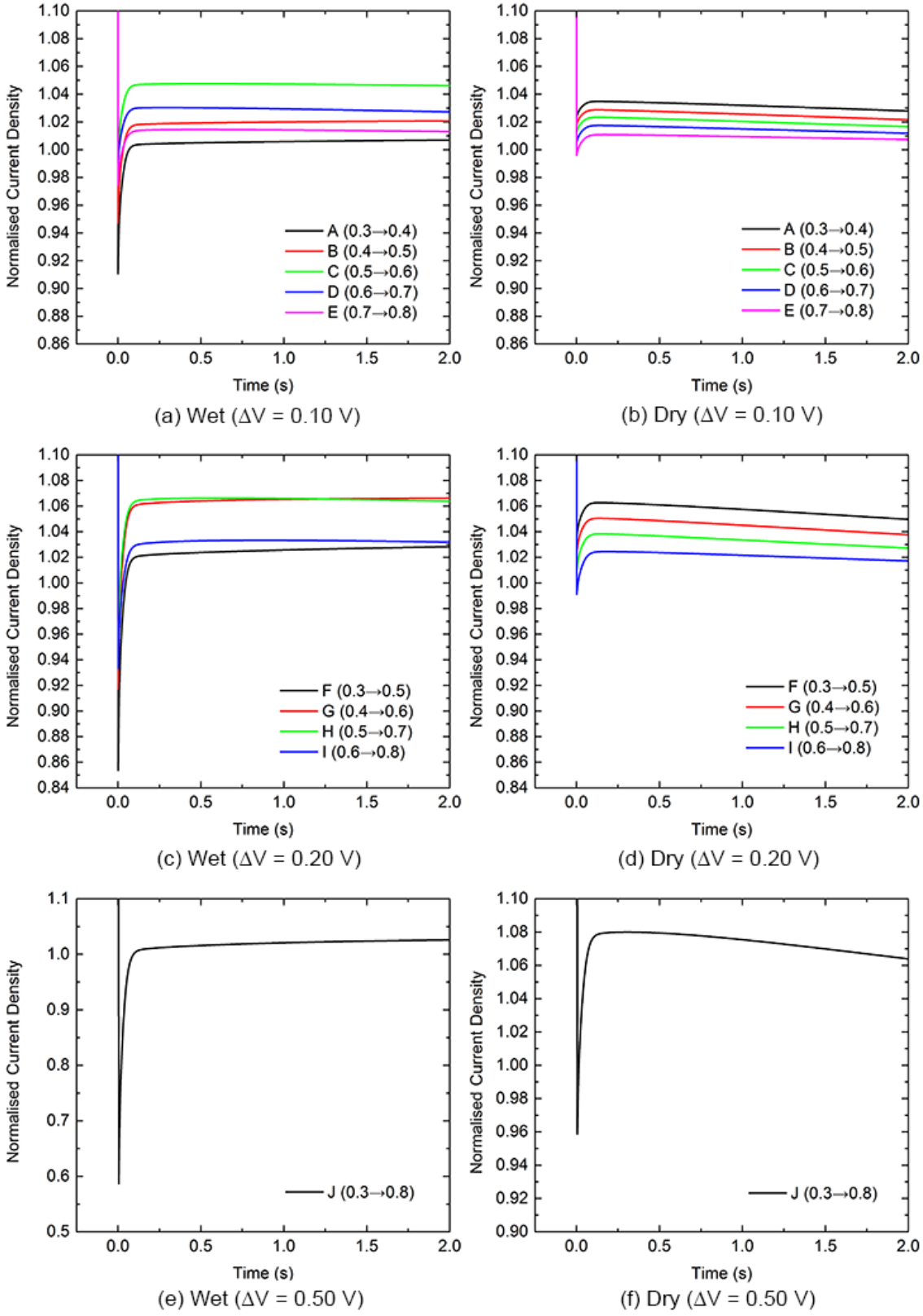

Figure 5.34 Normalised current responses under voltage step-up.

5.7 Chapter Summary

In this chapter, a single-channel computational domain has been used in a series of specially designed analyses to investigate the cell current response under four voltage change patterns. These are, in order, linear voltage sweep, sinusoidal voltage sweep, linear voltage change at a relatively fast rate of 1 Vs^{-1}, and voltage step change. The current responds promptly to all change patterns without any noticeable lag. This proves that a PEM fuel cell is a competent technology for transportation which is capable of providing a fast response under a transient operation. Moreover, if the voltage change rate is slow, then the current density follows the voltage smoothly with unnoticeable irregularity on the current response curve.

On the other hand, if the change is sufficiently fast, then the irregularity becomes more evident seen as a spike or trough on the current response curve. Due to the discrepancy of the characteristics time scales of different transport mechanisms, the current could not reach the equilibrium value in the first place. Besides, the cell responds in three steps known as the primary response, relaxation, and secondary response before reaching the final value.

The primary response is caused by the change in cathode overpotential which takes place almost instantaneously and therefore results in a sharp rise or drop of the current density. Immediately after the end of the voltage change process, the cell arrives at the relaxation period where the current density starts to decline or increase due to a slower species transport mechanism. The last step is known as the secondary response which spans over a much longer period than the first two steps. During this, the current density is mainly controlled by a slowly evolving membrane protonic conductivity therefore it increases or decreases gradually over time before reaching the equilibrium value at a much later time.

By using the normalised current response curve and concepts of current overshoot and undershoot as defined in the chapter, it has been found that a current spike or trough is not necessarily a current overshoot or undershoot. The magnitude of them is found to increase with the rate of voltage change. Even though their magnitude is negligibly small under a 1 Vs^{-1} change rate, the current is found to exceed its equilibrium value by 10%-40% when a step change is employed. This has a detrimental effect on the operation of the cell especially the membrane and hence deserves more attention.

Since the amplitude of current overshoot/undershoot is closely coupled to the distribution of reactant species at the reactive sites. The single-channel domain may be too small for the variation of flow-field variable to become significant, therefore the relationship between the overshoot/undershoot amplitudes and the rate of voltage change could not be established in this chapter.

Chapter 6
Results: Practical Cells

"The world's an exciting place when you know CFD"
John Shadid, Sandia National Laboratories

The analysis presented in this chapter was inspired by the works on a transient performance of a PEM fuel cell of Shimpalee et al. [128], [129], [131], [141]. They concluded that the magnitudes of current overshoot and undershoot were closely related to the local distribution of current density. In fact, due to a small dimension of the cell-width (x-axis) of the straight single-channel domain used in the previous chapter, the results obtained were not sufficient to establish the relationship between the current overshoot and current undershoot and flow-field configuration.

In this chapter, the current response to a step change in voltage of three square cells with different flow-field designs are presented and the chapter is structured in a similar order as Chapter 5. It should be noted that the mesh strategy developed in Chapter 4 is used for all simulations presented in this chapter whereas the initial and boundary conditions are the same as those presented in Chapter 3.

6.1 Problem Description

6.1.1 Computational Domains

In practical cells with larger active areas, the non-uniformity of flow-field variables across the cell-width direction, which corresponds to the x-direction in this thesis, becomes much more pronounced so that its effect on the cell performance cannot be overlooked. In order to capture this, the single-channel cell used in the previous chapter needs to be expanded.

As a result, three multi-channel square cells have been created for the analyses in this chapter. These are straight-parallel, single-serpentine, and triple-serpentine cells as shown in Figure 6.1-6.3, respectively. Except the flow-field configuration, the geometrical dimensions of the three cells are identical as summarised in Table 6.1.

Parameter	Value
Channel width (mm)	1*
Channel depth (mm)	1*
Rib width (mm)	1*
Cell width (mm)	23
Cell length (mm)	23
Active area (cm^2)	5.29
GDLs thickness (Toray Carbon Paper, T-090), δ_{GDL} (μm) [147]	280
CLs thickness, δ_{CL} (μm)	20*
PEM thickness (Nafion 115), δ_{PEM} (μm) [160]	164
GDLs porosity [147]	0.78
CLs porosity	0.3*
Specific surface area of CLs (m^{-1}) [144]	2×10^7

Table 6.1 Dimensions of multi-channel square cell computational domain (*typical value).

Even though various flow-field configurations exist, all flow-field designs can be conveniently categorised into three groups based on the type of transport mechanism they induce. These are diffusion-dominant, convection-enhanced, and forced-convection transport mechanisms. As a representative of the first group, the straight-parallel flow-field is chosen. As can be seen from Figure 6.1, all flow channels are connected to a common inlet manifold at one end and common outlet manifold at the other end. Between the inlet and outlet, the reactant species reach the active sites mainly by diffusion.

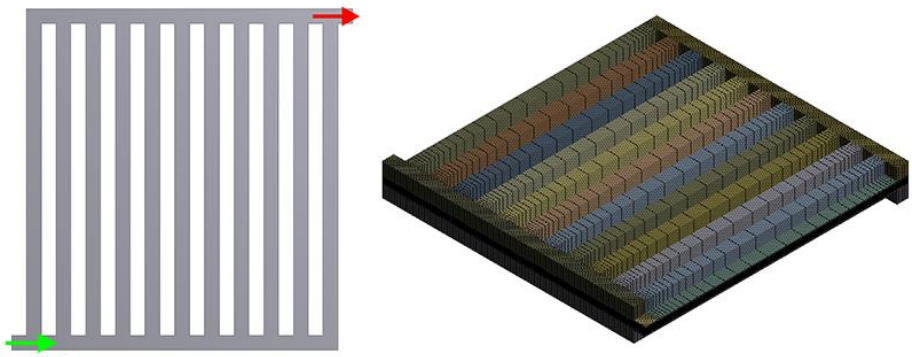

Figure 6.1 Straight-parallel flow-field (green arrow-inlet and red arrow-outlet).

The single-serpentine flow-field is chosen to represent the second group as given in Figure 6.2. For this flow-field configuration, its inlet and outlet are connected by a long channel that traverses over the entire cell in a serpentine manner, hence its name. The flow in the two adjacent channels therefore travels in the opposite direction and the regions where the flow makes a 180-degree turn are known as bends. Having a serpentine flow-field, the cell would benefit from a large pressure difference between the two adjacent channels. Instead of flowing along the channel in a normal way, this pressure difference encourages the reactant streams to take a shortcut underneath the current collector rib to the adjacent channel. As a result, the reactant species are said to be convected to the active sites in addition to diffusion and this convective-enhanced flow underneath the rib is known as cross-flow.

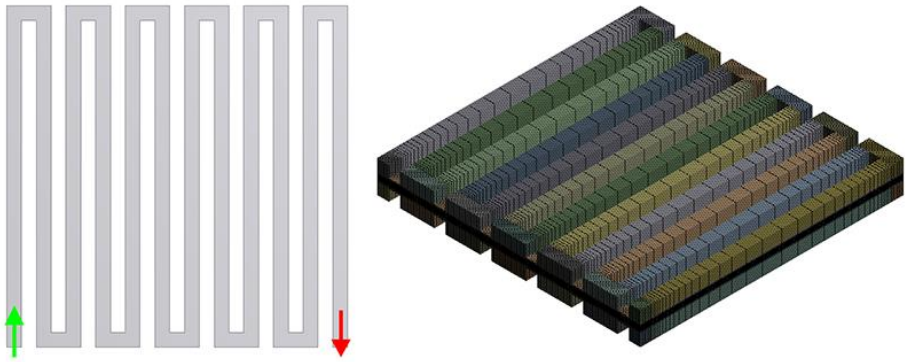

Figure 6.2 Single-serpentine flow-field (green arrow-inlet and red arrow-outlet).

Having a long and continuous channel, a large pressure drop between the inlet and outlet is inevitable. Additionally, if such configuration is used in larger cells this large pressure drop would be amplified and higher pumping power is required which consequently reduces the overall efficiency. Clearly, this is undesirable in a system design standpoint and thus the single-serpentine design is usually modified. The most common practise is by adding more

channels while maintaining the serpentine fashion. This results in a flow-field with multiple serpentine channels having the same number of inlets and outlets to the number of channels. The triple-serpentine flow-field is chosen as shown in Figure 6.3. With this configuration, the length of each channel is approximately one-third of the single-serpentine channel.

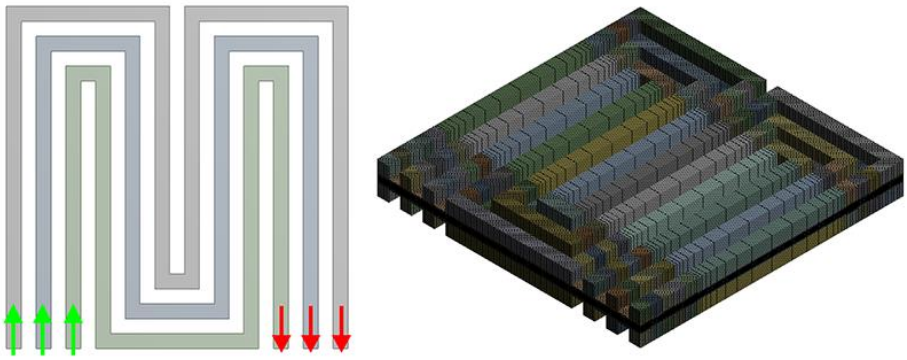

Figure 6.3 Triple-serpentine flow-field (green arrows-inlet and red arrows-outlet).

The flow-field configuration that belongs to the last group is the interdigitated design as seen in Figure 6.4. A typical interdigitated flow-field comprises of an array of dead-ended inlet channels and another array of dead-ended outlet channels. The inlet and outlet thus are completely disconnected. This forces reactant streams to flow inside the porous media in order to exit the cell at the outlet. The design proves to exhibit excellent water removal and outperform the straight-parallel and serpentine configurations especially at high current operations. Nevertheless, the major drawback of such a design stems from the fact that the inlet and outlet are separated which induces a very large pressure drop between them. From a numerical perspective, it also takes many more iterations for the solution to converge which is undesirable when computation resources are limited. The interdigitated flow-field is less common than the other two designs and thus not included in this study.

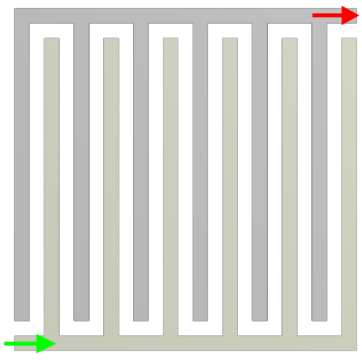

Figure 6.4 Interdigitated flow-field (green arrow-inlet and red arrow-outlet).

6.1.2 Operating Conditions

All three cells are operated under wet and dry reactant streams similar to those used in Chapter 5. Since the active area and flow channel cross-sectional area are the same in all cells, the anode and cathode inlet mass flow rates take the same value according to Equations (3.48)-(3.49), respectively. As a consequence, Cell 1 and Cell 2 share the same anode and cathode inlet velocities while Cell 3 takes a third of these values due to the fact that each reactant stream is equally distributed between the three inlets. The operating parameters for wet and dry conditions are summarised in Table 6.2 and Table 6.3, respectively.

Parameter	Value
Operating pressure (atm)	2
Operating temperature (°C)	80
Saturation pressure at operating pressure (atm)	0.4669
Relative humidity of anode/cathode streams (%)	100/50
Stoichiometry of anode/cathode streams	3/2
Anode gas inlet velocity for Cells 1 & 2 (Cell 3) (ms^{-1})	1.554 (0.518)
Anode gas inlet Reynolds number for Cells 1 & 2 (Cell 3)	61.96 (20.65)
Hydrogen/water vapour mole fractions	0.767/0.233
Cathode gas inlet velocity for Cells 1 & 2 (Cell 3) (ms^{-1})	2.141 (0.714)
Cathode gas inlet Reynolds number for Cells 1 & 2 (Cell 3)	192.15 (64.05)
Oxygen/water vapour mole fractions	0.185/0.117
Open-circuit voltage, V_{oc} (V)	1.182

Table 6.2 Wet operating conditions.

Parameter	Value
Operating pressure (atm)	2
Operating temperature (°C)	80
Saturation pressure at operating pressure (atm)	0.4669
Relative humidity of anode/cathode streams (%)	50/50
Stoichiometry of anode/cathode streams	3/2
Anode gas inlet velocity for Cells 1 & 2 (Cell 3) (ms^{-1})	1.349 (0.450)
Anode gas inlet Reynolds number for Cells 1 & 2 (Cell 3)	36.26 (12.09)
Hydrogen/water vapour mole fractions	0.883/0.117
Cathode gas inlet velocity for Cells 1 & 2 (Cell 3) (ms^{-1})	2.141 (0.714)
Cathode gas inlet Reynolds number for Cells 1 & 2 (Cell 3)	192.15 (64.05)
Oxygen/water vapour mole fractions	0.185/0.117
Open-circuit voltage, V_{oc} (V)	1.184

Table 6.3 Dry operating conditions.

6.2 Steady-state Performance

6.2.1 Wet Condition

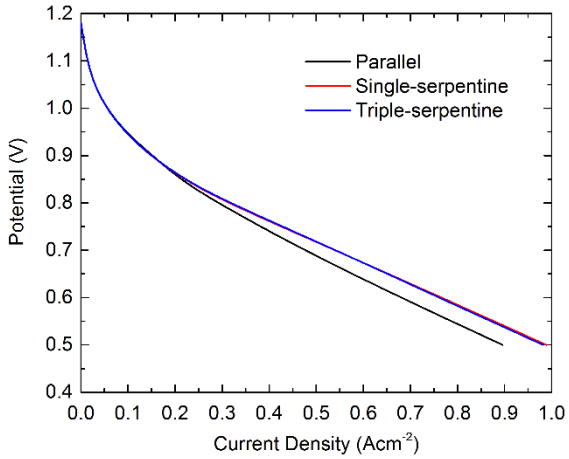

Figure 6.5 Polarisation curves of the three cells under wet operation.

Figure 6.5 shows the polarisation curves for all three cells under a wet condition. It is clear from the figure that the parallel cell comes last in the test while the other two serpentine cells perform equally well. Because the activation loss dominates other losses at low current operation and since all other electrochemical properties are the same in all cells, the performance of each cell is not dependent on the flow-field design. As a result, there is negligible difference in performance among the three cells within this region. On the other hand, as the operating voltage decreases, the fuel utilisation is increased while more water is present in the cell, the cell's output current becomes more sensitive to the water management within the cell. The effect of flow-field configuration starts to take place as a larger discrepancy exists in the polarisation curves within the ohmic and mass transport-limit regions. A close inspection on the polarisation curves suggests that the single-serpentine cell performs slightly better than its triple-serpentine counterpart.

One of the greatest benefits of CFCD is the ability to visualise virtually any flow-field variable with no extra cost whereas additional measuring devices or even a re-test might be required in an experimental study. In order to aid in the discussion, important flow-field variables are averaged over the region of interest and given in Figure 6.6. From the figure, it is seen that all water-related parameters (Figure 6.6a-d) of the parallel cell are higher than the two cells despite the fact that its performance is lower. This suggests that the parallel cell does not benefit from a higher protonic conductivity or the presence of more water in the cell. Rather, it suffers from liquid water flooding especially in the cathode gas diffusion layer.

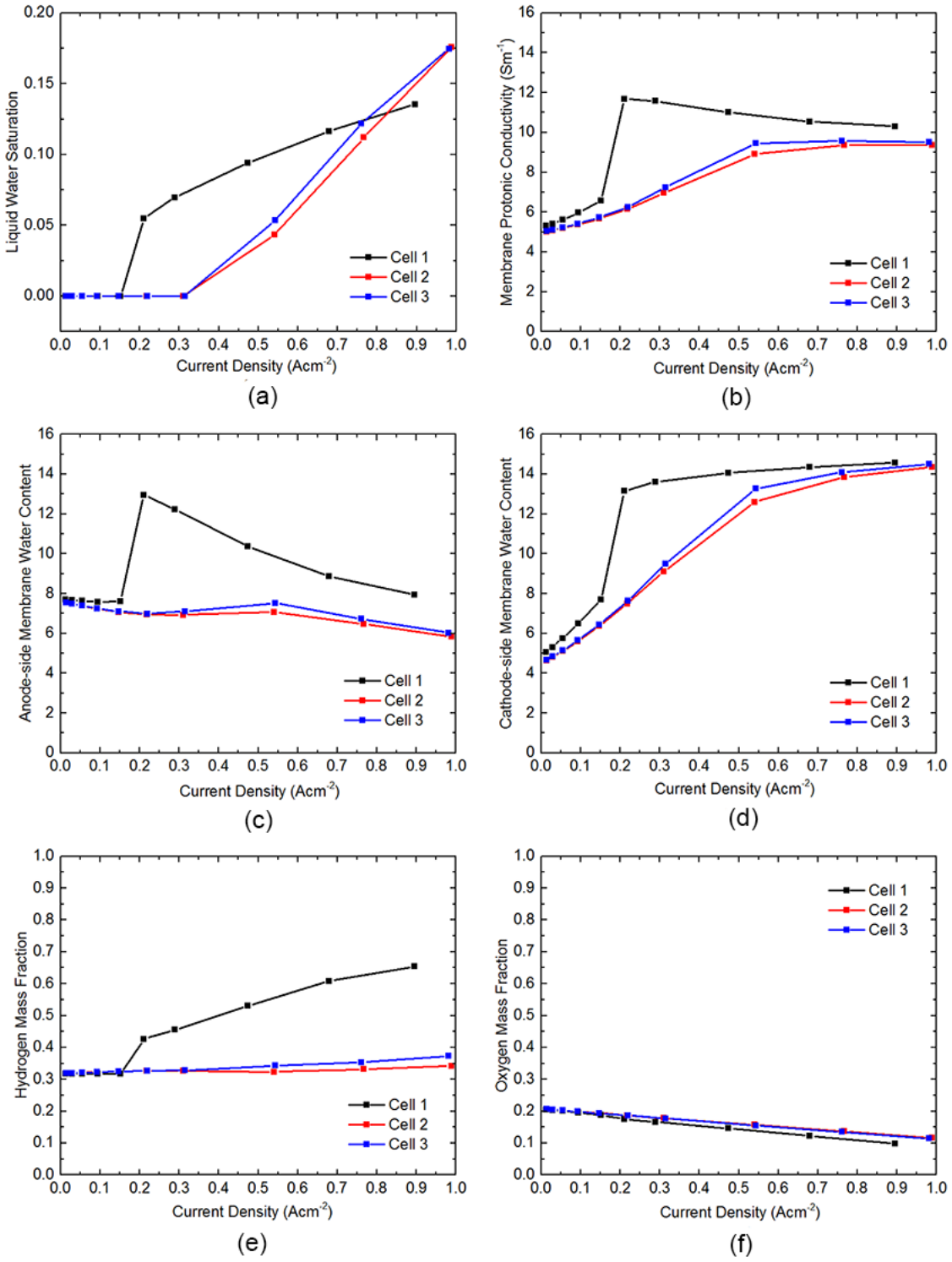

Figure 6.6 Flow-field variables: (a) volume-averaged liquid water saturation in GDL_{ca}, (b) volume-averaged protonic conductivity in PEM, (c) area-averaged anode-side membrane water content at CL_{an}/PEM interface, (d) area-averaged cathode-side membrane water content at CL_{ca}/PEM interface, (e) area-averaged hydrogen mass fraction at GDL_{an}/CL_{an} interface, and (f) area-averaged oxygen mass fraction at GDL_{ca}/CL_{ca} interface.

Figure 6.6c-d reveal an interesting behaviour of the membrane water content. Even though the membrane is very thin, having a thickness in the order of 100 microns, the water content on its two sides are noticeably different. Moreover, the behaviour of water content on the two sides also differs. It can be seen that the anode-side membrane becomes drier as the operating current increases which is caused by the electro-osmosis. At the cathode side of the membrane, the combination of incoming water flux from the anode and increased local water generation results in an accumulation of water as seen in the figure.

When a cell is operated at a higher current, more fuel and oxidant are consumed and the mass fractions at the active sites are expected to decrease. This is true for the oxygen as shown in Figure 6.6f. However, the mass fraction of hydrogen in Figure 6.6e is somewhat counter-intuitive where it increased with the operating current. It should be reminded that water in the anode gas stream is also consumed during the operation. Because a water vapour molecule is much heavier than a hydrogen gas molecule (comparing 18 kg $kmol^{-1}$ to 2 kg $kmol^{-1}$), hence the hydrogen mass fraction appears to increase when it is consumed.

In judging whether a particular flow-field design is superior to the others, using the polarisation curve as a sole indicator is not sufficient. Besides, local distribution of important variables must be investigated. In order for the performance of each flow-field design to become visible, all contours and velocity vector plots presented in the next sections are taken at the operating voltage of 0.50 V where the performance of the three cells differs the most.

Electrochemistry Aspect

The major task of a flow-field is to distribute the reactant species over the active area in order to promote a uniform current generation. Having achieved uniform current density means the temperature variation within the cell is minimum. This reduces thermal and mechanical stresses that can permanently damage the membrane's structure and its functions.

The local current density and hydrogen/oxygen mass fraction at the GDL_{ca}/CL_{ca} interface are shown in Figure 6.7, Figure 6.8, and Figure 6.9, respectively. For all cells, the current density is greatest near the inlet and decreases towards the exit. Taking uniformity of current density into account, Figure 6.7 reveals that Cell 2 has the most uniform current density followed by Cell 3 whereas Cell 1 has the worst uniformity. The minimum current seen as a blue patch in Cell 1 corresponds to the region with least electrochemical activity. This is mainly caused by liquid water flooding which prevents the reactant species from reaching the active sites. This is confirmed by low oxygen concentration and high water saturation on the same region in Figure 6.9 and Figure 6.10, respectively.

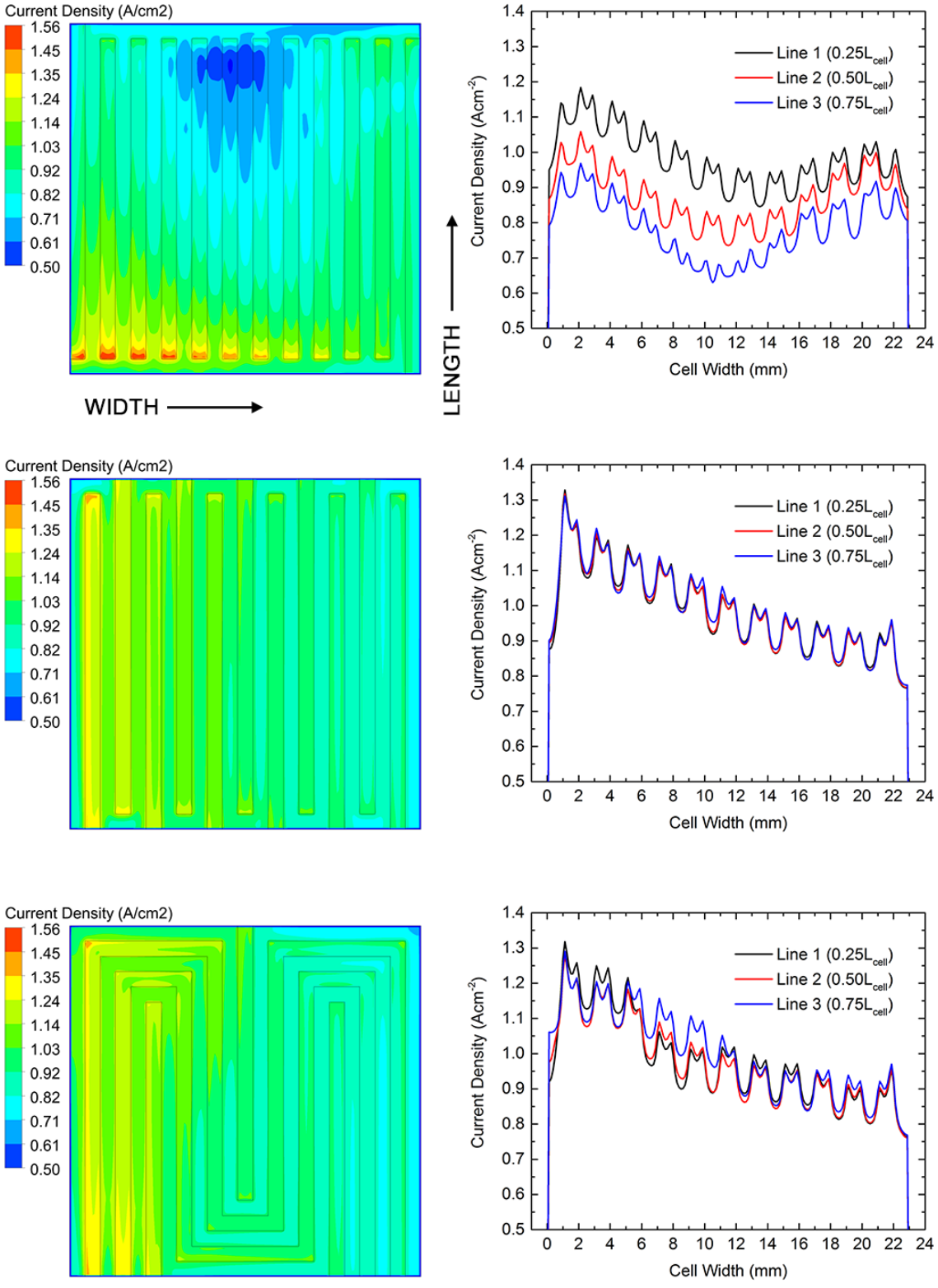

Figure 6.7 Current density contours of parallel (top), single-serpentine (middle), and triple-serpentine (bottom) cells. Corresponding local current density across cell width at three positions along cell length are shown on the right.

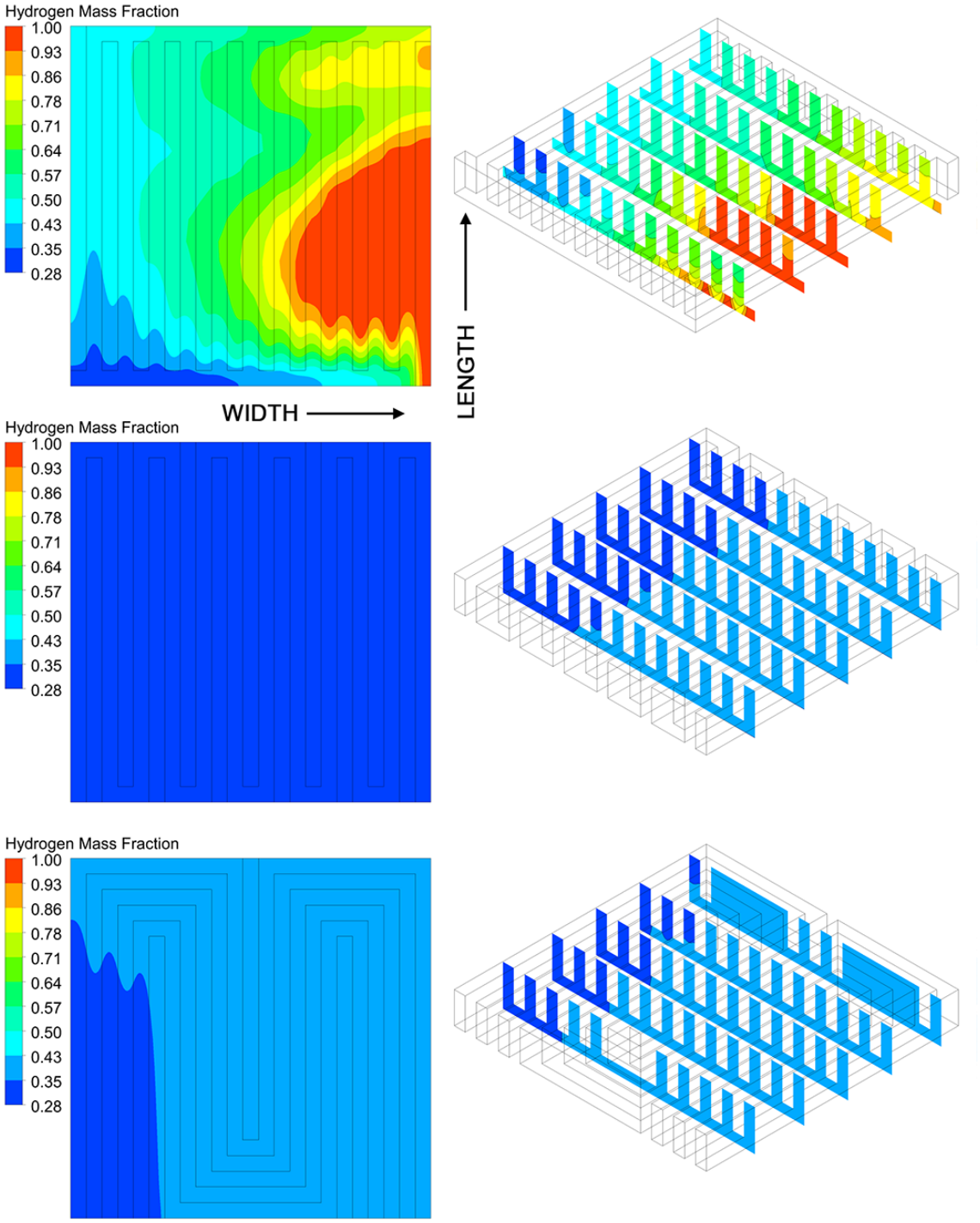

Figure 6.8 Hydrogen mass fraction contours of parallel (top), single-serpentine (middle), and triple-serpentine (bottom) cells. Cell width and length are scaled down by 65%.

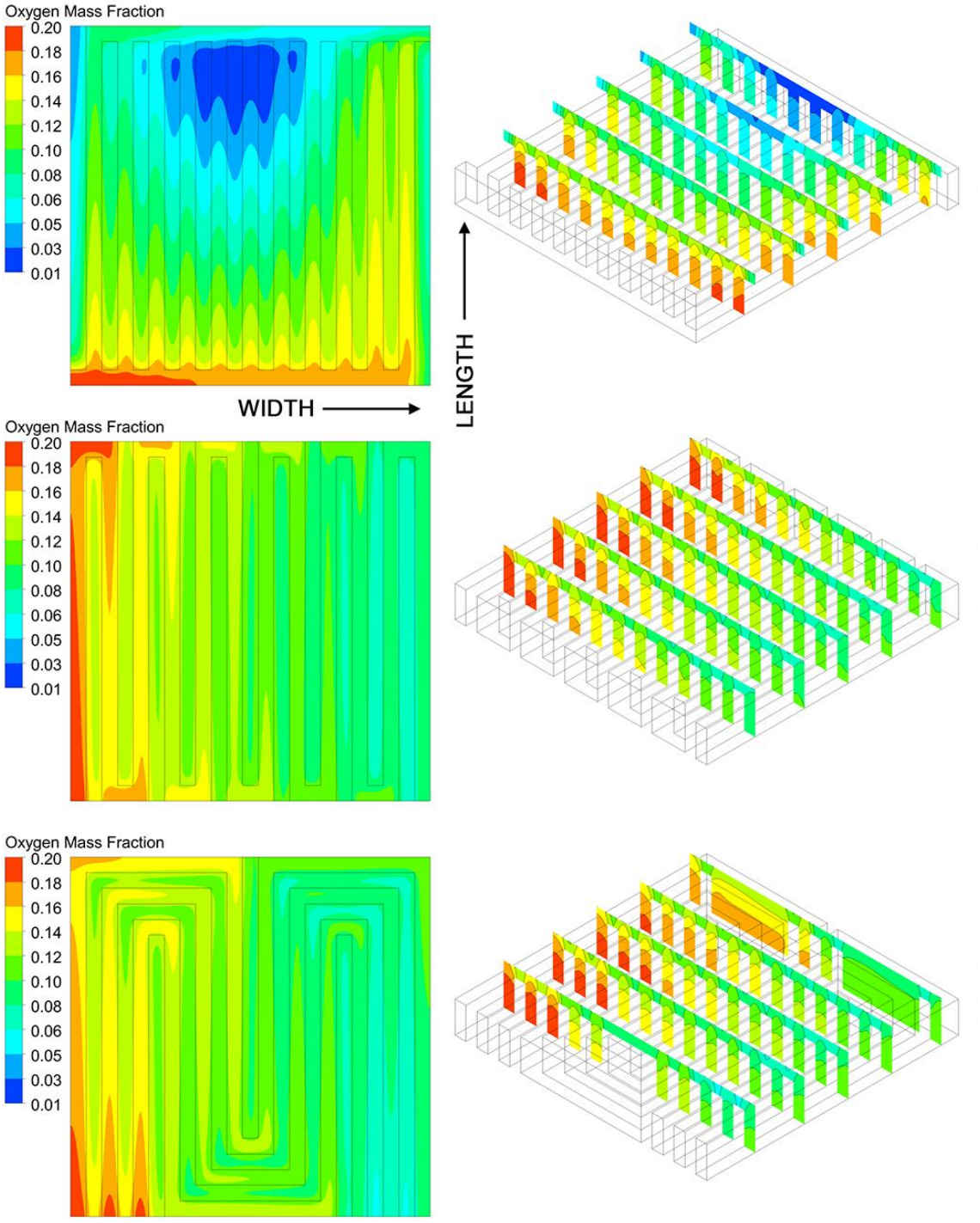

Figure 6.9 Oxygen mass fraction contours of parallel (top), single-serpentine (middle), and triple-serpentine (bottom) cells. Cell width and length are scaled down by 65%.

It should be emphasised that current density is related to the local concentration of reactant species to some extent. Higher species concentration simply suggests that more electron is being released locally. Besides, these electrons have to travel to the external circuit in order to make a useful electricity and the only path is through the contact patch between the rib and GDL surface. In other words, only the charge flux in the z-direction (through-plane) matters. In fact, the local current density is determined by the mutual effect of species concentration and resistance to the flow of electron therefore high current density does not necessarily occur at the region with high species mass fraction as discussed in the author's previous work [89].

The plots of local current density across the cell width at three locations along the cell length, $0.25L_{cell}$, $0.50L_{cell}$, and $0.75L_{cell}$, are also given next to each current density contour. As expected, the current density peaks at the interface between the flow channel and current collector rib rather than in the middle of the flow channel because it is the location that offers the balance between high reactant species concentration and the shortest path for electron to flow to the electronically conductive rib.

Figure 6.8 and Figure 6.9 show that significant variations of hydrogen and oxygen mass fractions exist in all directions. Both species are consumed in the reaction therefore their concentrations would have decreased along the channel from the inlet towards the exit. Nevertheless, compared to the inlet, hydrogen concentration at the outlet does not deplete as much due to a high stoichiometry used and therefore remains relatively constant. On the other hand, significant amount of water vapour, particularly near the exit region, is lost to the cathode through electro-osmosis resulting in an increase of hydrogen mass fraction towards the outlet. Unlike hydrogen, oxygen mass fraction decreases in all direction. From Figure 6.9, a large mass fraction gradient can be seen especially on the xz-plane. Because oxygen is much heavier than hydrogen thus not as readily diffusible. Oxygen concentration is therefore much lower in regions which are less accessible, in particular underneath the ribs.

Figure 6.9 also demonstrates the advantage of a serpentine flow-field over the conventional parallel design. In addition to diffusion, the transport of oxygen to the active sites is aided by a more effective convection-enhanced cross-flow that occurs between two adjacent channels. As a result, oxygen concentration in the GDLs and CLs is high and uniform for the two serpentine cells. The oxygen concentration in the parallel cell, on the other hand, is much lower and highly non-uniform. Additionally, the active area of the parallel is not fully utilised as oxygen depletion is seen over a large portion indicating the inferiority of such a design.

Fluid Dynamics Aspect

The velocity field in the flow channels is closely coupled to water removal ability of the cell. Once water vapour has condensed into liquid, it is transported through the porous layers by means of a capillary effect before emerging as droplets, slugs, or liquid films at the interface between the flow channel and GDL. These liquids are then pushed out of the flow channels at the outlet by the incoming reactant stream.

Figure 6.10 demonstrates this close relationship in which the contours of velocity and water vapour mass fraction at the middle plane of the cathode flow-field are shown. The maximum flow velocity of the parallel cell is comparable to the single-serpentine cell, however, this high velocity only occurs near the inlet and outlet regions whereas it stays low in most area of the flow-field. The cathode stream only flows through the two outermost channels whereas it bypasses the middle channels. This is confirmed by the contour on the right where high water vapour mass fraction is present in the middle region of the cell.

On the other hand, the velocity fields of the two serpentine cells are much more uniform than the parallel cell. This is likely due to the geometry of the flow channel in this type of flow-field. Unlike the parallel flow-field where the cathode stream could be "selective" in the way it chooses to flow through certain channels while avoids some, the cathode stream is "forced" to flow through a single and continuous channel in order to reach the outlet. This, however, has a great benefit in water removal and hence the water vapour mass fraction is significantly smaller as seen in the figure. Interestingly, there is a negligible difference between the water vapour mass fraction contours of the two cells even though the magnitude of velocity field of the triple-serpentine cell is one-third of the single-serpentine cell.

In contrast to the primary flow, which corresponds to the main flow along the channel, a cross-flow occurs in the directions orthogonal to the main flow and hence it is also known as the secondary flow. This secondary flow greatly enhances water removal especially from the porous media such as CLs and GDLs and their relationship are shown in Figure 6.11, Figure 6.12, and Figure 6.13 where the cathode-side velocity vector plot and contour of liquid water saturation at the middle of the cell length are given. Due to the fact that the through-plane dimension of a cell is much smaller than the other two, the cell is therefore scaled down to 20% of its original width in order for the velocity and liquid water saturation contours in the porous layers to become clearly visible. It should also be noted that since the velocity in the flow channels is much higher than in the porous regions, two separate colourbars are used in these figures.

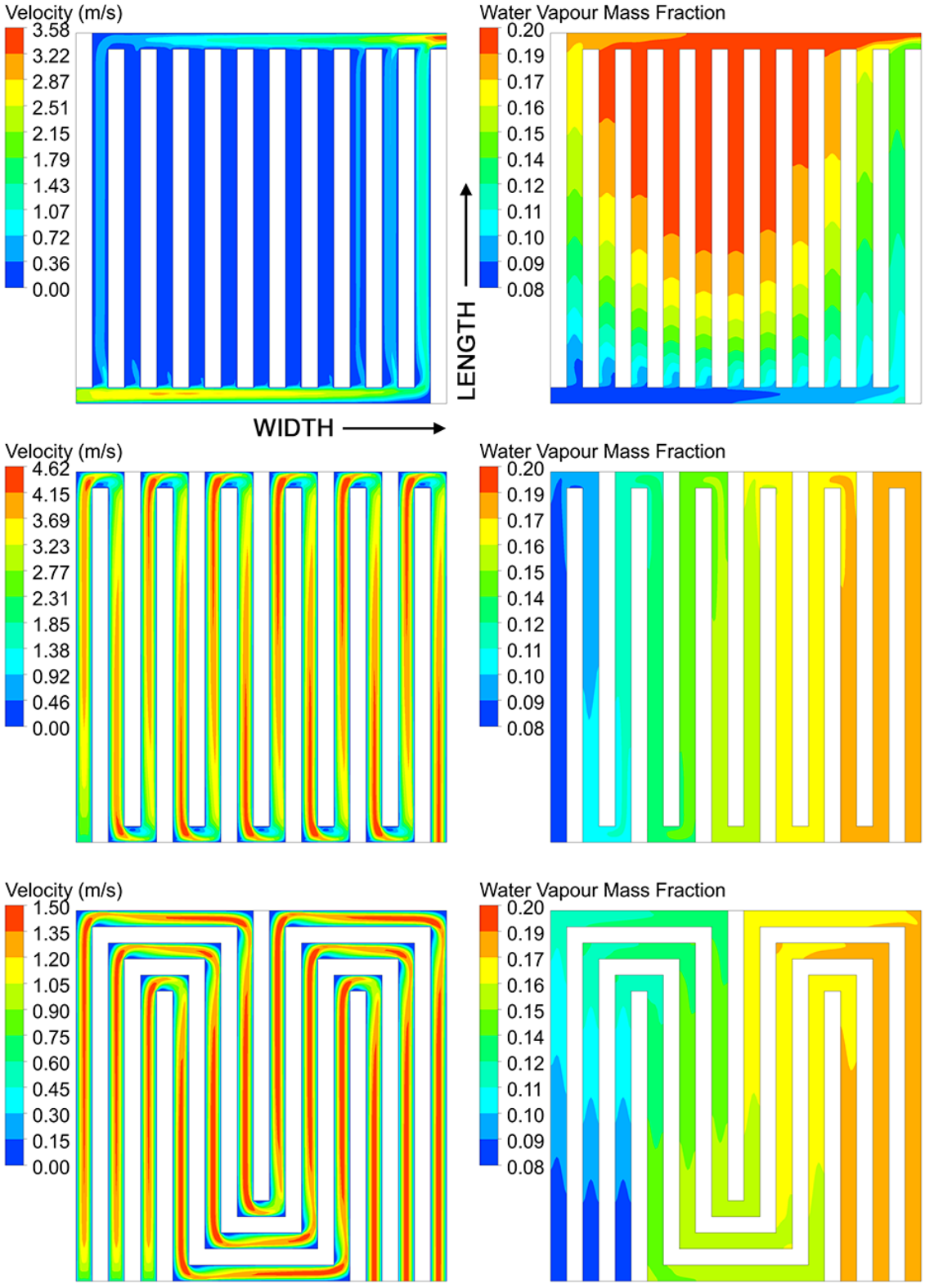

Figure 6.10 Velocity and water vapour mass fraction contours at middle plane of cathode flow-field of parallel (top), single-serpentine (middle), and triple-serpentine (bottom) cells.

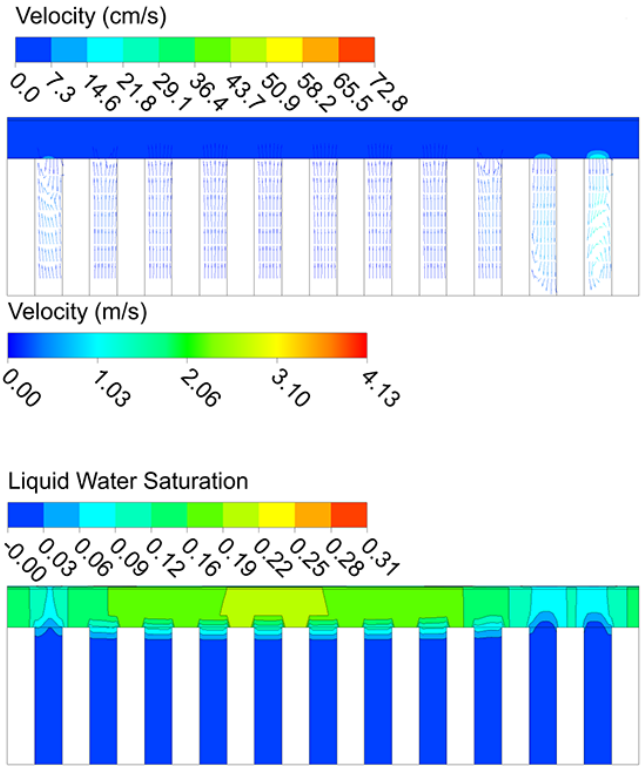

Figure 6.11 Cathode-side velocity and liquid water saturation contours of parallel cell. Top colourbar for porous regions, bottom colourbar for flow channels.

Due to the structure of the porous media which induces more resistance to the flow, the velocity in these regions is much lower than that in the flow channels. Compared to the parallel flow-field, the serpentine flow-field induces a large pressure difference between two adjacent channels which is sufficient for the flow to take the "shortcut" by flowing through the GDL rather than flowing along the channel. As a consequence, the cathode stream is able to penetrate deeper into the porous region as is evident from the velocity contours given in Figure 6.12 and Figure 6.13.

By examining the contours of liquid water saturation, it can be seen that more liquid water is present at the channel/GDL interface than other regions in the flow channels. Away from the flow channels, particularly the under-rib areas, liquid water saturation increases because the cathode stream could not penetrate into these regions. Compared to the parallel cell, water removal in the two serpentine cells is aided by the existence of cross-flows which tend to push water to the outlet. Therefore, more water is removed which results in lower liquid water saturation in these regions.

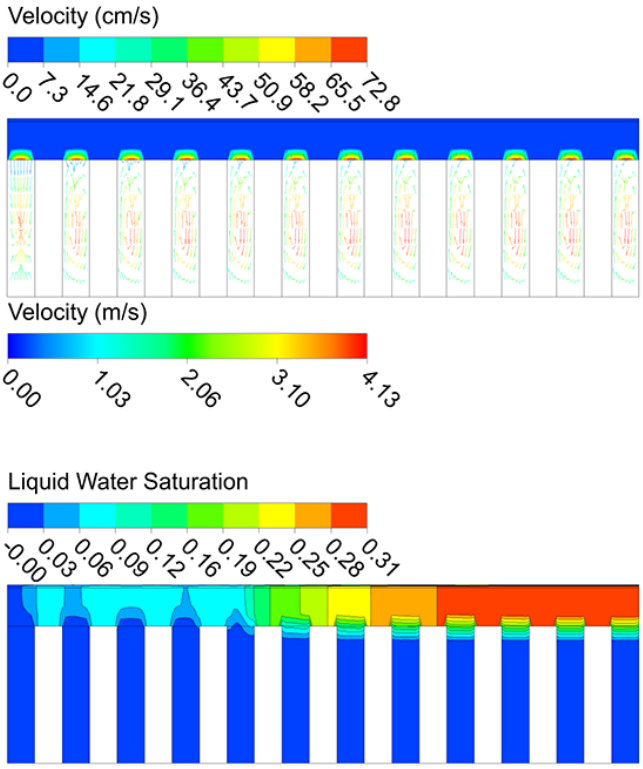

Figure 6.12 Cathode-side velocity and liquid water saturation contours of single-serpentine cell. Top colourbar for porous regions, bottom colourbar for flow channels.

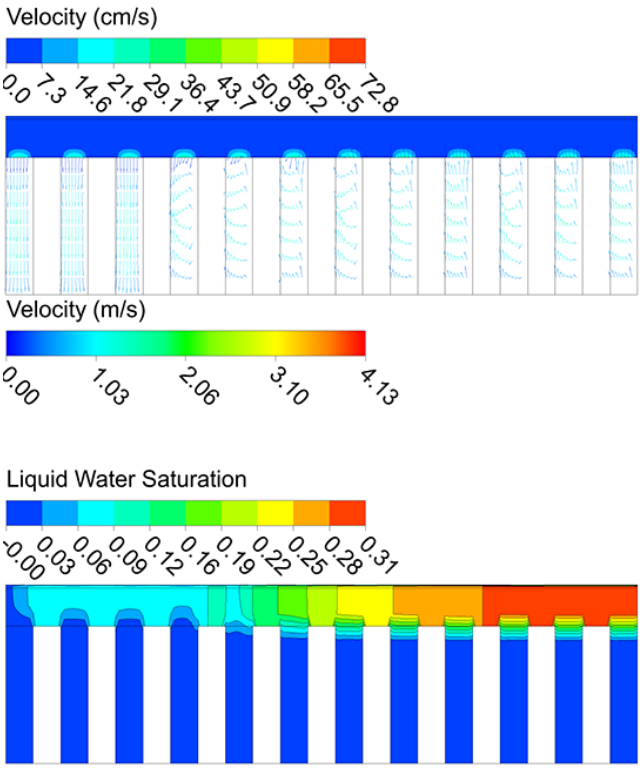

Figure 6.13 Cathode-side velocity and liquid water saturation contours of triple-serpentine cell. Top colourbar for porous regions, bottom colourbar for flow channels.

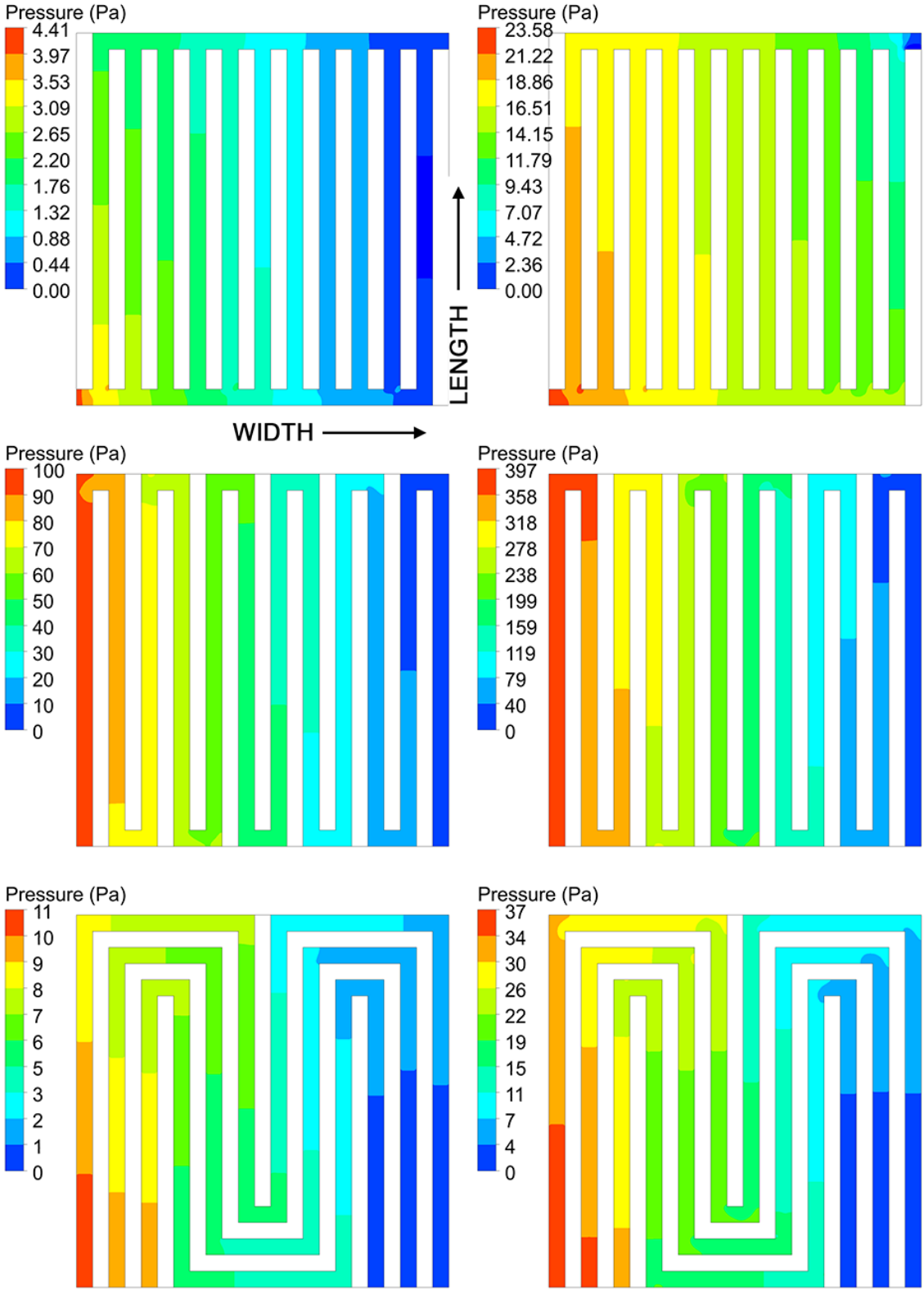

Figure 6.14 Contours of pressure drop between inlet and outlet at middle plane of anode (left) and cathode (right) flow-fields of parallel (top), single-serpentine (middle), and triple-serpentine (bottom) cells.

Lastly, the pressure drop between the flow inlet and outlet for both anode and cathode streams are shown in Figure 6.14. It is evident that pressure drop in the cathode flow-field is considerably larger than in the anode flow-field for all three cells due to a cathode stream being heavier than the anode stream. Additionally, more liquid water is present in the cathode flow-field hence it induces higher pressure drop in order to push this cathode stream through the channels.

A comparison between the three cells reveals that the single-serpentine cell induces the highest pressure drop while the triple-serpentine cell comes in second. This is caused by the relatively long flow channels compared to those in the parallel cell which gives the lowest pressure drop. It should be pointed out that even though the two serpentine flow-fields perform pretty much the same in all aspects as discussed previously, the pressure drop in the triple-serpentine cell is at least one order of magnitude smaller and might be considered advantageous over the single-serpentine flow-field.

6.2.2 Dry Condition

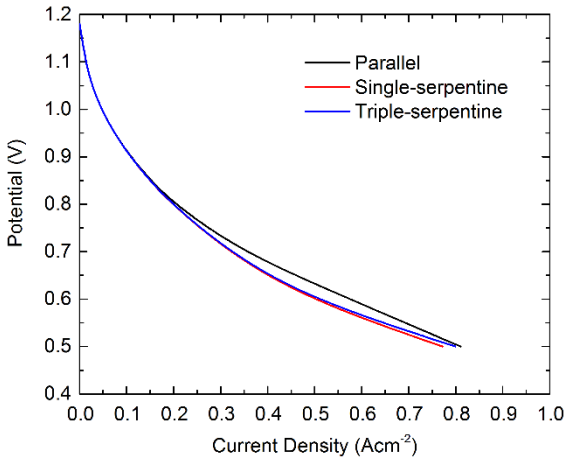

Figure 6.15 Polarisation curves of three cells under dry operation.

The polarisation curves of the three cells under dry reactant streams are shown in Figure 6.15. Compared to the wet operation, the drop in cell performance in terms of current density can be seen from all cells even though hydrogen concentration at the inlet is higher under the dry operation. This indicates the necessity of the humidification of reactant streams. Similarly, the effect of flow-field configuration is negligible at low current density operations hence the difference between the three curves cannot be seen. At elevated current operations, however, it is interesting to see that the parallel cell outperforms the two serpentine cells as opposed to what has been found in Figure 6.5.

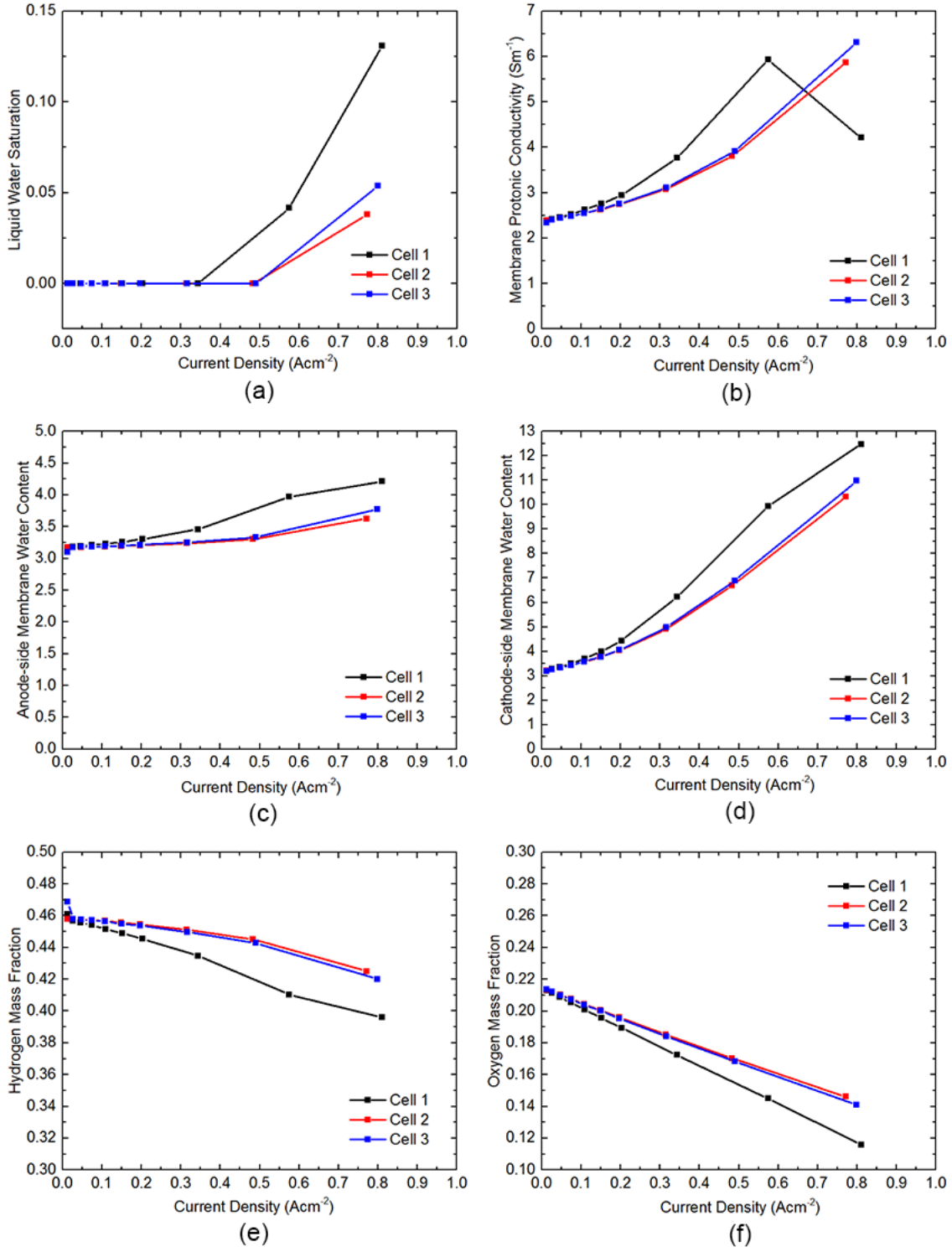

Figure 6.16 Flow-field variables: (a) volume-averaged liquid water saturation in GDL_{ca}, (b) volume-averaged protonic conductivity in PEM, (c) area-averaged anode-side membrane water content at CL_{an}/PEM interface, (d) area-averaged cathode-side membrane water content at CL_{ca}/PEM interface, (e) area-averaged hydrogen mass fraction at GDL_{an}/CL_{an} interface, and (f) area-averaged oxygen mass fraction at GDL_{ca}/CL_{ca} interface.

This reversed trend can be explained by examining the flow-field variables given in Figure 6.16. Due to the inferior water removal ability of a parallel flow-field, more water is left in the parallel cell and this in turn improves the membrane protonic conductivity as seen in Figure 6.16a and Figure 6.16b, respectively. Looking at the water content on the anode side of the membrane in Figure 6.16c, rather than losing water as seen in Figure 6.6c, water is accumulating as the operating voltage decreases. Additionally, Figure 6.16e shows the decrease in hydrogen mass fraction with the operating voltage as opposed to the behaviour found in the wet operation. Because the anode stream is partially humidified, the amount of water lost through electro-osmosis is too small to cause hydrogen mass fraction to increase as seen in Figure 6.6e.

From the above observations, it can be concluded that the performance of the three cells has been controlled by membrane hydration rather than GDL flooding which explains why the parallel cell outperforms the other two cells.

Electrochemistry Aspect

The current density contour together with local current density across the cell width for the three cells are shown in Figure 6.17. Surprisingly, rather than decreasing, the current density increases towards the outlet region where membrane hydration is higher. This confirms the conclusion above that when dry reactant streams are used the performance of the cell is governed by membrane hydration. Nevertheless, the current density distribution in the two serpentine cells is much more uniform than the parallel cell.

The mass fraction of hydrogen and oxygen are shown in Figure 6.18 and Figure 6.19, respectively. Because both species are consumed in the electrochemical reaction, their concentration depletes along the channel towards the outlet. However, oxygen mass fraction for each cell, especially in the porous layers, is greater than the ones in Figure 6.9. This is due to a higher inlet hydrogen mass fraction.

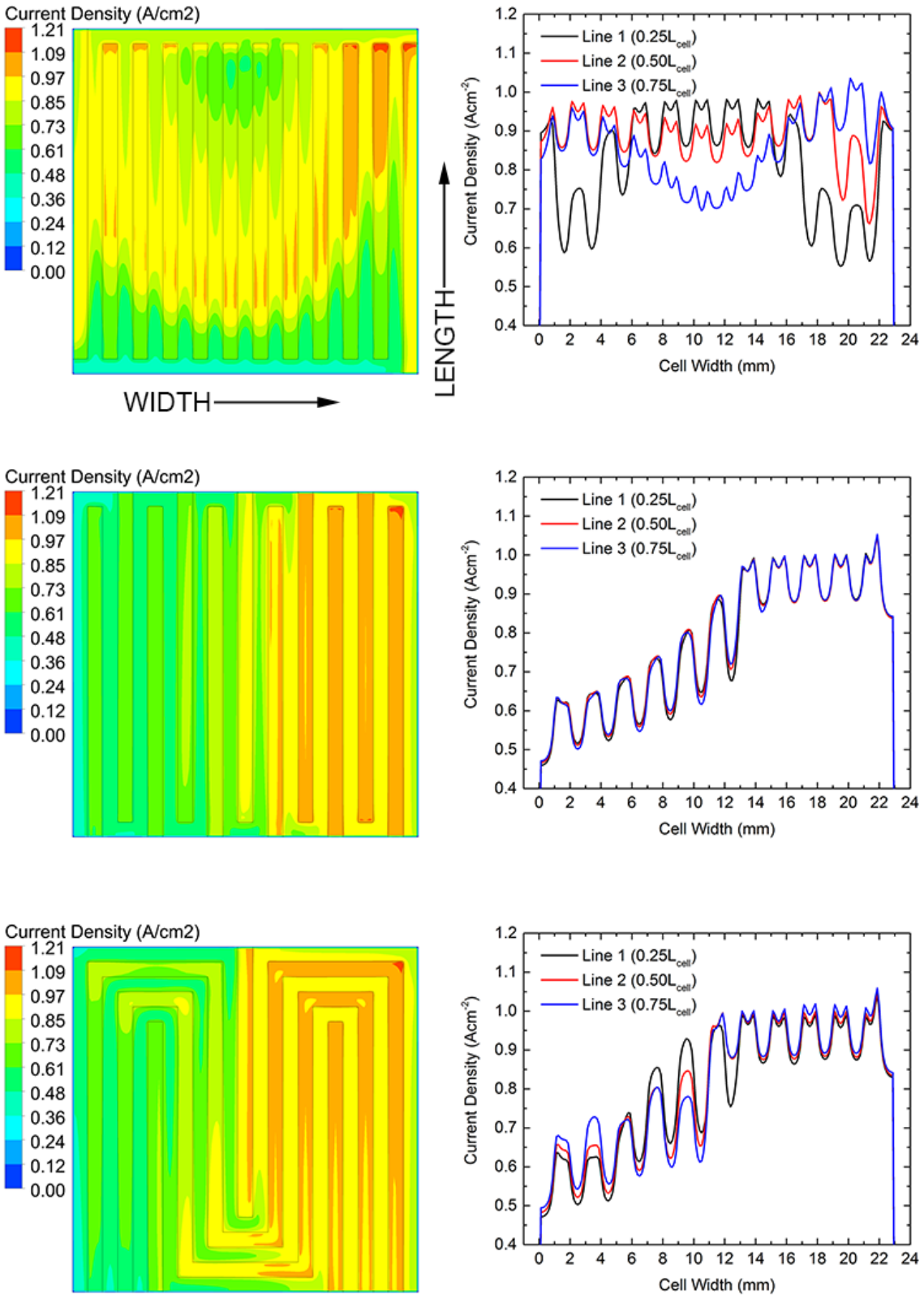

Figure 6.17 Current density contours of parallel (top), single-serpentine (middle), and triple-serpentine (bottom) cells. Corresponding local current density across cell width at three positions along cell length are shown on the right.

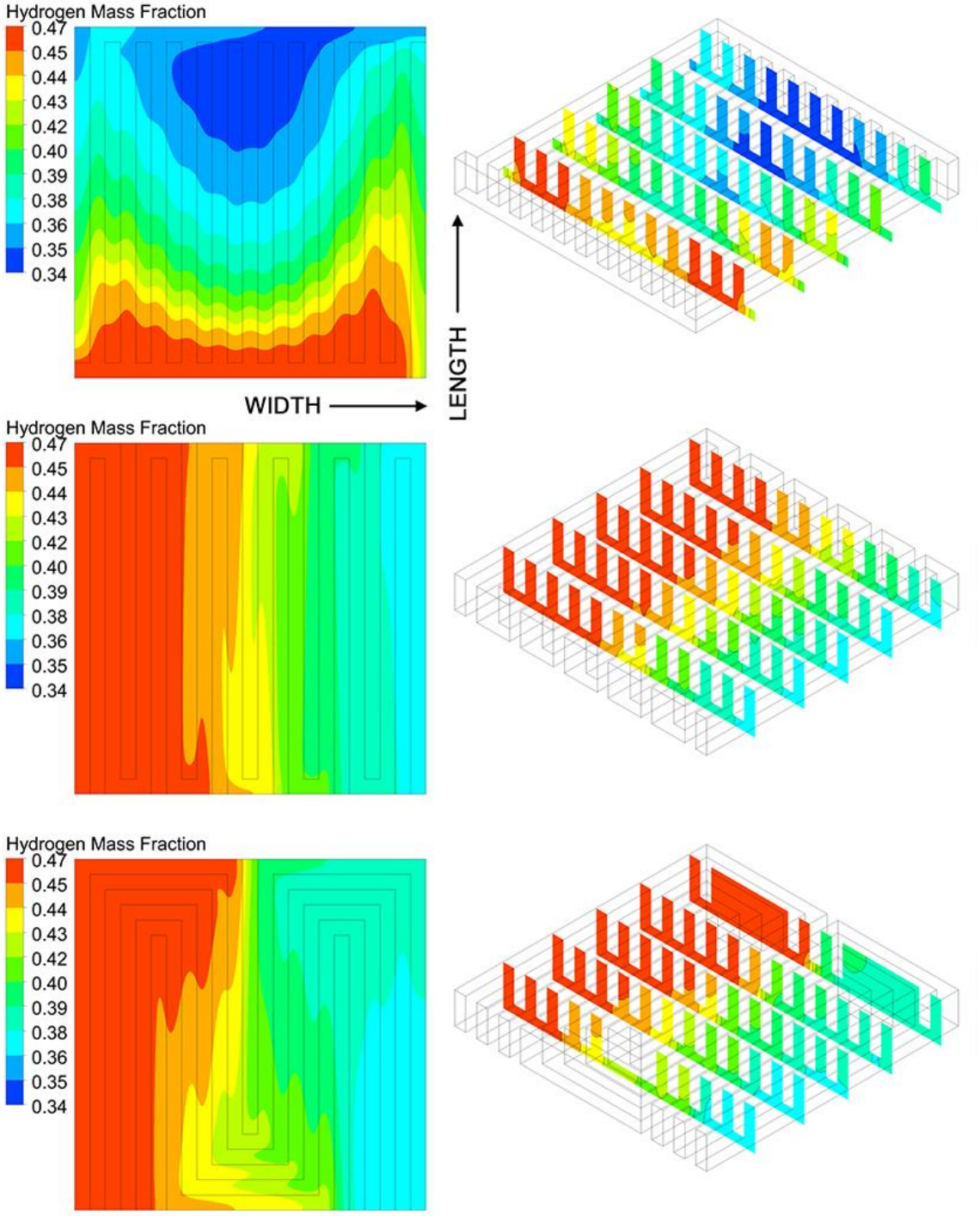

Figure 6.18 Hydrogen mass fraction contours of parallel (top), single-serpentine (middle), and triple-serpentine (bottom) cells. Cell width and length are scaled down by 65%.

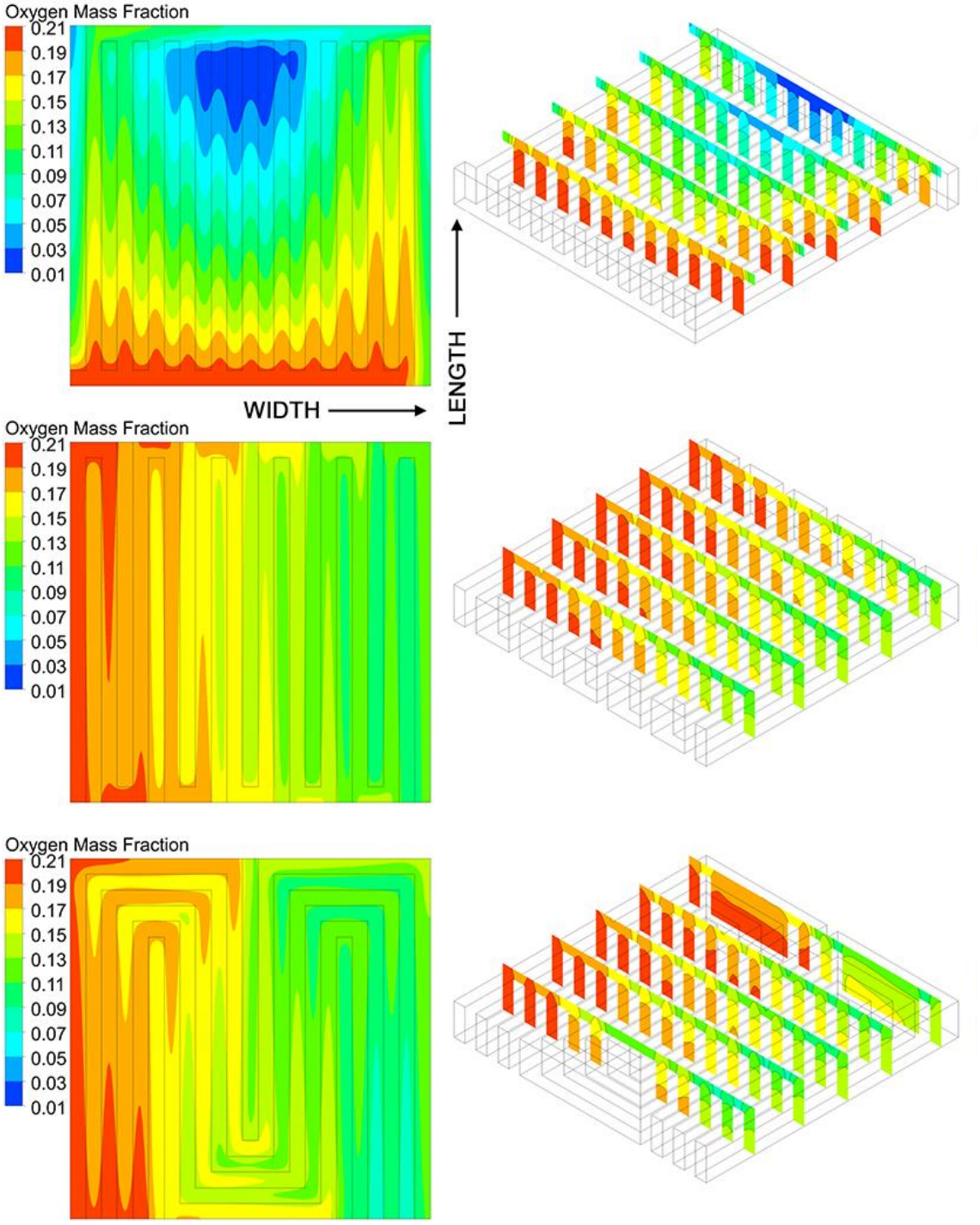

Figure 6.19 Oxygen mass fraction contours of parallel (top), single-serpentine (middle), and triple-serpentine (bottom) cells. Cell width and length are scaled down by 65%.

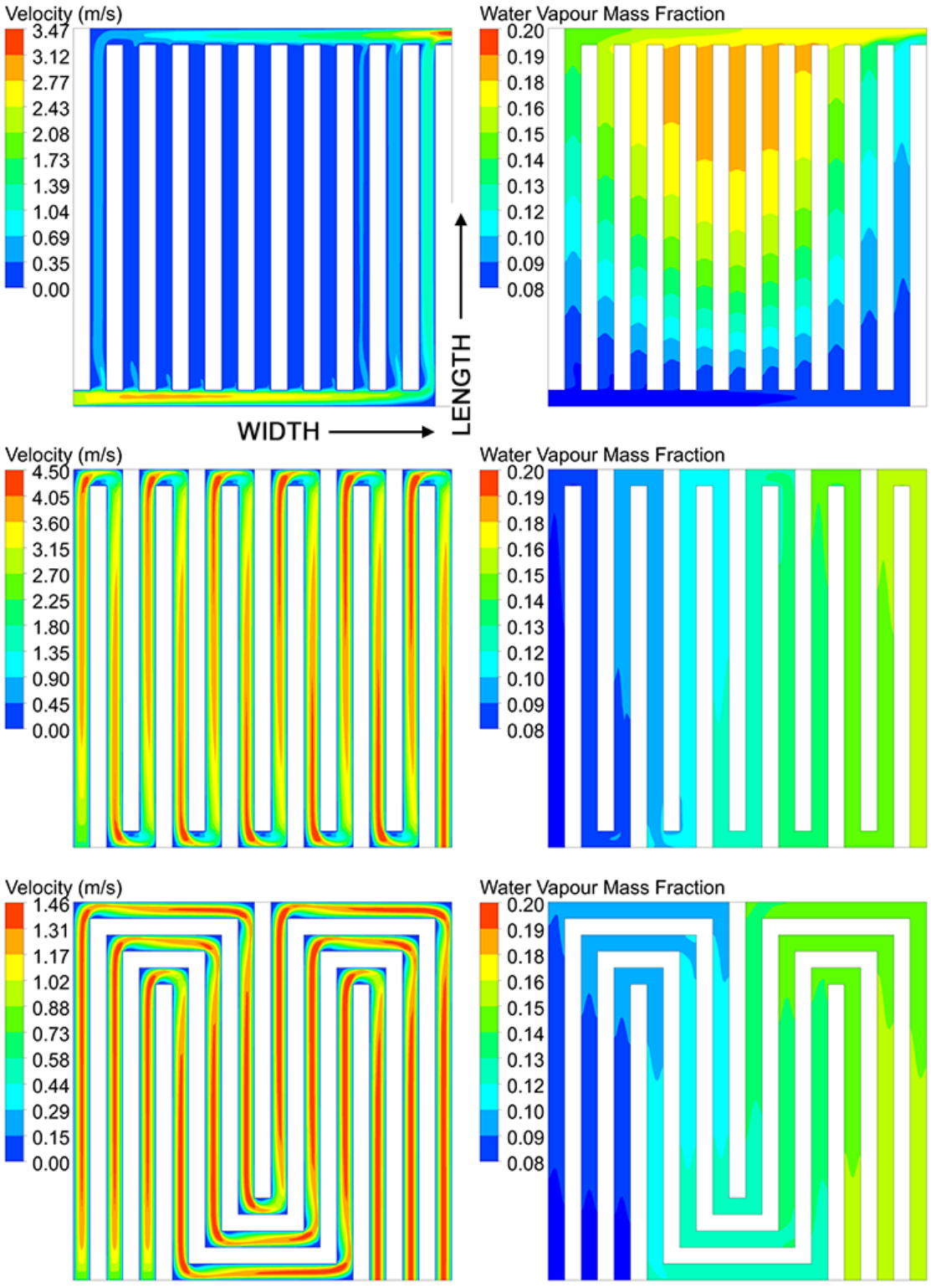

Figure 6.20 Velocity and water vapour mass fraction contours at middle plane of cathode flow-field of parallel (top), single-serpentine (middle), and triple-serpentine (bottom) cells.

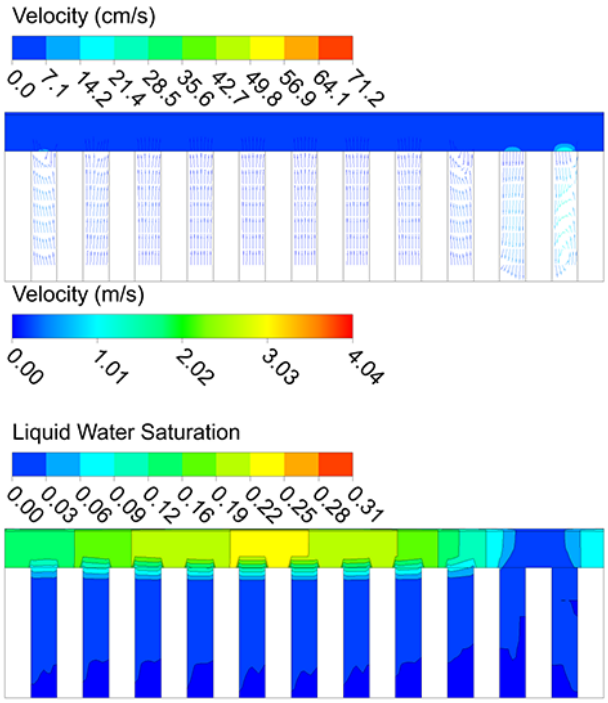

Figure 6.21 Cathode-side velocity and liquid water saturation contours of parallel cell. Top colourbar for porous regions, bottom colourbar for flow channels.

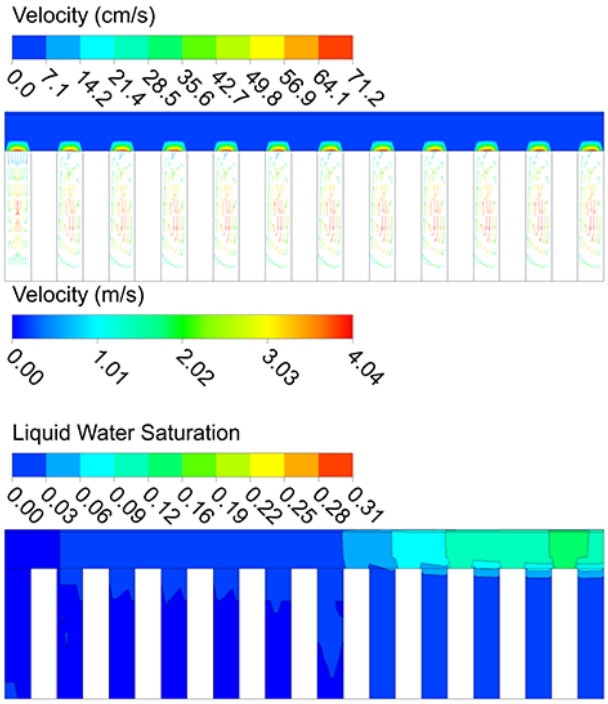

Figure 6.22 Cathode-side velocity and liquid water saturation contours of single-serpentine cell. Top colourbar for porous regions, bottom colourbar for flow channels.

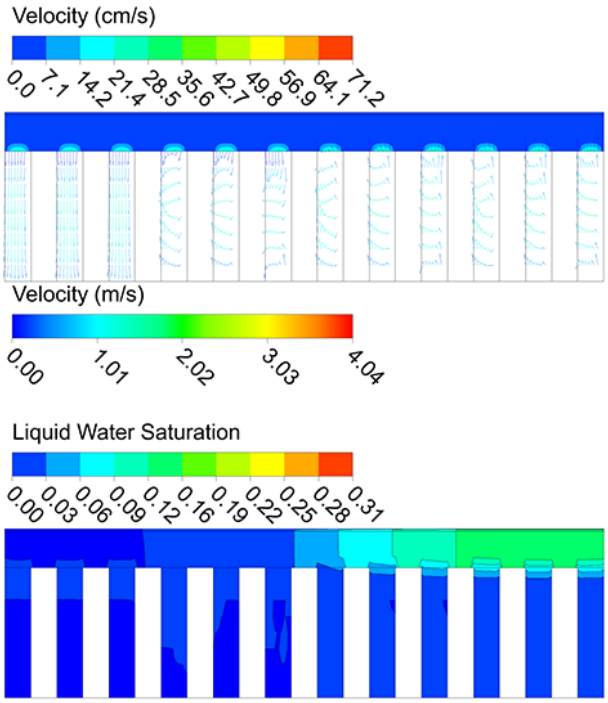

Figure 6.23 Cathode-side velocity and liquid water saturation contours of triple-serpentine cell. Top colourbar for porous regions, bottom colourbar for flow channels.

Fluid Dynamics Aspect

The contours of primary flow velocity and water vapour mass fraction at the middle plane of cathode flow-field are presented in Figure 6.20. Compared to Figure 6.10, the flow velocity in each cell is slightly lower whereas the distribution follows the same pattern. It is evident that much less water exists in the three cells under this dry operating condition.

The contours of water saturation for each cell shown in Figure 6.21, Figure 6.22, and Figure 6.23 suggest that most of the porous region remains relatively dry confirming that the three cells are not suffering from liquid water flooding even the operating voltage is as low as 0.50 V.

The contour of pressure drop in both anode and cathode flow-fields are shown in Figure 6.24. From the figure, no significant difference in the magnitude of pressure drop or distribution pattern can be detected when switching to a drier anode stream.

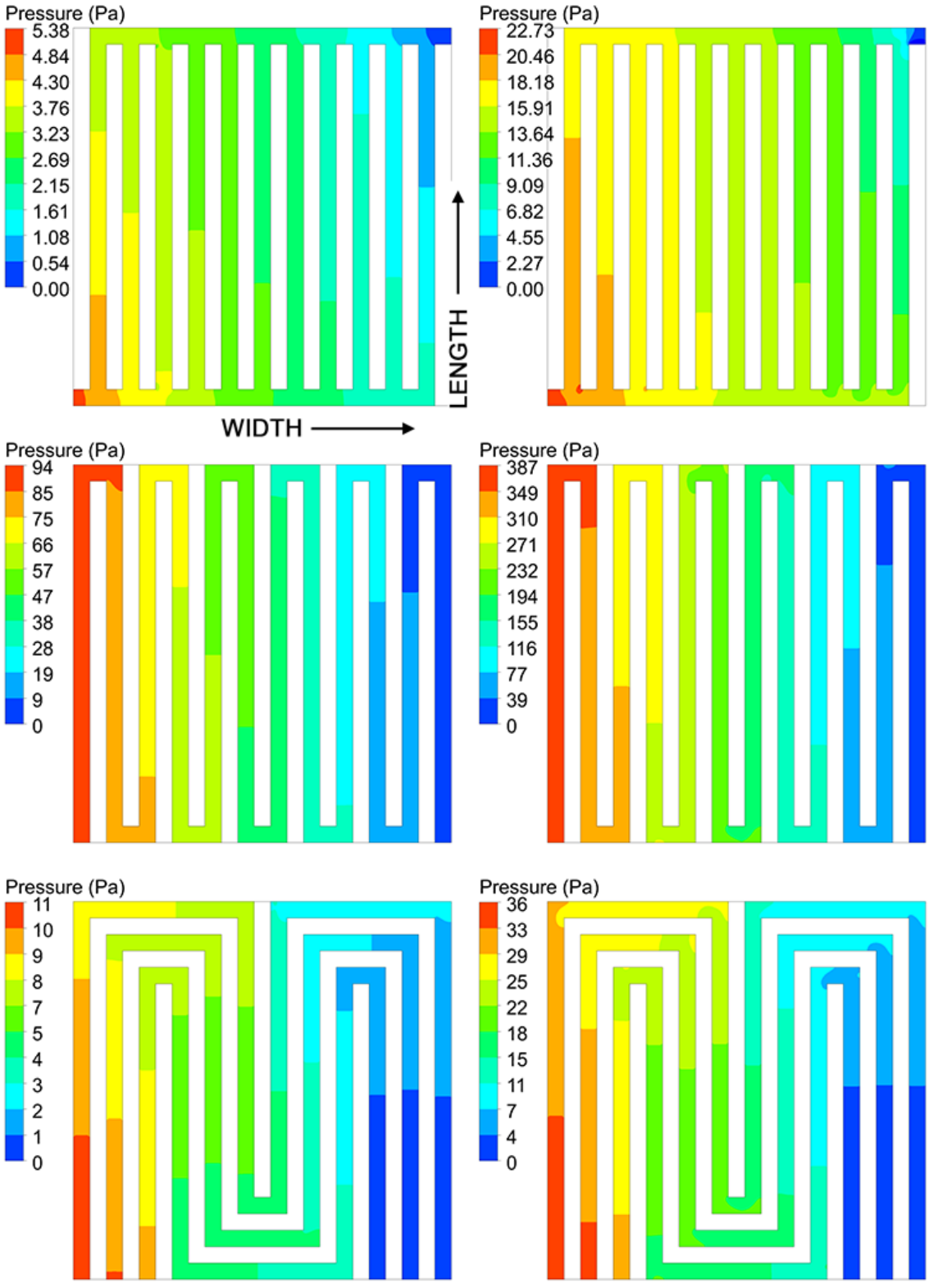

Figure 6.24 Contours of pressure drop between inlet and outlet at middle plane of anode (left) and cathode (right) flow-fields of parallel (top), single-serpentine (middle), and triple-serpentine (bottom) cells.

6.3 Transient Performance

The results from Chapter 5 reveal that the faster the voltage change rate, the greater the current spike or trough, and it is more likely for current overshoot and undershoot to occur. Therefore, a step change in voltage has been applied to the three cells in this study. To resemble the normal operating range of a practical PEM fuel cell, the voltage is stepped up and down between 0.6 V and 0.7 V as summarised in Table 6.4.

	Path (V)	Time (s)	Corresponding Rate (Vs^{-1})
Step Down	0.7→0.6	0.001	100
Step Up	0.6→0.7	0.001	100

Table 6.4 Details of voltage step-down and step-up used in current study.

Due to an extremely fast voltage change rate, a sufficiently small time-step size must be used. As mentioned previously in Chapter 4, varying time-step sizes will be adapted in each transient run. The total physical time is limited to three seconds in order to save the computational time while the number of inner iteration is set to thirty. All transient run-related parameters are summarised in Table 6.5.

Time Interval (s)	Time-step Size, Δt (s)	Number of Time Step
0.000 – 0.002	0.00001	200
0.002 – 0.100	0.00010	980
0.100 – 3.000	0.00500	580

Table 6.5 Transient run-related parameters.

All three cells have been operated under both wet and dry conditions and the current response under dry reactant streams are reported in Figure 6.25. From the figure, a three-step response can be seen in all cells. However, neither current overshoot nor undershoot is detected therefore the results from the dry operation are excluded from the discussions.

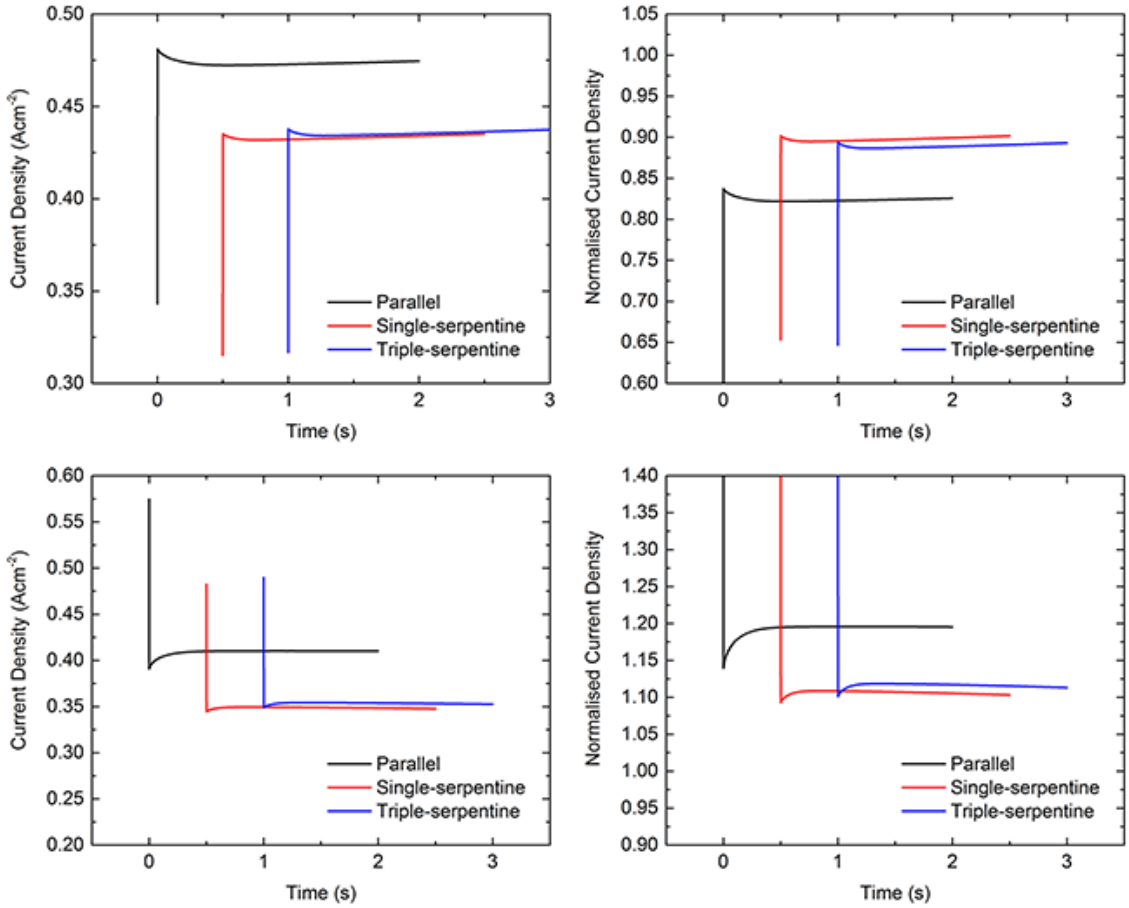

Figure 6.25 Current response curves of the three dry cells to voltage step-down (top) and voltage step-up (bottom).

6.3.1 The Downwards Path

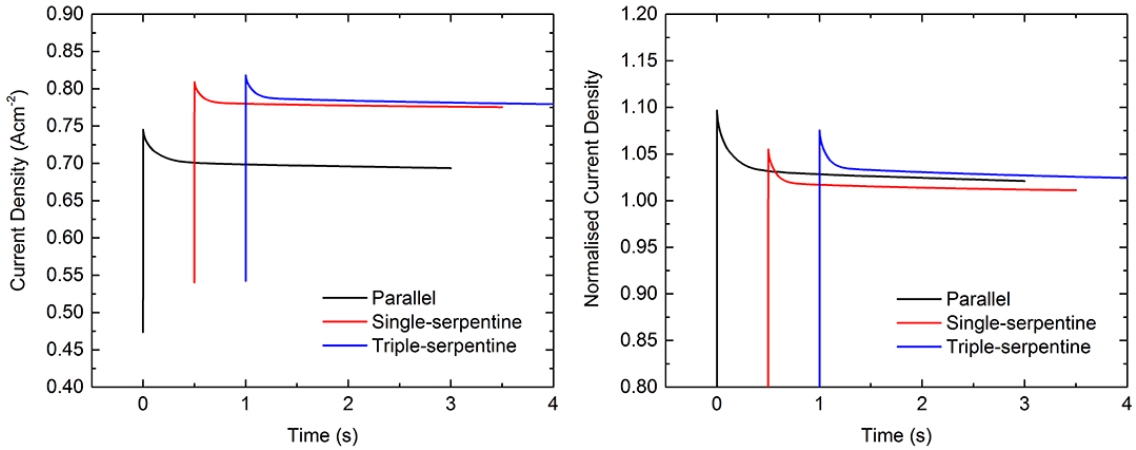

Figure 6.26 Current response (left) and normalised current response (right) to voltage step-down under wet operation.

The current response to a voltage step-down of each cell under wet reactant streams is shown in Figure 6.26. In addition, each current response curve has been normalised by its corresponding final value and is presented in the same figure. As expected, the current overshoots of the three cells are significantly larger than the ones found in the single-channel model where, for the parallel, single-serpentine, and triple-serpentine cells, the current overshoots its final value by approximately 10%, 5%, and 7.5%, respectively.

It is interesting that the three-step response, normally seen in the single-channel model, could not be seen in these square cells. Rather, the three cells respond with a sudden rise of current which peaks at the time when the final voltage is reached, which is followed by a sharp drop in current. The current then continues to decrease approaching the final value from the top margin.

Clearly, a noticeable difference in magnitude of current overshoot between the three cells can be seen and there must be certain parameters which determine this magnitude in each cell. A close inspection on the distribution of local current density along Lines 1, 2, and 3 (defined in Figure 6.7 and Figure 6.17) as shown in Figure 6.27, Figure 6.28, and Figure 6.29 reveals how these current overshoots are formed.

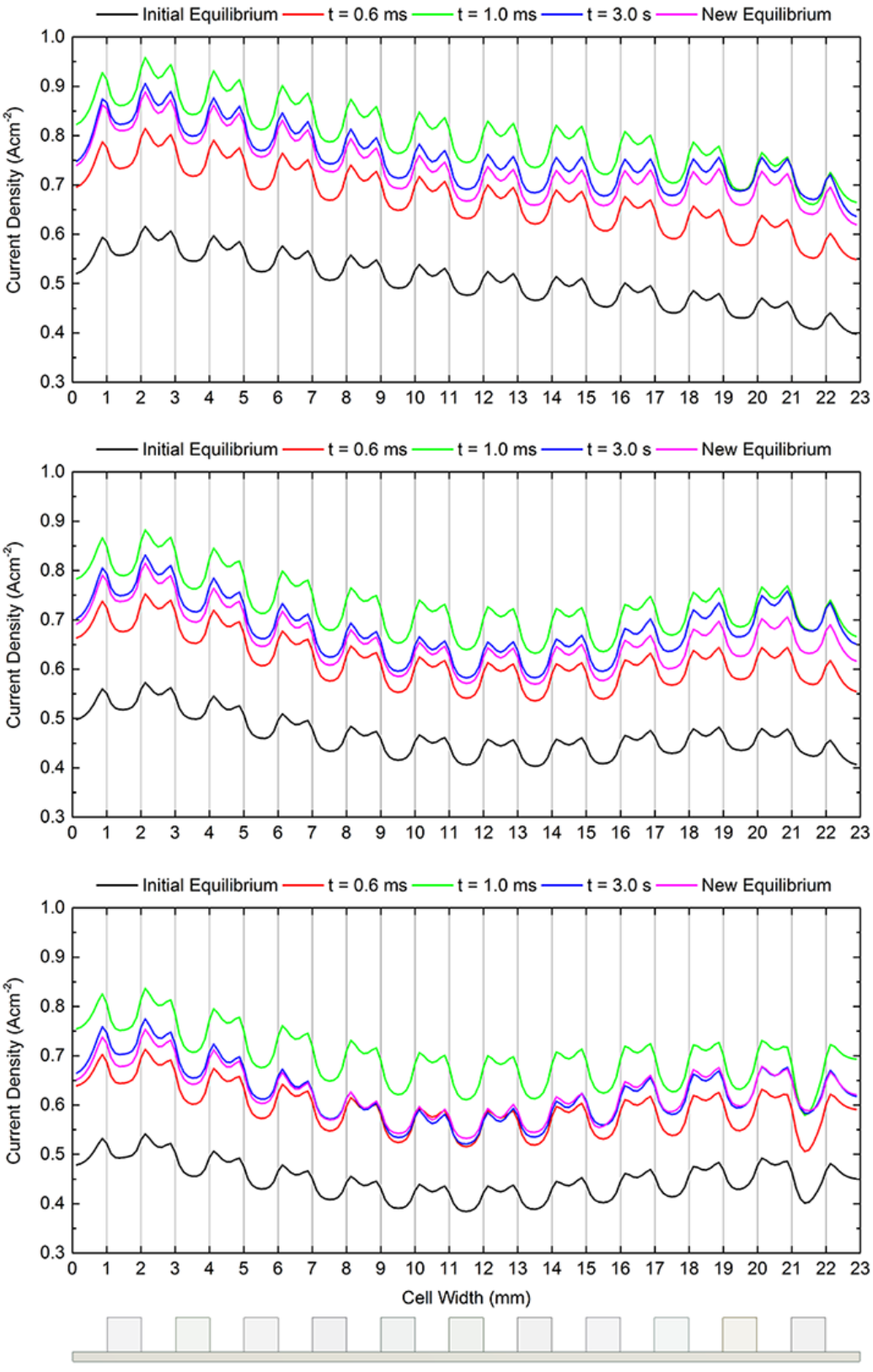

Figure 6.27 Time-history plots of local current density of parallel cell along Line 1 ($0.25L_{cell}$, top), Line 2 ($0.50L_{cell}$, middle), and Line 3 ($0.75L_{cell}$, bottom).

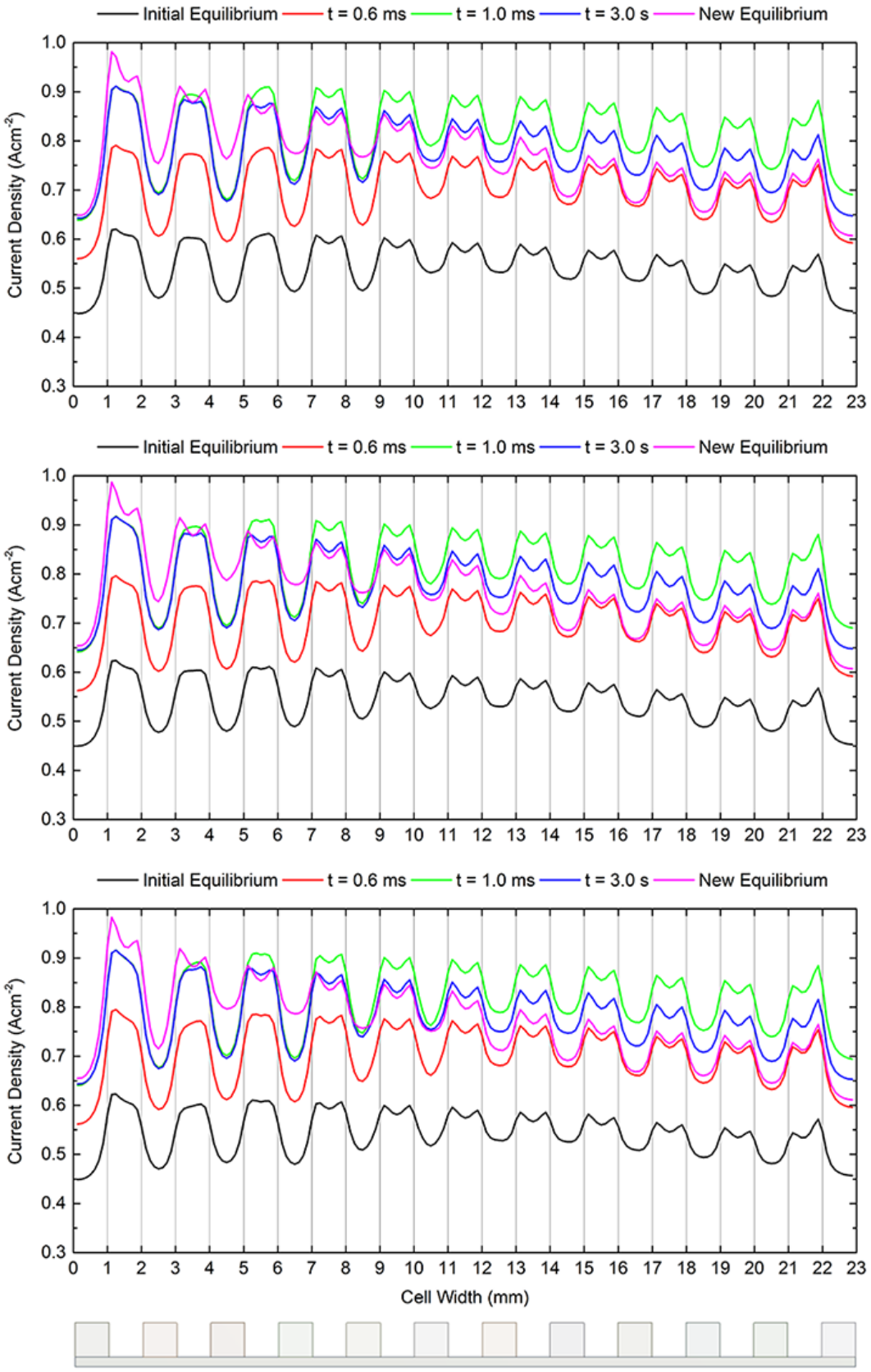

Figure 6.28 Time-history plots of local current density of single-serpentine cell along Line 1 ($0.25L_{cell}$, top), Line 2 ($0.50L_{cell}$, middle), and Line 3 ($0.75L_{cell}$, bottom).

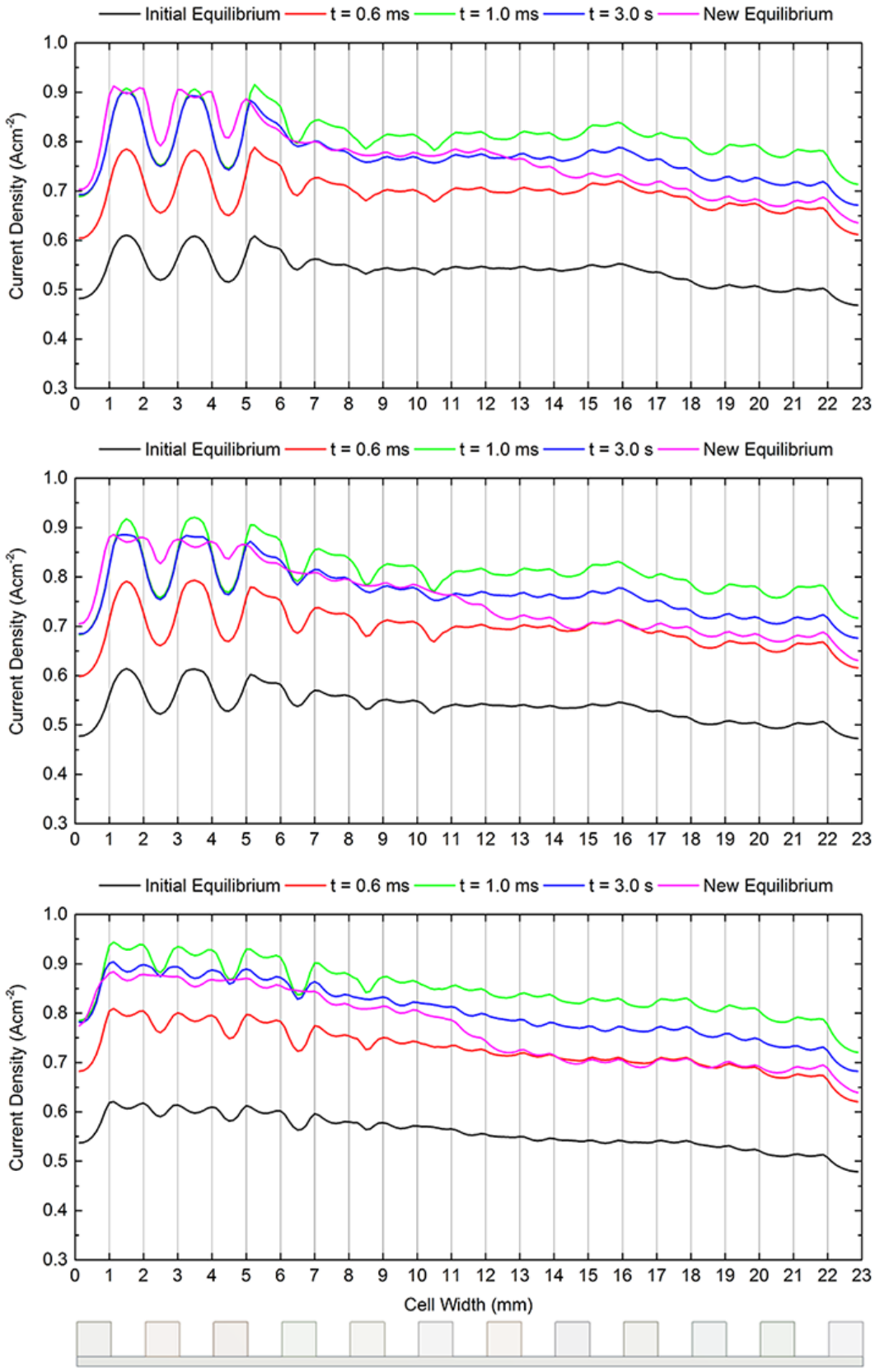

Figure 6.29 Time-history plots of local current density of triple-serpentine cell along Line 1 ($0.25L_{cell}$, top), Line 2 ($0.50L_{cell}$, middle), and Line 3 ($0.75L_{cell}$, bottom).

It has been discussed previously that the parallel cell performs worst in terms of the uniformity of current density and the curves in Figure 6.27 confirm this. The variation in current density is large in both cell-width and cell-length directions. The current is high at the edges and low at the middle of the cell where large amount of water exists. Looking at each individual curve, the current peaks have shifted towards the interface between the flow channel and rib indicating that the cell is operating in the mass-transport limit region. Under the flow channel, on the other hand, free electrons have to travel a longer distance in order to reach the rib. The flow of electron experiences more electronic resistance therefore the current density is lower in this region.

The patterns of current density distribution in the two serpentine cells, however, are similar. It is evident that the current density in the two cells is more uniform than the parallel cell. Overall, the current decreases towards the outlet region where the current peaks occurs at different locations depending on the distance from the inlet. Near the inlet, current peaks at the middle of the rib whereas the peaks further away from the inlet are shifted towards the channel/rib interface. This is due to the effect of cross-flow which enhances the transport of reactant species to the most restricted regions such as the under-ribs. As a result, the species concentration under the ribs becomes comparable to that directly underneath the flow channel. Combined with a shorter path for electron to flow, the current density is therefore highest at the middle of the rib as seen in the first three channels of both cells. Away from the inlet, the oxygen depletion becomes pronounced and outweighs the benefit from the cross-flow thus shifting the peaks to the channel/rib interface. It should be pointed out that the cross-flow in the triple-serpentine cell is weaker than that in the single-serpentine cell hence the current peaks on Line 3 does not occur at the middle of the rib while this same behaviour can be seen on all three lines in the single-serpentine cell.

With regard to time, it is evident that the current overshoots seen in Figure 6.26 are caused by the evolution of this local current density through time. At time t = 0 seconds, the operating voltage is 0.70 Volts and the corresponding current density, denoted by a solid black line, is most uniform. As the voltage decreases, the current increases accordingly but its distribution becomes less uniform. The cell reaches the final voltage of 0.60 Volts at the time t = 1 millisecond where the corresponding current (green) is found to exceed all other curves and marks the peak of current overshoot. As oxygen replenishment could not keep up with the accelerated reaction rate, the oxygen reservoir at the active site is gradually depleted as the cell adjusts to the new equilibrium. As a result, the current keeps on decreasing until the final distribution (magenta) has been reached.

Clearly, the difference between the green and magenta lines is directly proportional to the percentage overshoot reported in Figure 6.26. The larger the difference, the greater the current overshoot. By re-examining the current overshoots, especially the right plot, in Figure 6.26, an explicit trend can be seen. With respect to the final current density, the parallel cell induces the largest current overshoot followed by the triple-serpentine and single-serpentine cells, respectively.

Before proceeding to the next section, it is useful to visualise the area under each curve in Figure 6.27, Figure 6.28, and Figure 6.29 as the total current density generated at that instant. This will greatly simplify the discussions that follow. For the parallel cell, the green curve in Figure 6.27 stays above the magenta curve across the cell width and length which indicates that the current at an instant when the peak occurs locally exceeds the equilibrium value in all regions. This results in a large difference between the two areas enclosed by the green and magenta curves which subsequently cause a large percentage overshoot. This is related to the distribution of local liquid water saturation shown in Figure 6.30 where its value is initially high in all regions. Once the new operating voltage has been reached, water is generated at a higher rate than it was removed due to an ineffective water removal. As a consequence, severe liquid water flooding occurs in all regions of the cell and its effect is seen as the decline in current density on the magenta curve.

Referring to Figure 6.28 and Figure 6.29, unlike the parallel cell, the green curve does not remain above the magenta curve in all region. Besides, the magenta curve somehow overshoots the green curves in certain regions particularly near the inlet. This is due to the superior water removal ability of the serpentine flow-field. The liquid water saturation shown in Figure 6.30 confirms that the two serpentine cells remain relatively dry especially in the inlet region. Instead of causing GDL flooding, the increased water generation rate improves membrane hydration and its protonic conductivity. As a result, the current on the magenta curve over the inlet region is higher than the green curve. On the other hand, an excessively large amount of water accumulates at the outlet region. This portion of the cell could no longer benefit from an improved protonic conductivity but suffers from water flooding which is seen as the right portion of the magenta curve falls underneath the green curve. Since the difference between the green and magenta curves is reduced, the percentage overshoots of the two cells are smaller compared to the parallel cell. This is also why the percentage overshoot of the triple-serpentine cell is larger than the single-serpentine cell because more water is present in the former cell.

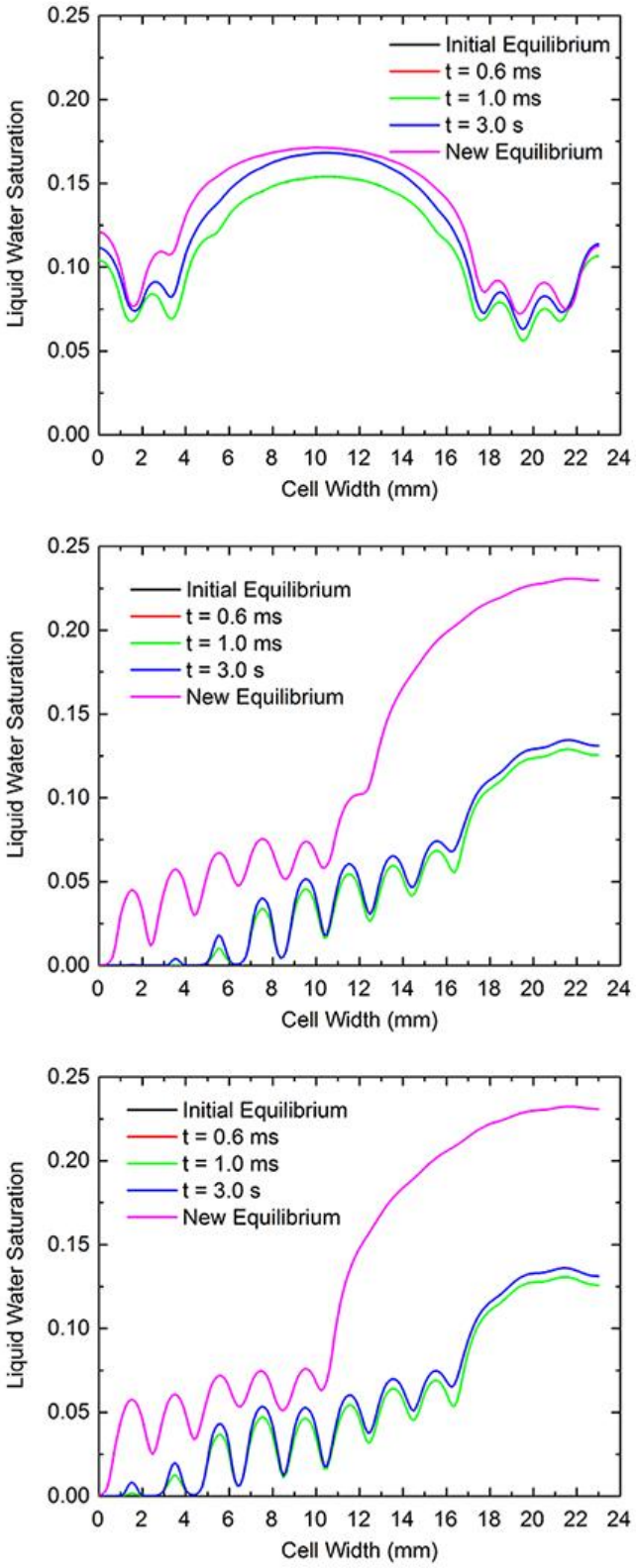

Figure 6.30 Time-history plots of local liquid water saturation along Line 2 ($0.50L_{cell}$) of parallel (top), single-serpentine (middle), and triple-serpentine (bottom) cells.

6.3.2 The Upwards Path

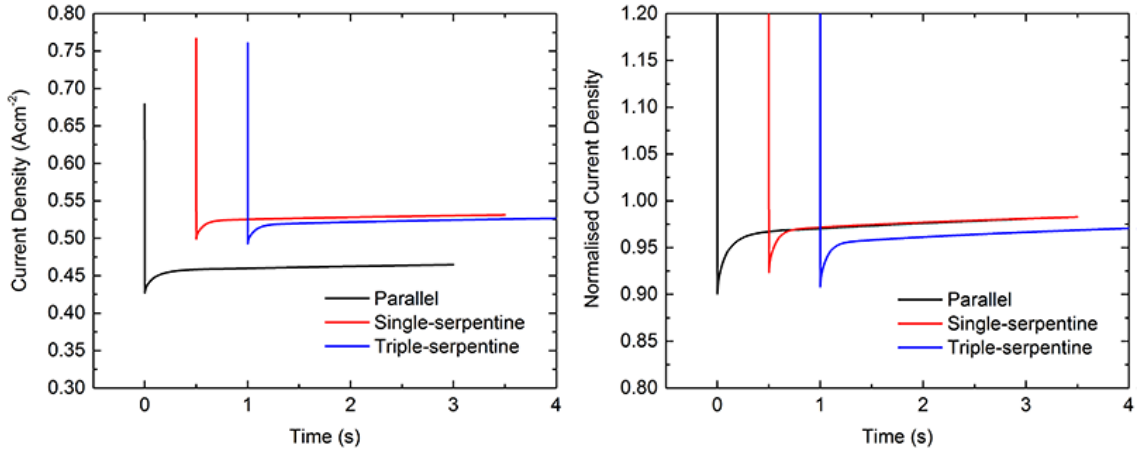

Figure 6.31 Current response (left) and normalised current response (right) to the voltage step-up under wet operation.

The current response to a voltage step-up of each cell under wet reactant streams is shown in Figure 6.31. Similarly, large current undershoots can be seen from the three cells and their corresponding percentage undershoot follows the same trend as discussed previously in Figure 6.26. The largest percentage undershoot of approximately 10% has been found in the parallel cell, followed by the triple-serpentine and single-serpentine cells with percentage undershoots of 8% and 7.5%, respectively.

In order to avoid a repetitive discussion, only the local current density along Line 3 is shown in Figure 6.32 while the local liquid water saturation is given in Figure 6.33. Similarly, but conversely, the current undershoots are caused by the difference in current density on the green and magenta curves where the former is lower than the latter.

At the start of the step-up, water saturation inside each cell is high suggesting that the effect of water flooding is more pronounced at this stage. When the final voltage has been reached at the time t = 1 millisecond, the reaction rate is reduced which means that less current is being generated. However, due to the sluggish water removal process, water could not be removed out of the cell in a timely manner hence liquid water flooding, especially at the outlet region, is still active. As a result, the current density is lowest at this instant corresponding to the trough of current undershoot. As time progresses, water flooding is alleviated thus improving the supply of reactant species at the active sites and the current density gradually increases to its new equilibrium value.

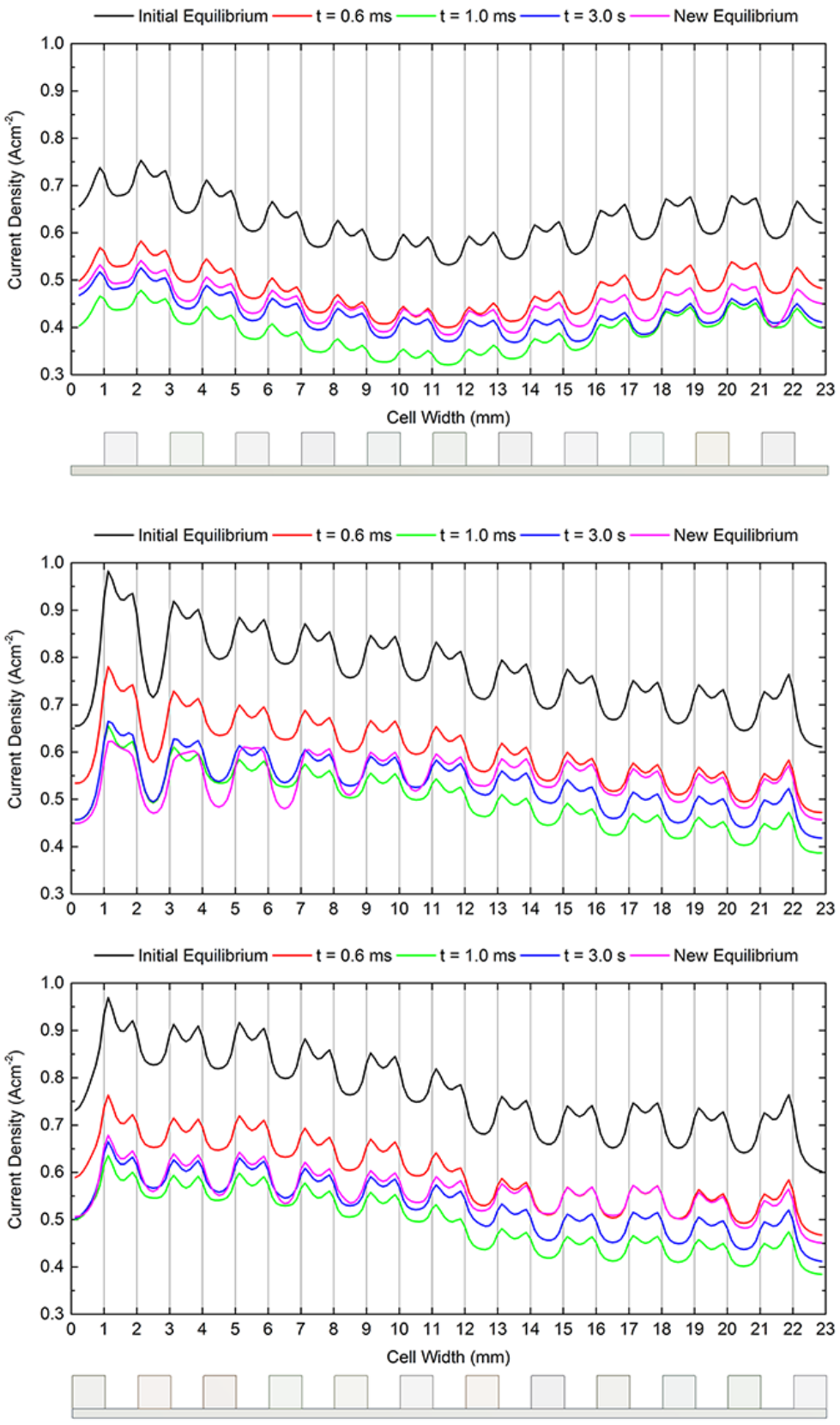

Figure 6.32 Time-history plots of local current density along Line 3 ($0.75L_{cell}$) of parallel (top), single-serpentine (middle), and triple-serpentine (bottom) cells.

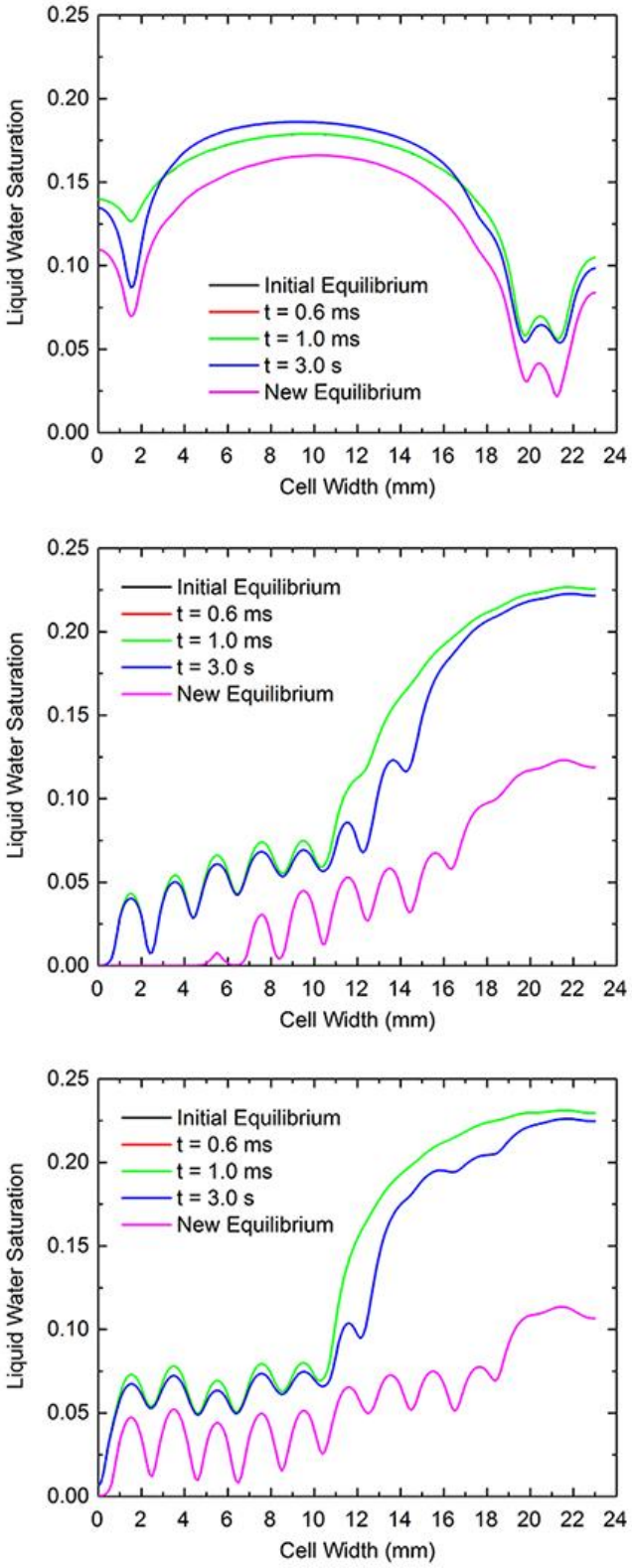

Figure 6.33 Time-history plots of local liquid water saturation along Line 3 ($0.75L_{cell}$) of parallel (top), single-serpentine (middle), and triple-serpentine (bottom) cells.

6.4 Chapter Summary

In this chapter, the multi-channel square cell computational domain with three different flow-field configurations has been used in the hope to establish the relationship between the magnitude of current overshoot/undershoot and the flow-field design. A step change in voltage between 0.60 Volts and 0.70 Volts is chosen so that the three cells would give meaningful results in terms of large overshoots and undershoots.

It has been found in the steady-state run that the performance of the cell is strongly dependent on the flow-field configuration. This is because the flow-field controls the supply of reactant species to the catalyst sites and membrane hydration through water removal at the same time. Under wet reactant streams, the cells are suffering from water flooding hence the two serpentine cells with superior water removal ability outperform the parallel cell. Nonetheless, when switching to drier reactant streams, the cross-flow induced by the serpentine flow-field proves to be disadvantageous to the cell performance as it tends to dry out the membrane causing high protonic resistivity. In such situation, the parallel cell benefits from its inferior water removal. Its membrane is most hydrated with highest protonic conductivity among the three cells and therefore gives the best performance.

The results from the transient run reveal that flow-field design not only affects the steady-state performance but also transient performance particularly the magnitude of current overshoot and undershoot. Such current overshoot and undershoot are caused by the evolution of local current density over time as the cell adjusts to its new equilibrium. Additionally, the relationship between the flow-field design and magnitude of percentage overshoot/undershoot has been identified.

It is found that the excessive water inside the porous layers acts as an amplifier to the overshoot and undershoot of the current. A cell with higher liquid water saturation inside its porous media will give larger current overshoot and undershoot and vice versa. This explains why the largest current overshoot and undershoot have been found in the parallel cell while the ones found in the two serpentine cells are smaller.

Chapter 7
Conclusion

"To be suspicious is not a fault. To be suspicious all the time without coming to a conclusion is the defect."

Lu Xun, Chinese Writer

This last chapter summarises all the results which have been obtained from the research and suggests how these can be applied to the design and development of a PEM fuel cell. Difficulties that arose during the research are discussed with advices on how to eliminate or at least avoid them. Finally, suggestions on the potential future work are given.

7.1 Summary of Research Findings

In this thesis, computational fluid dynamics has been used as a tool to develop the numerical model of a PEM fuel cell and all major components of a PEM fuel cell, except current collectors, are included. The result is a comprehensive, three-dimensional, and two-phase model capable of predicting both steady-state and transient performances of a PEM fuel cell under a wide operating range.

An effective meshing strategy specifically designed for a PEM fuel cell model has been proposed and proved to be valid regardless of cell size or flow-field configuration. It has been found that even though the transport mechanisms in the cell are highly three-dimensional, the variation of flow-field variables in one direction is less significant than another. Therefore the use of a uniform grid throughout the computational domain is not necessary. In fact, more grid elements must be placed in the through-plane direction while less elements are needed in the lateral direction. The mesh in the axial direction, on the other hand, can be least dense which offers a great way to reduce the number of elements. This strategy can greatly cut computational costs while acceptable level of accuracy is maintained.

Four voltage change patterns, the linear sweep, sinusoidal sweep, linear change with fixed rate of 1 Vs^{-1}, and step change, are applied to the single straight channel computational domain. Due to a sluggish membrane hydration that cannot adjust to its new equilibrium in a timely manner, hysteresis, which is defined as the discrepancy between the current response during the forwards and backwards sweeps, has been observed in the linear and sinusoidal voltage sweep analyses. It becomes less pronounced as the voltage change rate is increased. The deviation of the transient current response from its steady-state value, on the other hand, is found to increase with the voltage change rate. Using a milder voltage change in terms of either a smaller change amplitude or longer duration could resolve this issue.

On its path to the new equilibrium value, the current responds to voltage change in three steps which are defined as primary response, relaxation, and secondary response. The magnitude and time response of current during the primary response and relaxation period are the most important criteria in judging the transient performance of a PEM fuel cell while the secondary response can be safely ignored. Despite the fact that the current response cannot reach the equilibrium value at the end of the voltage change, it is able to follow the voltage almost instantaneously and its magnitude falls well within acceptable margins. Different initial voltages have been used in the hope for establishing the relationship between this parameter and the behaviour of current response. Two distinct behaviours of current response have been identified.

However, rather than the absolute value of initial voltage, the behaviour of a current response curve is controlled by the membrane hydration. Similarly, the difference in membrane hydration between the initial and final stages determines how well the current could response to the change in voltage rather than the absolute magnitude of the excitation amplitude. This suggests that membrane hydration has a strong effect on the transient performance of the cell, especially the current response and emphasises the necessity of maintaining the full-hydration status of the membrane at all time.

The results from the multi-channel square cell computational domain reveal that the variation of flow-field variables in the cell-width direction is significant and cannot be neglected. If realistic results or flow-field-related performance are to be obtained, a multi-channel model must be used wherever possible. This underlines the need for an effective meshing strategy like the one proposed in Chapter 4, for instance.

Not only the steady-state performance, but also the transient performance is strongly dependent on water management of the cell. With regard to the steady-state performance, a parallel flow-field is known to be inferior to the serpentine flow-field under normal to wet operations. However, when the condition of water inside the cell changes such as an operation with dry reactant streams, the parallel flow-field can outperform its serpentine counterpart.

With respect to the transient performance, the relationship between the flow-field configuration to the current overshoot and undershoot has been successfully identified. In fact, the flow-field is related to the magnitude of current overshoot and undershoot through its water removal ability. High liquid water saturation tends to enlarge the percentage overshoot and undershoot therefore a flow-field with excellent water removal is desirable if this is to be avoided.

7.2 Contributions to PEM Fuel Cell Research

The important findings that this research has contributed to the PEM fuel cell research community are highlighted as follows;

1) A mesh strategy has been specifically developed for PEM fuel cell modelling for the first time which is capable of reducing the number of mesh elements considerably while maintaining a good level of accuracy. Moreover, it has proved to be valid over a wide range of operating conditions, cell sizes, and flow-field configurations. Such proposed strategy is simple and easy to employ hence it can be used as a "guide-mesh" for those who are new to PEM fuel cell modelling.

2) It has been revealed that the current responds to a sufficiently fast voltage change in three steps; primary response, relaxation, and secondary response where the mechanism behind each of these step has also been uncovered. This is of prime importance since those parameters which affect the magnitude and time response of the current in each step can be identified. As a consequence, undesirable current over-/undershoot and time response can be controlled and reduced through a clever cell design.
3) The effect of flow-field design on a transient performance of the cell in terms of current over-/undershoot has been confirmed. This opens up a new research area in which the cell's transient performance can be improved through a better flow-field design.

7.3 Difficulties and Limitations of the Current Thesis

7.3.1 Reversed Flow at Pressure Outlet

One important problem that constantly arose during the research was the reversed flow at the channel outlet. This is the condition when the reactant stream re-enters the computational domain at some or all elemental faces of the outlet. Figure 7.1 shows the velocity vector plot at the middle plane of anode flow-field. It is seen that the flow enters the flow-field at two positions – at the actual inlet (bottom-left) and the outlet (top-right).

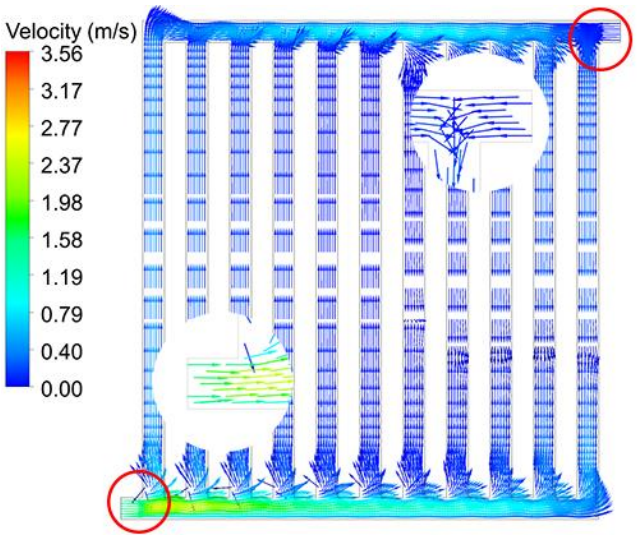

Figure 7.1 Velocity vector plot under operating voltage of 0.4 V with presence of reversed flow at all 64 faces of outlet.

The presence of reversed flow at the outlet delays convergence, if at all possible. The reported solution is inaccurate and must not be used. A good solution is the fully converged one without reversed flow on any face of the outlet. A close inspection on the pressure contour in Figure 7.2 reveals that reversed flow is caused by negative pressure at the outlet where it sucks the reactant stream back in to the domain as if it was another inlet.

Experiences gained during the research suggest that the reversed flow tends to occur at high current density operations where the cell is prone to liquid water flooding and at high fuel utilisation operations where reactant species are likely to deplete particularly near the outlet regions. Simply decreasing the under-relaxation factors, however, cannot solve this kind of problem. Rather, these must be tackled either by reducing the relative humidity of reactant streams or increasing the stoichiometries of fuel and oxidant.

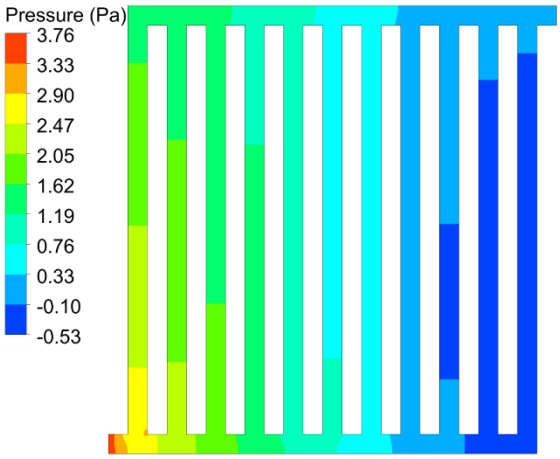

Figure 7.2 Pressure contour at mid-plane of anode flow-field when reversed flow occurs.

Additionally, a reversed flow can occur even when the cell is operated under a dry condition and surplus reactant species. This usually occurs in the cells, especially straight-parallel and interdigitated, where the location of its outlet is in the high-gradient flow region such as the one in Figure 7.1. The presence of flow separation and recirculation can prevent the flow through the outlet from settling down. Since this type of reversed flow is due to a numerical reason, it needs to be treated numerically.

The first method is by reducing the under-relaxation factors to aid in convergence. However, special care is needed here since too low values can potentially freeze the governing equations giving a false sense that a converged solution has been obtained. Another method is to coarsen the mesh near the outlet. This will artificially dampen out any recirculation in that region. The last method is to place the outlet further downstream to allow the flow to become fully developed before it reaches the outlet. This method is preferred by those cases

where certain flow stoichiometry and relative humidity are to be studied and hence cannot be changed.

However, it should be noted that the last method requires the modification of the flow-field. Even though the reversed flow can be completely eliminated, the resulting flow-field solution will be different and therefore, it should only be used when other methods fail.

7.3.2 Computational Resources

Most of the work is numerical simulation therefore this thesis relies heavily on the available computational resources. Since the commercial CFD code, ANSYS FLUENT, is used, the maximum number of computing cores is limited by the number of licenses available. This in turns poses a major restriction on the size of computational domain, mesh fineness, and physical time for a transient simulation.

Particularly, the physical time in all transient simulation cases was confined to a few seconds despite the fact that it takes several minutes for the current response to properly reach the new equilibrium value. However, as stated previously, the current response after primary response is assumed to reach the new equilibrium value at a much later time, hence it can be safely discarded from the simulation. To verify that this assumption is justifiable, Case A from Section 5.5.1 and Case J from Section 5.5.2 are chosen and their extended current responses are shown through Figure 7.3 and Figure 7.4.

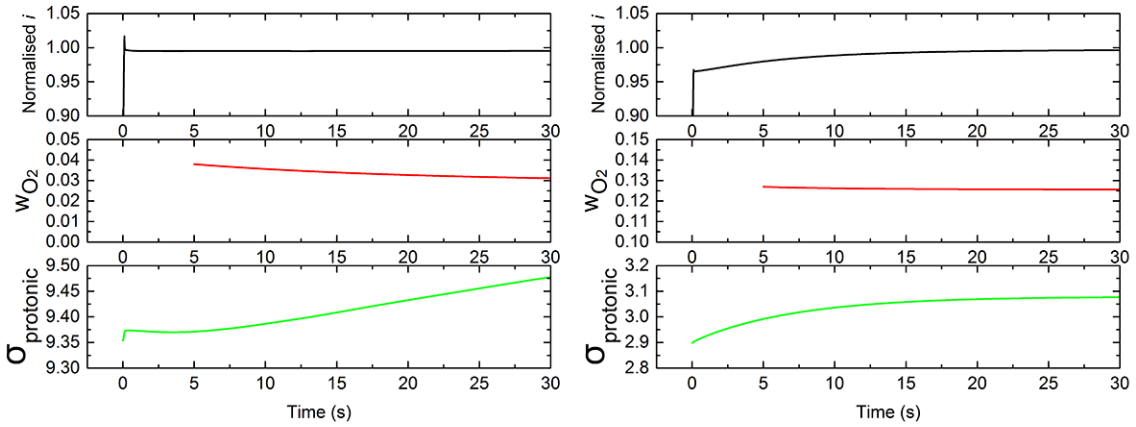

Figure 7.3 Extended current response, oxygen mass fraction, and membrane protonic conductivity from Case A (0.4V→0.3V) of wet (left) and dry (right) cells.

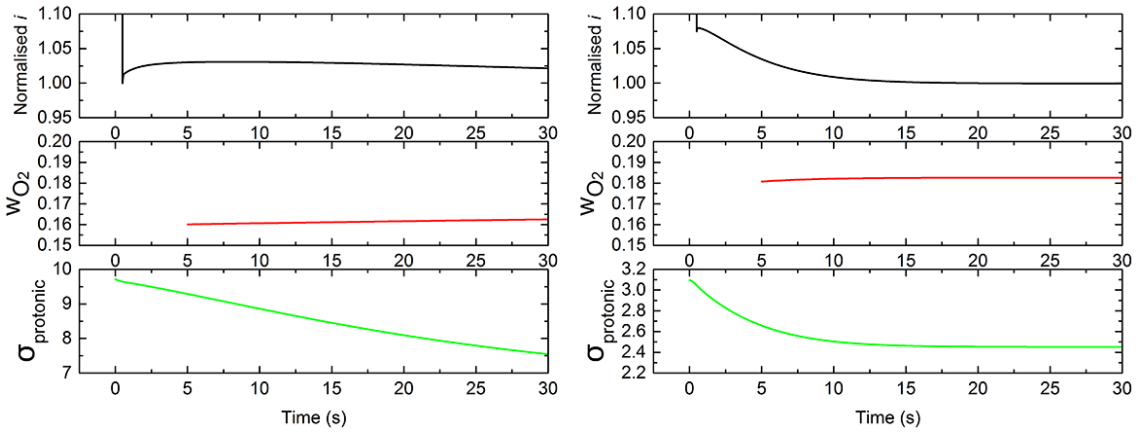

Figure 7.4 Extended current response, oxygen mass fraction, and membrane protonic conductivity from Case J (0.3V→0.8V) of wet (left) and dry (right) cells.

The above figures confirm that during the secondary response the oxygen mass fraction has already reached equilibrium while the protonic conductivity is still evolving. This suggests that the current density in this region is controlled solely by the membrane protonic conductivity and would eventually arrive at the equilibrium value. Therefore its response in this region can be safely neglected.

7.3.3 Exclusion of Current Collectors and Cell Cooling

The current model is said to be non-isothermal because the energy equation was included. The main purpose of this was, however, to improve the solution accuracy through the use of temperature-dependent values of model parameters, especially in the porous media. The current collectors were also excluded from the computational domain in order to reduce the computational expense. This means that the coolant channels that are typically embedded in these plates were also excluded. Moreover, all external boundaries were given a fixed temperature B.C. which is valid in small cells with high thermal conductivity material for current collectors such as graphite. As a consequence, the effect of temperature variation inside the current collectors and cell cooling on the cell performance were discarded.

It is known that the performance of a PEM fuel cell is strongly coupled to the operating temperature. Therefore, when cell cooling for a commercial-scale cell, where the variation in temperature over the cell body are much more significant, is of interest, the inclusion of current collectors and realistic boundary conditions on the cell's exterior other than a fixed temperature should be ensured.

7.3.4 Anisotropy of Gas Diffusion Layers

The gas diffusion layers were treated as being homogeneous and isotropic. Thus a single value was used for electronic and thermal conductivity or permeability regardless of the spatial coordinates. In fact, the structure of real GDL materials is fibrous and therefore their properties are highly direction-dependent. If their properties were treated anisotropically, then it would yield a more accurate solution to the one predicted by the current model.

However, the inclusion of anisotropy not only increases the computation time for each iterative, but also adds complication to the model hence a much stiffer solution algorithm is required. These gain and loss must be taken into consideration.

7.4 Potential Topics for Future Research Work

The results obtained from this thesis highlight potential research areas for future work as summarised below;

- The current response to a voltage change pattern that better represents the power demand of a vehicle than the ones used in this thesis such as NEDC or EUDC cycles, or a random driving cycle derived from a real car should be investigated.
- The effect of temperature variation in the current collector and different temperature boundary conditions on the exterior walls of the cell such as fixed temperature, adiabatic wall, and convective heat transfer boundary conditions should be studied.
- Effect of cell cooling on cell transient performance should also be studied. This means that the two current collectors must be included in the computational domain.
- The effect of anisotropy of gas diffusion layers, especially electronic conductivity and permeability to reactant species on the cell's transient performance should be investigated. This can be done relatively conveniently in ANSYS Fluent where the electronic conductivity and permeability in all three spatial directions can be defined through its User Defined Functions (UDFs).
- The effect of flow-field configurations on the transient performance of a full-scale commercial cell or even a stack should be investigated. This comes with the need for a more powerful computing facility such as parallel computing since the number of mesh elements in the computational domain can increase manifold.

References

[1] G. Mom, *The Electric Vehicle: Technology and Expectations in the Automobile Age*. Johns Hopskins University Press, 2004.

[2] U.S. Energy Information Administration, "International Energy Statistics." [Online]. Available: http://www.eia.gov/cfapps/ipdbproject/IEDIndex3.cfm?tid=5&pid=54&aid=2.

[3] M. Ehsani, Y. Gao, S. E. Gay, and A. Emadi, *Modern Electric, Hybrid Electric, and Fuel Cell Vehicles: Fundamentals, Theory, and Design*. CRC Press LLC, 2005.

[4] U.S. Energy Information Administration, "Annual Energy Outlook 2015 with Projections to 2040."

[5] U.S. Environmental Protection Agency, "U.S. Carbon Dioxide Emissions, By Source." [Online]. Available: http://www.epa.gov/climatechange/ghgemissions/gases/co2.html.

[6] U.S. Environmental Protection Agency, "Greenhouse Gas Emissions from a Typical Passenger Vehicle," 2014.

[7] Carbon Dioxide Information Analysis Center, "Global Fossil-fuel CO2 Emissions." [Online]. Available: http://cdiac.ornl.gov/trends/emis/tre_glob_2010.html.

[8] World Health Organization, "Health Aspects of Air Pollution with Particulate Matter , Ozone and Nitrogen Dioxide," 2003.

[9] BMW Media Information, "BMW hydrogen engine reaches top level efficiency," 2009.

[10] J. Larminie and A. Dicks, *Fuel Cell Systems Explained*, 2nd ed. John Wiley & Sons Ltd, 2003.

[11] R. L. Dekock and H. B. Gray, *Chemical Structure and Bonding*, 2nd ed. University Science Books, 1989.

[12] A. Chambers, C. Park, R. T. K. Baker, and N. M. Rodriguez, "Hydrogen Storage in Graphite Nanofibers," *J. Phys. Chem. B*, vol. 102, no. 22, pp. 4253–4256, May 1998.

[13] W. R. Grove, "On voltaic series and the combination of gases by platinum," *Philos. Mag. Ser. 3*, vol. 14, no. 86, pp. 127–130, Feb. 1839.

[14] F. Barbir, *PEM Fuel Cells: Theory and Practice*, 1st ed. Elsevier Academic Press, 2005.

[15] D. Gross, "Cleantech - Fuel Cell Special," pp. 46–47, Sep-2010.

[16] F. J. Barclay, *Fuel Cells, Engines, and Hydrogen - An Exergy Approach*, 1st ed. Wiley, 2006.

[17] H. K. Messerle, *Energy Conversion Statics*. New York: Academic Press, 1969.

[18] M. A. R. S. Al-baghdadi, *CFD Models for Analysis and Design of PEM Fuel Cells*. Nova Science Pub Inc, 2008.

[19] H. Dohle, J. Mergel, and D. Stolten, "Heat and power management of a direct-methanol-fuel-cell (DMFC) system," *J. Power Sources*, vol. 111, no. 2, pp. 268–282, Sep. 2002.

[20] C. Ball, "Fuel cells (finally) set to power composites growth." [Online]. Available: http://www.compositesworld.com/columns/fuel-cells-finally-set-to-power-composites-growth.

[21] "PEM Fuel Cell Assembly." [Online]. Available: http://www2.lbl.gov/publicinfo/newscenter/features/2008/apr/assets/img/hires/inside-fuel-cell.jpg.

[22] X. Li and I. Sabir, "Review of bipolar plates in PEM fuel cells: Flow-field designs," *Int. J. Hydrogen Energy*, vol. 30, no. 4, pp. 359–371, 2005.

[23] D. Spernjak, A. K. Prasad, and S. G. Advani, "Experimental investigation of liquid water formation and transport in a transparent single-serpentine PEM fuel cell," *J. Power Sources*, vol. 170, no. 2, pp. 334–344, 2007.

[24] N. Djilali, "Computational modelling of polymer electrolyte membrane (PEM) fuel cells: Challenges and opportunities," *Energy*, vol. 32, no. 4, pp. 269–280, 2007.

[25] A. Kahlon and S. Lower, "The Hydronium Ion." [Online]. Available: http://chemwiki.ucdavis.edu/Physical_Chemistry/Acids_and_Bases/Aqueous_Solutions/The_Hydronium_Ion.

[26] U.S. Department of Energy, "A NATIONAL VISION OF AMERICA'S TRANSITION TO A HYDROGEN ECONOMY — TO 2030 AND BEYOND," 2002.

[27] U.S. Department of Energy, "Basic Research Needs for the Hydrogen Economy," 2003.

[28] U.S. Department of Energy, "FINANCIAL ASSISTANCE FUNDING OPPORTUNITY ANNOUNCEMENT: Research and Development of Fuel Cells for Stationary and Transportation Applications," 2010.

[29] Y. Wang, K. S. Chen, J. Mishler, S. C. Cho, and X. C. Adroher, "A review of polymer electrolyte membrane fuel cells: Technology, applications, and needs on fundamental research," *Appl. Energy*, vol. 88, no. 4, pp. 981–1007, 2011.

[30] K. E. Martin, J. P. Kopasz, and K. W. McMurphy, "Status of fuel cells and the challenges facing fuel cell technology today," *ACS Symp. Ser.*, vol. 1040, pp. 1–13, 2010.

[31] R. K. Ahluwalia and X. Wang, "Fuel cell systems for transportation: Status and trends," *J. Power Sources*, vol. 177, no. 1, pp. 167–176, 2008.

[32] O. Erdinc and M. Uzunoglu, "Recent trends in PEM fuel cell-powered hybrid systems: Investigation of application areas, design architectures and energy management approaches," *Renew. Sustain. Energy Rev.*, vol. 14, no. 9, pp. 2874–2884, 2010.

[33] C. E. Thomas, "Fuel cell and battery electric vehicles compared," *Int. J. Hydrogen Energy*, vol. 34, no. 15, pp. 6005–6020, 2009.

[34] S. J. C. Cleghorn, D. K. Mayfield, D. a. Moore, J. C. Moore, G. Rusch, T. W. Sherman, N. T. Sisofo, and U. Beuscher, "A polymer electrolyte fuel cell life test: 3 years of continuous operation," *J. Power Sources*, vol. 158, no. 1, pp. 446–454, 2006.

[35] S. D. Knights, K. M. Colbow, J. St-Pierre, and D. P. Wilkinson, "Aging mechanisms and lifetime of PEFC and DMFC," *J. Power Sources*, vol. 127, no. 1–2, pp. 127–134, 2004.

[36] P. Pei, X. Yuan, P. Chao, and X. Wang, "Analysis on the PEM fuel cells after accelerated life experiment," *Int. J. Hydrogen Energy*, vol. 35, no. 7, pp. 3147–3151, 2010.

[37] F. B. Weng, C. Y. Hsu, and C. W. Li, "Experimental investigation of PEM fuel cell aging under current cycling using segmented fuel cell," *Int. J. Hydrogen Energy*, vol. 35, no. 8, pp. 3664–3675, 2010.

[38] R. Lin, B. Li, Y. P. Hou, and J. M. Ma, "Investigation of dynamic driving cycle effect on performance degradation and micro-structure change of PEM fuel cell," *Int. J. Hydrogen Energy*, vol. 34, no. 5, pp. 2369–2376, 2009.

[39] R. Lin, F. Xiong, W. C. Tang, L. Técher, J. M. Zhang, and J. X. Ma, "Investigation of dynamic driving cycle effect on the degradation of proton exchange membrane fuel cell by segmented cell technology," *J. Power Sources*, vol. 260, pp. 150–158, 2014.

[40] P. Pei and H. Chen, "Main factors affecting the lifetime of Proton Exchange Membrane fuel cells in vehicle applications: A review," *Appl. Energy*, vol. 125, pp. 60–75, 2014.

[41] M. Knowles, D. Baglee, A. Morris, and Q. Ren, "The state of the art in fuel cell condition monitoring and maintenance," *World Electr. Veh. J.*, vol. 4, no. 1, pp. 487–494, 2011.

[42] A. A. Shah, T. R. Ralph, and F. C. Walsh, "Modeling and simulation of the degradation of perfluorinated ion-exchange membranes in PEM fuel cells," no. May 2010, 2009.

[43] A. A. Shah, K. H. Luo, T. R. Ralph, and F. C. Walsh, "Recent trends and developments in polymer electrolyte membrane fuel cell modelling," *Electrochim. Acta*, vol. 56, no. 11, pp. 3731–3757, 2011.

[44] A. Parthasarathy, S. Srinivasan, a. J. Appleby, and C. R. Martin, "Pressure dependence of the oxygen reduction reaction at the platinum microelectrode/nafion interface - Electrode kinetics and mass transport," vol. 139, no. 10, pp. 2856–2862, 1992.

[45] H. M. Yu, C. Ziegler, M. Oszcipok, M. Zobel, and C. Hebling, "Hydrophilicity and hydrophobicity study of catalyst layers in proton exchange membrane fuel cells," *Electrochim. Acta*, vol. 51, no. 7, pp. 1199–1207, 2006.

[46] Q. Yan and J. Wu, "Modeling of single catalyst particle in cathode of PEM fuel cells," *Energy Convers. Manag.*, vol. 49, no. 8, pp. 2425–2433, 2008.

[47] P. B. Balbuena, E. J. Lamas, and Y. Wang, "Molecular modeling studies of polymer electrolytes for power sources," *Electrochim. Acta*, vol. 50, no. 19, pp. 3788–3795, 2005.

[48] U.S. Department of Energy, "Manufacturing for the Hydrogen Economy: Manufacturing Research & Development of PEM Fuel Cell Systems for Transportation Applications," Washington, 2005.

[49] V. Mehta and J. S. Cooper, "Review and analysis of PEM fuel cell design and manufacturing," *J. Power Sources*, vol. 114, no. 1, pp. 32–53, 2003.

[50] T. L. Smith, A. D. Santamaria, J. W. Park, and K. Yamazaki, "Alloy selection and die design for stamped proton exchange membrane fuel cell (PEMFC) bipolar plates," *Procedia CIRP*, vol. 14, pp. 275–280, 2014.

[51] "GM Equinox." [Online]. Available: http://i.livescience.com/images/i/000/010/241/original/071105-gm-equinox3-02.jpg.

[52] "1 kW Ballard Portable." [Online]. Available: http://www.fuelcell.no/1kWBallard_portable.jpg.

[53] "PEM Fuel Cell Single Cell." [Online]. Available: http://img.directindustry.com/images_di/photo-g/pem-fuel-cell-single-cell-22780-2692653.jpg.

[54] S. Pischinger, C. Schönfelder, and J. Ogrzewalla, "Analysis of dynamic requirements for fuel cell systems for vehicle applications," *J. Power Sources*, vol. 154, no. 2, pp. 420–427, 2006.

[55] M. Nadal and F. Barbir, "Development of a Hybrid Fuel Cell/Battery Electric Vehicle," vol. 2, no. 6, pp. 497–505, 1996.

[56] Y. Tang, W. Yuan, M. Pan, and Z. Wan, "Experimental investigation on the dynamic performance of a hybrid PEM fuel cell/battery system for lightweight electric vehicle application," *Appl. Energy*, vol. 88, no. 1, pp. 68–76, 2011.

[57] P. Piumsomboon, K. Pruksathorn, M. Hunsom, N. Tantavichet, K. Charutawai, W. Kittikiatsophon, B. Nakrumpai, A. Sripakagorn, and P. Damrongkijkarn, "Road testing of a three-wheeler driven by a 5 kW PEM fuel cell in the absence and presence of batteries," *Renew. Energy*, vol. 50, pp. 365–372, 2013.

[58] J. L. Shang and B. G. Pollet, "Hydrogen fuel cell hybrid scooter (HFCHS) with plug-in features on Birmingham campus," *Int. J. Hydrogen Energy*, vol. 35, no. 23, pp. 12709–12715, 2010.

[59] P. Corbo, F. Migliardini, and O. Veneri, "An experimental study of a PEM fuel cell power train for urban bus application," *J. Power Sources*, vol. 181, no. 2, pp. 363–370, 2008.

[60] P. Corbo, F. E. Corcione, F. Migliardini, and O. Veneri, "Experimental study of a fuel cell power train for road transport application," *J. Power Sources*, vol. 145, no. 2, pp. 610–619, 2005.

[61] M. Abu Mallouh, E. Abdelhafez, M. Salah, M. Hamdan, B. Surgenor, and M. Youssef, "Model development and analysis of a mid-sized hybrid fuel cell/battery vehicle with a representative driving cycle," *J. Power Sources*, vol. 260, pp. 62–71, 2014.

[62] C. H. Chao and T. C. Jen, "Transient behavior experiments for hybrid fuel cell-battery systems," *Proc. 2012 Int. Symp. Inf. Technol. Med. Educ. ITME 2012*, vol. 2, pp. 985–990, 2012.

[63] D. Webb and S. Møller-Holst, "Measuring individual cell voltages in fuel cell stacks," *J. Power Sources*, vol. 103, no. 1, pp. 54–60, 2001.

[64] Q. Shen, M. Hou, X. Yan, D. Liang, Z. Zang, L. Hao, Z. Shao, Z. Hou, P. Ming, and B. Yi, "The voltage characteristics of proton exchange membrane fuel cell (PEMFC) under steady and transient states," *J. Power Sources*, vol. 179, no. 1, pp. 292–296, 2008.

[65] P. Corbo, F. Migliardini, and O. Veneri, "Performance investigation of 2.4kW PEM fuel cell stack in vehicles," *Int. J. Hydrogen Energy*, vol. 32, no. 17, pp. 4340–4349, 2007.

[66] J. He, S.-Y. Choe, and C.-O. Hong, "Analysis and control of a hybrid fuel delivery system for a polymer electrolyte membrane fuel cell," *J. Power Sources*, vol. 185, no. 2, pp. 973–984, 2008.

[67] I. S. Han, J. Jeong, and H. K. Shin, "PEM fuel-cell stack design for improved fuel utilization," *Int. J. Hydrogen Energy*, vol. 38, no. 27, pp. 11996–12006, 2013.

[68] W. Mitchell, B. J. Bowers, C. Garnier, and F. Boudjemaa, "Dynamic behavior of gasoline fuel cell electric vehicles," *J. Power Sources*, vol. 154, no. 2, pp. 489–496, 2006.

[69] M. De Francesco and E. Arato, "Start-up analysis for automotive PEM fuel cell systems," *J. Power Sources*, vol. 108, no. 1–2, pp. 41–52, 2002.

[70] P. Corbo, F. Migliardini, and O. Veneri, "Experimental analysis of a 20kWe PEM fuel cell system in dynamic conditions representative of automotive applications," *Energy Convers. Manag.*, vol. 49, no. 10, pp. 2688–2697, 2008.

[71] F. Philipps, G. Simons, and K. Schiefer, "Dynamic investigation of PEFC stacks in interaction with the air supply system," *J. Power Sources*, vol. 154, no. 2, pp. 412–419, 2006.

[72] S. G. Kandlikar and Z. Lu, "Thermal management issues in a PEMFC stack - A brief review of current status," *Appl. Therm. Eng.*, vol. 29, no. 7, pp. 1276–1280, 2009.

[73] G. Zhang and S. G. Kandlikar, "A critical review of cooling techniques in proton exchange membrane fuel cell stacks," *Int. J. Hydrogen Energy*, vol. 37, no. 3, pp. 2412–2429, 2012.

[74] K. P. Adzakpa, J. Ramousse, Y. Dubé, H. Akremi, K. Agbossou, M. Dostie, a. Poulin, and M. Fournier, "Transient air cooling thermal modeling of a PEM fuel cell," *J. Power Sources*, vol. 179, no. 1, pp. 164–176, 2008.

[75] A. P. Sasmito, E. Birgersson, and A. S. Mujumdar, "A novel flow reversal concept for improved thermal management in polymer electrolyte fuel cell stacks," *Int. J. Therm. Sci.*, vol. 54, pp. 242–252, 2012.

[76] M. Matian, A. Marquis, and N. Brandon, "Model based design and test of cooling plates for an air-cooled polymer electrolyte fuel cell stack," *Int. J. Hydrogen Energy*, vol. 36, no. 10, pp. 6051–6066, 2011.

[77] A. Franco, "Optimum design of bipolar plates for separate air flow cooling system of PEM fuel cells stacks," *Heat Mass Transf.*, 2015.

[78] J. Chen and B. Zhou, "Diagnosis of PEM fuel cell stack dynamic behaviors," *J. Power Sources*, vol. 177, no. 1, pp. 83–95, 2008.

[79] P. Pei, M. Ouyang, W. Feng, L. Lu, H. Huang, and J. Zhang, "Hydrogen pressure drop characteristics in a fuel cell stack," *Int. J. Hydrogen Energy*, vol. 31, no. 3, pp. 371–377, 2006.

[80] A. Oheda, B. Omar, S. C. Chai, A. Aseeri, and A. Savvaris, "Experimental analysis of the dynamic performance of PEM fuel cell under various load changes," *Mech. Electr. Technol. (ICMET), 2010 2nd Int. Conf.*, no. Icmet, pp. 604–609, 2010.

[81] Y. Tang, W. Yuan, M. Pan, Z. Li, G. Chen, and Y. Li, "Experimental investigation of dynamic performance and transient responses of a kW-class PEM fuel cell stack under various load changes," *Appl. Energy*, vol. 87, no. 4, pp. 1410–1417, 2010.

[82] X. Yan, M. Hou, L. Sun, H. Cheng, Y. Hong, D. Liang, Q. Shen, P. Ming, and B. Yi, "The study on transient characteristic of proton exchange membrane fuel cell stack during dynamic loading," *J. Power Sources*, vol. 163, no. 2, pp. 966–970, 2007.

[83] H. Kim, C. Y. Cho, J. H. Nam, D. Shin, and T.-Y. Chung, "A simple dynamic model for polymer electrolyte membrane fuel cell (PEMFC) power modules: Parameter estimation and model prediction," *Int. J. Hydrogen Energy*, vol. 35, no. 8, pp. 3656–3663, 2010.

[84] Y. Hou, Z. Yang, and G. Wan, "An improved dynamic voltage model of PEM fuel cell stack," *Int. J. Hydrogen Energy*, vol. 35, no. 20, pp. 11154–11160, 2010.

[85] J. Garnier, M. C. Pera, D. Hissel, F. Harel, D. Candusso, N. Glandut, J. P. Diard, a. De Bernardinis, J. M. Kauffmann, and G. Coquery, "Dynamic PEM fuel cell modeling for automotive applications," *2003 IEEE 58th Veh. Technol. Conf. VTC 2003-Fall (IEEE Cat. No.03CH37484)*, vol. 5, no. 2, pp. 3284–3288, 2003.

[86] S. Yerramalla, A. Davari, A. Feliachi, and T. Biswas, "Modeling and simulation of the dynamic behavior of a polymer electrolyte membrane fuel cell," *J. Power Sources*, vol. 124, no. 1, pp. 104–113, 2003.

[87] C. Panos, K. I. Kouramas, M. C. Georgiadis, and E. N. Pistikopoulos, "Modelling and explicit model predictive control for PEM fuel cell systems," *Chem. Eng. Sci.*, vol. 67, no. 1, pp. 15–25, 2012.

[88] I. S. Martín, A. Ursúa, and P. Sanchis, "Modelling of PEM fuel cell performance: Steady-state and dynamic experimental validation," *Energies*, vol. 7, no. 2, pp. 670–700, 2014.

[89] P. Choopanya and Z. Yang, "Transient Performance Investigation of Different Flow-field Designs of Automotive Polymer Electrolyte Membrane Fuel Cell (PEMFC) Using Computational Fluid Dynamics (CFD)," in *10th International Conference on Heat Transfer, Fluid Mechanics and Thermodynamics 14th-16th July*, 2014, pp. 583–592.

[90] P. Choopanya and Z. Yang, "A CFD Investigation of Effects of Flow-field Geometry on Transient Performance of an Automotive Polymer Electrolyte Membrane Fuel Cell," *Comput. Therm. Sci. An Int. J.*, vol. 7, no. 2, pp. 93–104, 2015.

[91] C. Y. Wang, "Fundamental models for fuel cell engineering," *Chem. Rev.*, vol. 104, no. 10, pp. 4727–4765, 2004.

[92] K. Haraldsson and K. Wipke, "Evaluating PEM fuel cell system models," *J. Power Sources*, vol. 126, no. 1–2, pp. 88–97, 2004.

[93] C. Siegel, "Review of computational heat and mass transfer modeling in polymer-electrolyte-membrane (PEM) fuel cells," *Energy*, vol. 33, no. 9, pp. 1331–1352, 2008.

[94] D. Cheddie and N. Munroe, "Review and comparison of approaches to proton exchange membrane fuel cell modeling," *J. Power Sources*, vol. 147, no. 1–2, pp. 72–84, 2005.

[95] T. E. Springer, T. a. Zawodzinski, and S. Gottesfeld, "Polymer electrolyte fuel cell model," *J. Electrochem. Soc.*, vol. 138, no. 8, pp. 2334–2342, 1991.

[96] D. M. Bernardi and M. W. Verbrugge, "A Mathematical Model of the Solid-Polymer-Electrolyte Fuel Cell," *J. Electrochem. Soc.*, vol. 139, no. 9, pp. 2477–2491, 1992.

[97] D. M. Bernardi and M. W. Verbrugge, "Mathematical model of a gas diffusion electrode bonded to a polymer electrolyte," *AIChE J.*, vol. 37, no. 8, pp. 1151–1163, 1991.

[98] T. A. Zawodzinski, M. Neeman, L. O. Sillerud, and S. Gottesfeld, "Determination of water diffusion coefficients in perfluorosulfonate ionomeric membranes," *J. Phys. Chem.*, vol. 95, no. 15, pp. 6040–6044, Jul. 1991.

[99] C. Y. Wang, W. B. Gu, and B. Y. Liaw, "Micro-Macroscopic Coupled Modeling of Batteries and Fuel Cells: I. Model Development," *J. Electrochem. Soc.*, vol. 145, no. 10, pp. 3407–3417, 1998.

[100] W. B. Gu, C. Y. Wang, and B. Y. Liaw, "Micro-Macroscopic Coupled Modeling of Batteries and Fuel Cells: II. Application to Nickel-Cadmium and Nickel-Metal Hydride Cells," *J. Electrochem. Soc.*, vol. 145, no. 10, pp. 3418–3427, 1998.

[101] V. Gurau, H. Liu, and S. Kakac, "Two-Dimensional Model for Proton Exchange Membrane Fuel Cells," *AIChE J.*, vol. 44, no. 11, pp. 2410–2422, 1998.

[102] T. F. Fuller and J. Newman, "Water and Thermal Management in Solid-Polymer-Electrolyte Fuel Cells," *J. Electrochem. Soc.*, vol. 140, no. 5, pp. 1218–1225, 1993.

[103] T. V Nguyen and R. E. White, "A Water and Heat Management Model for Proton-Exchange-Membrane Fuel Cells," *Water*, vol. 140, no. 8, pp. 2178–2186, 1993.

[104] N. P. Siegel, M. W. Ellis, D. J. Nelson, and M. R. Von Spakovsky, "A two-dimensional computational model of a PEMFC with liquid water transport," *J. Power Sources*, vol. 128, pp. 173–184, 2004.

[105] A. Kazim, H. T. Liu, and P. Forges, "Modelling of performance of PEM fuel cells with conventional and interdigitated flow fields," *J. Appl. Electrochem.*, vol. 29, pp. 1409–1416, 1999.

[106] S. Karvonen, T. Hottinen, J. Saarinen, and O. Himanen, "Modeling of flow field in polymer electrolyte membrane fuel cell," *J. Power Sources*, vol. 161, pp. 876–884, 2006.

[107] S. Dutta, S. Shimpalee, and J. W. Van Zee, "Three-dimensional numerical simulation of straight channel PEM Fuel Cells," *J. Appl. Electrochem.*, vol. 30, pp. 135–146, 2000.

[108] X. D. Wang, Y. Y. Duan, W. M. Yan, and X. F. Peng, "Effects of flow channel geometry on cell performance for PEM fuel cells with parallel and interdigitated flow fields," *Electrochim. Acta*, vol. 53, pp. 5334–5343, 2008.

[109] W.-M. Yan, H.-C. Liu, C.-Y. Soong, F. Chen, and C. H. Cheng, "Numerical study on cell performance and local transport phenomena of PEM fuel cells with novel flow field designs," *J. Power Sources*, vol. 161, pp. 907–919, 2006.

[110] D. H. Jeon, S. Greenway, S. Shimpalee, and J. W. Van Zee, "The effect of serpentine flow-field designs on PEM fuel cell performance," *Int. J. Hydrogen Energy*, vol. 33, pp. 1052–1066, 2008.

[111] S. Shimpalee and J. W. Van Zee, "Numerical studies on rib & channel dimension of flow-field on PEMFC performance," *Int. J. Hydrogen Energy*, vol. 32, pp. 842–856, 2007.

[112] X. D. Wang, Y. Y. Duan, W. M. Yan, and X. F. Peng, "Local transport phenomena and cell performance of PEM fuel cells with various serpentine flow field designs," *J. Power Sources*, vol. 175, pp. 397–407, 2008.

[113] J. E. Dawes, N. S. Hanspal, O. a. Family, and a. Turan, "Three-dimensional CFD modelling of PEM fuel cells: An investigation into the effects of water flooding," *Chem. Eng. Sci.*, vol. 64, pp. 2781–2794, 2009.

[114] P. T. Nguyen, T. Berning, and N. Djilali, "Computational model of a PEM fuel cell with serpentine gas flow channels," *J. Power Sources*, vol. 130, pp. 149–157, 2004.

[115] A. Kumar and R. G. Reddy, "Effect of channel dimensions and shape in the flow-field distributor on the performance of polymer electrolyte membrane fuel cells," *J. Power Sources*, vol. 113, pp. 11–18, 2003.

[116] X.-D. Wang, Y.-Y. Duan, and W.-M. Yan, "Novel serpentine-baffle flow field design for proton exchange membrane fuel cells," *J. Power Sources*, vol. 173, no. 1, pp. 210–221, 2007.

[117] R. Roshandel, F. Arbabi, and G. K. Moghaddam, "Simulation of an innovative flow-field design based on a bio inspired pattern for PEM fuel cells," *Renew. Energy*, vol. 41, pp. 86–95, 2012.

[118] F. Hashemi, S. Rowshanzamir, and M. Rezakazemi, "CFD simulation of PEM fuel cell performance: Effect of straight and serpentine flow fields," *Math. Comput. Model.*, vol. 55, no. 3–4, pp. 1540–1557, 2012.

[119] S. Kim, S. Shimpalee, and J. W. Van Zee, "The effect of stoichiometry on dynamic behavior of a proton exchange membrane fuel cell (PEMFC) during load change," *J. Power Sources*, vol. 135, pp. 110–121, 2004.

[120] S. Kim, S. Shimpalee, and J. W. Van Zee, "Effect of Flow Field Design and Voltage Change Range on the Dynamic Behavior of PEMFCs," *J. Electrochem. Soc.*, vol. 152, pp. A1265–A1271, 2005.

[121] S. Kim, S. Shimpalee, and J. W. Van Zee, "The effect of reservoirs and fuel dilution on the dynamic behavior of a PEMFC," *J. Power Sources*, vol. 137, pp. 43–52, 2004.

[122] H. Sun, G. Zhang, L. Guo, and H. Liu, "A Study of dynamic characteristics of PEM fuel cells by measuring local currents," *Int. J. Hydrogen Energy*, vol. 34, no. 13, pp. 5529–5536, 2009.

[123] J. Peng, J. Y. Shin, and T. W. Song, "Transient response of high temperature PEM fuel cell," *J. Power Sources*, vol. 179, pp. 220–231, 2008.

[124] K. S. C. Sukkee Um, C.Y. Wang, "Computational Fluid Dynamics Modeling of Proton Exchange Membrane Fuel Cells," *J. Electrochem. Soc.*, vol. 147, no. 12, pp. 4485–4493, 2000.

[125] P. S. Raju, P. V. V. N. R. P. Raju, K. V Sharma, and B. J. J. Raju, "Dynamic Modeling of a PEM Fuel Cell," *Eur. J. Sci. Res.*, vol. 43, no. 1, pp. 138–147, 2010.

[126] Y. Wang and C.-Y. Wang, "Transient analysis of polymer electrolyte fuel cells," *Electrochim. Acta*, vol. 50, pp. 1307–1315, 2005.

[127] H. Wu, X. Li, and P. Berg, "Numerical analysis of dynamic processes in fully humidified PEM fuel cells," *Int. J. Hydrogen Energy*, vol. 32, pp. 2022–2031, 2007.

[128] S. Shimpalee, W. K. Lee, J. W. Van Zee, and H. Naseri-Neshat, "Predicting the transient response of a serpentine flow-field PEMFC: I. Excess to normal fuel and air," *J. Power Sources*, vol. 156, no. 2, pp. 355–368, Jun. 2006.

[129] S. Shimpalee, W. K. Lee, J. W. Van Zee, and H. Naseri-Neshat, "Predicting the transient response of a serpentine flow-field PEMFC: II. Normal to minimal fuel and air," *J. Power Sources*, vol. 156, pp. 369–374, 2006.

[130] Y. Wang and C.-Y. Wang, "Dynamics of polymer electrolyte fuel cells undergoing load changes," *Electrochim. Acta*, vol. 51, pp. 3924–3933, 2006.

[131] S. Shimpalee, D. Spuckler, and J. W. Van Zee, "Prediction of transient response for a 25-cm2 PEM fuel cell," *J. Power Sources*, vol. 167, no. 1, pp. 130–138, 2007.

[132] G. Hu and J. Fan, "Transient computation fluid dynamics modeling of a single proton exchange membrane fuel cell with serpentine channel," *J. Power Sources*, vol. 165, pp. 171–184, 2007.

[133] S. Pasricha and S. R. Shaw, "A Dynamic PEM Fuel Cell Model," *IEEE Trans. Energy Convers.*, vol. 21, no. 2, pp. 484–490, 2006.

[134] X. D. Wang, J. L. Xu, W. M. Yan, D. J. Lee, and A. Su, "Transient response of PEM fuel cells with parallel and interdigitated flow field designs," *Int. J. Heat Mass Transf.*, vol. 54, pp. 2375–2386, 2011.

[135] P. R. Pathapati, X. Xue, and J. Tang, "A new dynamic model for predicting transient phenomena in a PEM fuel cell system," *Renew. Energy*, vol. 30, pp. 1–22, 2005.

[136] D. Natarajan and T. Van Nguyen, "A Two-Dimensional, Two-Phase, Multicomponent, Transient Model for the Cathode of a Proton Exchange Membrane Fuel Cell Using Conventional Gas Distributors," *J. Electrochem. Soc.*, vol. 148, no. 12, pp. A1324–A1335, 2001.

[137] K. H. Loo, K. H. Wong, S. C. Tan, Y. M. Lai, and C. K. Tse, "Characterization of the dynamic response of proton exchange membrane fuel cells - A numerical study," *Int. J. Hydrogen Energy*, vol. 35, no. 21, pp. 11861–11877, 2010.

[138] J. C. Amphlett, R. F. Mann, B. a Peppley, P. R. Roberge, and a Rodrigues, "A model predicting transient responses of proton exchange membrane fuel cells," *Journal of Power Sources*, vol. 61. pp. 183–188, 1996.

[139] J. Zou, X.-F. Peng, and W.-M. Yan, "Dynamic analysis of gas transport in cathode side of PEM fuel cell with interdigitated flow field," *J. Power Sources*, vol. 159, no. 1, pp. 514–523, 2006.

[140] M. Najjari, F. Khemili, and S. Ben Nasrallah, "The effects of the gravity on transient responses and cathode flooding in a proton exchange membrane fuel cell," *Int. J. Hydrogen Energy*, vol. 38, no. 8, pp. 3330–3337, 2013.

[141] S. Shimpalee, "Dynamic Simulation of Large Scale PEM Fuel Cell under Driving Cycle," *J. Electrochem. Soc.*, vol. 161, no. 8, pp. E3138–E3148, 2014.

[142] C. Y. Wang and P. Cheng, "A multiphase mixture model for multiphase, multicomponent transport in capillary porous media - I. Model development," *Int. J. Heat Mass Transf.*, vol. 39, no. 17, pp. 3607–3618, 1996.

[143] V. Starikovicius, "The multiphase flow and heat transfer in porous media," 2003.

[144] H. Wu, "Mathematical Modeling of Transient Transport Phenomena in PEM Fuel Cells," University of Waterloo, 2009.

[145] ANSYS Inc., "ANSYS FLUENT 12.0 Fuel Cells Module Manual," 2009.

[146] S. Mazumder and J. V. Cole, "Rigorous 3-D Mathematical Modeling of PEM Fuel Cells I. Model Predictions without Liquid Water Transport," *J. Electrochem. Soc.*, vol. 150, no. 11, pp. A1503–A1509, 2003.

[147] "Toray Carbon Fiber Paper - TGP-H-090." [Online]. Available: http://fuelcellstore.com/toray-carbon-paper-090.

[148] H. Wu, P. Berg, and X. Li, "Non-isothermal transient modeling of water transport in PEM fuel cells," *J. Power Sources*, vol. 165, no. 1, pp. 232–243, 2007.

[149] H. Ju and C.-Y. Wang, "Experimental Validation of a PEM Fuel Cell Model by Current Distribution Data," *J. Electrochem. Soc.*, vol. 151, pp. A1954–A1960, 2004.

[150] H. K. Versteeg and W. Malalasekera, *An Introduction to Computational Fluid Dynamics - The Finite Volume Method*, 2nd ed. Pearson Education Limited, 2007.

[151] S. V. Patankar and D. B. Spalding, "A calculation procedure for heat, mass and momentum transfer in three-dimensional parabolic flows," *Int. J. Heat Mass Transf.*, vol. 15, no. 10, pp. 1787–1806, Oct. 1972.

[152] Z. J. Peng and P. Choopanya, "CFD Investigation into Internal Flows of PEM Fuel Cell for Optimal Performances," *Adv. Mater. Res.*, vol. 724–725, pp. 757–761, 2013.

[153] P. Choopanya and Z. Peng, "An investigation on steady-state performance of conventional and serpentine flow-fields for automotive polymer electrolyte membrane fuel cell," in *1st SCODECE Internal Conference (2012 International Forum on Vehicle Control)*, 2012, p. 59.

[154] Fluent Inc., "Fluent 6.3 User's Guide," 2006.

[155] H. Wu, P. Berg, and X. Li, "Steady and unsteady 3D non-isothermal modeling of PEM fuel cells with the effect of non-equilibrium phase transfer," *Appl. Energy*, vol. 87, no. 9, pp. 2778–2784, 2010.

[156] ANSYS Inc., "Tutorial : Modeling a Single-Channel , Counter-Flow Polymer Electrolyte Membrane (PEM) Fuel Cell," 2011.

[157] M. M. Mench, C. Y. Wang, and M. Ishikawa, "In Situ Current Distribution Measurements in Polymer Electrolyte Fuel Cells," *J. Electrochem. Soc.*, vol. 150, pp. A1052–A1059, 2003.

[158] H. Weydahl, "Dynamic behaviour of fuel cells," Norwegian University of Science and Technology, 2006.

[159] H. Yu and C. Ziegler, "Transient Behavior of a Proton Exchange Membrane Fuel Cell under Dry Operation," *J. Electrochem. Soc.*, vol. 153, no. 3, pp. A570–A575, 2006.

[160] J. J. Baschuk and X. H. Li, "Modelling of polymer electrolyte membrane fuel cells with variable degrees of water flooding," *J. Power Sources*, vol. 86, no. 1–2, pp. 181–196, 2000.

List of Publications

1. P. Choopanya and Z. Peng, "An investigation on steady-state performance of conventional and serpentine flow-fields for automotive polymer electrolyte membrane fuel cell," in *1st SCODECE Internal Conference (2012 International Forum on Vehicle Control)*, 2012, p. 59.

2. Z. J. Peng and P. Choopanya, "CFD Investigation into Internal Flows of PEM Fuel Cell for Optimal Performances," *Adv. Mater. Res.*, vol. 724–725, pp. 757–761, 2013.

3. P. Choopanya and Z. Yang, "Transient Performance Investigation of Different Flow-field Designs of Automotive Polymer Electrolyte Membrane Fuel Cell (PEMFC) Using Computational Fluid Dynamics (CFD)," in *10th International Conference on Heat Transfer, Fluid Mechanics and Thermodynamics 14th-16th July*, 2014, pp. 583–592.

4. P. Choopanya and Z. Yang, "A CFD Investigation of Effects of Flow-field Geometry on Transient Performance of an Automotive Polymer Electrolyte Membrane Fuel Cell," *Comput. Therm. Sci. An Int. J.*, vol. 7, no. 2, pp. 93–104, 2015.